Nanostructured III-nitride light emitting diodes

Nuño Amador-Méndez

THESE DE DOCTORAT

NNT : 2022UPAST018

université PARIS-SACLAY

Nanostructured III-nitride light emitting diodes

Diodes électroluminescentes nanostructurées à base de nitrures d'éléments III

Thèse de doctorat de l'université Paris-Saclay

École doctorale n°575, Electrical, optical, Bio: Physics and Engineering (EOBE)
Spécialité de doctorat : Electronique et Optoélectronique, Nano- et Microtechnologies
Graduate School : Sciences de l'ingénierie et des systèmes.
Référent : Faculté des sciences d'Orsay

Thèse préparée dans l'unité de recherche **Centre de Nanosciences et de Nanotechnologies** (Université Paris-Saclay, CNRS), sous la direction de **Maria TCHERNYCHEVA**, Directrice de Recherche

Thèse soutenue à Paris-Saclay, le 18 Février 2022, par

Nuño AMADOR-MENDEZ

Composition du Jury

Jean-Christophe HARMAND Directeur de Recherche, CNRS-C2N, France	Président
Enrique CALLEJA Professeur, ISOM-UPM, Espagne	Rapporteur & Examinateur
Rachel GRANGE Professeure, ETH, Suisse	Rapportrice & Examinatrice
Benjamin DAMILANO Chargé de recherche, CNRS-CRHEA, France	Examinateur
Anna FONTCUBERTA i MORRAL Professeure, EPFL, Suisse	Examinatrice
Maria TCHERNYCHEVA Directrice de Recherche, CNRS-C2N, France	Directrice de thèse

université PARIS-SACLAY | DOCTORAL SCHOOL Electrical, Optical, Bio: Physics and Engineering (EOBE)

Titre : Diodes électroluminescentes nanostructurées à base de nitrures d'éléments III

Mots clés : nanofils, III-V, Nitrures, LEDs, GaN poreux

Résumé : Les diodes électroluminescentes (DEL ou LED en anglais) flexibles font l'objet d'une recherche intense, motivée par des applications telles que les écrans pliables, les sources de lumière conformables, les dispositifs biomédicaux, etc. La rigidité mécanique des dispositifs à base de semi-conducteurs inorganiques rend la fabrication de dispositifs flexibles à partir de structures à couches minces assez difficile, une micro-structuration de la couche active étant nécessaire. Dans cette thèse, à la place des couches bidimensionnelles, deux types de nanostructures de nitrure du groupe III sont étudiés, à travers deux approches : (i) approche ascendante (bottom-up) utilisant des nanofils cœur-coquille, et (ii) approche descendante (top-down) utilisant une structure poreuse.

L'encapsulant des nanofils dans une matrice de polymère permet de combiner la haute efficacité et la longue durée de vie des matériaux semi-conducteurs inorganiques avec la flexibilité des polymères. Des nanofils cœur-coquille, épitaxiés par MOCVD, ont permis la fabrication de LEDs à nanofils flexibles bleues et vertes.

Des nano-phosphores de couleurs d'émission différentes ont, en parallèle, été utilisés pour fabriquer une deuxième génération de LEDs blanches ainsi que des LEDs à nanofils flexibles rouges. Pour ces dernières, différentes stratégies ont été mises à l'épreuve : l'utilisation de nanofils à puits quantiques multiples InGaN/GaN enrichis en In, la conversion d'émission du bleu vers le rouge à base de phosphore ou bien l'emploi de nanofils en GaAsP.

Une approche par sublimation sélective fut appliquée pour porosifier des structures telles que puits quantiques simples InGaN/GaN et des structures de LED p-i-n. Dans ce manuscrit, je présente différentes études de structures poreuses. Les études optiques sont réalisées par cathodoluminescence. Je décris également l'optimisation de la technologie de fabrication des LEDs, qui a permis de démontrer la première LED InGaN/GaN poreuse, en comblant les pores avec du parylène afin d'isoler électriquement la structure.

Title : Nanostructured III-nitride light emitting diodes

Keywords : Nanowires, III-V, Nitrides, LEDs, porous GaN

Abstract : Flexible light emitting diodes (LEDs) are today a topic of intense research driven by applications such as bendable displays, conformable light sources, bio-medical devices, etc. The conventional inorganic semiconductor devices are mechanically rigid; the fabrication of flexible devices from thin film structures is quite challenging and requires micro-structuring and lift-off of the active layer. Instead of two-dimensional films, in this thesis two types of III-nitride nanostructures are studied: (i) a bottom-up strategy using core shell nanowires, and (ii) a top-down strategy using a porous structure.

Polymer-embedded nanowire membranes combine the high efficiency and the long lifetime of inorganic semiconductor materials with the high flexibility and transparency of polymers. I used MOCVD cores shell NWs for the fabrication of flexible blue and green NW LEDs, I also combined them with nanophosphors of different emission colors to produce a second generation of white LEDs with an improved color quality.

For the fabrication of red flexible NW LEDs, I tested different strategies, namely an all-InGaN route based on In rich InGaN/GaN MQW NWs with a down-conversion of the blue light by a red phosphor and a red emission from GaAsP NWs.

Selective area sublimation was demonstrated to be a promising approach to improve the luminous efficacy of defective GaN layers on Si. In my work, I analyzed the impact of porosification on InGaN/GaN single quantum wells and on p-i-n light emitting diode structures. The optical analyses were performed by cathodoluminescence demonstrating that the high temperature sublimation process does not degrade the QW emission while electron beam induced current microscopy showed that the p-i-n junction profile is also preserved after sublimation. I also describe the optimization of the technology for porous LED fabrication following several strategies. As a result, I demonstrated the first porous InGaN/GaN blue LED using parylene pore filling for electrical insulation.

A mi padre y a mi madre,
Gracias

ACKNOWLEDGMENTS

First of all, I would like to thank my thesis director, Maria Tchernycheva, for giving me the opportunity to do PhD under her supervision. During the last years, Maria taught me how to overcome different scientific challenges that we faced. She involved me in various exciting projects and gave me the opportunity to enjoy, learn and grow simultaneously during these last years.

I would like to thank all the members of the jury: Rachel Grange, Enrique Calleja, Benjamin Damilano, Jean Christophe Harmand and Anna Fontcuberta i Morral, for being part of this journey.

I would like to express my gratitude towards my teammates, Francois, Lu lu, Martina, Ahmed, Lorenzo, Omar and other colleagues from C2N, for sharing this amazing experience with me. Especially to Dr. Nan Guan, who introduced me to this topic and taught me how to work in the cleanroom, and Camille Barbier who helped me to start a social life in France.

My sincere thanks to Dr. Valerio Piazza, because from the very beginning he helped me in the lab, with administration, with social life, in hard times, and of course in good ones. I feel lucky to have shared this experience with you.

I would also like to thank my current C2N colleagues and ODIN team: Sophie, Tiphaine, Arup, Jules, Amaury, Anton, Mario, Linh, Stefanito, Arnaud, Marina, Adel, Oussama, Paul, Mathieu, and Jean Michel for the daily life, coffee breaks, and funny moments. Especially I want to thank future doctor Tanbir Sodhi for bearing with me these last years, but also for the fun and the moments when we were each other's confidantes.

In 2019, I had the opportunity to spend 6 months at Laboratory of semiconductor materials, at EPFL, headed by Anna Fontcuberta i Morral. From the first day, I became an LMSC member. My deepest gratitude to Anna and her amazing team: Wonjong, Akshay, Nick, Nico, Lea, Andrea, Simon, Lucas, Didem, Anna, etc... “Moltes gràcies, ha estat un gran plaer”.

Thanks to all the INDEED fellows and professors for all the schools, conferences and all the really nice shared moments around the world, Sabbir, Alex, Ridvan, Pablo, Aswathi, Timur, Vasilii, Nemanja, Manuel, Egor and Michael.

Last but not the least, I would like to thank the PIMENT team for all the training and help in the cleanroom, as well as for sharing good moments together: Nathalie, Etienne, Abdou, David, Cedric, Christophe, Jean Luc, Fabien, Xavier, etc... Thank you to all the staff of C2N who were kind and helpful at every moment.

Quiero agradecer todo el apoyo, la compañía, los viajes, las risas y los intensos debates a mis amigos en Paris, por todos los buenos momentos, gracias a Laura, Ana, Álvaro, Raquel, Víctor, Abel, Marina, Ander, Alba, etc… Y especialmente a Helena por aguantarme, tirar de mí, cuidarme y todo el apoyo durante este tiempo. Muchas gracias.

También a todos mis amigos en España, al grupo del Peñascales y Montellano y especialmente a Laura, Alvarito, Jose, y Víctor. To every friend who come to Paris too visited me and my friends from Berlin: Anna, Adi, Katerina and Eyyup.

Para terminar, quiero agradecer a mi familia, a mis primos, a mi tío Carlos y a mi tía Marian, a mis hermanas Cucus, Sonsoles y Gador, y sobretodo y especialmente a mi madre Marisol, por ser un ejemplo de lucha, sacrificio, no rendirse nunca y mirar adelante, cuidarme y quererme. El apoyo constante para alcanzar mis logros. Muchas gracias mama, te quiero mucho. También me gustaría recordar a mi padre, Eduardo, un ejemplo que siempre estará conmigo.

INDEX

ACKNOWLEDGMENTS ..... **IV**

INDEX ..... **VI**

INTRODUCTION **1**

1 SCIENTIFIC BACKGROUND **7**

1.1 III-NITRIDE MATERIAL SYSTEM 7
1.1.1 Structural properties of III-nitrides *8*
1.1.2 Polarization in III-nitrides *11*
1.1.3 Band structure *12*
1.1.4 Defects of III-nitrides *17*
1.1.5 Substrates *17*
1.2 LIGHT EMITTING DIODES 19
1.2.1 III-V LEDs *20*
1.2.2 Conventional thin film III-Nitride LEDs *21*
1.3 NANOWIRES 25
1.4 STATE OF THE ART OF III-N NW LEDS 28
1.4.1 MOCVD grown LEDs *28*
1.4.2 MBE grown LEDs *33*
1.4.3 Larger wavelength LEDs by MBE *38*
1.4.4 White LEDs *39*
1.5 SUMMARY 42

2 FLEXIBLE NW LIGHT EMITTING DIODES **43**

2.1 INTRODUCTION 43
2.1.1 Direct growth on flexible substrates *45*
2.1.2 Transferred nanowire leds on flexible substrates *45*
2.2 STATE OF THE ART IN OUR GROUP 46
2.2.1 Blue LED *47*
2.2.2 Green LED *48*
2.2.3 Multilayer LED *50*
2.2.4 White LED *50*
2.2.5 Nanophosphors *51*
2.2.6 Remaining open issues at the beginning of my PhD *53*
2.3 FLEXIBLE NANOWIRE LEDS FABRICATION 53
2.3.1 Nanowires growth *53*
2.4 FABRICATION PROCESS 56
2.4.1 Semi-transparent thin metallic p-contact *57*
2.4.2 PDMS encapsulation and peeling off *58*
2.4.3 n-contact *60*
2.4.4 p-contact: etching and silver nws *60*
2.5 IMPROVING THE LIGHT QUALITY OF FLEXIBLE NANOWIRE LEDS 64
2.5.1 Phosphors for white light quality optimization *64*
2.5.2 Pumping flexible nanowire LEDs *67*

2.5.3 Second generation flexible white nanowire LEDs *71*
2.5.4 Demonstration of a high-colour quality white flexible LED *72*
2.6 MECHANCIAL FLEXIBILITY 78
2.7 STRETCHABLE LIGHT EMITTING DIODES 79
2.8 THERMAL STUDY 81
2.9 CONCLUSION 86

3 TOWARDS RED FLEXIBLE LEDS 89

3.1 INTRODUCTION 89
3.2 FLEXIBLE NW LEDS BASED ON INGAN/GAN 91
3.2.1 Red phosphors for down conversion *92*
3.2.2 Structure of the selected phosphors *93*
3.2.3 Cathodoluminescence analyses of the phosphor emission: evidence of the green band *96*
3.3 INTEGRATION OF THE RED PHOSPHOR WITH INGAN NANOWIRES 100
3.4 INTEGRATION OF THE RED PHOSPHOR INTO THE BLUE FLEXIBLE LED 101
3.5 PERSPECTIVE: UV FLEXIBLE NW LED PUMP 102
3.6 RED LEDS BASED ON ARSENIDE-PHOSPHIDE NANOWIRES 102
3.6.1 Synthesis of GaAsP nanowires *103*
3.6.2 Nanowire optical characterization *104*
3.6.3 LED fabrication and testing *105*
3.6.4 Flexible red GaAsP LED *107*
3.7 CONCLUSIONS 109

4 POROUS NITRIDE LEDS 111

4.1 INTRODUCTION: POROUS SEMICONDUCTORS AND THEIR PROPERTIES 111
4.2 POROUS NITRIDES BY SELECTIVE AREA SUBLIMATION 114
4.3 GROWTH AND POROSIFICATION OF SINGLE QUANTUM WELL SAMPLES 116
4.3.1 Morphology of the porosified single quantum well sample *117*
4.3.2 Low-porosity central region *119*
4.3.3 Medium-porosity intermediate region *123*
4.3.4 High-porosity edge region *124*
4.4 ANALYSES OF THE ANNEALING TEMPERATURE ON THE FULL LED STRUCTURE 127
4.4.1 LED structure growth *127*
4.4.2 Effect of high temperature annealing while avoiding porosification *129*
4.5 LED POROSIFICATION, OPTICAL AND STRUCTURAL ANALYSES 131
4.5.1 CL studies of Porous LED *131*
4.5.2 Structural analyses of porous and reference LEDs *132*
4.5.3 Room temperature cathodoluminescence analyses of the low porosity region *136*
4.5.4 Low temperature Cathodoluminescence mapping of the porous LED *138*
4.5.5 EBIC on the cross-section *140*
4.5.6 LED fabrication and testing *142*
4.6 CONCLUSIONS 144
4.6.1 Flip Chip *144*

5 CONCLUSIONS 147

APPENDIX A: QUALITY OF THE LIGHT 151

CHROMATICITY COORDINATES AND CHROMATICITY DIAGRAM 151
CCT 153
CRI 154
REFERENCES 157
LIST OF PUBLICATIONS 177
ARTICLES 177
CONFERENCES 178
DIODES ELECTROLUMINESCENTES NANOSTRUCTUREES A BASE DE NITRURES D'ELEMENTS III 181

INTRODUCTION

The phenomenon called "electroluminescence" was reported in the first years of the XXth century. Henry Joseph Round observed that yellowish light was emitted by silicon carbide (SiC) Schottky diode when an electrical current flows through it [1], [2]. In the 1920s Oleg V. Losev studied this phenomenon [2], [3], however his works had not been relevant until the 1950s, already after his death in 1942 in the blockade of Leningrad. In 1955, Wolf et al. [4] demonstrated a light emitting diode (LED) based on a GaP single crystal that emitted deep a red and orange colour. GaP is an indirect bandgap semiconductor, so the luminescence was attributed to a transition through an energy level caused by an impurity within the bandgap [5].

A few years later, another important step to LED technology development was demonstrated by Folberth [6], who proposed to use ternary and quaternary alloys of III-V semiconductors and demonstrated the complete miscibility of GaP and GaAs which form $GaAs_xP_{1-x}$ (GaAsP). The first infrared LEDs based on GaAs were reported in 1962 simultaneously by several groups [7]–[10]. At the same time, first works on Ga(As)P p-n junctions LEDs were initiated for bringing up red LEDs [2]. In the mid of 70s, the introduction of nitrogen as a dopant for Ga(As)P enhanced the emission efficiency introducing an impurity level which allows efficient recombination. Consequently, yellow (GaAsP:N) and green (GaP:N) LEDs became possible [11].

The LED technology has continuously been improving and in the early 80s, heterostructures of materials with different energy bandgaps were introduced. A semiconductor sandwiched between two materials with larger bandgaps increases the luminescence efficiency by improving carriers localization in the same region and also introducing the 2D density of states characteristic for the quantum confinement in quantum wells [11].

In the short wavelength range, SiC blue LEDs were demonstrated, but with a very

poor efficiency and the work on II-VI semiconductors like ZnSe didn't improve the luminescence yield which was not compatible with commercial applications [11].

At the same time when H.J. Round achieved for the first time the light emission from semiconductors, in 1907, the first growth of polycrystalline AlN was reported [12]. Later, the growth of polycrystalline GaN [13] and InN [14] was demonstrated in 1932 and 1938, respectively. The growth of epitaxial thin films of monocrystalline GaN was not made until 1969 [15] when it was enabled by hybrid vapor phase epitaxy (HVPE) on sapphire. Finally, the epitaxial growth of nitrides was also achieved by metalorganic vapor phase epitaxy (MOVPE) [16] and molecular beam epitaxy (MBE) [17], in 1971 and 1974, respectively.

Although the technology of conventional III-V LEDs was available since the 70s and the synthesis of direct bandgap III-N semiconductors was achieved, GaN blue LED had not been demonstrated till 1993. The main problems to overcome in making nitride-based devices were the growth of high quality smooth films, the control over the n-doped conductivity, the p-type doping and the growth of AlGaN and InGaN alloys.

Initially the films were rough and cracked, which was attributed to the three-dimensional growth mode and the choice of a foreign substrate. In 1971 Dingle et al. [18] demonstrated the growth of epitaxial GaN layers and explore its optical and electrical properties. Later, in 1983, Yoshida et al. [19] demonstrated an improvement of electrical and luminescent properties of GaN films grown on AlN coated sapphire substrate. In 1986 Akasaki and Amano [20] reported high quality and smooth GaN films using an AlN buffer layer. Akasaki also demonstrated an effective and controlled n-doping by Silane (SiH_4). Regarding the p-type doping, magnesium was expected to be a good acceptor, but GaN:Mg was very resistive and didn't introduce hole carriers. Again, Akasaki and Amano in 1989, demonstrated that the highly resistive GaN:Mg films turned to p-type GaN with a high concentration of holes by low-energy electron beam irradiation (LEEBI) [21]. Magnesium forms a compound with hydrogen during the GaN growth, which can be dissociated either by LEEBI or by a thermal annealing after the growth, which allows to activate the Mg acceptor by removing the H atoms linked to it. This allowed to produce the first p-n junction blue LED [21]. Finally, Nakamura et al. reported the fabrication of efficient blue LEDs by introducing an InGaN quantum well in the junction in 1993 [22]. The Nobel Prize in Physics 2014 was awarded jointly to Isamu Akasaki, Hiroshi Amano and Shuji Nakamura "*for the invention of efficient blue light-emitting diodes which has enabled bright and energy-saving white light sources*" [23].

During the last decades, III-Nitrides have become one of the most promising candidates for novel applications in electronics, photonics, and optoelectronics domains. III-nitride materials, as third generation of semiconductors, have great capabilities compared with the first generation of semiconductors (Si and Ge) and

with the second one (GaAs-InP) such as a direct bandgap tunable in the near infrared to ultraviolet spectral range together with a high electron mobility.

The historical development of blue, green, red and "white" LEDs is summarized in Figure 0-1. Today's efficient LEDs are GaN-based.

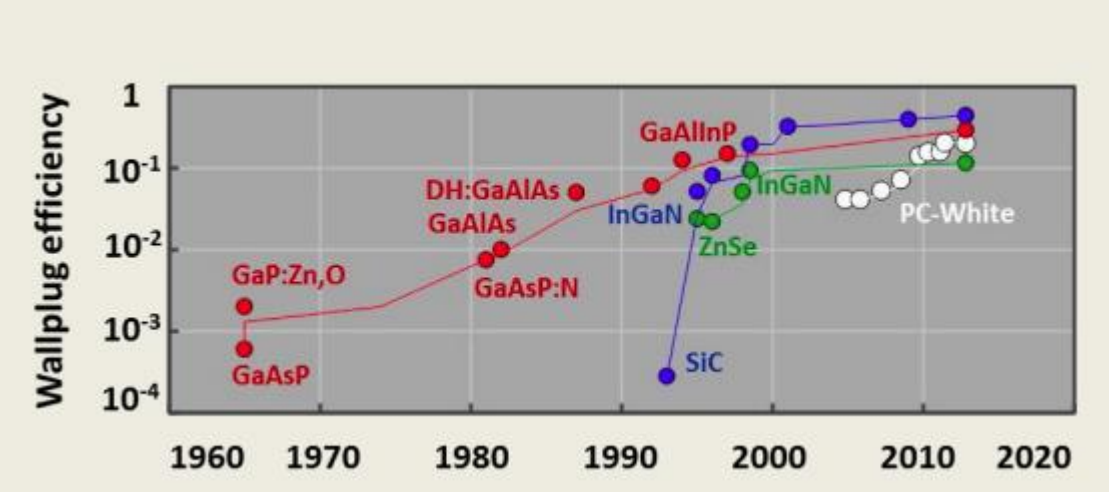

Figure 0-1.Historical evolution of red, green, blue and white (phosphor-converted) LEDs and their wallplug efficiency(ratio between emitted light power and supplied electrical power) [23].

Between 20-30 % of the electricity is used for lighting [23]. Illumination technology is going through a revolution: the light bulb of Edison invented in 1879 has an efficiency of only 16 lm/W, which represents a wall-plug efficiency of 4%. The fluorescent tube, invented by P.Cooper Hewitt in 1900, reached 70 lm/W. Nowadays, a white LED reaches 300 lm/W. This efficiency evolution is illustrated in Figure 0-2. Replacing the light bulbs and fluorescent tubes by LEDs is presently leading to a drastic reduction of electricity requirements.

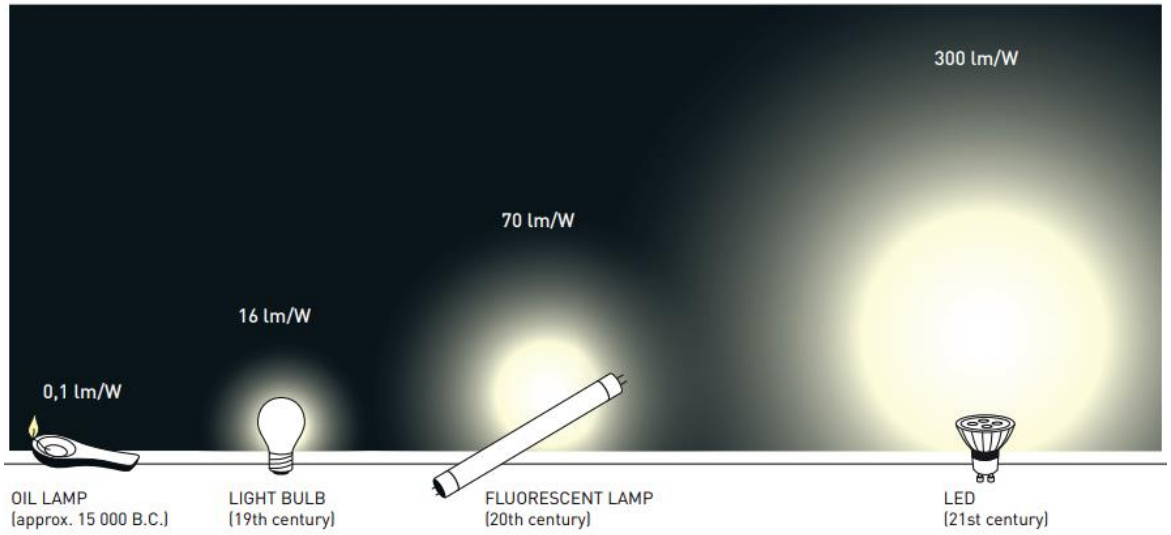

Figure 0-2. History of lighting tools and its light flux [23].

While the device design and the quality of GaN-based LEDs continue to progress,

alternative approaches for light emission using semiconductor nanostructures have emerged and attract today much interest. Semiconductor nanowires (NWs) are considered as a promising alternative for substitution of thin film technology thanks to their mechanical, optical and electrical properties. In addition, their high surface-to-volume ratio and the nanoscale dimensions can be exploited for the n fabrication of µ-LEDs with micronic sizes. III-nitride NWs also have a potential for novel applications overcoming the thin film technology such as for example devices with a high flexibility, biological sensors or high-resolution displays.

The objective of my PhD research is to develop novel III-nitride nanostructured LEDs with improved efficiency and presenting mechanical flexibility. My work was financially supported by three research grants : the European ITN project "INDEED -- Innovative Nanowire Device Design", ANR project "NAPOLI -- Nanoporous III-N semiconductors made by selective sublimation for optoelectronic" and "CEFIPRA" Franco-Indian programme Collaborative Research Programme entitled "Nanowire white LEDs based on innovative nano-phosphors". I have benefited from many scientific collaborations for the materials synthesis and characterizations. Namely, Akanksha Kapoor and Christophe Durand from CEA-Grenoble, who do the growth of MOCVD NWs used for flexible LEDs fabrication, Vladimir Neplokh from Alferov State University and his work on reinforced PDMS, Benjamin Damilano from CRHEA who develops and produces the porous LED samples, Pierre Ruterana who did the TEM characterization, Subrata Das who developed and synthetized the different phosphors used and Anna Fontuberta i Morral and Nicolas Tappy who taught me the cathodoluminescence technique and it analysis.

The manuscript is organized as follows:

Chapter 1 is dedicated to the scientific background. First, I describe the III-nitride materials system, namely their structural properties, polarization, band structure, defects and the substrates used for their synthesis. Then I introduce light emitting diodes, with a brief introduction to III-V LEDs and focusing on III-nitride LEDs. Next, I describe the properties of NWs and the advantages and drawbacks of these nanostructures. To conclude this first chapter, I present the state of art of III-Nitride NW LEDs.

Chapter 2 is fully dedicated to flexible NW LEDs. Our team has been working on these devices for several years, so I start the chapter with the state of the art in our group. Then I continue with the work I did on this topic, starting from the fabrication process and its optimization, improvement of the white flexible LEDs by phosphor conversion, the fabrication of a second generation of white flexible LEDs with improved light quality. For concluding this chapter, mechanical flexibility and thermal studies are presented.

Chapter 3 is devoted to red flexible NW LEDs. While in chapter 2, green and blue LEDs are described, one important building block for achieving a RGB flexible device

is the red flexible LED. Development of this missing part would allow further progress towards high-resolution flexible displays or flexible white sources with high ability for light tunning. This third chapter is dived in two main sections: (i) Attempts to elaborate red NW LEDs based on InGaN-GaN NWs grown by MOCVD and (ii) Red NW LEDs based on GaAsP NWs grown my MBE.

Chapter 4 focusses on porous LEDs. First, I introduce previous works on III-nitride porous materials, then I describe the effect of the pores on a GaN sample containing a single InGaN quantum well. Next, the effect of the high temperature annealing on a full LED structure is presented and the chapter is concluded with the demonstration of the first fully-porous LED.

In the last part of the manuscript, I summarize the main results of this thesis and present some perspectives for future work on these research topics.

1 SCIENTIFIC BACKGROUND

In this chapter, the main properties of III-nitrides are presented. In addition, the working principle of conventional LEDs are discussed as well as the innovative nanostructures and different approaches for developing better devices.

1.1 III-NITRIDE MATERIAL SYSTEM

Group III-nitrides are a third generation of semiconductor materials composed by nitrogen and metallic atoms from the third column, GaN, InN, AlN, their ternary alloys or even a quaternary alloy. The importance of these materials for optoelectronic applications arises from their direct bandgap and the possibility to tune it over a wide range of wavelengths, from the near infrared for InN (about 1900 nm), the UV (360 nm) for GaN, up to the UVC range, namely 210 nm for AlN [24], [25]. The bandgap energy vs. the lattice constant for the III-nitrides and other relevant semiconductor materials is shown in Figure 1-1.

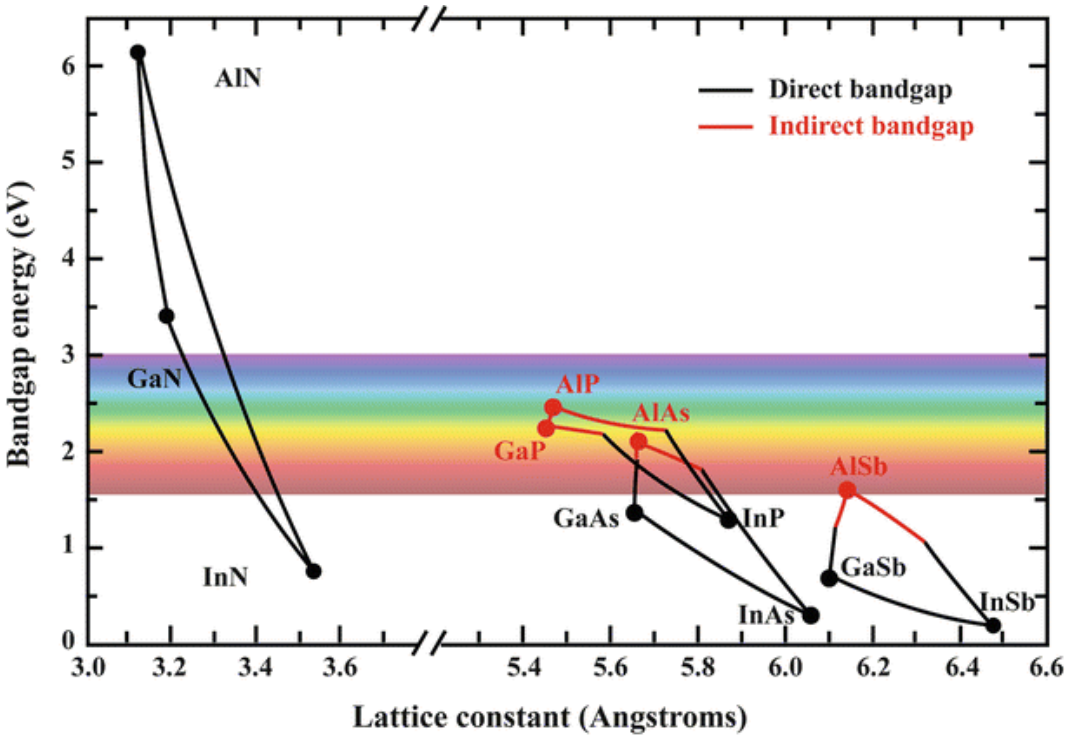

Figure 1-1. Bandgap energy in eV of the most important binary semiconductors versus their lattice constant at 300 K. Black dots and lines denote direct bandgap and red dots and lines indirect bandgap. Solid line between two binary compounds presents the parameters for the ternary alloy [26].

Ternary alloys bandgap energy follows the curve showed on Figure 1-1. For an alloy $A_xB_{1-x}C$, the bandgap energy can be calculated by the following equation [27]:

$$Eg_{(A_xB_{1-x})C} = xEg_{AC} + (1-x)Eg_{BC} - bx(1-x) \qquad (1\text{-}1)$$

where b is the bowing parameter (b_{AlGaN}=0.62, b_{InGaN}=1.43, b_{AlInN}=4.9 eV).

The covalent bonds between nitrogen and group-III atoms exhibit an ionic character that results from a huge difference in electronegativity. These materials have chemical resistance, high melting point (higher than 2500 K in the case of GaN [28]) and stability because of the strong bond[25].

1.1.1 Structural properties of III-nitrides

The group-III nitride materials crystallize in three different phases: i) the hexagonal wurtzite structure, ii) the cubic zinc-blende structure, and iii) the cubic rock-salt structure. The cubic rock salt-structure is not stable under standard conditions, it can be only induced at very high pressures. The stacking sequences of the zinc blende (ABCABC…) and wurtzite (ABABAB…) structures are shown in Figure 1-2 (a) and (b), respectively. Zinc-blende and wurtzite phases have similarities between them leading to a small energy difference of only 9.88 meV/atom between them in the case of GaN [29]. This small difference is detrimental for the crystalline quality due to the easy incorporation of crystal phase changes.

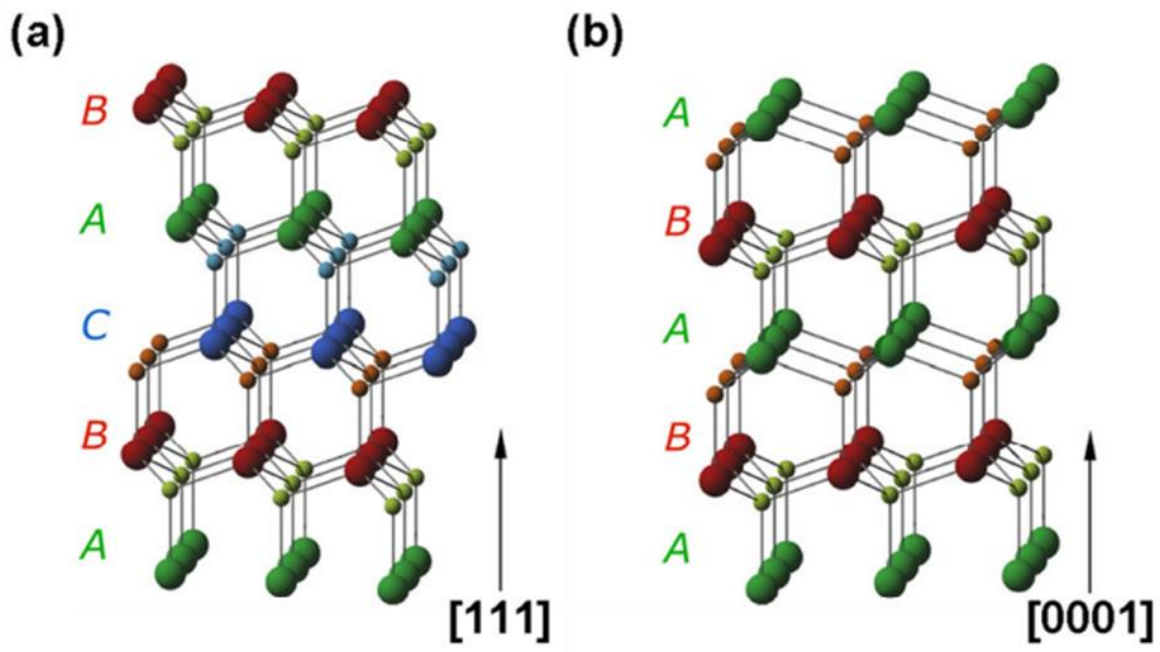

Figure 1-2. Stacking sequence of (a) zinc-blende structure and (b) wurtzite structure. The large balls represent group-III atoms (In, Ga or Al) and the small balls show N atoms, the arrow denotes the direction [111] for (a) zinc-blende and [0001] for (b) wurtzite. A, B and C in green, red and blue represent the lattice planes[2].

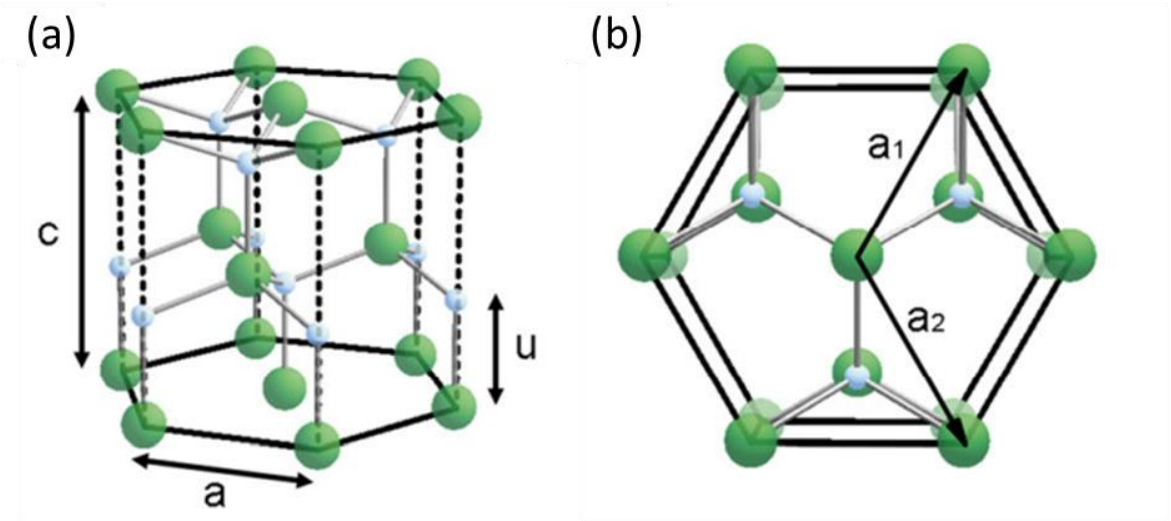

Figure 1-3. (a) and (b) are the lattice structure of hexagonal wurtzite along c-axis and top view, respectively. a, c are the lattice constants of the wurtzite structure and u is the offset between the two sublattices [31]

At thermodynamical equilibrium, group-III nitrides exhibit a wurtzite lattice structure, which can be seen as two hexagonal close packed sublattices, shifted from each other, one describing the position of group-III atoms, and the other that of nitrogen atoms.

The crystallographic planes in a hexagonal system are given by the Miller Bravais indices in the form (hkil) and the directions [hkil]. The hexagonal unit cell of the

wurtzite is characterized by two lattice constants, "a" and "c", which give the extension of the cell along the [1000] and [0001] directions, respectively. For an ideal wurtzite structure, between the two hexagonal close packed sublattices, the offset along the c axis is $u = \frac{5}{8}c$ and $\frac{c}{a} = \sqrt{\frac{3}{8}}$. These parameters are illustrated in Figure 1-3. The real structure deviates from the ideal one. The lattice parameters and the offset between the sublattices of AlN, GaN and InN at RT are shown in Table 1-1.

Table 1-1. Lattice parameters of wurtzite structure (a and c) and the offset between the sublattices for AlN, GaN and InN [32].

	a (Å)	c (Å)	u (Å)
AlN	3.08	4.950	0.3824
GaN	3.15	5.137	0.3815
InN	3.53	5.761	0.3780

The lattice constant for ternary alloys are defined by Vegard's law [33]:

$$a_{(A_xB_{1-x})C} = xa_{AC} + (1-x)a_{BC} \qquad (1\text{-}2)$$

The active region of the LEDs could be grown on the conventionally used (0001) polar c-plane, but also on non-polar (11-20) a-planes or (1-100) m-planes. All planes between the non-polar planes and the polar plane are termed semipolar planes. Schema of different planes of the wurtzite structure are shown on Figure 1-4.

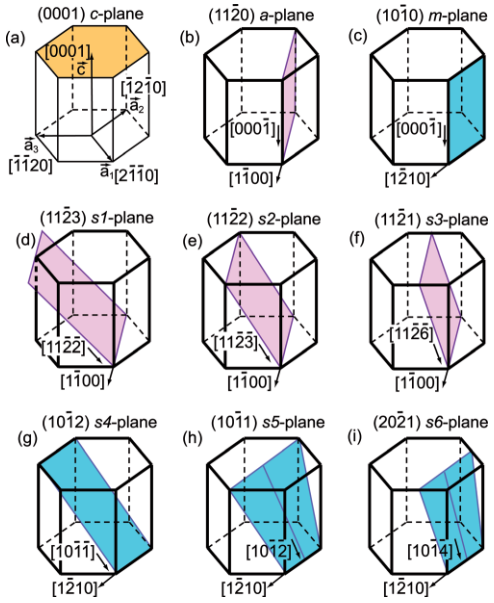

Figure 1-4. (a) Polar c-plane (b) and (c) nonpolar a-plane and m-plane, respectively. (d)-(i) examples of different semipolar planes [34].

1.1.2 Polarization in III-nitrides

An important issue for the wurtzite structure is the lack of inversion symmetry. In particular, it means that the direction [0001] is not equivalent to [000-1]. Group III-nitrides are called polar since the Ga-N dimmers, in the GaN case, can be described by a polarization vector pointing from N to Ga. This vector can be aligned parallel or antiparallel with respect to the growth axis, in the first case, the crystal structure is called N-polar, and for the antiparallel alignment, it is called Ga-polar (Al-polar or In-polar in case of AlN or InN). Figure 1-5 (a) and (b) shows the N-polar and group III polar structures, respectively, where the large green balls represent group III atoms, and the small blue balls show N atoms.

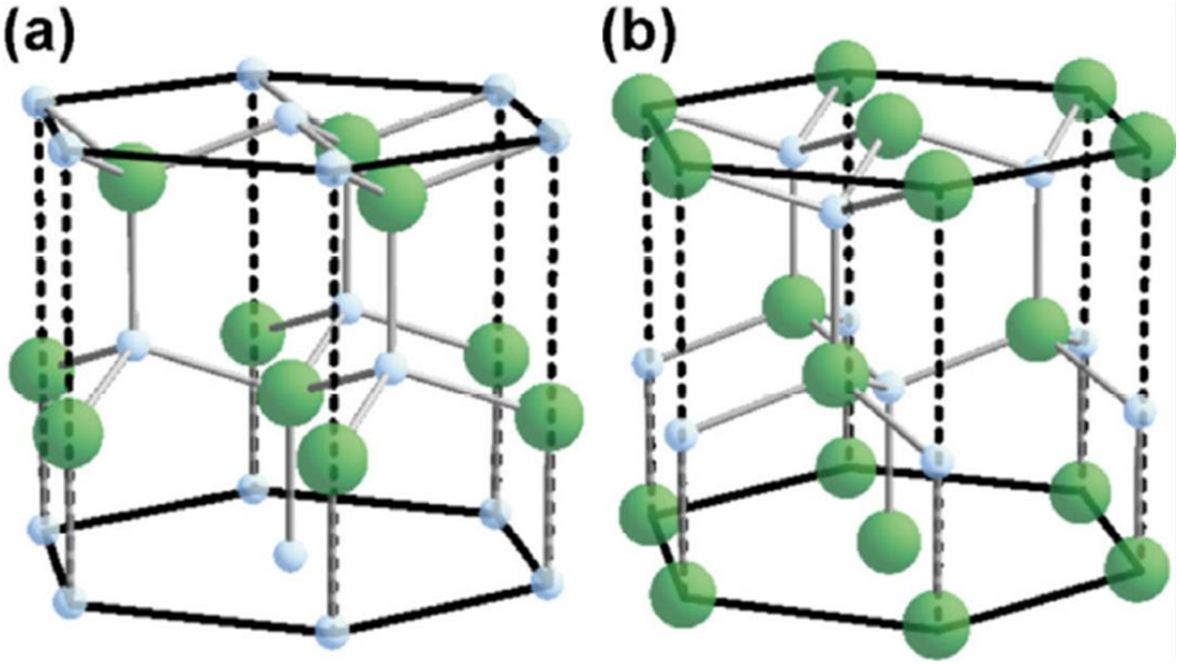

Figure 1-5. Schema of the wurtzite structure of (a) N-polar and (b) Group III polar III-nitride. The large green balls represent group III elements and small balls -- N atoms [31].

Due to the lack of inversion symmetry, the partial ionic character of the bond, and the tetrahedral arrangement in the wurtzite structure, III-nitrides are subject to strong polarization effects leading to spontaneous polarization. The spontaneous polarization is produced due to two reasons: i) the electronegativity difference between the atoms, which generates a local dipole moment between two bonded atoms ii) the non ideality of the crystal structure induces a net dipole moment, leading to a macroscopic polarization P_{sp} [30]. Since the spontaneous polarization partially depends on the electronegativity difference between the N and the group III atoms, the magnitude of P_{sp} increases from InN, passing by GaN, to AlN. The absolute values of the III-nitride materials of P_{sp} are: $P_{sp}(AlN)=0.09$ C/m^2, $P_{sp}(GaN)=0.034$ C/m^2 and $P_{sp}(InN)=0.043$ C/m^2 [35]. In addition to the spontaneous polarization P_{sp}, any mechanical strain will result in a polarization which is called the piezoelectric polarization P_{pz}. The total polarization can be calculated as the sum of

both, $P_{total}=P_{sp}+P_{pz}$.

III-Nitride LEDs are based on heterostructures consisting of AlGaN, GaN and InGaN, so the lattice could be under different strain states, compressive (e.g. InGaN on GaN) or tensile (e.g. AlGaN on GaN) strain, which generates a piezoelectric polarization in the LED structure. The difference of the spontaneous and piezoelectric polarization of different layers induces an internal electric field. In a LED, the light emission is produced by the carrier recombination in the quantum wells (QWs) (e.g. QWs formed by GaN/InGaN heterostructures). The presence of an internal electric field in the QWs leads to a spatial separation of the electrons and holes inside the confining potential, known as quantum confined Stark effect (QCSE) [30], [36]–[38]. The internal electric field produces energy band bending, which induces two relevant effects on the QWs: i) a redshift of the band transition energy because of the modification of the confined carrier energy level, resulting in a reduction of the transition energy when electron hole pair recombines and ii) the spatial separation of the carriers, reducing the wave function overlap, thus the probability of recombination ($|\psi|^2$), leading to large radiative lifetime and lower efficiency. The potential profile of a non-polar and polar InGaN QW with GaN barriers is schematized in Figure 1-6. The non-polar planes are not subject to any polarization field, neither spontaneous nor piezoelectric, therefore there is no QCSE in this case. For the polar QW, the bands are tilted as explained above.

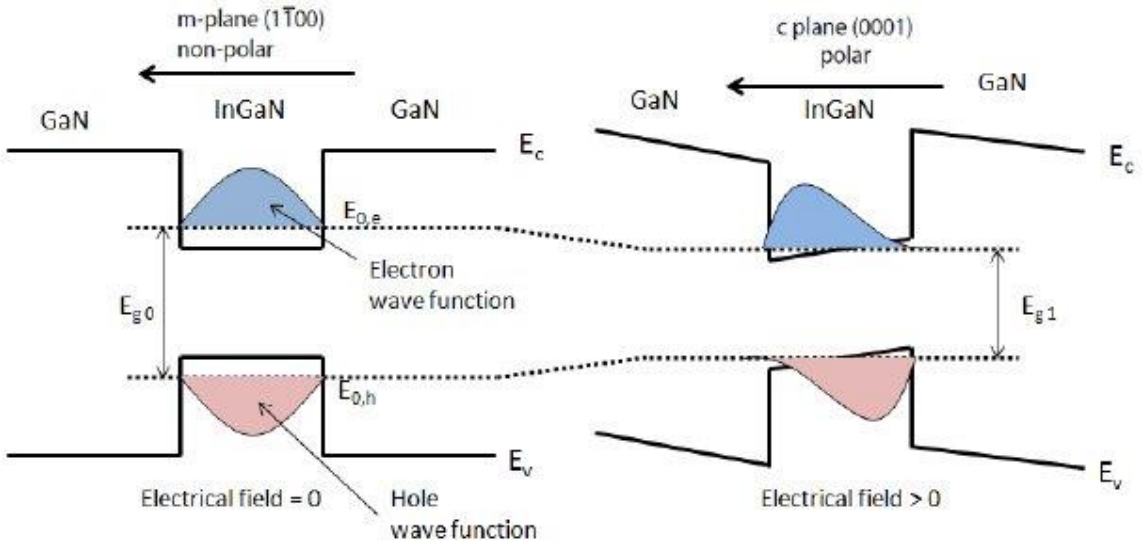

Figure 1-6. Schema of a InGaN/GaN QW for (a) non polar plane and (b) polar plane. The energy bandgap of the non polar plane Ego is larger than Eg1 on the polar plane reduced due to the band bending. In addition, the electron and hole wavefunctions have a stronger overlap on the non polar plane than on the polar plane [39].

1.1.3 Band structure

When atoms are arranged together in order to form a crystal, the electron wave function overlap leads to the formation of energy bands. In the case of

semiconductor materials, there is an energy gap between the conduction and the valence band edges. In direct bandgap semiconductors, like III-N materials, the conduction band minimum and the valence band maximum are located at the same position in k-space. The conduction band shape in GaN is mainly defined by Ga s-orbitals, in a parabolic dispersion, while the valence band maximum is formed by the N p-orbitals.

Electrons excited in the conduction band can recombine with holes releasing the excess energy in different ways. There are two main types of recombination processes. In the case of radiative recombination, the excess of energy is released by emission of photons. For non-radiative recombination, the excess of energy is released by other ways, such as phonon emission or Auger recombination.

The particularity of the semiconductors is that the carrier density in the bands can be tuned by changing the temperature as well as by incorporation of impurities, which we refer as dopants. Dopants are foreign atoms which are incorporated into the crystal lattice in order to modify the properties of the semiconductor. There are two different types of dopants, acceptors or p-dopants and donors or n-dopants. Acceptors have one electron less than the host atom while donors have one excess electron. In the case of a classical semiconductor material like Silicon or Germanium, with valence 4, the atoms of valence 5 will be donors while the atoms with valence 3 will be acceptors. In the case of the compound semiconductors, it depends on the nature of the host atom replaced by the dopant. For GaN, Si, O or Ge are used for n-doping while Mg is the typical acceptor. The semiconductor materials which include dopants in its lattice are named extrinsic semiconductors while the ones that do not include them are called intrinsic semiconductors.

In the intrinsic semiconductor materials, the energy in which the probability to find an electron or a hole is at the middle of the bandgap. This energy of equal probability is known as the Fermi energy, and it can be tuned by adjusting the amount of dopants. If the dopant quantity is very high, it is possible that the Fermi energy becomes higher than the conduction band minimum, in the case of donors, or lower than the valence band maximum if the dopants are acceptors. In these cases, the semiconductor materials are called degenerated.

Group-III-nitrides present a direct bandgap in the whole compositional range. The energy bandgap of unstrained GaN at 10 K is 3.504 eV [32]. With increasing temperature, the dilation of the material leads to a decrease in the energy gap. This decrease may be described using Varshni's law [40]:

$$E_g(T) = E_g(0) - \frac{\alpha T^2}{\beta + T} \qquad (1\text{-}3)$$

where α and β are fitting parameters. For GaN, $\alpha = 0.8\, meV/K$ and $\beta = 800\, K$ [32],

[41]. However, Varshni's law is purely empirical without physics behind it. A physically motivated model for the bandgap energy has been developed by Pässler:

$$E_g(T) = E_g(0) - \frac{\alpha\Theta}{2}\left(\sqrt[4]{1+\frac{\pi^2}{6}\left(\frac{2T}{\Theta}\right)^2+\left(\frac{2T}{\Theta}\right)^4}-1\right) \qquad (1\text{-}4)$$

where Θ is the effective phonon temperature and the parameter α represents the limiting slope [42]. Varshini's law [40] or Pässler model [42] fits well the evolution of the peak energy with temperature for GaN, however, InGaN/GaN heterostructures don't follow any of these models. As InGaN/GaN is the basic building block for an LED based on III-nitrides, the evolution of the bandgap energy has been largely studied by photoluminescence [43] and electroluminescence [44]. The behaviour observed is a so-called "S-shaped" peak energy shift. With the increasing temperature, between 10 and 70 K a redshift is observed, then a blueshift in the 70-150 K range takes place, and finally a redshift happens for temperatures above 150 K. In the low temperature range, the carrier motion is frozen, they are localized in local potential minima, with increasing temperature, the thermal energy of the carriers allows them to relax towards energy minima with a higher In content producing a redshift. This redshift is pronounced for high In content heterostructures like green InGaN/GaN LEDs because the In composition fluctuations produce a large amount of localization states. For temperatures in the range between 70-150 K the carriers get delocalized, they recombine not only in potential minima, but also in other regions, which increases the recombination energy, leading to a total blueshift of the energy peak. Finally, for temperatures above the 150 K the band gap decreases following Varshini's law [40] or Pässler model [42].

The In incorporation in InGaN/GaN is inhomogeneous and sometimes leads to In clusters. In principle, this is a drawback preventing a precise bandgap engineering and obtaining a narrow emission. However, in InGaN/GaN based devices, due to the In content fluctuations, the carriers are localized at potential minima. This localization of the carriers prevents them from travelling in the QW plane and being captured by non-radiative recombination defects. This localization increases the luminescence efficiency of the light emitting devices [45].

The most common approximation used for modeling the valence bands of GaN is the quasi-cubic description, which consists in modeling the wurtzite structure in a way similar to the zinc blende. This approximation is based on the fact that the first and the second closest neighbors are at the same position in both structures. The [0001] axis of the wurtzite corresponds to the [111] axis of zinc blende crystals. To model the anisotropy of the wurtzite, one introduces an uniaxial strain along the c-axis [41], [46].

In the wurtzite structure, the c-axis anisotropy leads to a splitting of the valence band into two subbands. The energy difference between the two subbands is called the crystal field splitting Δ_{cr} and the reported values for GaN are between 9 and 36 meV [47]. In addition, the spin orbit interaction splits the higher subband into two new subbands with an energy difference Δ_{so} of approximately 19 meV [47].

GaN thus presents three distinct valence bands, which are called A, B and C when going from high to low energies as illustrated in Figure 1-7. These bands are the analog of the heavy hole, light hole and split-off hole in Si, respectively. The excitons implying a hole from the corresponding band are called A, B and C excitons, respectively.

It is possible to analytically obtain the conduction, E_c and valence energies, $E_{v,A}, E_{v,B}$ *and* $E_{v,C}$ as a function of Δ_{cr} and Δ_{so}.

$$E_c = E_g + \Delta_{cr} + \Delta_{so} \tag{1-5}$$

$$E_{v,A} = \Delta_{cr} + \frac{\Delta_{so}}{3} \tag{1-6}$$

$$E_{v,B} = \frac{1}{2}\left(\Delta_{cr} + \frac{\Delta_{so}}{3}\right) + \sqrt{\frac{1}{4}\left(\Delta_{cr} + \frac{\Delta_{so}}{3}\right)^2 + \frac{2\Delta_{so}{}^2}{9}} \tag{1-7}$$

$$E_{v,C} = \frac{1}{2}\left(\Delta_{cr} + \frac{\Delta_{so}}{3}\right) - \sqrt{\frac{1}{4}\left(\Delta_{cr} + \frac{\Delta_{so}}{3}\right)^2 + \frac{2\Delta_{so}{}^2}{9}} \tag{1-8}$$

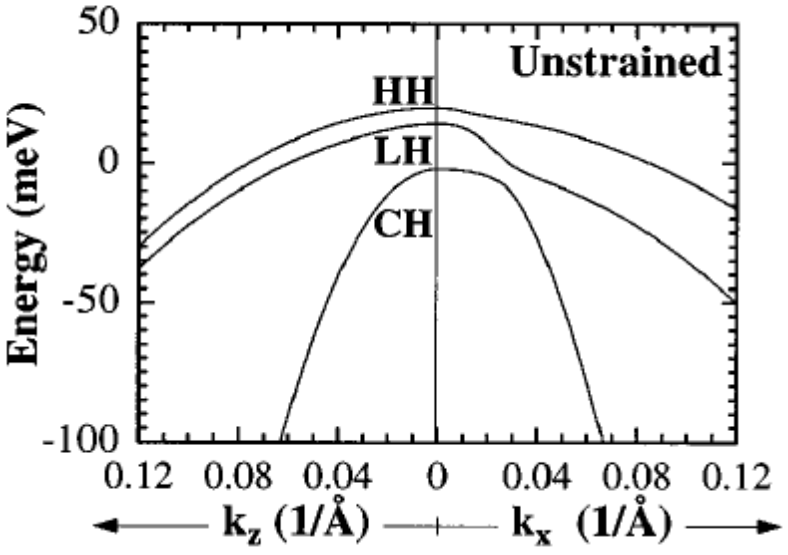

Figure 1-7. Valence band dispersion for unstrained wurtzite GaN crystal. The y-axis is the energy of the valence bands and the x-axis shows the reciprocal space for x and z directions

[48].

The energy dispersions near the band edges are deduced as a result of **k·p** simulations, and are approximated by a parabola [25], [28], [49].

$$E(k) = E_0 + \frac{\hbar^2 k^2}{2m_{eff}} \qquad (1\text{-}9)$$

where ħ is the Planck constant and E_0 is the energy at the center of the Brillouin zone ($k = 0$). The second derivative of this equation is the curvature of the energy band, which is inversely proportional to the effective mass, m_{eff}. In GaN, the effective mass of the electron is $m_e^* = 0.2m_0$, where m_0 is the electron rest mass. The effective masses for the valence bands in GaN are $m_A^* = 1.44m_0, m_B^* = 0.29m_0$ and $m_C^* = 0.57m_0$ [50].

As mentioned earlier, the radiative recombination of an electron with a hole leads to the emission of a photon. Upon excitation of GaN with an energy larger than the bandgap, free electrons and holes release the excess energy by emission of optical and acoustic phonons until they reach the band edges. At low temperatures and carrier densities, the Coulomb interaction between electrons and holes produces bound states called excitons. A free exciton can be described by the Hydrogen atom model, where the hole plays the role of the proton. The energy of the exciton, E^X is given by:

$$E^X = E_G + \frac{\hbar^2 k^2}{2(m_e^* + m_h^*)} - E_b^{FX} \qquad (1\text{-}10)$$

where the first term is the bandgap energy, the second term refers to the kinetic energy of the exciton and the last term is the free exciton binding energy. m_e^* and m_h^* are the effective masses of the electron hole pair involved in the exciton. In bulk GaN, at low temperature, the excitonic energies are $E_A^X = 3.477\ eV, E_B^X = 3.482\ eV\ and\ E_C^X = 3.498\ eV$ [51].

The exciton binding energy is given by

$$E_b^{FX} = -\frac{1}{n^2}\frac{\mu R_y}{\varepsilon^2} \qquad (1\text{-}10)$$

where Ry is the Rydberg constant (13.6 eV), μ is the reduced mass of the exciton which is given by $\frac{1}{\mu} = (\frac{1}{m_e^*} + \frac{1}{m_h^*})$, n the excitation state of the exciton and ε is the background dielectric constant of the material. Clearly exciton recombination energy is lower than that of free e-h pairs. The exciton binding energy is $E_b^{FX} = 25\ meV$. Because of the high binding energy, GaN presents excitons up to RT,

becoming a promising material for RT exciton-based applications.

1.1.4 Defects of III-nitrides

The wurtzite cell corresponds to an ideal case where all the atoms are fixed at the lattice position. In a real crystal, the atoms positions are affected by thermal fluctuations, strain, as well as by the presence of defects in the structure [47].

The strain of the lattice structure changes important properties of the materials such as the bandgap energy. The bandgap energy decreases under tensile strain while increasing under compressive strain.

Dislocations are one dimensional imperfections in the crystal also called extended defects. Misfit dislocations are generated by a strain accommodation at the interface of two materials with different lattice constants. Threading dislocations are related to crystallographic misorientation formed at the coalesced boundaries of microcrystals. Theses defects are non-radiative recombination centers.

Other extended defects in GaN are stacking faults (SF). They are defects in the stacking sequence of the different planes. At a stacking fault, wurtzite stacking sequence turns locally into the zinc blende stacking. As mentioned previously, the zinc blende phase has crystallographic similarities with the wurtzite structure leading to a small energy difference between them of $\Delta E_{wz\text{-}zb}$=-9.88 meV/atom [41]. This fact is detrimental for the crystal quality due to the easy change of crystal phase. In bulk GaN the stacking faults are introduced by dislocations. This phenomenon is known as polytypism [6], it also leads to localization of carriers resulting from the difference in the energy gap of the different structures [47]. In GaN this phenomenon is difficult to control [28] due to the small energy difference, however, in other semiconductor, like GaAs, confinement of carriers can be engineered by controlling the crystal phase change [53].

1.1.5 Substrates

To obtain a device with a good luminescence efficiency, regardless of the semiconductor, it was believed that very low dislocation densities are required, less than 10^6 cm^{-2}. However, InGaN based LEDs exhibit a good luminescence efficiency despite dislocation densities four orders of magnitude higher. Unlike the majority of semiconductors, in InGaN dislocations up to a certain density can be tolerated – they do not dramatically degrade its optical and electrical properties thanks to in-plane carrier localization on alloy fluctuations [54]. Nonetheless, a high quality material is needed to reach even higher efficiencies.

Perhaps the largest obstacle for the growth of high quality III-nitrides devices has been the lack of a good lattice-matched substrate. It is difficult to obtain large GaN crystals of high structural perfection, which could be used as substrates for the

growth of heterostructures. Although, it is possible to produce GaN wafers, they are still very expensive [41].

GaN and its group-III-nitride alloys have been grown by heteroepitaxy on a large variety of single crystalline substrates like Si, 6H-SiC [55], 3C-SiC [56], MgO [57], ZnO [58], GaAs [59] or sapphire. Among these substrates, the most popular are sapphire (α-Al_2O_3), silicon carbide (SiC) or silicon (Si) [30], [41], [60], [61].

The favorable physical properties, high quality, and low cost of silicon (Si) make it a very attractive substrate for GaN-based devices. Silicon technology is mature and allows large-scale production. The substrate thermal stability under GaN epitaxial growth conditions is good and the crystal perfection of silicon is better than that provided by any other substrate. The possibility of integrating optoelectronic GaN devices with Si electronic devices is also very attractive. However, the quality of GaN epitaxial layers on silicon has been poorer than that on sapphire or silicon carbide, due to the mismatch in lattice parameters and the difference in the thermal expansion coefficient, which results in large densities of extended defects (10^7-10^{10} cm^{-2})[47] and eventually in the appearance of cracks. Instead of using the conventional Si (100) orientation, the heteroepitaxy of III-nitrides is performed on Si (111) which shows a more suitable symmetry, even though, the lattice mismatch is 16.9%. Nevertheless, the incentives for using Si substrates remains high [54].

SiC is the best suited substrate for nitride devices due to a smaller mismatch (3.3%) and higher thermal conductivity, it also can be electrically conductive. Conductive substrate is a great advantage from the fabrication point of view, it allows to make electrical contacts on the backside. In addition, Si-polar and C-polar SiC substrates are available, which potentially can facilitate the polarity control of GaN. However, SiC substrates present several disadvantages such as a poor wetting, high surface roughness, and also high cost [54].

Finally, sapphire (α-Al_2O_3) was the original substrate used by Maruska et al. [15] for GaN epitaxy by HVPE, and it remains the most commonly used GaN substrate. Sapphire wafers are relatively cheap and present the best properties in terms of mismatch in thermal expansion coefficient. To reduce the high lattice mismatch (~15%), the planes between the sapphire and the GaN epitaxy layer are turned by 30^0 degrees. The growth on the sapphire substrates is the most used nowadays in commercial LEDs [54].

The use of buffer layers has dramatically improved crystallinity, film morphology, and electrical and optical properties of the epitaxial layers. A buffer layer is an intermediate layer which is used to accommodate mismatch between the epitaxial layer and the substrate. The defect generation is reduced but it also increases the costs, the complexity, and the reproducibility of the full stack.

The problem of dislocations and cracks in thin films can potentially be solved by a

3D structure engineering. For example, either bottom-up approaches such as nanowires (NWs) or top-down ones as porosified structures are alternatives for high quality crystal growth on lattice mismatched substrates.

1.2 LIGHT EMITTING DIODES

There are three basic interactions between a photon and an electron in a crystal: absorption, spontaneous emission and stimulated emission (cf. Figure 1-8). Solar cells and photodetectors are devices based on the photon absorption, lasers are based on stimulated emission and light emitting diodes are based on the spontaneous emission of photons.

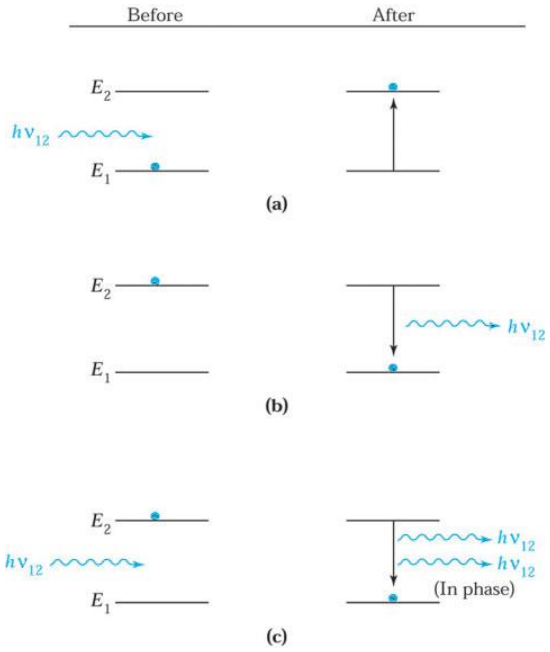

Figure 1-8. The three basic transition processes between two energy levels. 1 Blue dots indicate the state of the atom. The initial state is at the left; the final state, after the transition, is at the right. (a) Absorption. (b) Spontaneous emission. (c) Stimulated emission [62].

The basic structure of a LED is a p-n junction. Under forward bias electrons are injected from the n-side and holes from the p-side, and when the injected carriers are in the vicinity of the junction, electron hole recombination takes place, and a photon is emitted as illustrated in Figure 1-9 (a) and (b). The real structure of a LED consists in a heterostructure of quantum wells, made by a material with a lower bandgap energy, where the injected carriers are confined (cf. in Figure 1-9 (a)). The radiative recombination lifetime is shortened due to the high electron hole wavefunctions spatial overlap, and a more efficient radiative recombination is obtained. It is useful to note that to convert the wavelength to photon energy, the relationship showed below is used

$$\lambda = \frac{c}{v} = \frac{hc}{hv} = \frac{1239.847}{hv\ (eV)}\ nm \qquad (1\text{-}11)$$

where c is the speed of light in the vacuum, v is the frequency of light, h is Planck's constant and hv is the energy of a photon in eV [62].

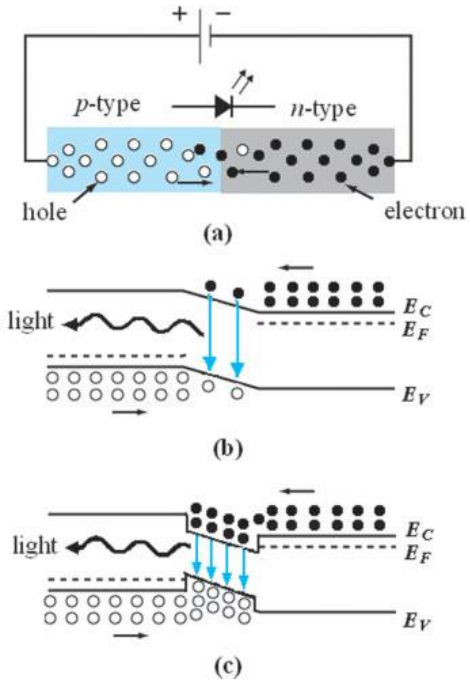

Figure 1-9.(a) Under forward bias of a p-n junction, electrons injected from the n-side recombine with holes injected from the p-side. (b) Energy band scheme of the electron hole recombination in a p-n junction and (c) Energy band scheme in a p-n junction containing a double heterojunction [62].

1.2.1 III-V LEDs

The advent of visible LEDs made of III-V semiconductors dates back to 1955, when Wolf et al. [4] demonstrated a LED of GaP single crystal that emitted deep red and orange colors. GaP is an indirect bandgap semiconductor, so the luminescence was attributed to a transition through an energy level caused by an impurity within the bandgap [5]. Few years later, an another important step to LED technology development was done by Folberth [6], who proposed to use ternary and quaternary alloys of III-V semiconductors and demonstrated the complete miscibility of GaP and GaAs which forms $GaAs_xP_{1-x}$ (GaAsP). In addition, Forbeth proposed and demonstrated p-n junction devices using ternary alloys which led to the first commercial red GaAsP LED offered by General Electric company in the early 1960s [5].

At the same time, GaP pn junction devices were developed by introducing impurities such as N or O to generate levels within the indirect bandgap to increase the efficiency of the red LEDs, technique which later was extended to GaAsP LEDs for the same purpose. However, GaAsP or GaP grown on GaAs substrates are lattice mismatched system, which leads to defective materials, resulting in poor efficiencies

despite introducing impurity levels.

At the end of the 1980s, the AlGaInP material system was thoroughly investigated leading to the demonstration of red, orange and yellow LEDs [63]–[65]. This technology dominates the large visible wavelength LEDs market until nowadays, with improved structures such as using multiple QWs and distributed Bragg reflectors [5], [66].

The dominant technology is based on $(Al_xGa_{1-x})_{0.5}In_{0.5}P$ alloy. AlP and GaP have a similar lattice constant, $(Al/Ga)_{0.49}In_{0.51}P$ is lattice matched to GaAs substrates which ensures a high quality epitaxial growth, leading to good optoelectronic properties. $Ga_{0.5}In_{0.5}P$ produces a red light emission at 650 nm. By introducing Al into GaInP, the bandgap can be increased up to 2.52 eV in AlP (indirect bandgap). The Al/Ga ratio in the AlGaInP alloy can also be tuned to form an electron blocking layer [64], [67].

Nowadays the available green LEDs are realized by using GaP:N or AlGaInP LEDs, but also InGaN/GaN heterostructures with a high In content (called "true-green" LEDs [68]) [69].

Blue has been for a long time the missing colour (while green and red LEDs were available since the 1970s). It appeared only in 1993, when Nakamura et *al.* reported the fabrication of efficient blue LEDs [22].This triggered a big interest in the development of white LEDs for general illumination because LEDs have a much higher efficiency and a longer lifetime than the incandescent lamps. White light can be produced by mixing two or three colours in an appropriate ratio. There are two approaches for achieving white light. The first consists in combining the three-light LED primary colours, red, green and blue, and the second approach, most commonly used, consists in the use of a single LED, covered by a colour converter, generally by a phosphor. The classical approach in commercial devices uses a blue LED covered by a yellow phosphor. The conversion efficiency of the phosphor can be close to 90% and the phosphor reemits light with a broader spectrum than the pump LED [70]. The mixture of the blue light from the LED with the broadband yellow emission of the phosphor results in a white light.

1.2.2 Conventional thin film III-Nitride LEDs

Conventional thin film LED based on III-nitrides are normally grown on a sapphire substrate. A basic LED structure consists of a buffer layer, an n-doped GaN layer for electron injection, several InGaN/GaN QWs as an active region, and a p-doped GaN layer for hole injection. In addition to these basic layers, an electron blocking layer (EBLs) of AlGaN, with a higher bandgap can be added, commonly used to reduce the electron overshoot into the p-contact region, leading to an efficiency enhancement [71]. Another common layer in these devices is an InGaN/GaN superlattice, which consists of a periodic structure on the n-side part of the LED, before the MQWs, which improves the LED performance [72]. The typical LED

structure is schematically illustrated in Figure 1-10

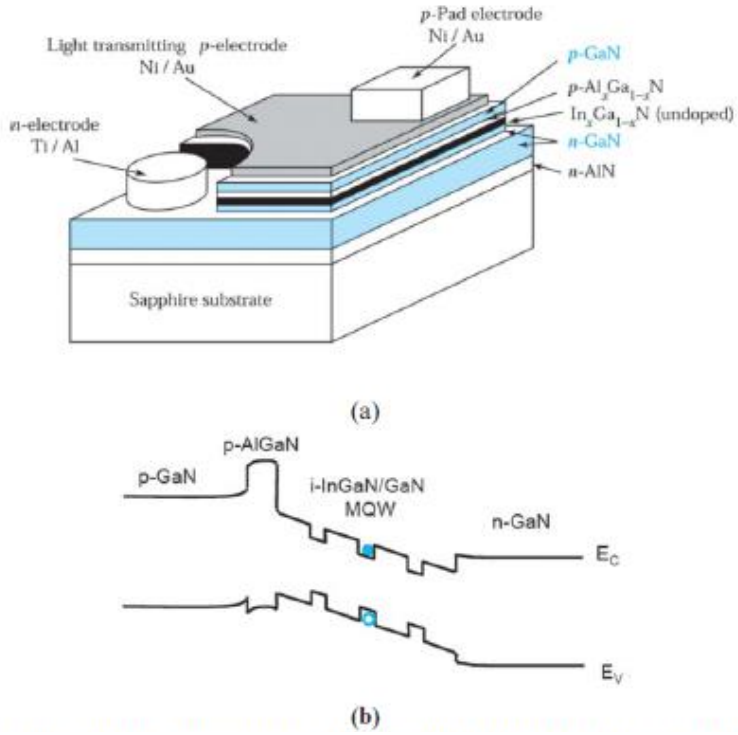

Figure 1-10. (a) Schema of a III-nitride LED grown on a sapphire substrate and (b) energy band schema of the device, the active region is embedded between the n-GaN and p-GaN layers, electron blocking layer of AlGaN, and intrinsic region of InGaN/GaN multi quantum wells are shown. [62].

It has been observed that III-nitride LEDs suffer from the loss of efficiency for (i) operation under a high current injection (referred to as "efficiency droop") and (ii) for increasing In content in the MQW to achieve emission in the green-yellow range. The decrease of the radiative recombination with increasing In amount is stronger than what can be expected from the QCSE [73]. To interpret the efficiency of III-nitride LEDs, the ABC model is often used [74], which describes the total recombination rate as:

$$R = An + Bn^2 + Cn^3 \qquad (1\text{-}12)$$

where A is the defect-related Shockley-Read-Hall recombination parameter, B is the radiative recombination related parameter, C is the Auger related recombination coefficient and n is the carrier density. The internal quantum efficiency (IQE) is defined as the ratio between the number of photons emitted from the active region to the number of electrons injected into the LED. Using this model, the IQE is given by

$$IQE = \frac{Bn^2}{An + Bn^2 + Cn^3} \qquad (1\text{-}13)$$

Bn^2 term is related to the radiative recombination (Figure 1-11 (b)), it becomes dominant at medium injection currents. Defect related non-radiative recombination is defined by the first term of the ABC model, An, which assumes that the non-radiative recombination is proportional to the carrier density. Defects introduce energy levels states inside the bandgap, which allow for the electron hole recombination without light emission.

Cn^3 describes the efficiency droop at high currents, this term becomes dominant because of the high values of n^3. In this situation of high injection current, the interaction between high density carriers produces a three-body Auger effect (e.g. an electron from the conduction band recombines with a hole transferring the energy to another electron as kinetic energy, later dissipated as heat, without light emission, as schematized in Figure 1-11 (c)) [30], [75], [76]. In addition, under high injection a carrier overflow over the EBL appears as schematically shown in Figure 1-11 (a) also leading to the efficiency loss.

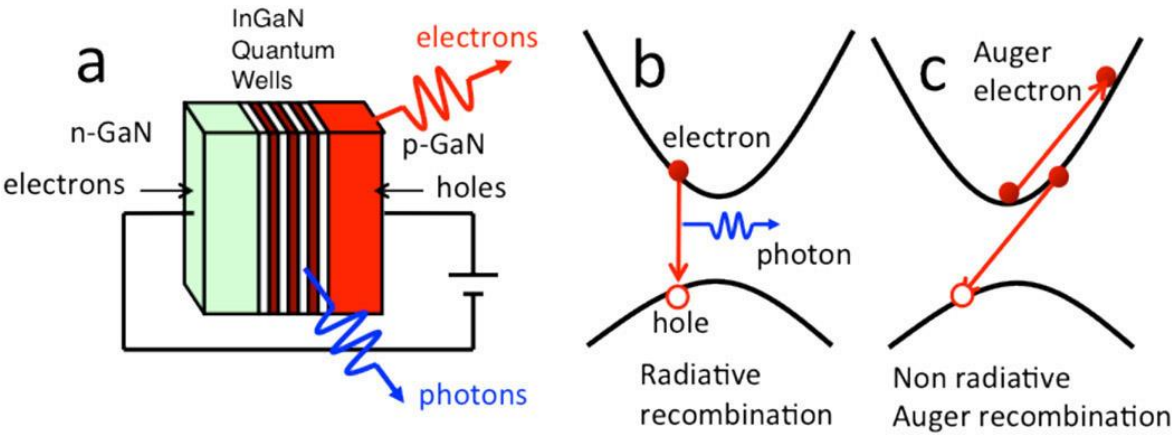

Figure 1-11. (a) Schematic of an LED under current injection. (b) Electrons and holes recombine radiatively in the quantum wells by emitting photons. (c) example of the Auger recombination: an electron-hole pair recombines without emitting a photon by exciting another electron to a high kinetic energy state [75].

The "green gap" refers to the efficiency reduction for high In content LEDs [77]. Increasing the In content leads to InGaN alloy fluctuations, In clusters and defects induced by the strain in the active region, which reduce the efficiency. Another contribution to the green gap is due to the QCSE: the piezo polarization increases, enhancing QCSE therefore the electron-hole wavefunction overlapping is reduced. We note that for conventional phosphide LEDs (right part of Figure 1-12) the efficiency is also reduced when coming to the green domain since the material approaches the direct/indirect bandgap crossing and the barriers become indirect bandgap materials.

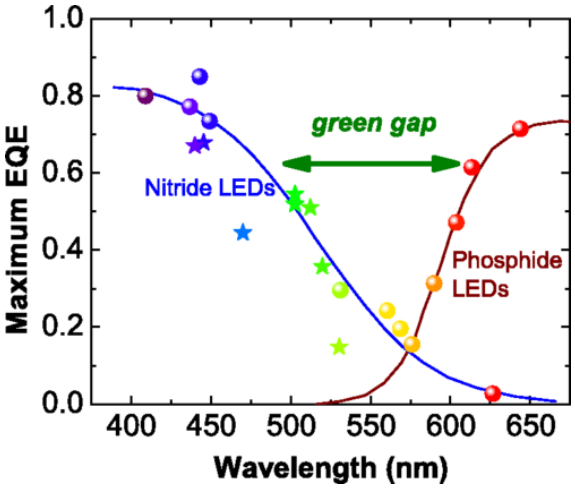

Figure 1-12. Maximum EQE efficiency of different nitride and phosphide LEDs illustrating the so called "green gap" [77].

The external quantum efficiency (EQE) is defined as the number of photons emitted per injected electron. It can be separated into internal quantum efficiency (IQE), discussed above, and optical photon extraction efficiency n_{ext}.

$$EQE = n_{ext}\, IQE \qquad (1\text{-}14)$$

The extraction efficiency depends mainly on the two following factors: i) the material reabsorption (photons produced have to go out of the LED structure, but before escape, they can be reabsorbed by the material), and ii) the total internal reflection (TIR) at the interface device-air, which traps photons inside the device, that become extinct through the reabsorption as illustrated in Figure 1-13

Since the reabsorption losses are unavoidable, it is important to reduce the effects of the TIR to enhance the EQE of the device [78]. Surface treatment, roughening, texturization, use of shaped substrates or micropatterning are classical methods to improve the light extraction [48]–[55]. It can also be achieved by the growth of nanorods [83], dry etching [81], wet etching [80] or surface porosification [82].

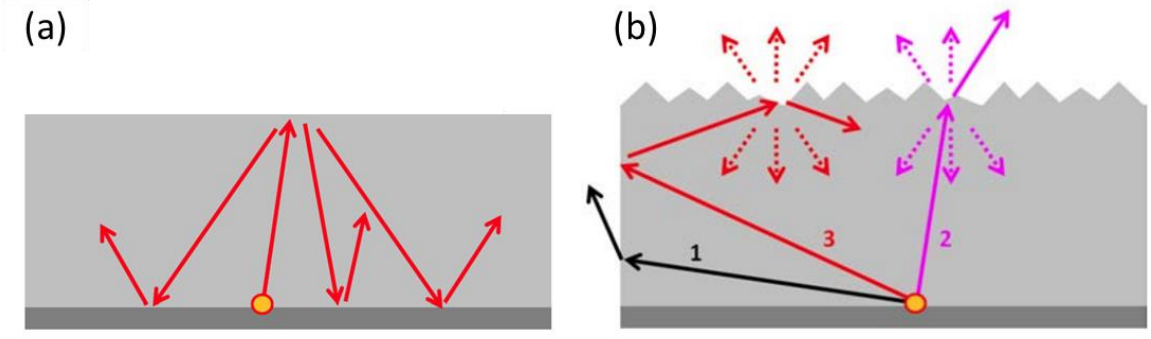

Figure 1-13. Schema of the TIR on (a) a planar surface and (b) texturized surface [85].

Any substrate lattice mismatch, QCSE on polar planes, bad extraction efficiency and bad crystal quality with high dislocation densities is source of efficiency losses, which

have motivated a strong research effort on alternative LED architectures based on III-nitrides nanostructures.

Nanostructuring can be obtained by either a top-down or a bottom-up method. The top-down approaches typically use lithography and dry etching of a thin film LED to form needles, NWs or other structures at well-controlled positions. In my PhD I have investigated an original top-down approach – selective area sublimation (SAS), which produces porous layers. Recently, Damilano et al. have reported a significant improvement of GaN crystal quality and optical properties with this novel SAS procedure [86]. A more detailed description and the application of SAS to LEDs will be given in chapter 4 Porous nitride LEDs.

Another nanostructuring approach that I have worked with is based on the bottom-up growth of nanowires. Below I present the nanowire properties and the present state of the art of NW LEDs.

1.3 NANOWIRES

In 1964, Wagner and Ellis developed a method for the growth of Si wires from vapor, named as vapor-liquid-solid (VLS) mechanism [87]. This was the first report on nanowires, which were named at that time as "whiskers". Today the VLS mechanism is one of the most used methods for the synthesis of NWs and an intensive review can be found in ref. [88] by Fontcuberta i Morral et al.

Nanowires are structures with a big aspect ratio which allows them to accommodate the lattice mismatch with the substrate either by the deformation of the free sidewall or, for larger diameters, through a network of misfit dislocations at the interface [89]. Thus, NWs are single crystals that are fully relaxed and free of dislocations which can be grown on a large variety of substrates, without lattice matching constraint.

There are two different approaches for the fabrication of NWs, the top-down or bottom-up approaches, the bottom-up approaches being the most used since it offers the best crystal quality. The top-down approaches use lithography and dry etching of a thin film [90], [91], it allows a good control over the layer thickness and doping profile in addition to the possibility to relax the strain. However, dry etching induces surface damages. Bottom-up approaches also give a larger design freedom. NWs arrays can be grown in an arbitrary way in case of self-assembled NWs, or at predefined positions in case of selective area growth (SAG). The resulting NWs have a high structural quality, however the self-assembled NWs present some dispersion in the fill factor, length, and diameter while the selective area growth NWs provides a high control over the size and density of NWs.

Since the late 90s, when the growth of GaN NWs was achieved by molecular beam epitaxy [92], [93] the growth of group III-nitride NWs has been the subject of an intense research effort. The high quality of the crystal improves the optical and

electrical properties, making these structures very promising candidates for high efficiency devices.

Different approaches (axial and radial) can be used to design NW LEDs, as shown on Figure 1-14. Schematic illustration of a NW LED with an (a) axial structure and (b) a radial structure [36].Figure 1-14 (a) and (b), respectively. InGaN/GaN LED in axial structure consists of a heterostructure along the wire axis, where the active region is sandwiched between a p-doped segment and n-doped segment. The strain relaxation in NWs reduces the internal field, which is particularly important for In-rich green LEDs. However, a main drawback of the axial structure is that non-radiative recombination may happen on the surface, so a thorough surface passivation is needed. Radial, or core shell structure consists in a n/p-doped core, surrounded by radial QWs and covered by a p/n-doped shell. It benefits from the high surface to volume ratio, maximizing the light emission around all the surfaces [36].

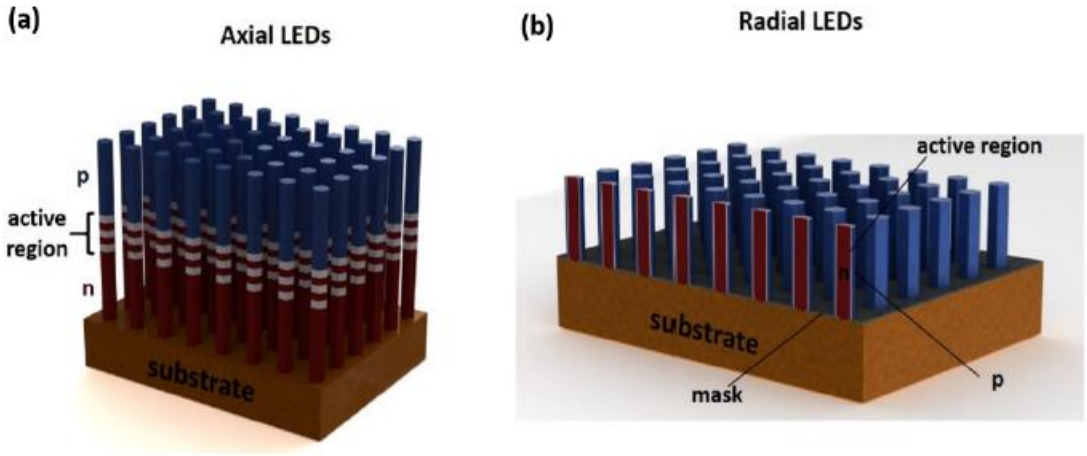

Figure 1-14. Schematic illustration of a NW LED with an (a) axial structure and (b) a radial structure [36].

Thanks to the small footprint, NWs accommodate the strain arising from the lattice mismatch or thermal expansion coefficient mismatch, and this eliminates the defects. The strain relaxation is not only happening on the NW/substrate interface, but also at the heterostructure interfaces in an axial NW. The reduction of defects lead to an enhancement of the quantum efficiency of NWs devices compared with thin films [36]. The core-shell structure is the most advantage for NW LEDs. Indeed, this geometry significantly increases the active area [94]. An approximation of the increase of the active surface, assuming the shape of each NW as a perfect cylinder, can be estimated as:

$$\frac{S_{NW}}{S_{film}} = \frac{2\pi Rh}{\pi R^2} F = \frac{2h}{R} F \qquad (1\text{-}15)$$

where S_{NW} is the active surface of a cylindrical NW LED, S_{film} the respective LED area

for an equivalent surface, R the NW radius, h the NW height and F is the fill factor. Thanks to the larger active area, the carrier density in QWs decreases in comparison with a chip of the same size in thin film technology, for the same injected current. Therefore, the Auger efficiency droop in core/shell NW emitters will happen at higher currents [94] (assuming a homogeneous current injection in the NW QW, which is not always the real case). The LED structure is grown on non-polar planes, as a benefit there is no internal electrical field effect and no QCSE. The potential advantages of core/shell NW LEDs over the thin film technology is well reviewed in ref [95].

Finally, light scattering is improved, the 3D geometry provides more escape paths for the light generated in the NWs compared to the thin film LEDs. In this case, the core-shell geometry facilitates more the light reabsorption than the axial NW LEDs, which can be reemitted or lost by non-radiative recombinations [96], [97].

Accounting for these advantages, NWs array LED are potential competitors to the standard thin film LEDs technology for lighting and displays. In the literature, there are several works focusing on white light emission by phosphor down conversion [98] or by RGB mixing [99], as well as on RGB displays [100] based on NWs LEDs. In addition to the standard applications, NW LEDs opened the way for novel devices with new functionalities. For example, the dependence of the In incorporation in the NW on the diameter can be used for tuning the emission color of the NWs LEDs using a patterned substrate [101], [102]. Such tuning for monolithic RGB integration is not possible in thin film devices. Other possible applications are single NW LEDs as μ-LEDs without the need of patterning which can be integrated in photonic circuits [103], [104] or functionalized as a matrix of μ-pixels [105], [106]. Thanks to the small footprint and mechanical flexibility, NW LEDs can be encapsulated into a plastic membrane producing a flexible device, as it will be discussed in more detail in chapter 2: Flexible NW light emitting diodes [107]–[109].

The two dominant growth techniques of III-nitride NWs are molecular beam epitaxy (MBE) and metalorganic chemical vapor deposition (MOCVD). The main difference between these techniques is that MOCVD requires chemical reactions for the crystal growth, while MBE depends on physical deposition. The MOCVD technique can facilitate the radial growth for core shell heterostructures while MBE growth is more suited for axial heterostructures.

During the growth, two inhomogeneities can be distinguished, the wire-to-wire dispersion and the intra-wire compositional variations, both of them are critical for the NW LED performance. SAG allows to achieve a good control over the NW size distribution which reduces the wire-to-wire fluctuations. However, the homogeneous In incorporation in the NWs is a problem even for SAG NWs. It has been observed that there is a variation of the carrier injection induced by the In inhomogeneities: at lower bias, regions with a high amount of In are preferentially

injected, however, at higher bias, the regions with lower In dominate the light emission. This emission shifting, due to different injection current and In composition, has been observed in self-assembled NWs [110] but also in organized NW array LEDs [111]–[113]. The complexity of the structure's geometry and the composition of the material make the growth challenging.

To facilitate the In incorporation for growing an InGaN alloy, the amount of In in the alloy can be controlled by the growth temperature. Lower temperature of growth leads to larger In incorporation. This effect is illustrated in Figure 1-15 showing the luminescence of quantum discs in NWs grown at different temperatures.

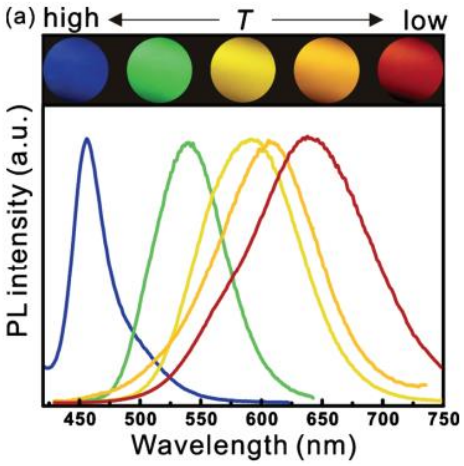

Figure 1-15. PL spectrum of quantum disks in nanowires grown at different temperatures [99].

1.4 STATE OF THE ART OF III-N NW LEDs

NW based LEDs are considered as competitors to thin film LEDs due to their ability to overcome the thin film technology problems described above. Several research groups, enterprises and start-ups have done a strong effort in the last years to explore this topic, with different strategies. The main achievements in the area of III-N NWs based LEDs are described in this section.

1.4.1 MOCVD grown LEDs

There are several works on MOCVD NW LEDs using different approaches of growth, mainly self-assembled catalyzed [114], or non catalyzed growth [115], but also selective area growth on sapphire [95] and on GaN templates [112]. Below I describe several examples of NW LED realizations.

The first example is a realization from our team in collaboration with CEA-Grenoble InGaN/GaN core shell NWs were grown using a non catalyzed self-assembled (Figure 1-16 (a)) strategy for the fabrication of single NW LEDs [110], [115]. The active region consisted of five radial QWs grown on the upper part of GaN NW stems. The QWs were formed on the non-polar m-planes but also on the NW top, polar *c*-plane

as can be seen in Figure 1-16 (b). The NWs were dispersed on SiO_2/Si substrates and contacted by e-beam lithography. The radial (non polar) and axial (polar) quantum wells In content and the thickness were different, which led to different emission wavelengths, as shown by the CL measurements of Figure 1-16 (e). The carrier injection competition in the axial and radial quantum wells caused the change of the electroluminescence colour as a function of the injection current [82]. An electrical model of two parallel diodes allowed to describe the behaviour of the injection in the radial and axial quantum wells which produced the EL colour shifting.

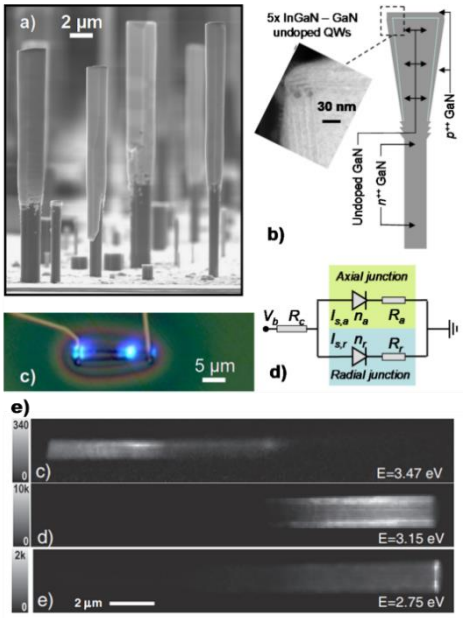

Figure 1-16. (a) SEM image of self-assembled core shell InGaN/GaN NWs grown by MOCVD, (b) Schematic representation of the NW internal structure and a TEM image of the top region evidencing the presence of radial an axial QWs, (c) Optical micrscope picture of the single NW LED under operation, (d) equivalent electrical circuit of the LED representing the radial and axial junctions, (e) CL maps filtred at different energies, depending on the In incorporation on different planes [110].

Self-assembled NWs suffer from structural and compositional fluctuations which have a big impact on the EL. The wire-to-wire homogeneity can be improved using the SAG mode. Hong et al. [112] used nanopatterned GaN on sapphire substrates with a SiO_2 mask for the growth of SAG GaN NWs to demonstrate color-tunable LEDs. After the NWs growth, the sample was planarized with a p-GaN layer. The LED color changed with the applied bias from a broad peak at 690 nm under 3V to a blue emission under 10 V, showed in Figure 1-17 (a)(b). The change of color with the bias is explained by a field distribution model, at low bias the high resistivity of the p-GaN layer allows to inject in the NW top, and with increasing current, the injection in the m-planes was promoted [112].

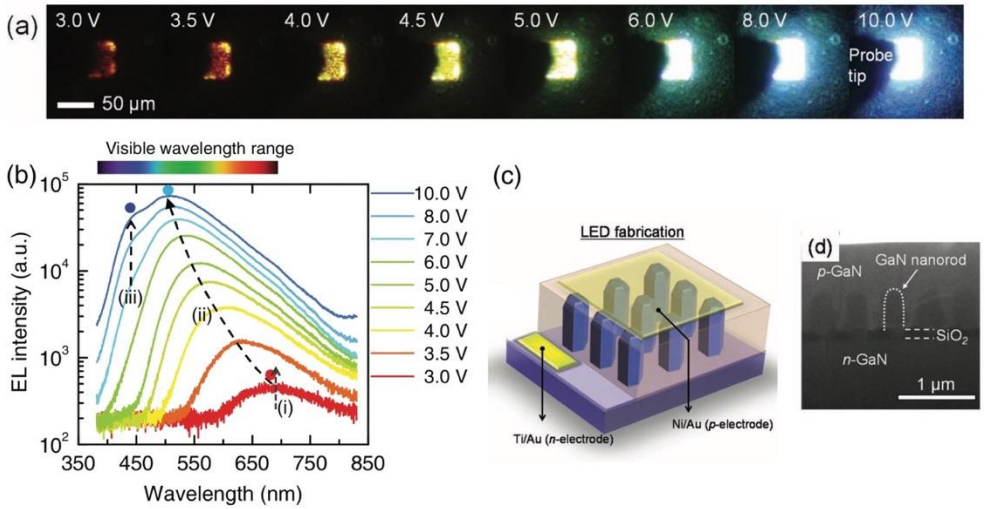

Figure 1-17. (a) Optical microscope pictures of the LEDs showing different emission colours under different biases, from 3 to 10 V, (b) EL spectra for the different biases, (c) Schematic representation of the device, consisiting in the GaN NWs, p-GaN layer and both contacts, (c) SEM of the cross section GaN nanorods buryed by a p-GaN layer [112].

For standard narrow band LEDs, the variation of color emission is undesirable. NW LEDs with a stable emission color were also demonstrated by MOCVD SAG on GaN on sapphire templates shown on Figure 1-18 (a)(b) reported by Chen et al. [116]. The LED lights up at 6 V with a broad emission centered at 463 nm and keeps a stable emission color with increasing injected current density, from 16 to 224 A/cm2, Figure 1-18 (c). The large spectral width (FWHM of 40 nm) is attributed to different emission wavelengths of the QWs at different regions [116]. Figure 1-18 (d) shows the device normalized output intensity (left axis) and the spectral peak position (right axis) with the injection current density. The blue shift of the LED emission is just 1.1 nm, smaller than that of a planar LED at a similar emission wavelength [117].

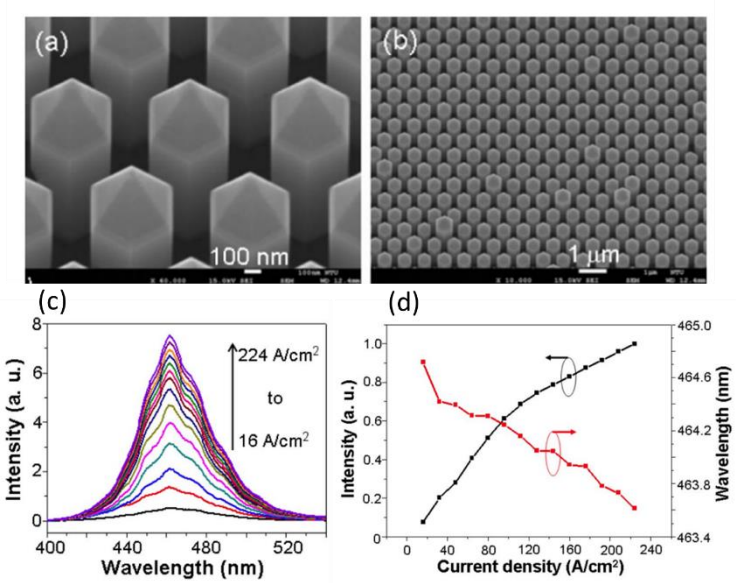

Figure 1-18. (a) and (b) are tilted SEM pictures of the MOCVD NW LEDs array with a larger and smaller magnification, respectively (c) EL spectra with increasing injection current density, (d) normalized device output intensity (black curve and left coordinate axis) and spectral peak position (red line and right coordinate axis) variations with increasing injected current density [116].

Besides research teams, big companies like the OSRAM group, have explored the advantages that NW LEDs can bring to the market [98], [118]. They have demonstrated blue and white NW LEDs by SAG of core shell NW arrays. They used a design with a single InGaN QW, grown on the non-polar m-planes and semipolar facets. An increase of the In amount in semipolar planes was observed by CL mapping compared to the content in the non-polar QWs. EL spectra evolve with injection current as previously mentioned. At low injection current, semipolar QWs produce green emission, and it turns to blue emission from m-planes. A blue shift is observed, attributed to an In content gradient in the m-plane along the NW facet.

Glo-AB company also developed their own core shell SAG NW LEDs, using GaN on sapphire templates and nano-masking using a SiN mask patterned by nanoimprint [119]–[121]. The NWs have a single InGaN QW on the non polar m-planes, however CL revealed an In-rich region in the QW, at the junction between the m-plane and the semi-polar planes as shown in Figure 1-19 (b). The electroluminescence measurements revealed a color switch both for a single NW device [113] and for a NW LED array [119], shown in Figure 1-19 (c) and (d), respectively. The color switching is explained by a simple model, representing the core shell NW as a network of parallel connected diodes and the current distribution in this network was calculated at different biases and different contact layouts. To account for the In inhomogeneities, a different saturation current was ascribed to the diodes, depending on the bandgap. In In-rich regions, the lower bandgap results in a larger saturation current. Therefore, at low biases, the In rich segment was preferentially injected, however, for higher biases, the parallel and radial shell resistances start to

play an important role and the current concentrated in the lower In content m-plane QWs, which results in the color switching. This model is well described by Tchernycheva *et al.* in ref [113]. The EL spectra evidencing the color switching, for a single NW LED and for an NW array LED, as a function of the injection current are shown in Figure 1-19 (c) and (d), respectively.

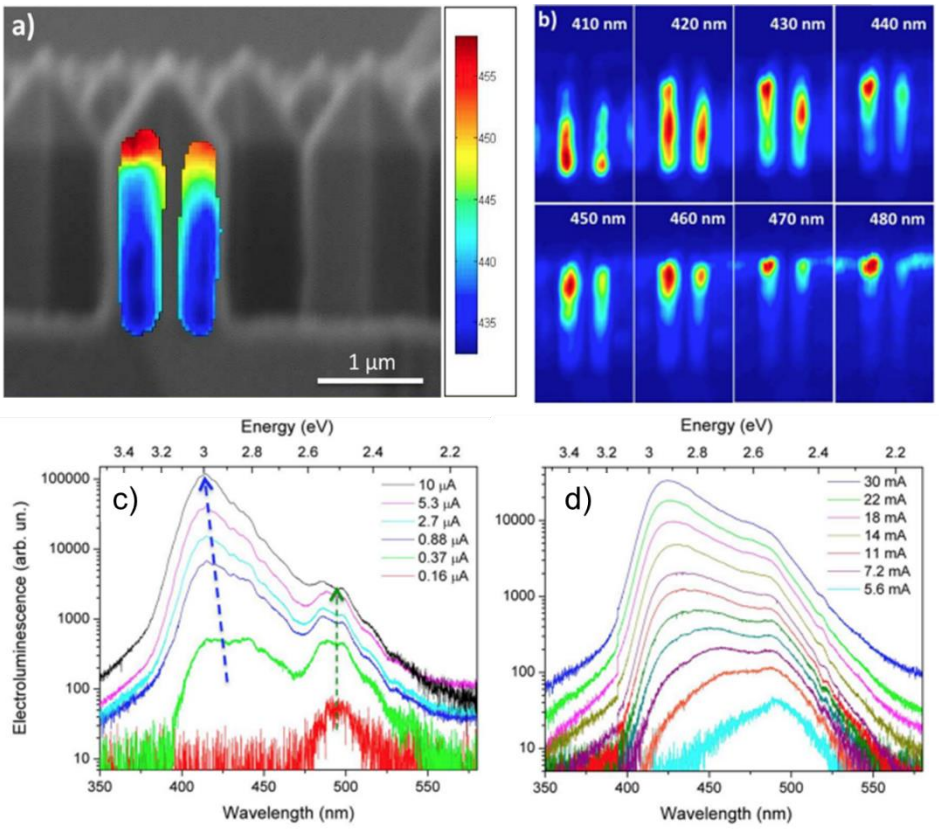

Figure 1-19.(a) SEM image of cleaved single NW with the CL average wavelength, (b) CL filtered maps at different wavelengths, evidencing an In content gradient and an In-rich region, (c) EL spectra of a single NW LED and (d) EL spectra of a NW array LED at different currents [113].

Later, it was demonstrated that the color emission can be controlled by modifying the contact layout [119]. By removing the ITO contact from the top part of the NWs and inhibiting the conductivity of the exposed region by a plasma treatment of CHF_3, the emission at larger wavelength was suppressed. Another option for removing the large wavelength emission is to etch the top part of the NWs by ICP etching. Figure 1-20 shows the EL spectra of a nominally blue core shell NW LED, with a high In content at the junction between the non-polar m-plane and the semi-polar plane and with a ITO conformal contact (black line), after removing the ITO top and CHF_3 plasma treatment (red line) and for the NW top part removed by ICP etching (blue line). The EL spectrum of the conformal ITO contact shows two emission peaks, around 525 and 475 nm related to the emission from the high In concentration regions and from the low In concentration regions on the m-planes, respectively. Both contact treatments suppressed the emission at 525 nm, while the plasma

treatment enhanced the emission at lower wavelength for the same injection power, ICP etching decreased the intensity of the emission.

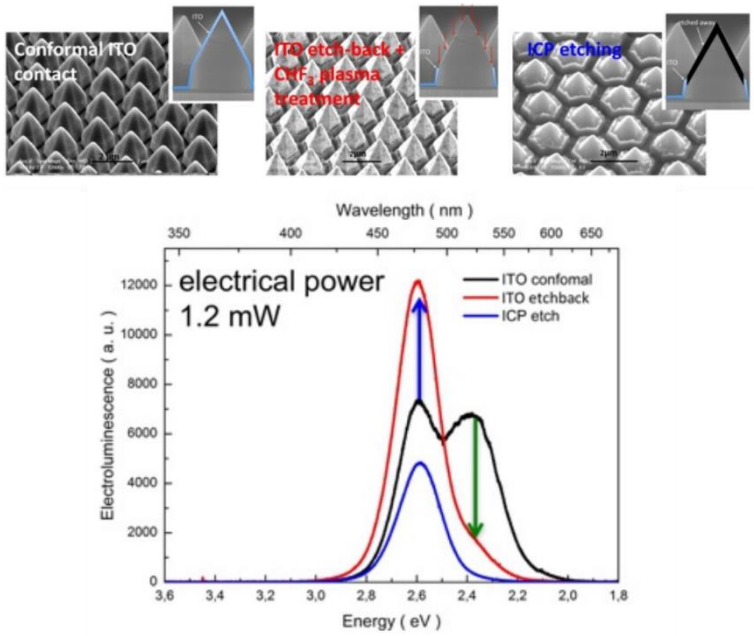

Figure 1-20. Comparison of the EL spectra under the same electrical power injection of core shell NW LEDs processed with a conformal ITO contact (black solid line), partially ITO etched contact (red solid line), and NW top region removed by ICP etching (blue line). The top line shows the SEM tilted view for the three situations with a schema of the contact in the insets [119].

1.4.2 MBE grown LEDs

Molecular beam epitaxy is a technique well suited for In-rich LEDs because of the low growth temperature, compared to the MOCVD technique. Due to the difficulties for In incorporation, a strong effort was committed to demonstrate and optimize MBE grown NW LEDs emitting in the long wavelength spectral range (from green to near IR).

Kishino et al. demonstrated self-assembled GaN NWs LEDs with axial InGaN/GaN multiple quantum disks grown on (111) Si substrate, with different emission wavelengths, from green to red [122], [123]. Later on, Kishino's group focused on SAG NW LEDs, which open the path to new functionalities namely the monolithic integration of the NW morphology with an In composition controlled by the mask design [102].

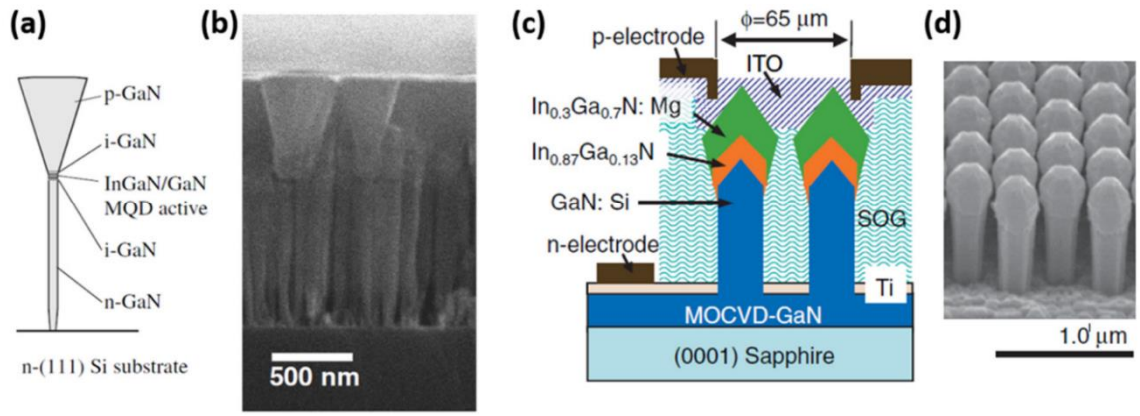

Figure 1-21. (a) Schematic and (b) cross section SEM of self-assembled InGaN/GaN NW LEDs grown on Si substrate [95]. (c) Schematic and (d) SEM image of SAG InGaN/GaN NW LEDs grown on Ti masked GaN on sapphire substrate [124].

Figure 1-21 (a)(b) shows, respectively, a schema of the NW LED structure and the SEM picture of the self-assembled GaN NWs and in Figure 1-21 (c)(d) the respective schema and the SEM picture for the SAG NWs. SAGs NW LEDs were grown on GaN on a sapphire template with a Ti mask. The NWs exhibit a Ga-polarity which is revealed by their pencil-like shape, with sixfold side facets (semipolar planes) on the top, where the quantum wells were grown, as seen in Figure 1-21 (c). In this approach, the QWs are grown on semipolar planes, with a lower internal field compared to the axial quantum disk grown on polar c-plane of self-assembled GaN NW LEDs.

In 2010, Kishino et al. [101] achieve the first milestone for monolithic integration – the growth of InGaN/GaN QWs with different In composition in the same growth run by changing the NW diameter and pitch by SAG. Diameters ranging from 143 to 270 nm LED to NWs with InGaN QWs emitting from blue to red. Figure 1-22 (a)-(f) show the SEM bird view and the picture of the different diameter NWs under He-Cd laser excitation. In panel Figure 1-22 (g) are plotted the respective PL spectra for the different diameters NWs, covering all the visible range.

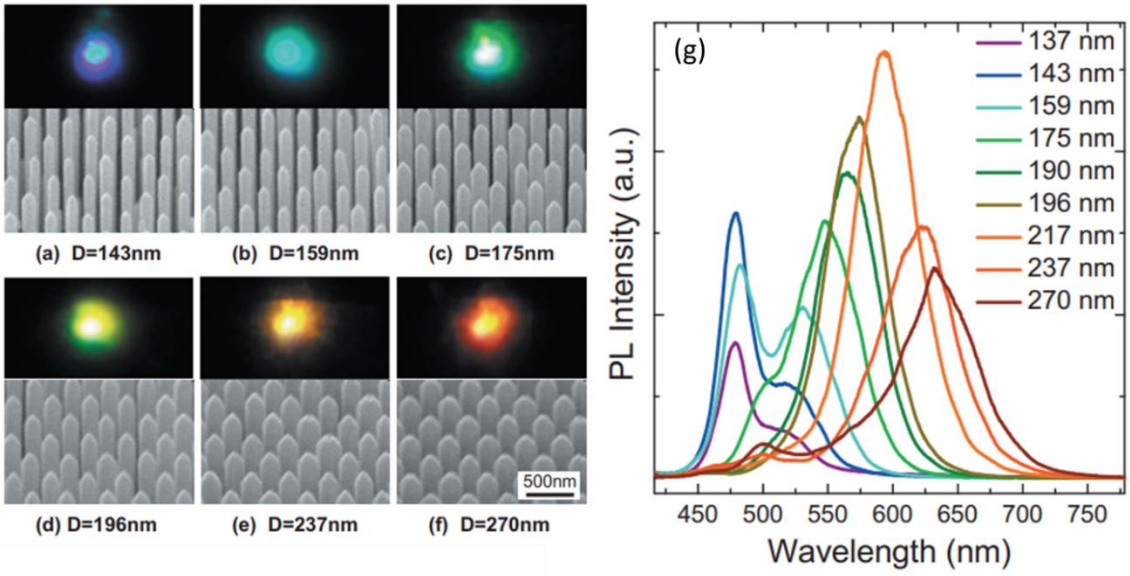

Figure 1-22.(a)-(f) SEM bird view and emission picture for the NWs with different diameters, indicated below each picture. The sample is excited with He-Cd laser for the emission picture. (g) PL spectra for different diameter NWs [73].

In 2012, first NW LEDs relying on monolithic integration were demonstrated [125]. InGaN/GaN based NW LEDs with emission at 544, 583 and 597 nm were grown by SAG on GaN on sapphire substrate using the same Ti-nanomasking in a single growth run. Figure 1-23 (a) shows the microscope image of the device under operation, and the respective EL spectra are displayed on Figure 1-23 (c). The NWs were encapsulated into a spin-on-glass and contacted with a ITO layer on top, as shown in the schema of Figure 1-23 (b).

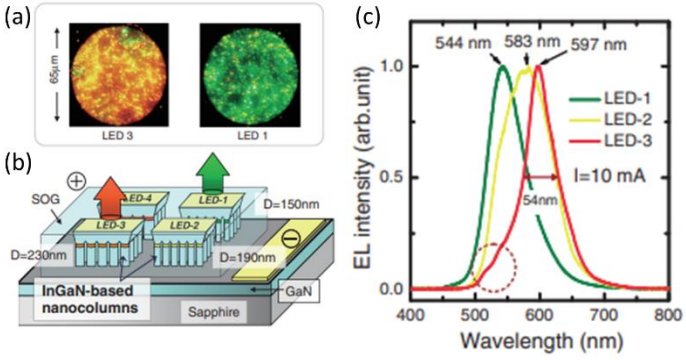

Figure 1-23.(a) Optical microscope images of green and orange emission from InGaN/GaN NW LEDs, (b) schematic diagram of monolithically integrated NW LEDs on GaN template on a sapphire substrate. (c) EL spectra of the LEDs under an injection current of 10 mA [125].

In 2015 a monolithic integration of four colour InGaN-based NW LEDs was achieved [102]. Using the same growth run, NW LEDs emitting in blue (465 nm), sky-blue (489 nm), green (510 nm) and yellow (550-560 nm) were demonstrated by modulating the diameter of the growth and keeping a pitch of 300 nm. The missing red color NW LED is also demonstrated in this work, using a pitch of 350 nm, with an emission

peaked at 650 nm. Figure 1-24 (a) shows the EL spectra of the NW LEDs and (b) shows the emission images of the LEDs under an injection current of 10 mA, accompanied by a SEM bird view of the SAG NW LEDs of the green LED [102]. It is remarkable that a similar colour control method can also be performed in SAG MOCVD, although the growth mechanisms are different [126].

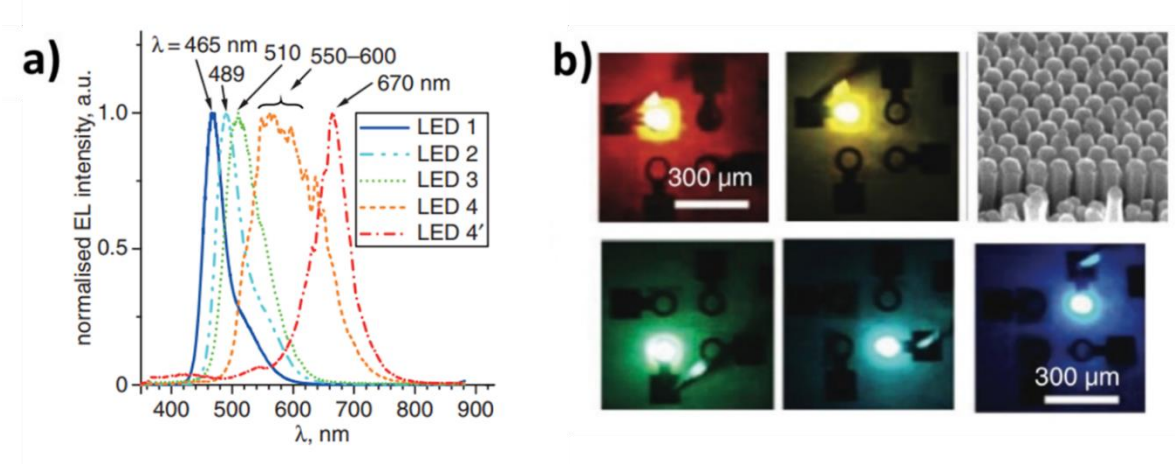

Figure 1-24. (a) EL spectra of the blue, sky blue, green and yellow LEDs, grown in the same run with a pitch of 300 nm, and the EL spectrum of the red LED, achieved using a pitch of 350 nm. (b) emission images of the LEDs under 10 mA injection current and SEM bird's view of green LED [102].

Finally, in 2017 Kishino's group culminate this stunning work with the monolithic integration of a RGBY micro-LEDs array with independent drive via matrix wiring electrodes [127], [128]. The growth is done on a GaN template on sapphire, patterned with a 5 nm Ti layer, with different pitches of 100, 150, 250 and 350 nm for blue, green, yellow, and red NW LEDs, respectively. Figure 1-25 (a) shows the top view of the full device, with independent electrodes for each pixel, an enlarged picture of each independent pixel is seen in Figure 1-25 (b). Figure 1-25 (d) shows the emission picture of each independent pixel, and Figure 1-25 (c) the normalized EL spectra of each colour pixel, centred in 478, 508, 564 and 654 nm for blue, green, yellow, and red, respectively.

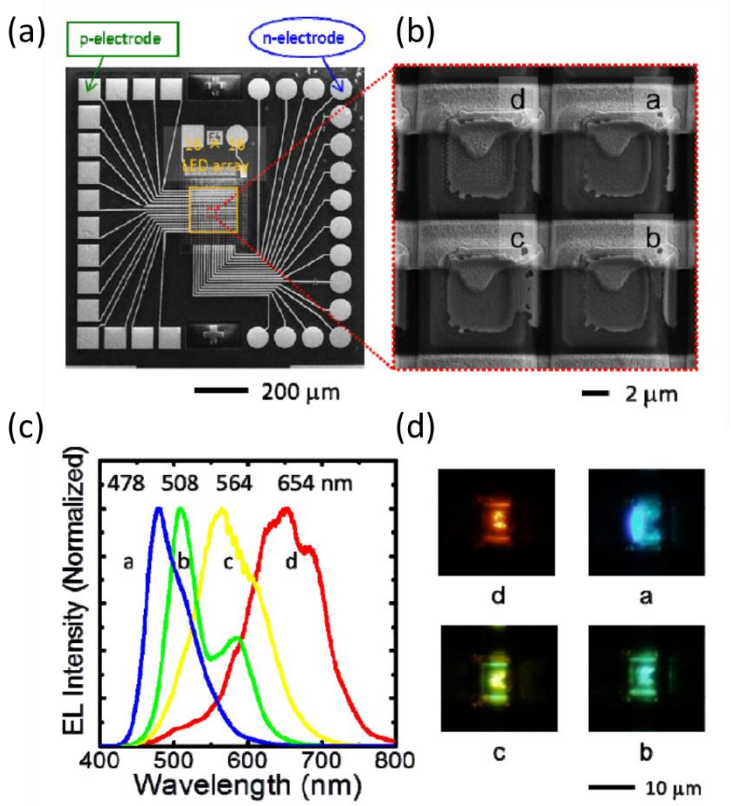

Figure 1-25. (a) Top-view SEM images of the integrated NW LED array and matrix wiring electrodes, (b) zoom in of the micro-LEDs composed by four pixels, one of each RGBY colour. (c) normalized EL spectra of the RGBY InGaN/GaN NW LEDs, (d) emission picture of each pixel under an injection current of 1 mA [127].

Zetian Mi et al. [129] demonstrated a drastically different approach for monolithic RGB integration. The active material in their work consists of InGaN quantum dots grown inside the NWs. The process consisted in a three step MBE growth of InGaN/GaN dot-in-a-wire self-assembled NWs on Si substrate in particular regions, microscale openings defined by SiO_2 allowing to grow blue InGaN/GaN NWs in the Si opening, but also on the top of the SiO_2 layer. The SiO_2 mask was removed by chemical etching, together with the NW LEDs formed on the top. Then, a second layer of SiO_2 was deposited, covering blue NW pixels formed on the Si substrate, and defining another Si openings on the new SiO_2 layer, for doing the second step MBE growth of green NW LEDs. Then the process was repeated for the third step of red NW LED. The schema of the three steps is shown in Figure 1-26.

Zetian Mi's group worked on AlInGaN insertions in GaN NWs [130]. It was demonstrated that an Al rich shell was formed spontaneously during the growth, which protected the carriers from surface recombination, resulting in a AlGaN/InGaN core shell heterostructure with improved efficiency of the NW LEDs [131] by surface passivation. The Shockley-Read-Hall non-radiative recombination in NW LEDs can be also reduced by another surface passivation with octadecyl thiol ($CH_3(CH_2)_{17}SH$) [132].

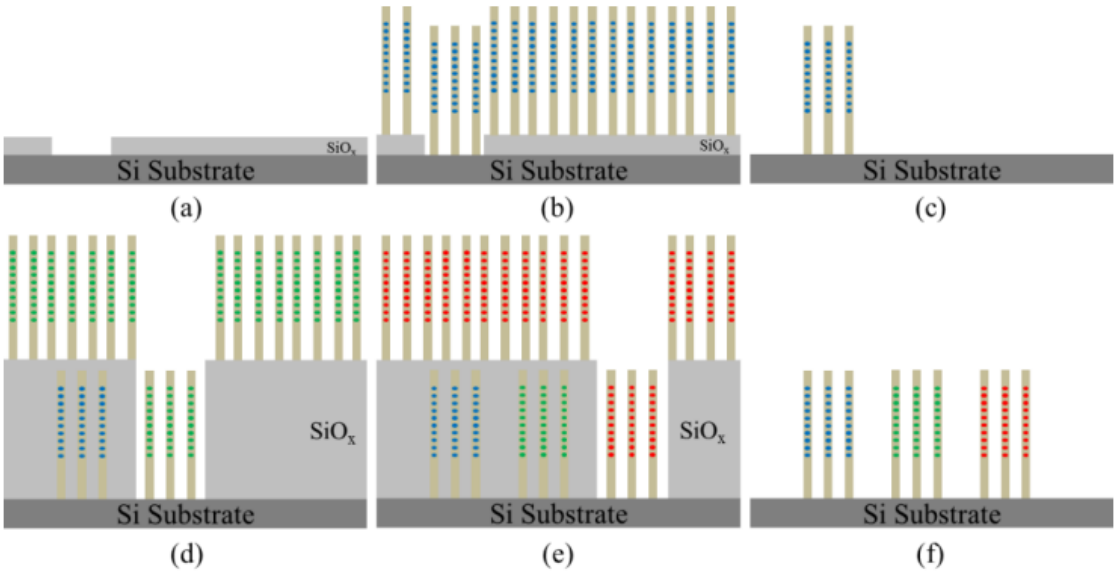

Figure 1-26. Schema of the three-step substrate preparation and epitaxial growth. (a) Si substrate patterned with SiO_x layer (b) first epitaxial growth step of blue NW LEDs (c) SiO_x together with the NWs grown on the top were selectively removed (d) Blue NWs LEDs covered by SiO_x and second epitaxial growth of green NW LEDs (e) blue and green NW LEDs covered by SiO_x and the third epitaxial growth of red NW LEDs (f) resulting multicolour NW LEDs array on Si substrate [129].

An alternative current (AC) powered multi active region InGaN/GaN NW LED [133] was reported. The NWs contain three emitting regions connected by tunnel junctions, following the strategy developed in thin films. The tunnel diode consists in a highly doped p^{++}-GaN/ n^{++}-GaN junction, generally enhanced by the polarization induced electric field of an AlN [134] or InGaN [135] insertion. One of the advantages of tunnel junctions in III-nitrides devices is the possibility to do an ohmic contact on the n-GaN for hole injection, which is much easier than doing it on p-GaN since the p-GaN is highly resistive. In addition, it enables stacking of multiple LEDs [136] in series to produce higher emission power for a given current, which was applied to NWs in the work reported in ref. [133].

1.4.3 Larger wavelength LEDs by MBE

Many other groups have been working on green and yellow NW LEDs. Narrow yellow SAG NW LEDs arranged into a photonic crystal exhibit high directionality due to light diffraction with an angle of ±20° [137]. Flip chip structure NW array LEDs were developed, showing an improvement of the thermal management in NW devices [138]. Limbach et al. [139] demonstrated a self-assembled InGaN/GaN NW green LED grown on Si substrate, peaked at 540 nm. Bencove et al. [140] demonstrated a MBE axial InGaN/GaN NW LED showing a spotty green emission, however, it was observed that these devices produce a polychromatic emission covering from 450 nm blue range up to 650 nm red light.

Regarding NW LEDs at longer emission wavelengths, there are several works on red and near-IR LEDs grown by MBE. Jahangir et al. [141] reported self-assembled red NW LEDs based on InGaN disks in GaN NWs on (100) Si substrate with a red emission centred at 650 nm. In this work, it was also reported that a post growth passivation with parylene or SiN_x improves the carrier lifetime, increasing the non-radiative recombination life time, which led to an increase of the IQE from 10 to 52%. Kishino's group also contributed to develop red [123] and IR [124] InGaN/GaN SAG NW LEDs on GaN templates on sapphire. Red LED showed an emission peaked at 633 nm and the IR LED was emitting at 1.46 µm, with an In concentration up to 86%. Also, the Zetian Mi's group applied their dot-in-a-wire approach for fabricating red NW self-assembled LEDs with an emission centred at 633 nm at 400 mA [130]

Alternative approaches for red emission have been explored. Extending the work done on Eu doped QDs [142], Eu doped GaN NWs, grown on Si substrates by MBE were reported [143]. A GaN:Eu segment was grown axially between n-GaN and p-GaN. This alternative approach showed two peaks, centred in 620.3 and 633.8 nm, coming from the optical transitions in Eu.

The MBE epitaxy growth of nitride NW LEDs was also demonstrated on metal substrates. Visible NW LEDs were grown on Ti [144] and Mo [145], [146] films, with comparable performance with respect to those grown on Si substrates. These approaches open a great opportunity for large-scale fabrication of devices and a huge improvement in terms of thermal management. In addition, the NW-on-metal LEDs can be used in novel applications requiring flexible optoelectronic devices. Detailed discussion is reported in chapter 2: Flexible NW light emitting diodes.

1.4.4 White LEDs

One of the main applications of LEDs is the general lighting. White emission can be produced by two different routes: conventional approach consisting in using phosphor down conversion, and a direct mixing of RGB light.

1.4.4.1 Phosphor-converted white LEDs

The first approach uses the conventional and well-developed approach of thin film technology to NW based LEDs. This approach consists of using a blue LED covered by a yellow phosphor which partially absorbs the blue light and reemits yellow light. By adjusting both light relative intensities of the remaining part of the blue light and of the yellow luminescence from the phosphor, it is possible to obtain white light [147]. Another way to obtain white light, and of even better quality, is by mixing phosphors of different colours, e.g. yellow and red phosphors [148]. The OSRAM team has transferred this technology to NW LEDs [98], by the use of small phosphor particles, of sub-micron size, which fit between the NWs, as seen in Figure 1-27 (a), guarantying an efficient light conversion. In the conventional thin film phosphor converted white LEDs, the phosphor is encapsulated in a silicon matrix, leading to

heating problems, however, using this approach, phosphor particles are in contact with the active NWs, which helps the heat evacuation. By using red nitride-silicate and yellow YAG:Ce phosphors, cool white emission with a correlated colour temperature (CCT) of 6600 K and a colour rendering index (CRI) of 76 was demonstrated, as shown in Figure 1-27 (b).

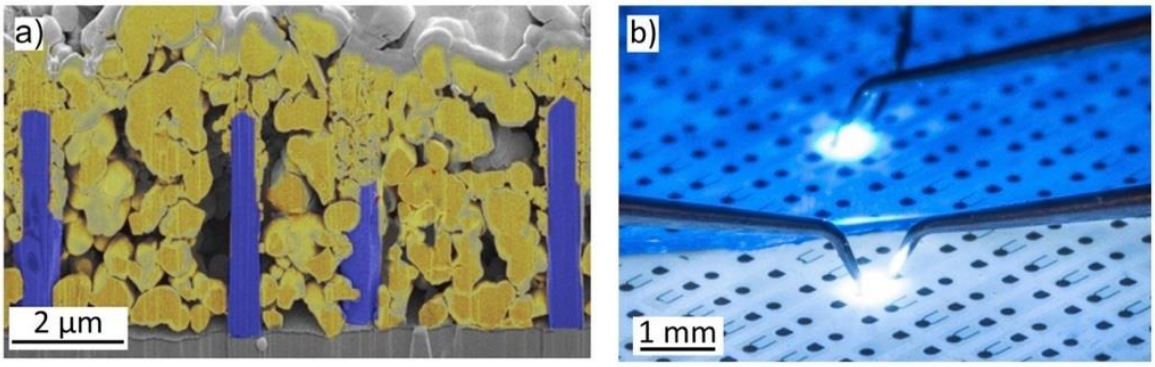

Figure 1-27. (a) Cross section SEM of a white NW LED, where sub-micron size phosphor particles (artificial yellow) are integrated between NW LEDs (artificial blue) (b) Picture under operation of phosphor converted white LEDs [98].

The main drawback of the phosphor converted white LEDs resides in the fundamental principle of the down conversion: the energy difference between the pump and the phosphor is inevitable lost as heat. This reduces the total efficiency of these devices, in addition to other losses such as light backscattering in the phosphor layer or conversion efficiency of the phosphor. These drawbacks have motivated research for phosphor-free white LEDs.

1.4.4.2 Phosphor free white LEDs by RGB color mixing

Thanks to the energy bandgap tuning over the whole visible range, InGaN alloy with different compositions is well suited for developing monolithic white LEDs. Several investigations focused on the InGaN LEDs RGB mixing for white emission have been performed in thin film technology, by QWs or QDs as active region [149], [150], [150], [151]. However, high Indium content InGaN layer suffers from poor crystal quality due to the lattice mismatch, the polarity on thin film heterostructures inducing a strong QCSE. Therefore, the green and red nitride LEDs suffer from a very low efficiency, compared to blue LEDs. Theoretical analysis of monolithic InGaN RGB LEDs for a white source show that a significant improvement of the red and green emitters efficiency is needed to be competitive with the phosphor down conversion white sources [152].

With the emerging of NW based LEDs technology, the InGaN monolithic integration of RGB LEDs has gained a renewed interest. As previously mentioned, thanks to the strain relaxation and the lower internal field, NWs show lower defect density and lower piezoelectric effects compared to thin films. This makes the NW based LEDs excellent candidates for InGaN RGB monolithic integration device development.

Regarding the growth technique, MBE allows the fabrication of In-rich alloys, therefore, it is the most used technique for this kind of device realization.

Lin et al. [99] performed spontaneous NW growth by MBE on Si (111) substrate, growing axial InGaN/GaN quantum disks in a p-n junction at different growth temperatures. Thus, the In content in the discs was modified. The different In composition led to blue, yellow and red emission coming from the quantum disks. A schematic of the device and images at different magnifications of the NW white LEDs under operation are shown in Figure 1-28.

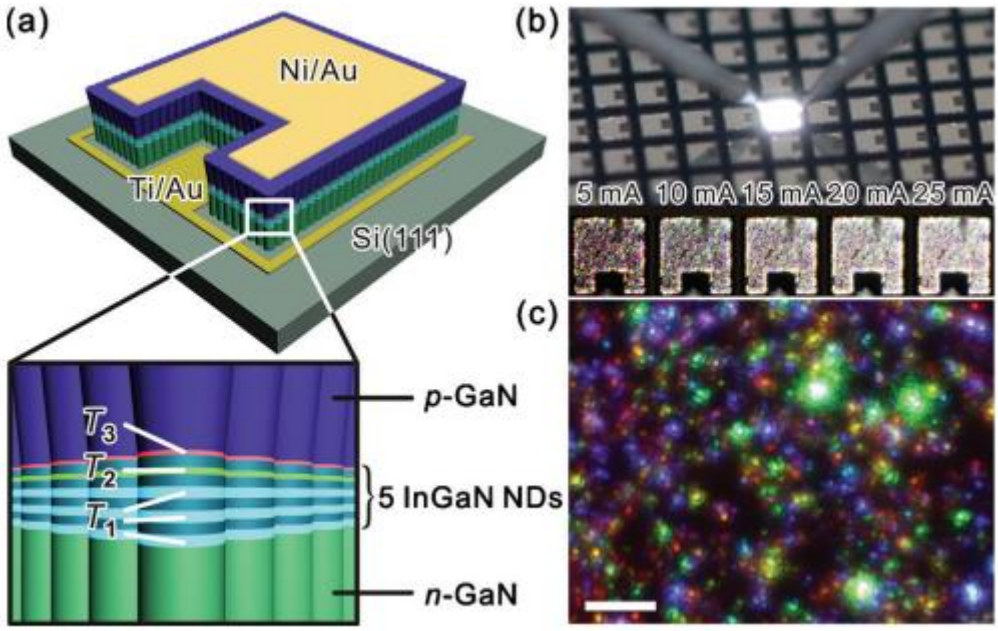

Figure 1-28.(a) Schematic of a NW white LED with axial InGaN/GaN quantum disks grown at different temperatures, embedded in a GaN p-n junction (b) Photograph of the device under operation, the inset show a close-up LED photo at different injection currents (c) micro-electroluminescence image of the NW white LED under operation at 20 mA injected current, where multicolor emission is seen. The scale bar is 10 µm [99].

Guo et al. [153] followed the same approach, transferring the growth of self-assembled GaN NWs with axial InGaN/GaN quantum disks of different composition to a Si (100) substrate. A broad visible emission with a CCT ranging from 5500 to 6500 K, and a stable emission with no dependence on the injection current variation was demonstrated. Armitage and Tsubaki [154] demonstrated white NW LEDs by mixing different emission from axial and radial InGaN insertions on NWs grown by MBE.

Zetian Mi's group applied their dot-in-a-wire approach for fabricating phosphor free white NW self-assembled LEDs by stacking quantum dots of different colours within the same wire [155], [156], using the AlGaN/InGaN core shell NW LEDs structures [157]. Another approach was the use of simultaneous emission of the different

colour pixels from the monolithic integration of RGB NW LEDs described above [129].

Kishino's team also demonstrated white light emission from the monolithic integration described above, applying voltage simultaneously to the different pixel LEDs, mixing the colours to obtain white emission [128]. In this case, each colour pixel has independent contacts, therefore it is possible to tune the intensity of each colour which allows to achieve different white light emission.

1.5 SUMMARY

In this chapter, I have briefly described the basic mechanisms governing the LED operation, the fundamental properties of nitride semiconductors, the advantages and drawbacks of nitride technology, the formation of nitride NWs and the advantages of using these nanostructures for the LED market. Then I presented the state of art of nitride NW LEDs grown by MOCVD and by MBE.

Nowadays the LED market is dominated by thin film technology. The existing prototypes of NW LEDs show lower efficiency compared to the mature technology based on thin films. For general lighting applications, a strong boost of efficiency is necessary to be competitive with the actual technology. However, for challenging applications or novel functionalities, nitride NWs, or nanostructured LEDs can be competitive. For challenging spectral ranges, such as green-red LEDs or deep UV LEDs, nanostructured or NW LEDs can exploit their unique properties and become competitive. In addition, nanostructured LEDs can bring new functionalities which are not possible making use of thin film technology. The work reported by Zetian Mi's group or Kishino's group, namely the monolithic integration of RGB LEDs in a single growth run, is something that only NWs can offer. Another attractive functionality which nanostructured LEDs offer is the realization of flexible NW LEDs based in inorganic materials, with high luminescence and long lifetime.

2 FLEXIBLE NW LIGHT EMITTING DIODES

2.1 INTRODUCTION

Flexible electronics and optoelectronics are key emerging technologies, attracting a huge interest in the last years, and becoming nowadays the topic of intensive research. Flexible devices which are light weight, with a good ductility and small thickness will dominate the market in the coming years.

The development of flexible light emitting diodes (LEDs) is driven by applications such as bendable displays, conformable light sources, or wearable devices [158]. Furthermore, deformable lighting is highly demanded in advanced biological research, such as bio-medical, biological and optogenetic studies or bio-medical implants [158][159].

Mechanical flexibility also allows to reduce fabrication costs and improves the transportability. Roll-to-Roll (R2R) is a process route for fabrication of flexible optoelectronic devices, which allows to save time, costs and provides a continuous operation. The method consists in using two rolls, starting with a first roll of a flexible material (e.g. a roll of a flexible substrate). This flexible material is processed by the traditional techniques of nanofabrication, and re-reeled on a second roll where the flexible device can be stored or transported in a more efficient way. Another advantage of this kind of process is the scalability for large industry.

Today, all the flexible technology is dominated by organic semiconductors. Regarding optoelectronics, the most used technology for flexible LEDs is organic LEDs (OLEDs). Indeed, OLED displays have been already commercialized thanks to their low material and processing cost and good flexibility. Also they are compatibles with plastic substrates, which simplifies the fabrication and makes them more suitable for large scale production [160].

However, organic devices are facing instabilities caused by oxidation, recrystallization, or temperature variations, which degrade the electrical conductivity of the organic layers, interfaces and active region. Moreover, organic LEDs in the visible range (especially in the blue spectral region) are limited in terms of quality, and suffer from differential aging, especially for different colors. An extensive review of OLED degradation can be found in ref. [161]

If we compare an organic blue LED with an inorganic LED, the properties of the inorganic LED are better, as shown in Table 2-1. Compared to inorganic LEDs, organic blue LEDs have lower luminance (10^2-10^4 cd/m^2) [162], [163], lower external quantum efficiency (EQE) (2%-30%) and shorter lifetime (up to 3700 h for T50, which is defined as the time for the luminescence to become 50% of the initial luminance)[164], [165].

Blue emitter	Luminance	EQE	Lifetime
OLEDs	10^2-10^4 cd/m^2	2-30%	10^3-10^4 h
III-N LEDs	10^6 cd/m^2	80%	10^5-10^6 h

Table 2-1. Comparison between blue OLEDs and InGaN blue LEDs.

Nitride semiconductor LEDs, InGaN/GaN LEDs, provide the best performance with a luminance of 10^6 cd/m^2 [106], [161], [166], EQE above 80% [167] and a lifetime of more than 100 000 h [166].

Conventional blue nitride-based devices are very stable and efficient, however the conventional thin film technology does not provide flexibility due to the mechanical rigidity of the materials and their substrates, which limits their widespread application in deformable optoelectronic devices. The process and integration on a flexible substrate are challenging. Flexible LEDs based on thin-film and micro-pyramid inorganic materials can be produced by micro-transfer printing techniques, which allows the integration of different structured materials into organized layouts on almost any kind of substrate [168]. Micro-transfer printing relies on a soft stamp, which serves for removing patterned elements from a source substrate and transferring them to a foreign substrate. For transferring thin films from the native substrate laser, lift-off (dry technique) [169]–[174] or epitaxial lift off (selective wet etch of a sacrificial layer [175] or of the entire native substrate [176]) are needed. Alternatively, the mechanical transfer of a whole layer can be facilitated by inserting a quasi-2D layered structure, such as graphene or hexagonal boron nitride, taking advantage of the weak Van der Waals forces [177], [178]. The first flexible III-V LEDs were demonstrated by Park et al. [179] by printing arrays of micro-structured layers containing AlInGaP QWs onto ultrathin plastic substrates. Moreover, besides the

complex fabrication and additional steps needed, one drawback of transferred thin film LEDs is the propensity to change the emission wavelengths with the bending radius due to the strain. This strain induces shifts of the bandgap energy, but also for the case of nitride semiconductors leads to a variation of the piezoelectric field in the quantum wells, which also modifies the emission wavelength.

Instead of using the thin film technology, it is advantageous to make use of nanostructures which are naturally micro or nano-structured, such as nanowires. Nanowires show remarkable mechanical and optoelectronic properties. Besides the properties mentioned in chapter 0, section 1.3, NWs can stand high deformations without plastic relaxation [180] and have a small footprint size compared to typical bending curvature radius. The high aspect ratio will facilitate peel-off of the active material compared to thin films or other structures strongly attached to their substrate like nanopyramids. These properties make NWs excellent candidates for the fabrication of flexible inorganic LEDs.

2.1.1 Direct growth on flexible substrates

A straightforward approach is the direct growth of nanowires on a flexible substrate, followed by the polymer encapsulation. This method can be applied to several semiconductor materials. For example, ZnO nanostructures can be grown in solution on any substrates at low temperatures [181]. Several groups have demonstrated flexible LED devices based on ZnO nanowires on flexible substrates [181]–[183].

The direct growth of nanowires on flexible substrates facilitates the fabrication process, however it is limited to few kinds of semiconductors. Plastic substrates limit the growth temperatures (typically below 200 °C with a possibility to reach 400°C for some materials like Kapton), so this approach is limited to those kinds of semiconductors which can be grown by electrodeposition [184] or hydrothermal deposition[185].

An alternative to plastic, which is mechanically flexible and can stand high temperatures is metal in the form of foils. There have been different studies reporting direct growth of NWs on metal foils. Recently GaN nanowire growth on metal foils by MBE have been reported on Ti [144] and Ta [186], moreover AlGaN nanowire flexible LEDs grown directly on Ta foils were demonstrated [186].

2.1.2 Transferred nanowire leds on flexible substrates

As an alternative of the direct growth, it is possible to transfer the nanowires to a flexible substrate. The nanowires can be placed in-plane or vertically for producing the device. Regarding the in-plane transfer approach, hybrid LEDs have been demonstrated using ZnO NWs-organic semiconductor [187]. Some advances have been achieved regarding the alignment of nanowires, assisted by an electric field, magnetic field, fluid flow or capillarity forces. However, the complexity of this

alignment and the integration for flexible devices restricted the widespread of this approach.

On the other hand, it is possible to transfer a vertical array of nanowires on a flexible substrate preserving their orientation. This is the approach that I used in my PhD work. Nanowire arrays are embedded in a flexible polymer material and lifted off from their growth native substrate. One of the advantages of this transfer approach is the possibility to combine layers of different NW materials with different bandgaps without any constraint related to the growth conditions or lattice-matching. This approach allows for a large design freedom and modularity since it is possible to stack different layers with different functionalities and thus to overcome the limitations of monolithic growth.

There are several studies about flexible LEDs based on polymer embedded NWs arrays lifted off from their native substrate [107]–[109], [158], [188], [189]. First realization used GaN/ZnO coaxial nano-rod structures [188] and GaN micro-rods [189] grown on graphene films. Active nanorods grown on graphene on a SiO_2/Si substrate were embedded in an insulating polymer layer, then lifted off through a wet etching of a sacrificial SiO_2 layer by BOE. Then, the whole layer was transferred to a flexible substrate coated with a metal layer and finally, Ni/Au semi-transparent top contact was deposited [188].

2.2 STATE OF THE ART IN OUR GROUP

Our group has been working since 2014 on the fabrication of flexible LEDs based on NWs. I have continued the work on flexible NW LEDs initiated by a former postdoctoral fellow of our group, Xing Dai, and the former PhD students Vladimir Neplokh and Nan Guan. They demonstrated blue, green, bicolor, and white flexible NW based LEDs [107]–[109]. I will first introduce the devices they reported and their limitations, which sets the starting point of my PhD work, then I will describe my contribution to the flexible NW LED development.

Our approach combines the outstanding optoelectronic properties of III-Nitrides NWs with the flexibility and transparency of a polymer. The fabrication process consists in encapsulating the LED NWs into PDMS, peeling them off from the native substrate, transferring to a flexible substrate and contacting them with a flexible and transparent contact. The details of the fabrication process will be discussed later.

III-nitride LEDs NWs are self-assembled, with a core shell structure, grown by MOCVD at CEA-Grenoble by the group of Christophe Durand. The NWs have a n-GaN base, and the upper part contains the core-shell structure with multiple quantum wells (MQW) of InGaN/GaN covered by a p-GaN shell. Their structure is shown in the SEM image of Figure 2-1

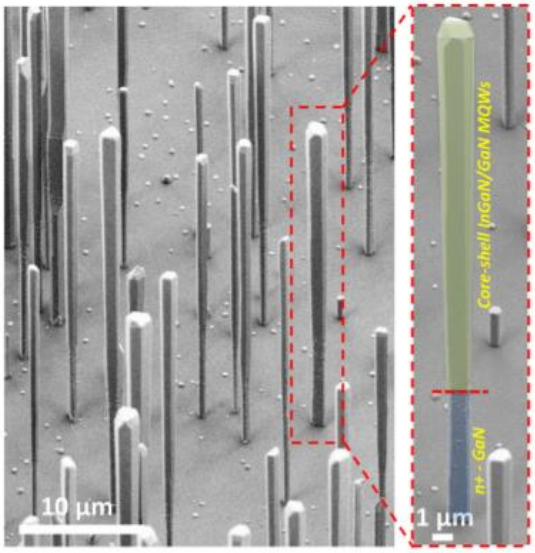

Figure 2-1. SEM image of self-assembled core shell NWs, grown by MOCVD. The close-up image highlights the n-GaN base, in blue, and the core shell InGaN-GaN MQW, covered by p-GaN in yellow [107].

The InGaN/GaN NWs LEDs arrays can be grown with different In composition. By increasing the In concentration in the InGaN MQWs the bandgap energy reduces, thus the emission wavelength increases. The necessary amount of In depends on the target wavelength emission for the LED, the growth conditions should be adjusted accordingly.

2.2.1 Blue LED

To demonstrate blue LED, the array of core shell LEDs NWs was grown on a c-sapphire wafer. The growth temperature of the InGaN QWs was 750 °C, which yielded an In composition of about 15% for blue emission [107]. The active region consisted of seven periods of 5 nm InGaN quantum wells, delimited by 10 nm thick GaN barriers.

The crystalline structure of the core/shell QWs was probed by transmission electron microscopy (TEM) and energy dispersive X-ray (EDX) spectroscopy. TEM images revealed a presence of radial (m-plane) and axial (semipolar plane and c-plane) QW systems. The semipolar QWs located at the nanowire tip had a larger thickness and a higher In content than the m-plane QWs coating the nanowire side walls. The QWs on the c-plane were distorted and presented structural defects [107].

The devices showed bright blue emission displayed in Figure 2-2 (a)-(c) with no performance degradation neither under outward or inward bending down to 3 mm curvature radius neither in time for more than one month storage in ambient conditions without any protecting encapsulation [107].

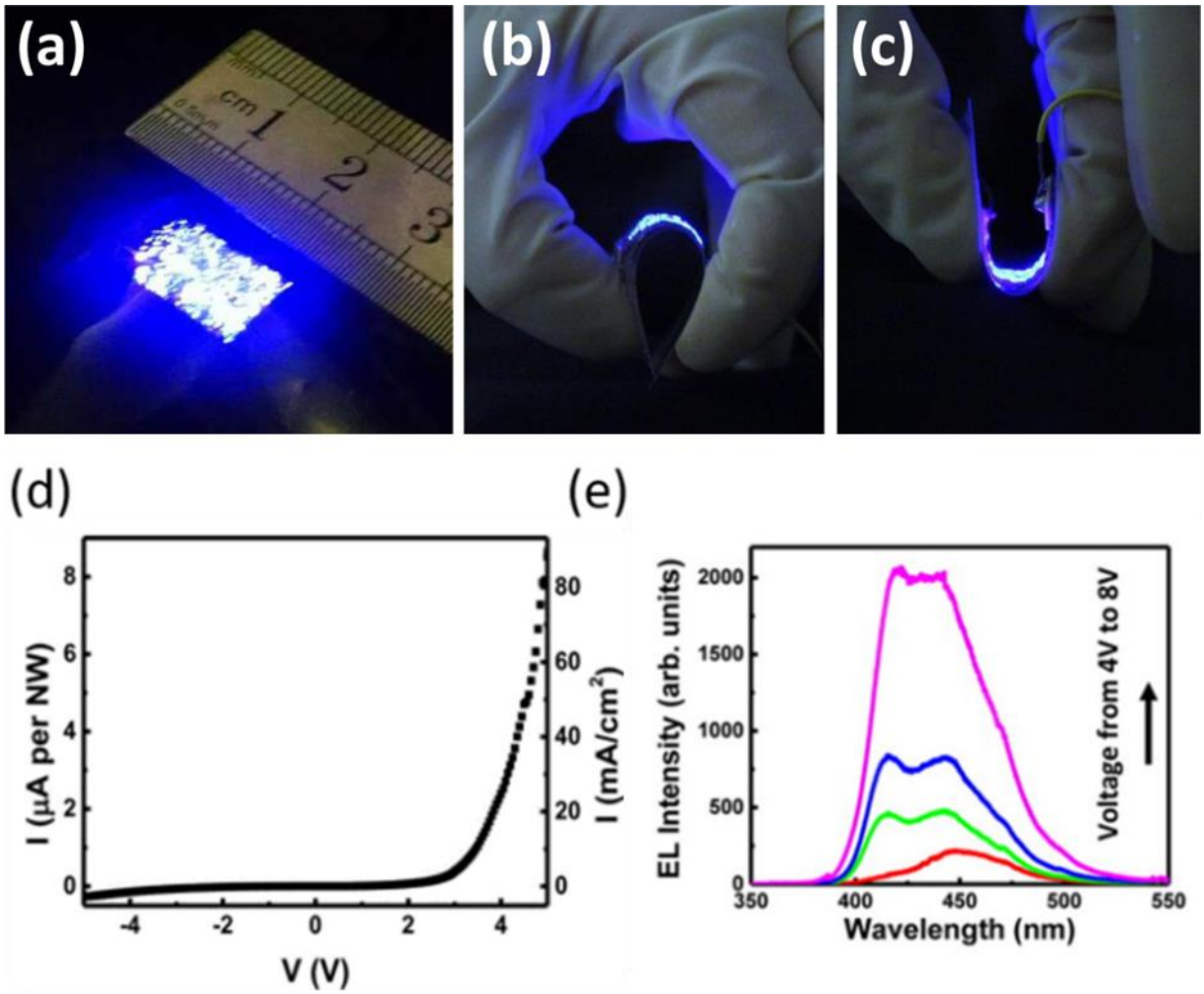

Figure 2-2. Pictures of the blue flexible NW LED in operation under a fixed bias of 5V under flat conditions (a) and at the bending curvatures of 3.5 mm (b) and -2.5 mm (c). (d) is the current-voltage curve of the blue flexible LED showing diode like behaviour (e) Shows the RT EL spectra of the blue flexible NW LED under different biases from 4 V to 8 V [107].

Figure 2-2 (d) shows the IV characteristic of a diode with low leakage current on the reverse bias and Figure 2-2 (d) the EL spectra at different voltages (from 4 to 8 V) with a broad emission characterised by two peaks, at 415 nm and 447 nm covering the 400−500 nm range.

The current voltage (IV) curve was measured. It shows a typical rectifying behaviour of a diode. The opening voltage is about 3 V and the leakage on the reverse bias is weak. The electroluminescence (EL) spectra have been recorded under bias from 4V to 8V. At 4V the spectrum is dominated by a peak at 447 nm. Increasing the voltage, a peak centred at 415nm shows up and becomes more pronounced. It is known that the peak at 415 nm is originated from the radial QWs whiles the peak at 447 nm arises from the axial QW, which contains more In.

2.2.2 Green LED

To reach green emission, NWs with a higher In content are required. The key

parameter for achieving a higher In content is the use of a lower growth temperature for the QWs. After growth optimization, green emission from the nonpolar m-plane wire sidewalls was successfully achieved for the wells grown at 650°C (2.7 nm thick wells sandwiched by 11 nm-thick GaN barriers) [39].

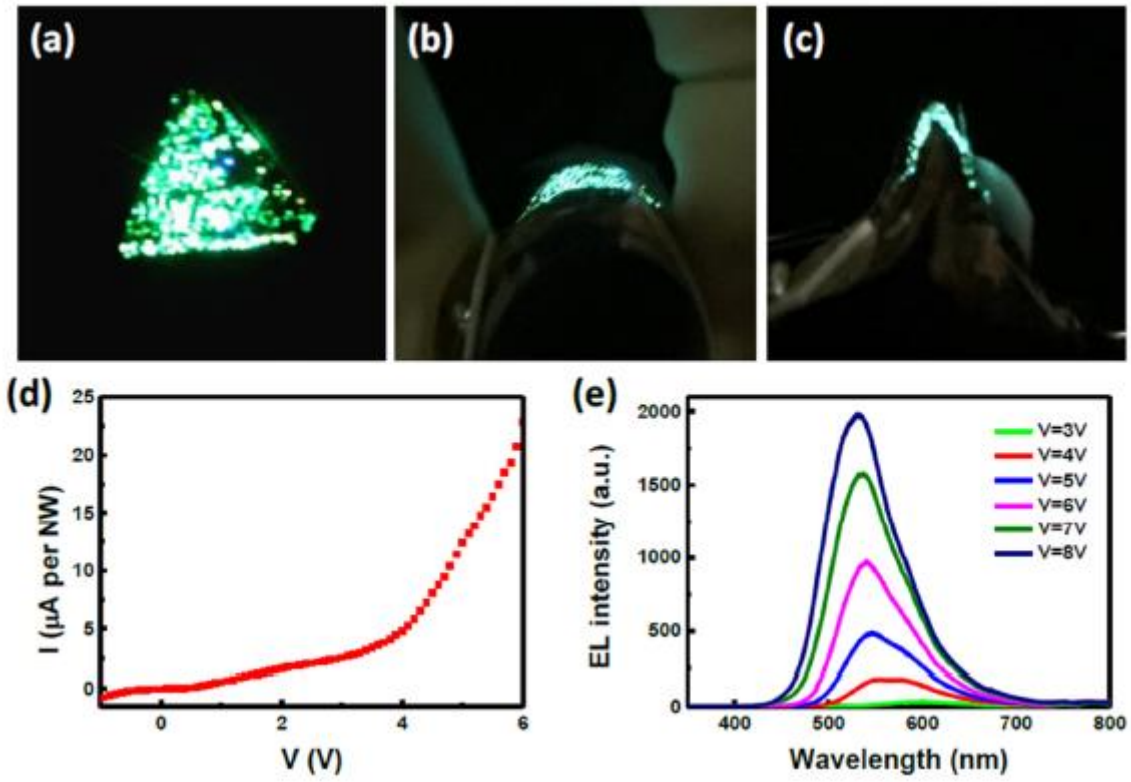

Figure 2-3. Pictures of the operational green flexible NW LED. Top view flat device on (a) moderate outward curvature on (b) and extremely outward curvature on (c). (d) is the current-voltage curve of the green flexible LED showing diode like behaviour (e) Shows the RT EL spectra of the green flexible NW LED under different biases from 3 V to 8 V [107].

The IV curve of the green flexible LED illustrated in Figure 2-3 (d) showed a diode like behaviour with an opening voltage of 3.5 V, however the reverse leakage current was significantly stronger than for the blue LED. EL spectra at different biases, from 3V to 8V, showed a peak centred at 530 nm presenting a blueshift with injection. The observed emission wavelength of 500-550 nm was consistent with an average In-content of MQWs measured in the range of 24 ± 4 % by energy dispersive X-ray (EDX) and atom probe tomography (APT) [190], [191]. Zones with a higher In-content up to 30% were also observed in structural analyses related to a strongly inhomogeneous In composition in the wells. It should be noted that for higher In compositions (i.e. lower growth temperature) the inhomogeneities are further increased as will be discussed in next chapter 3: Towards red flexible LED, where the attempts to achieve red emission are described. The broad spectrum is due to these composition inhomogeneities, along the wire, but also between wires.

2.2.3 Multilayer LED

The fabrication of this kind of flexible LEDs based on nanowire membranes offers a large design freedom and modularity. It is possible to combine different layers of different materials without constraints related to lattice constant or growth conditions. This concept is illustrated in Figure 2-4 (a).

By mounting a fully transparent blue flexible NW LED on a semi-transparent green LED, flexible NW multicolour green-blue LED was demonstrated [107]. The bias could be applied at the same time on both layers or individually on one of the layers. Figure 2-4 (b) shows the independent EL emission for each LED and the emission of the two LEDs together. Blue flexible LED emission was centred at 400 nm while green emission was centred at about 530 nm. The EL spectra of the two layers is perfectly matched with the sum of the two individual EL spectra.

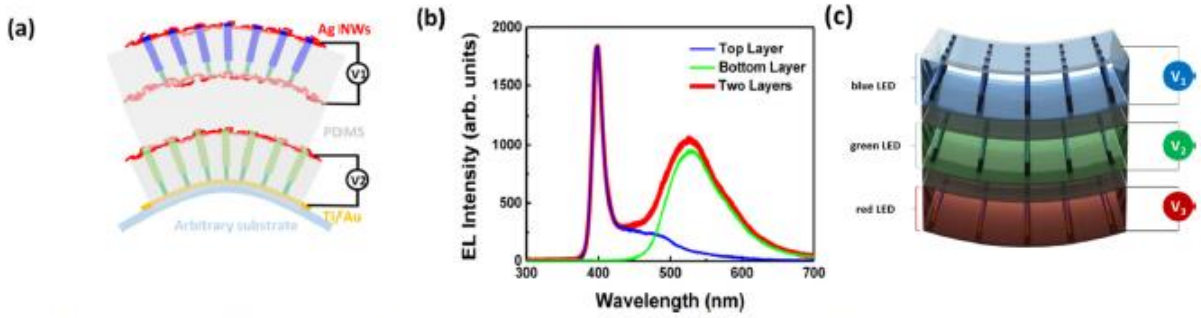

Figure 2-4. (a) Schematic of the flexible NW multicolour green-blue LED. (b) EL spectra of the top blue layer, of the bottom green layer and both layers at the same time. (c) Schematic of a flexible NW RGB LED [158].

The large design freedom enables enormous possibilities to combine materials and different functionalities. This concept can potentially be applied to flexible NW LED stacking three layers, red, green, and blue for producing a white light source or an RGB display. The optimization of the transparency of the top two layers is the key parameter to address. Connecting the three layers in series would simplify the architecture, however, an independent connection has the advantage to allow tuning of the current to achieve colour intensity matching.

2.2.4 White LED

White LED can be obtained by mixing the three primary colors of the light, red, green, and blue. Another way to achieve white light is the conventional phosphor down conversion using blue light and a yellow phosphor. The mixture of the blue light of a LED and the yellow emission from a phosphor excited by the same blue light results in a white emission, well suited for lighting applications. Based on the blue flexible NW LED, white flexible LED was produced by adding nano-phosphors to the PDMS mixture where the NWs were encapsulated [108], [109].

2.2.5 Nanophosphors

Nanosized YAG: Ce (3.3%) was the phosphor selected for this realization, it absorbs the blue light coming from the NWs LED radiation and emits yellow light. It has a strong absorption of blue light and a fast decay time, which inhibits the saturation quenching and it exhibits only weak degradation in time, in adverse environment, or under optical excitation. The quantum efficiency of this material can be higher than 85%. Notwithstanding, to optimize the conversion efficiency and the color rendering, new materials using other ions (Eu^{2+}, Mn^{4+}) or ceramics (oxides, halides) are still under research as will be discussed in Section 2.5.1 Phosphors for white light quality optimization.

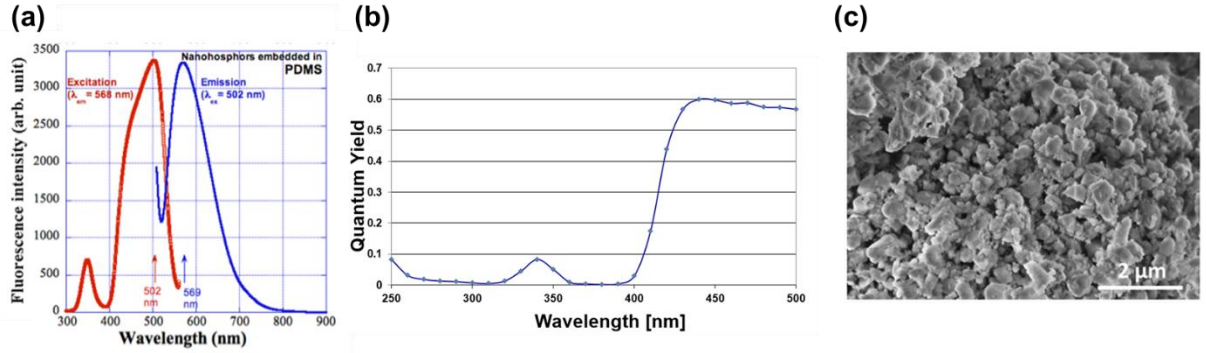

Figure 2-5. (a) Excitation spectrum (solid red line) and emission spectrum (solid blue line) of the nanophosphor YAG:Ce embebed in a PDMS layer, emision wavelength detected at 568 nm and excited wavelength at 502 nm. (b) Absolute quantum yield of the YAG:Ce phosphor in PDMS and (c) SEM image the the YAG:Ce nanophosphor particles [109].

The wavelength dependence of the quantum yield of the YAG: Ce nanophosphor used for the first white flexible LED generation is shown in Figure 2-5 (b). The quantum yield is about 60% in the blue wavelength range. SEM picture (Figure 2-5 (c)) shows that the grain size is less than 500 nm, compatible with penetration in spaces between the wires.

Ref. [192] presents a detailed study about the environment of the nanophosphor and its different agglomerations due to the ionicity of the matrix and mixing conditions.

The emission and excitation spectra of the nanophosphor were measured already embedded in the PDMS layer. The excitation spectra show two broad bands, at about 350 nm and 500 nm. They are both generated from the $4f^1$ to $5d^1$ ($4f^1$ $5d^0$ to $4f^0$ $5d^1$) transition from the electronic configuration of Ce^{3+}. The peak about 500 nm shows a shoulder at shorter wavelength at 450 nm, attributed to the interaction with the PDMS or agglomeration. The excitation suits well with the flexible blue led wavelength emission for pumping the phosphor.

In order to couple the nanophosphors with the flexible LED emission, the PDMS used

for encapsulating the NWs was doped with the phosphor. The used mass ratio between YAG:Ce and PDMS was 1:20. In addition to the nanophosphors integrated in the encapsulation layer of PDMS, an extra PDMS layer doped with nanophosphors was used as a capping layer of 300 µm thick to enhance the blue-yellow conversion.

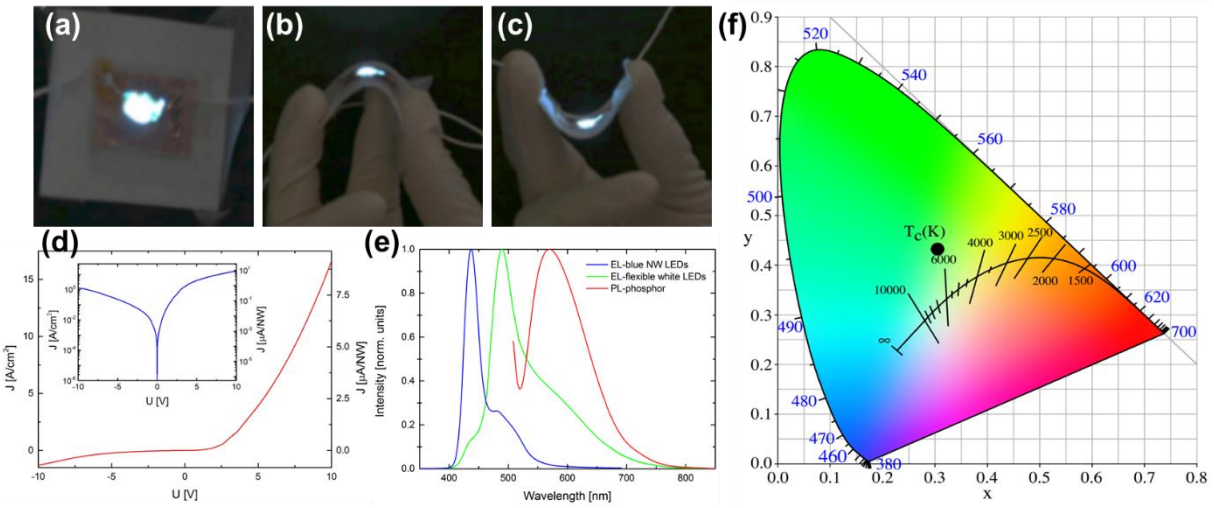

Figure 2-6. Pictures of the white flexible NW LED under operation. Top view flat device in (a), moderate outward curvature in (b) and inward curvature in (c). (d) displays the current-voltage curve of the green flexible LED showing diode like behaviour (e) Shows the RT EL spectra of the pump flexible NW LED and of the white LED with the PL of the nanophosphor. (f) CIE 1931 chromaticity diagram with the location of the first generation of white flexible NW LED shown with a black dot [107].

The mechanical properties of the flexible LED were tested, going from outward to inward bending with a 5 mm radius, as shown in Figure 2-6 (b) and (c). No significant change of either current or luminescence were observed during the bending test, neither after storage of the LED up to 50 days in ambient conditions.

The current density versus applied bias is shown in Figure 2-6 (d). It has a similar rectifying diode like behaviour as the blue flexible LED with an open voltage of 3 V. The phosphor doping on the PDMS doesn't affect the electrical behaviour, the device has a low leakage current.

Figure 2-6 (e) shows the normalized EL spectra of both the reference and the white LEDs with the photoluminescence spectrum of the nanophosphor. The EL spectra show a very broad emission covering a range from 400 nm to 700 nm. The dominant emission is peaked at 489 nm with a shoulder at 437 nm, which corresponds to the unconverted blue light of the LED. The EL spectra of the white LED have a good correspondence with the emission spectra of the phosphor.

For this first generation of white flexible LEDs the quality of the produced white light was modest. The parameters used for quantify the light quality, and the calculation of the chromaticity coordinates in the CIE 1931 chromaticity diagram are detailed in Appendix A: Quality of the light. Indeed, under an injection current of 3.9

A/cm^2 the chromaticity coordinates are located at x=0.3011, y=0.4688 as shown in Figure 2-6 (f). The CCT is 6306K corresponding to a cool white light with a poor CRI of 54. The cool white of the first generation of white flexible NW-based LEDs is well observed in Figure 2-6 (a), it has a blueish colour. The desired values for a high quality white light source should have a lower CCT (generally ranges between 4000 K-5000 K) and a CRI higher than 80.

2.2.6 Remaining open issues at the beginning of my PhD

To summarize, when I started my PhD work, the technology for flexible NW LEDs was established and the first demonstrations of blue, green and white LEDs were done. However, several issues remained unsolved. First, the quality of the white flexible LED had room for improvement, namely for reaching larger CRI values and achieving a lower CCT, closer to the values used in the lighting market. Next, detailed studies regarding the mechanical properties have not been performed, and the robustness of the flexible LEDs under current stress and their thermal degradation have not been performed.

Finally, LEDs at higher wavelengths are required to develop a RGB device for white emission or a display. Green flexible LEDs were demonstrated, however the leakage was already strong, therefore red LEDs using InGaN approach seem challenging. Alternative approaches should be explored for this purpose as will be described in chapter 3:89 Towards red flexible LEDs.

In my PhD, I have worked on the optimization of the white light [193] using the phosphor down conversion approach, on the fabrication of a flexible red LED for assemble a RGB device, and also analysed the robustness of our flexible LEDs on terms of heat [194].

In the next sections of this chapter, I describe the contributions I did to this technology: (i) optimization of the fabrication process, especially of the transparent contacts, (ii) Studies of different phosphors and their implementation for improved white light flexible sources, (iii) Analyses of the degradation of flexible LEDs by mechanical and thermal stress and (iv) stretchable device.

2.3 FLEXIBLE NANOWIRE LEDS FABRICATION

2.3.1 Nanowires growth

The growth of the NWs investigated in this chapter was performed in CEA-Grenoble by MOVPE in the group of Christophe Durand by Akanksha Kapoor. Detailed analysis of the wire growth and the influence of different growth parameters have been very well documented in her thesis [190]. Here I will briefly describe the main steps used to grow the nanostructures involved in my work.

The GaN NWs having a core-shell structure with InGaN/GaN multiple QWs were grown by metal-organic vapor phase epitaxy (MOVPE) on c-sapphire substrates [191], [195].

The c-sapphire substrate is first baked in hydrogen atmosphere at 1040°C for 20 minutes to clean the surface. The annealing is followed by a nitridation step under ammonia (NH_3) gas flow (2000 sccm) during 30 s to form a thin AlN layer on the substrate to favor the N-polarity seed growth [190].

Then, the nitridated substrates are exposed to simultaneous flow of NH_3 and silane (SiH_4) with a mass flow of 4000 and 200 nmol/min respectively, to grow a thin SiN_x of about 1.5 nm. Nucleation of the GaN NWs takes place with NH3 flow of 1000 sccm and Trimethylgallium (TMGa) flow of 60 sccm under the N2 carrier gas flow of 8000 sccm at 1040°C. Once the NWs were nucleated, the growth parameters are fixed for the wire formation.

The key parameters governing the wire dimensions are the growth temperature, pressure, V/III ratio, precursor flow and silane addition. The influence of these parameters on the NW growth can be found in ref. [190]. From these parameters, it is important to highlight the growth temperature. With increasing the growth temperature, the wire density and length decrease, while the diameter of the wires increases. Therefore, an optimum temperature of 1040 °C is used for the wire growth.

In first place, n-doped GaN NWs were grown based on high silane flux. Silane gas not only acts as a n-type dopant but also leads to the formation of a SiN_x layer around the wire sidewalls [196]. This SiN_x layer provides passivation of wire sidewall facets that prevents any lateral growth and favors the vertical growth leading to the wire-geometry.

The Si atoms incorporate inside the wire core leading to a strong n-type doping. As a result, the base part of the GaN NWs is highly n-doped ($\approx 10^{-20}$ cm^{-3}) with a typical length of 10 µm and a diameter between 700 nm-1.5 µm [197].

Direct growth of InGaN around the wire is not possible when the SiN_x passivation layer is present on the sidewalls. However, the wires can continue to grow vertically even if the silane flux is stopped. After forming the n-doped base part, a non-intentionally n-doped GaN segment of 20±10 µm length was grown without silane flux leading to a reduced doping concentration ($\approx 10^{-18}$ cm^{-3}) [197]. This led to a structure with a heavily doped bottom part, named “n-part”, and an unintentionally doped part on the top, named “upper-part”.

The next step consists in the deposition of the active MQW region, directly on the side walls. The growth mode switched from axial to radial mode, thanks to the growth temperature reduction from 1040 °C. The pressure is also reduced. Because

of the presence of the SiN_x layer around the NW base sidewalls of the "n-part", the radial growth on this region is inhibited and the core shell heterostructure is only grown on the "upper part" of the NW, around the non-intentionally doped wire segment [198], [199].

Finally, to complete the LED structure, the growth was pursued with the deposition of about 100 nm p-GaN shell at 920 °C using Cp_2Mg as a precursor for incorporation of the Mg acceptor. After the activation annealing at 700°C for 20 min, the estimated hole concentration is about 10^{-16} – 10^{-17} cm^{-3} [110].

It is noteworthy that this design of the core-shell wire geometry with only a partial coverage of the core with the active region is beneficial for the final electrical contacting when integrating the wires in a LED device, as it allows the access to p-GaN (wire-top) and n-GaN (wire-bottom) without additional etching steps [190].

Figure 2-7 (a) shows 30° tilted SEM picture of the core-shell NWs array, panel (b) displays a single NW magnification where the n-part and the upper-part are indicated accompanied by a schema showing the MQW and the internal structure of the "upper-part" of the NW. Figure 2-7 (c) is a transversal cross-section STEM picture taken along c-axis where all the radial growth is well shown, internal non-intentionally doped core of n-GaN, seven QWs of InGaN/GaN, and the p-GaN shell.

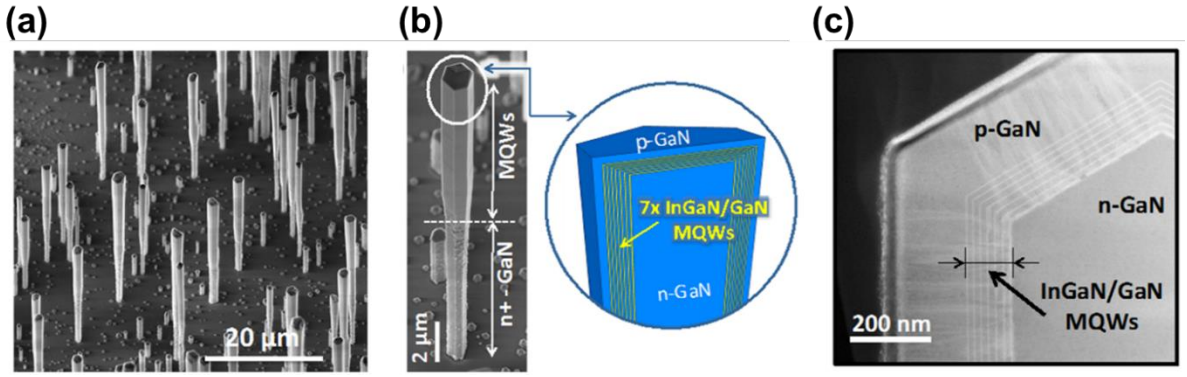

Figure 2-7. (a) 30° tilted SEM image of core-shell InGaN/GaN NWs grown on c-sapphire. (b) Detail of a single wire showing the core/shell MQW region and its schematics. (c) Transversal cross-sectional STEM-HAADF image taken along the c-zone axis showing the shell structure with the MQWs and the p-GaN [Figures reproduced from PhD thesis of A. Kapoor [190]].

Note that the key parameters governing the growth of the active material, InGaN MQWs and GaN barriers, are tuned to achieve the desired amount of In corresponding to the targeted emission wavelength. The precursor used for In is Trimethylindium (TMIn). Samples with different In concentrations were grown by varying only the growth temperature of the InGaN QWs: a lower growth temperature favours higher In incorporation.

Figure 2-8 (a)-(d) show 30° tilted SEM pictures of the core-shell NWs arrays where the InGaN MQWs were grown at different temperatures, 620 °C, 650 °C, 685 °C and

710 °C, respectively. On top of each image, a cross-sectional SEM image of a single NW is shown. Figure 2-8 (e) shows normalized PL spectra of the respective arrays, showing the GaN near band edge peak and the InGaN QWs emission, which redshifts with decreasing growth temperature.

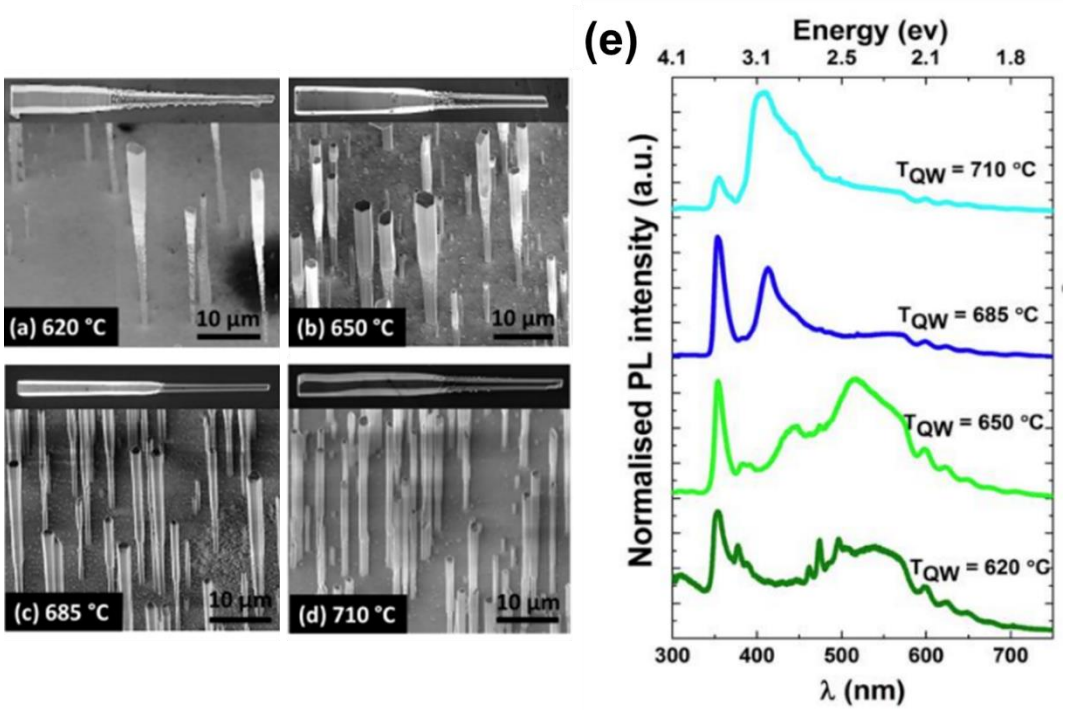

Figure 2-8. (a)-(d) 30° tilted SEM pictures of the core-shell NWs arrays where the InGaN MQWs were grown at different temperatures, on the top, respective single NW cross section. (e) Normalized PL spectra of the respective arrays, evidencing the redshift of the InGaN emission when decreasing the InGaN growth temperature [190].

2.4 FABRICATION PROCESS

The fabrication process of the flexible NW LEDs was developed by previous PhD students and postdocs in our team. In my work, I have worked on the improvement of the peel-off reproducibility and on the quality of the transparent contacts. Moreover, I have reestablished the fabrication recipes after the move to the new clean-rooms of C2N-Palaiseau.

The flexible NW LED process consists in the following steps: (i) deposition of a thin semi-transparent metal layer on the p-GaN shells to improve the ohmicity of the p-contact, (ii) encapsulation in PDMS, (iii) mechanical peel-off of the composite layer, (iv) n-metal contact deposition, (v) dry etching of the excess of the PDMS on the NW tops, (vi) spin coating of Ag NWs to form the top transparent contact. A detailed schema is shown in Figure 2-9.

In the following, I detail the key steps and related challenges.

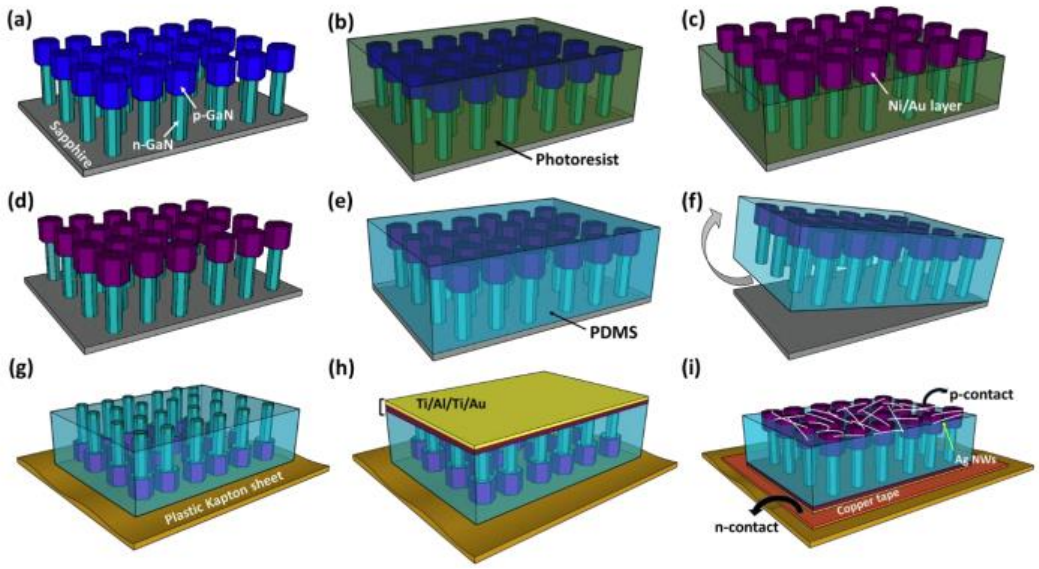

Figure 2-9. Detailed schema of the different steps used for flexible NW fabrication. (a) As-grown InGaN/GaN NWs on sapphire substrate, (b) NWs after positive photoresist spin coating, (c) Ni/Au layer deposited on the top part of the NWs, uncovered after flood exposure and development, (d) Lift-off of the positive photoresist I PDMS encapsulation (f) Peeling off the PDMS membrane with the embedded NWs, (g) PDMS layer is flipped and mounted on a Kapton film, as a temporal host substrate, (h) n-GaN contact by Ti/Al/Ti/Au layer deposition, (i) PDMS membrane is flipped again, stuck on a cooper tape, giving access to the n- bottom contact, PDMS etching and top p-contact made of a Ag NWs mesh [190].

2.4.1 Semi-transparent thin metallic p-contact

Due to its high work function, a low resistivity ohmic contact on p-doped GaN is difficult to achieve. There are different metal alloys in the literature, however metals are not optically transparent and conventional ohmic contacts to p-GaN cannot be applied for flexible NW LEDs. In this work we decided to use a hybrid contact consisting of a semi-transparent metal combined with silver nanowires. For the metallization, we chose a conventional approach relying on thermally annealed thin Ni/Au sandwich. The Ni/Au layers should be thin enough to have high optical transmittance [200]. The study of ref. [200] about this semitransparent thin metal contact reveals a specific contact resistance of 1.7 $10^{-2}\,\Omega\,cm^2$ after annealing at 450 °C of 2 nm Ni / 6 nm Au, and a light transmittance about 85% at 470 nm.

Table 2-2. Photolithography parameters for discover the top region of the NWs for an average length of 30 µm.

Spin coating			Soft bake		Exposure	Development
Ramp (s)	Speed (rpm)	Time (s)	Temperature (°C)	Time (min)	Time (s)	Time (s)
1s	1000	60	110	4	3	35

The metallization should be applied only on the upper part of the NWs, i.e. on the p-GaN shell. To insulate the n-GaN NW base from the deposition, a preparation step of encapsulation needs to be done. A positive photoresist (S1818) is spin coated at 1000 rpm for 60 s followed by a soft bake and short flood exposure. The development of the sample is done using 351 developer diluted in water (1:4). The photolithography parameters described in Table 2-2 are those used for an average NW length of 30 µm. The length of the NWs varies depending on the sample, therefore the values need to be adapted, especially flood exposure (2.1 s for 20 µm and up to 4.5 s for 50 µm), and the development time 35s and rinse with deionized water for stopping the reaction.

Under these conditions, the development of the photoresist only happens on the upper part of the wires, leaving the n-doped base parts of the NWs protected. Diluted $HCl{\cdot}H_2O$ (1:4) treatment is used for removing the native surface oxide of the p-shell previous to metallization. By e-beam evaporation a semitransparent thin metal layer (4 nm Ni/4 nm Au) is deposited on the sample surface. The deposition is done using a very slow deposition rate, with a tilt angle of 30° and in a rotation mode. In this way the thin metal layer is deposited on the top of the NW, but also on the sidewalls of the p-shell. After the metal deposition, the lift-off in acetone is performed. It allows to remove the metal film between the NWs while keeping it on the NW top parts. Finally, an annealing at 450°C in O_2 atmosphere oxidizes Ni, which ensures that the semitransparent metal layer provides a low resistance to the p-GaN shell. Figure 2-10 shows an SEM image after the metal deposition step: the Ni/Au shell is visible around the NW top parts.

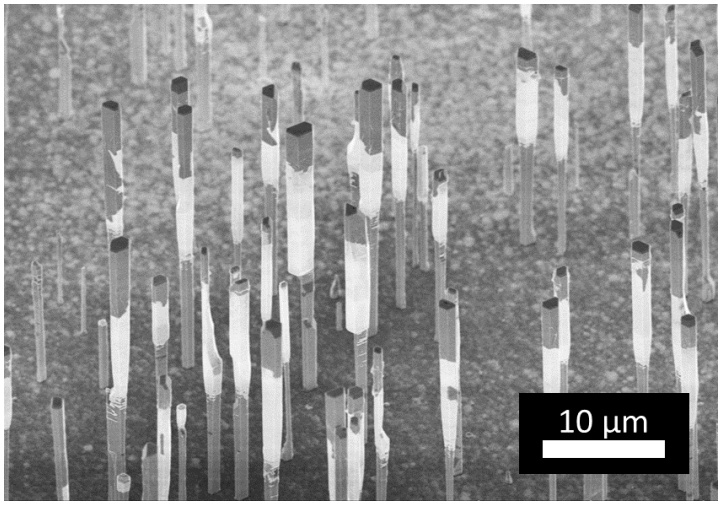

Figure 2-10. SEM image at 45° after thin metal layer deposition, the metal layer is seen on the top regions of the NWs as a dark contrast.

2.4.2 PDMS encapsulation and peeling off

Polydimethylsiloxane (—[O-Si$(CH_3)_2]_n$—) or PDMS is the polymer we chose for the NWs encapsulation because of its optical transparency, mechanically flexibility, and

electrical insulation. Its properties make PDMS an excellent encapsulation material for LEDs.

For PDMS preparation, it is needed to mix liquid PDMS with a curing agent at a weight ratio of 10:1. While mixing some bubbles are generated. To evacuate these bubbles from the PDMS, the liquid PDMS is left under vacuum for 20 minutes. Once the bubbles were removed from the liquid PDMS, it is spin coated at 5000 rpm for 180s on the NWs LEDs. At this step, a PDMS layer of about 30 μm is formed, encapsulating the NWs into it. For curing, i.e. to eliminate the liquid solvent and cross-link the PDMS, the sample is baked at 80°C in an oven, for at least 120 minutes.

Table 2-3. PDMS spin coating and curing parameters.

Spin coating			Curing	
Ramp (s)	Speed (rpm)	Time (s)	Temperature (°C)	Time (h)
5s	5000	180	80	2-24

Then, the PDMS membrane with the LED NWs inside is peeled off from the sapphire substrate and bottom-up flipped on a temporal host substrate. This is the most challenging step of the fabrication process. For the PDMS peel off procedure I have explored different techniques. The first technique is to peel off the PDMS membrane from the substrate mechanically using a microscalpel. In this way, most of the NWs are detached from the substrate being broken at their foot. However, this technique is not efficient, it is highly dependent on the user, takes a long time (30 min for 1 cm2), and requires a lot of experience for a successful peel off. Because of these drawbacks, other techniques for the peel off have been tried. The second technique consists in peeling off the PDMS membrane with an adhesive tape. The adhesive tape is stuck to the PDMS membrane surface, and then it is carefully removed together with the underlying PDMS. In this case, the PDMS membrane remains stuck to the adhesive tape, and detached from the sapphire substrate. Then, the adhesive tape stuck to the membrane is introduced in a bath of isopropanol, which dissolves the glue. Finally, the membrane is placed on a host substrate to continue the process. In this way, the procedure is easier and more efficient. However, a recurrent problem of this technique is that sometimes the PDMS membrane is removed, but some NWs are not detached from the substrate, leaving a hole in the membrane. Later this hole may produce current leakage or can even completely shorten the device by connecting the p-contact with the n-contact.

For difficult cases, I also tried other approaches to improve the efficiency of both techniques, like depositing a very thin layer of photoresist before PDMS encapsulation (with the respective UV flood exposure to remove the residual photoresist on the NWs surface). After an acetone bath, this thin layer of photoresist

is dissolved, producing an air gap between the sapphire substrate and the PDMS membrane, which facilitates the peeling off. In addition, ultrasounds treatment can also facilitate the peeling off, breaking the NWs on their base, facilitating the subsequent peeling off. Different techniques were used for the devices discussed in this work depending on the specific properties of the NWs (their length, diameter and density). As conclusion, the best suited technique is to peel of the membrane mechanically with the microscalpel although it takes a long time and experience.

2.4.3 n-contact

Once the PDMS membrane with the embedded NWs is peeled off, it is transferred to a host substrate, with the n-GaN base of the NWs on the top. The n-contact, Ti/Al/Ti/Au (10 nm/20 nm/10 nm/150 nm), is deposited on the surface of the PDMS, connecting the n-GaN cores in parallel. Then, the back contact is mounted on a flexible substrate such as Aluminium tape. Due to limitations imposed by the PDMS layer, the annealing for the n-contact is avoided. However, the high doping level of the n-GAN base parts ensures low contact resistance.

2.4.4 p-contact: etching and silver nws

The PDMS membrane mounted on the flexible substrate is flipped again, leaving the n-contact on the bottom, and the p-GaN shells covered by PDMS on the top. For removal of the excess of PDMS from the NW tops, it is etched by RIE, using CF_4:O_2 with a typical etch rate of 100 nm/min. The parameters of the RIE for PDMS etching are noted in Table 2-4. The etching time depends on the length of the NWs, for the typical NW length of 20-30 µm this time is around 10-15 min. The etch time is divided in two steps to avoid overheating the sample otherwise cracks in PDMS may appear. Figure 2-11 SEM displays images at 30° tilt of the p-GaN top of the NW LEDs protruding from the PDMS layer after the RIE etching step.

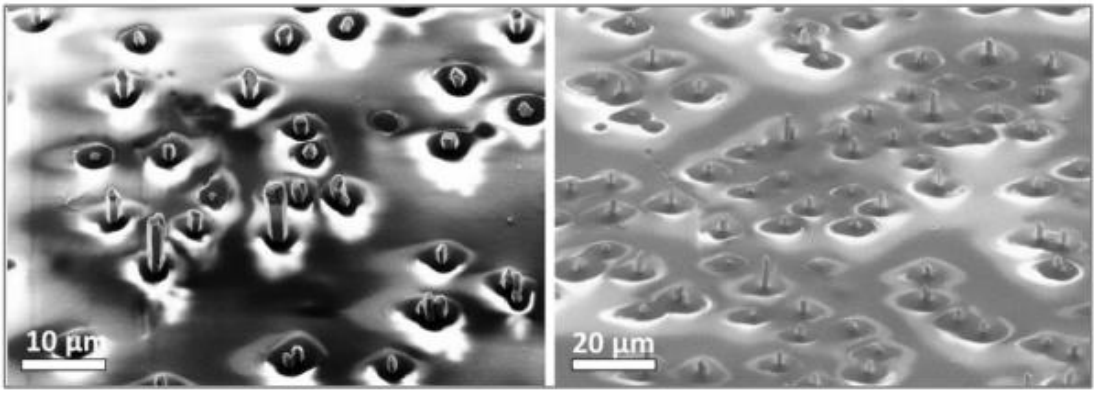

Figure 2-11. 30° tilt SEM image of the p-GaN top of NWs protruding out of the PDMS after RIE etching step.

We note that the thin metal layer deposited in the first step of the fabrication for electrical reasons, also helps to protect the top of the NWs from the RIE plasma,

which otherwise may introduce shallow donor states compensating the p-GaN [201] and even a slow etch of the NW material [202].

Table 2-4. Reactive ion etching parameters for PDMS etching.

RF Power (W)	Pressure (mTorr)	O2 flow (sccm)	CF4 flow (sccm)
270	50	14	40

One of the key elements of this fabrication process is the use of a silver NWs mesh as a flexible contact. Because of the small diameter of the Ag NWs the contact has a high transmittance, and the mesh is flexible. A trade-off must be found between the light transmittance and the sheet resistance.

It was previously analysed in our team that thermal annealing at 200°C for 20 min can be applied, melting the Ag nanowires at their junctions, forming a connected Ag network. The annealing enhances the optical transmittance to 80% and reduces the sheet resistance from 40 to 18 Ω/sq [109]. Figure 2-12 (a) shows how the silver NWs are welded between them on a SEM picture, Figure 2-12 (b) shows transmittance measurements of the Ag NWs mesh with and without annealing, and also on a fully transparent LED device, which will be described at the end of this section. Annealing at higher temperatures or longer times, will melt the silver NWs, leading to an array of silvers drops which are isolated from each other, and hence increasing the in-plane resistance of the contact.

Once the top part of the LED NWs is discovered, silver NWs dispersed in isopropanol (IPA) are spin coated on the top of the membrane to form a mesh of silver NWs interconnected between them and with the LED NWs. Figure 2-13 shows the silver NWs network connecting the NW LEDs. It is important to notice that the In amount of the MQW is different depending on the growth direction (i.e. in the axial and in the radial QWs), so the light emission will differ if the current is preferentially injected through the sidewalls like in the case of contact geometry shown in Figure 2-13 (b), or through the top facet like in the case of Figure 2-13 (c).

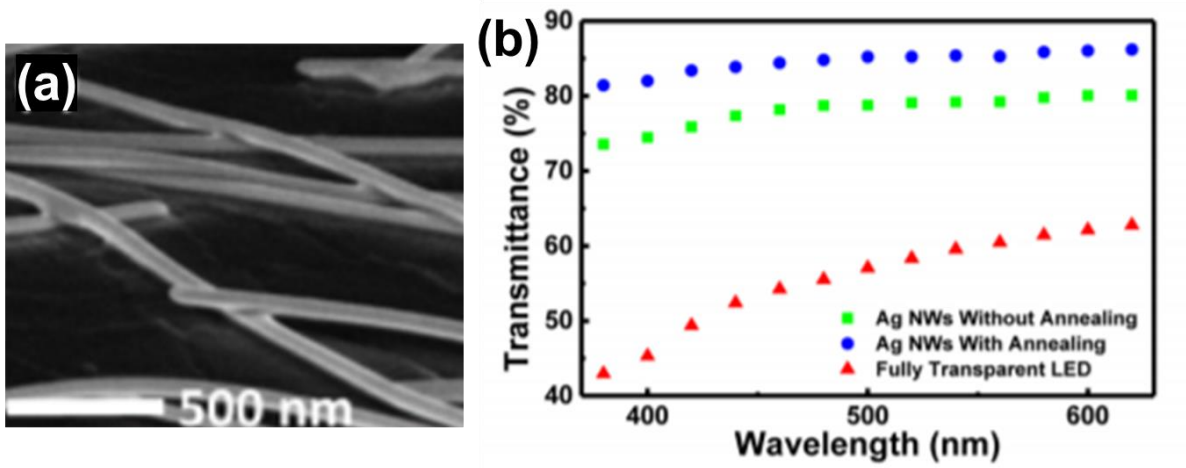

Figure 2-12. (a) SEM picture of the silver NWs network after annealing showing partial melting. (b) Optical transmittance of a single layer of silver NWs before and after annealing, and of a fully transparent device [107].

For improving the contact properties, in some devices I used a mixture of two different sizes of silver NWs. Short and thin Ag NWs (length=12 μm, diameter=20 nm) provide a good contact to NW LEDs while long and thick Ag NWs (length=40 μm, diameter=60 nm) facilitate the long-range current spreading.

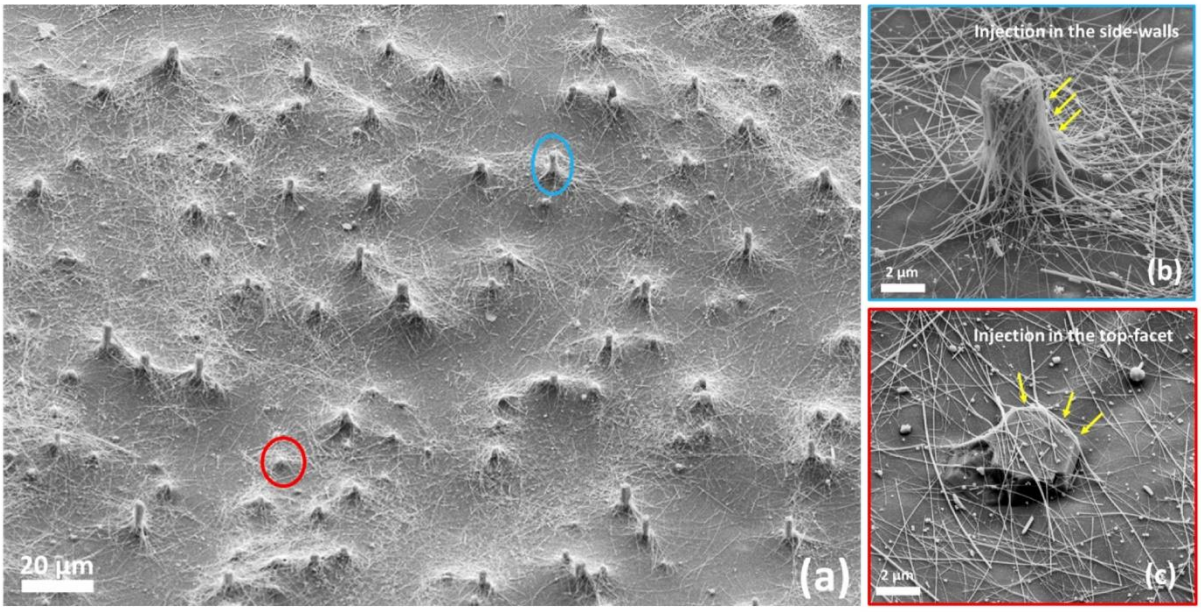

Figure 2-13. (a) SEM image at 45 of the transparent contact made of a network of silver NWs contacting the NW LEDs by (b) the side walls or (c) the top facet.

We have also tried plasmonic welding following the procedure described in ref. [203] under 1 sun intensity light, however without obtaining any morphological modification neither electrical improvement.

It is noteworthy that the optimal density of silver NWs depends on the density of the active NWs. In other types of flexible devices studied in our team, like dense NW

solar cells [204], it is not possible to use the silver nanowire mesh alone. Indeed, the density or silver NWs required to contact every active solar cell NW in the ensemble is too high to maintain a good transparency. Therefore, a multilayer consisting of ITO beneath the silver NWs was used. The ITO allows to contact homogeneously the active NWs, while the Ag NWs interconnections results in a reduction of the sheet resistance and ensures mechanical flexibility. The lowest resistance was achieved with a hybrid contact consisting in 80 nm of ITO with the dispersion of Ag NWs on the top, reducing the sheet resistance to 15 Ω/sq. This optimization was performed in the PhD thesis of T. Mathieu-Pennober. I have tested this strategy on NW LEDs. However, the difference between the sheet resistance with or without the use of an ITO thin underlayer was insignificant, so the benefit did not justify the complexification of the process. Moreover, the mechanical stability of the ITO/silver NWs sandwich on the PDMS membrane was limited. Therefore, I chose the silver NW mesh alone as a transparent top contact for NW LEDs.

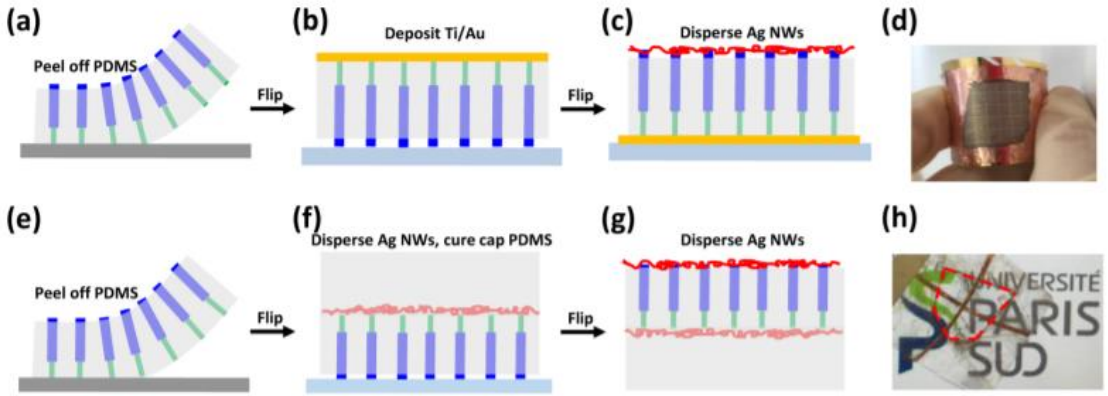

Figure 2-14. Schematic of the fabrication process flow of a flexible LED based on vertical nitride NWs arrays. Panels (a-c) illustrate the fabrication steps for a semi-transparent flexible LED with Ti/Au and Ag NWs as back and top contact, respectively. (d) Photo of a semi-transparent LED. Panels (e-g) shows the fabrication steps for a transparent LED using Ag NWs for both top and back contact. (h) Photo of a fully transparent LED.

The above-described fabrication process is schematically summarized in Figure 2-14 (a-d). Following this procedure, I have fabricated semi-transparent flexible NW LEDs.

Fully transparent flexible LEDs can also be fabricated following a modified process illustrated in Figure 2-14 (e-h), in which the thick metal bottom contact is replaced with a Ag NWs network. The dispersion of Ag nanowires is followed by the spin-coating and curing of another thick PDMS capping layer for backside electrical insulation. A short RIE PDMS etching step can be done first, to uncover a longer segment of the n-core of the NWs. Even, a thin metal layer can be deposed of Ti/Al/Ti/Au (less than 10 nm thick in total to maintain high optical transmittance) for improving the contact. The final optical transmittance for a fully flexible LED is about 40%-60%. Fully transparent LEDs are the building blocks for producing multicolor emitters. An assembling of flexible membranes of different materials with different

bandgaps can be used for future RGB displays.

2.5 IMPROVING THE LIGHT QUALITY OF FLEXIBLE NANOWIRE LEDS

As described previously, the first generation of flexible white LEDs produced cool white light and had a poor light quality with a CRI of 54, and a CCT above 6300 K. This light is unpleasant for the human eye. To improve the quality of the light emitted by the flexible LEDs different devices have been fabricated and tested [193].

For this purpose, the relevant elements which build up the LEDs have been systematically changed in order to produce LEDs which different properties and to select the one yielding the best white light quality. The optimization concerned the following LED ingredients: (i) two different LEDs with different emission were tested, (ii) different pump injection current, at 200 and 300 mA, (iii) amount of phosphors, increasing the mass ratio and two different thickness of the capping layer, 150 and 300 µm, (iv) five different phosphors.

2.5.1 Phosphors for white light quality optimization

Phosphor is a material consisting of a dielectric host matrix doped with an activator (typically consisting of rare-earth metal ions and responsible of the excitation and emission wavelength ranges. First generation white LED integrated the nanophosphors into the encapsulation layer of PDMS between the NWs and also in a capping layer on the top. The used mass ratio was 1:20. In this present optimization, we decided to avoid adding phosphors in the encapsulation layer of NWs and keep only the capping layer doped with the fluorescence material. In this way, it is possible to use the same LED pump for different PDMS-phosphor layers, obtaining reproducible results and analysing solely the effect of the phosphor on the colour quality. In addition, some of these phosphors have a grain size significantly larger than the YAG: Ce^{3+} phosphor used in the first study (this phosphor will be referred to as "Y1"), up to 20 µm, which is larger than the distance between NWs preventing their incorporation in the LED membrane. The phosphor mass ratio was increased to 1:10. To optimize the amount of phosphor, two different layers of each phosphor were prepared. To test low amount of phosphor 150 µm thick capping PDMS doped layer was used, for larger amount of phosphor, 300 µm thick layer was used. After the fabrication and testing of the devices, the 150 µm thick layer leads to cooler white light than the 300 µm thick layers, which can be distinguished by naked eye. Detailed spectroscopic analyses confirmed that as expected, the total conversion of the blue light for a thin cap is lower, keeping larger blue components and lower phosphor emissions [193].

For the colour optimization, in addition to the, YAG: Ce^{3+} phosphor used in the first generation white LED, four different phosphors have been tested. The phosphors were provided by Subrata Das, from CSIR-NIIST in the framework of a French-Indian collaborative CEFIPRA project. Two phosphors are characterized with a yellow

emission (labelled Y2 and Y3), one has orange emission (O1) and one is green (G1). The details of each phosphor are included in Table 2-5.

The phosphors Y1, Y2 and Y3 are the well-known Ce^{3+} doped garnet ($Y_3Al_5O_{12}:Ce^{3+}$). Using Xe electronic configuration s reference, cerium electronic configuration is [Xe] $4f^1\ 5d^1\ 6s^2$. Then, ion Ce^{3+} electronic configuration is [Xe] $4f^1\ 5d^0\ 6s^0$. Due to local symmetries of the material, crystal field, and spin orbit coupling the energy levels of the bands are split.

Ce^{3+} doped garnets ($Y_3Al_5O_{12}:Ce^{3+}$) excitation bands are centred at 450 and 340 nm, which corresponds to the transition of 4f ($^2F_{5/2}$) ground state to the first and second excited levels of 5d configuration of Ce^{3+}. Both transitions are originated by the transition $4f^1\ 5d^0$ to $4f^0\ 5d^1$ at different energy levels due to the spin orbit coupling in the 4f level and crystal field splitting on 5d electronic levels [205]–[208]. The emission band centred at ~547 nm is attributed to the overlap of the emissions centred at 520 nm and 580 nm of Ce^{3+}, which correspond to the transitions from 5d lowest energy level, reached after thermal relaxation, to the two levels of 4f configuration ($^2F_{7/2}$ and $^2F_{5/2}$) of Ce^{3+} [209]. A schema of these transitions is illustrated in Figure 2-15.

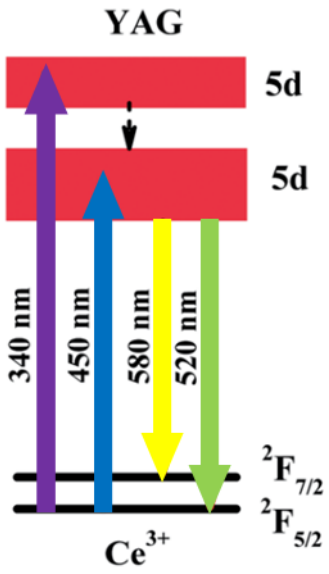

Figure 2-15. Schema of the electronic transitions of a YAG: Ce^{3+} phosphor. 4f1 ground state splits in F5/2 and 2 F7/2 due to spin coupling. When a photon is absorbed, electrons are excited to 5d electronic level, which is split to several energy levels due to the crystal field, electrons thermally relax to 5d ground state and return to 4f1 state, emitting a photon at lower energy [210].

The YAG: Ce phosphors lack the red spectral component, compared to the natural solar spectrum. One method to boost the red emission is to substitute Y^{3+} with larger ions (e.g. Tb^{3+}, La^{3+} and Gd^{3+}) to increase the crystal field splitting and to tune the Ce^{3+} emission to a longer wavelength [205], [211]. For the phosphor Y3, the doping with Gd^{3+} leads to a redshift of the central emission wavelength to 556 nm,

compared with~547 nm in Y1 and Y2. The Gd^{3+} doping also results in a flat and broad excitation spectrum from 300–460 nm. The redshift of the emission band for Y3 in comparison with Y1 and Y2 makes it more appropriate for producing white light with a warmer colour and a higher CRI.

We also tested a green phosphor (G1) on flexible NW LEDs in view of combining together different phosphors for getting a more extended spectrum. One of the widely used green phosphors compatible with blue pumping is an Eu^{2+} activated $(Sr, Ba)_2SiO_4$ orthosilicate. This system can be excited with a wide range of wavelengths from near-UV to blue (from 380 nm to 475 nm) and shows intense green or yellow emissions with the peak wavelength ranging from 490–580 nm. The emission colour depends on the Sr to Ba ratio. Also, the Eu^{2+} emission is effectively influenced by the surrounding crystal environment and crystal field. In Ba^{2+}/ Sr^{2+} sites, the doped Eu2+ ions usually exhibit green emission (yellow-green emission), respectively. Furthermore, this intermediate $(Sr,Ba)_2SiO_4$: Eu^{2+} composition presents a better photoluminescence stability at elevated temperatures [212]. G1 shows a broad green emission peaked at around 509 nm under a 473 nm blue excitation. The emission arises from the $4f^65d^1$ to $4f^7$ transitions of Eu^{2+} ions [213].

To improve the light quality, a stronger emission at the long wavelength side of the spectrum is necessary, so we analysed an orange emitting phosphor O1. A nitride-based $Sr_2Si_5N_8$: Eu^{2+} system is well known for exhibiting long-wavelength orange-red emission bands upon UV and blue excitations. This phosphor system is excitable in a wide range of wavelengths from 360–470 nm. It is characterized by an excellent thermal stability at elevated operating temperatures because of its robust host covalency of N^{3-} [214]. The orange phosphor O1 is an $Sr_2Si_5N_8$: Eu^{2+} compound, which shows an orange emission, ranging from 550 to 700 nm and peaked at around 612 nm under the blue excitation with 451 nm due to the spin-allowed $4f^65d^1$ to $4f^7$ transitions of Eu^{2+} ions [215]. The O1 phosphor was tested alone, but also in a combination with Y2 to demonstrate a suitable white LED system with a warmer white colour.

All the above-described phosphors are widely used for rigid white LEDs due to their high photoluminescence efficiency and adequate thermal stability. The PL excitation and emission spectra of all phosphors tested, mixed in the PDMS layer, intended for capping are shown on Figure 2-18.

Table 2-5 Summary of different phosphor materials used for white felxible LEDs

Phosphor	Emission Colour	Composition	Grain size
Y1	Yellow	$Y_{2.94}Ce_{0.06}Al_5O_{12}$	500 nm
Y2	Yellow	$Y_{2.94}Ce_{0.06}Al_5O_{12}$	5-10 µm
Y3	Yellow	$Y_{2.91}Ce_{0.06}Gd_{0.03}Al_5O_{12}$	2-20 µm
G1	Green	$(SrBa)_{1.9}Eu_{0.1}SiO_4$	5-20 µm
O1	Orange	$Sr_{1.95}Eu_{0.04}Tb_{0.01}Si_5N_8$	5-10 Um

2.5.2 Pumping flexible nanowire LEDs

Two different pumping LEDs with different In content in the MQWs were used to excite the phosphor doped PDMS membranes. The EL spectra of these two LEDs are shown in Figure 2-16 for an injection current of 200 mA (dashed lines) and 300 mA (solid lines). The emissions are spectrally shifted and therefore have a different matching with the absorption of the analysed phosphors.

Self-assembled MOCVD NW LEDs have shown In composition inhomogeneities. In incorporation on the polar c-plane QWs is larger than the incorporation on the non-polar sidewalls QWs. It has been observed that there is a competition for the carrier injection produced by In inhomogeneities: at lower bias the high resistivity of the p-GaN layer allows to inject into the NW top, which corresponds to the In rich axial QW. While, with increasing current, the hole transport in the shell toward axial QWs leads to a potential drop and becomes unfavourable, the injection in the non-polar m-planes is promoted [112]. This effect becomes critical at high In contents. In Figure 2-16, both pumps show larger emission of In rich regions at the low injection current, while at 300 mA, the light emission is dominated by the peaks at larger energy.

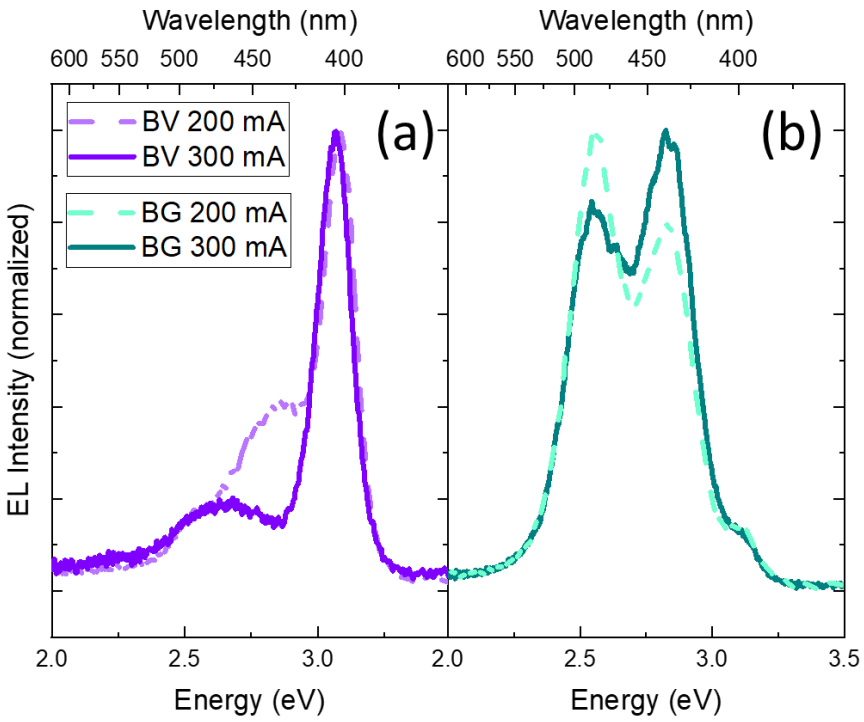

Figure 2-16. Normalized EL spectra of the two different pumps at different injection current. violet colour refers to the pump named blue-violet (a), in cyan the pump named blue-green (b), dashed line indicated 200 mA injection current and solid line corresponds to 300 mA.

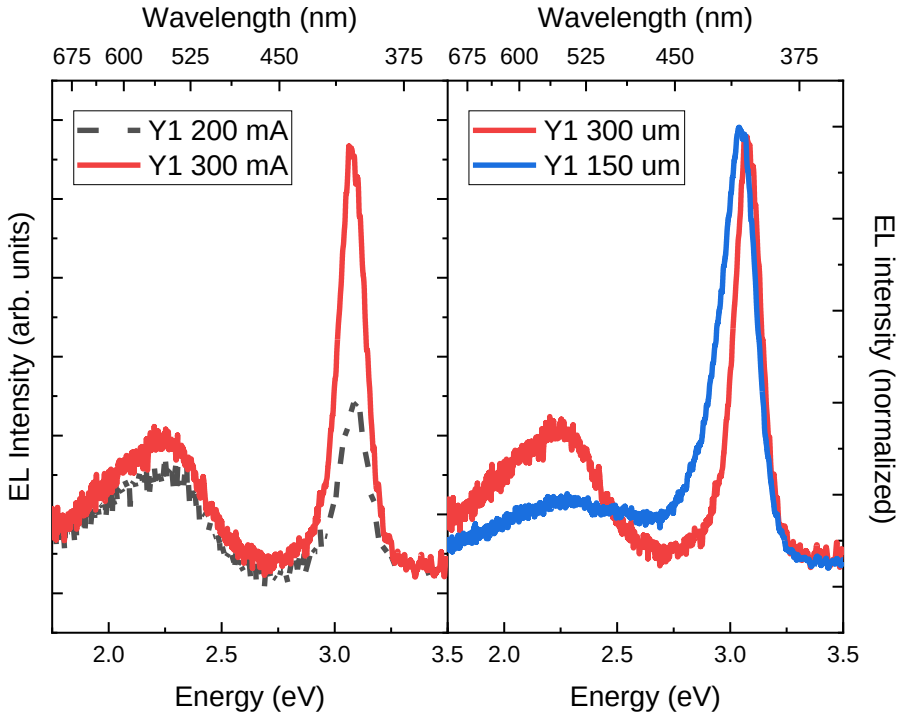

Figure 2-17. EL spectra of white flexible LEDs using BV pump and phosphor Y1, (a) capping the LED wth 300 µm PDMS layer at 200 mA (black dashed line) and 300 mA (solid red line) injection current, (b) keeping 300 mA as injection current for a capping layer of 150 µm (blue solid line) and 300 µm (red solid line).

After systematically changing the previous mentioned building blocks of the white flexible LEDs, (i) different pump LEDs, ii) their injection current, at 200 and 300 mA, iii) different thickness of the capping layer, 150 and 300 µm, iv) five different phosphors) we measured the EL of each combination, calculate the position on the CIE map, and the respective CCT and CRI values. We concluded that the 150 µm thick capping layer does not contain a sufficient amount of phosphors, the device emission is blueish (CCT values are larger than 100000). The pump LEDs injected at 200 mA show low intensity and less conversion of the light. Figure 2-17 (a) illustrates the first effect by showing the EL spectra of a white flexible LED using BV pump at different injection current (200 and 300 mA) with a 300 µm thick Y1 capping layer. It can be seen that the conversion and intensity are larger at 300 mA injection current. In Figure 2-17 (b) the injection current is kept constant at 300 mA, while the thickness of the capping layer of Y1 embedded in PDMS changes from 150 to 300 µm. The spectra are normalized in this case to better visualize the light conversion. From now to the end of this section, we will focus on the white flexible LEDs with the best properties, using a 300 mA injection current and a capping layer of 300 µm thick.

The LED, referred to as 'VB' (for *violet-blue*), has a violet emission peak at 404 nm and a broad blue shoulder centred at 464 nm. By comparison with the excitation spectra of the phosphors traced in Figure 2-18, the blue shoulder overlaps very well with the excitation spectra of all the five phosphors. However, the violet peak overlaps only with the excitation spectra of phosphors Y3, O1, and G1, but it is mismatched with respect to those of Y1 and Y2. This may lead to an insufficient conversion of the violet light in the resulting spectrum of the white LED, thus emitting a cool white colour [193].

The EL emission of the LED referred to as 'BG' (for *blue-green*) consists of one blue peak at 439 nm and one cyan peak at 485 nm. The spectrum of the LED BG shows a good overlap with the excitation spectra of the phosphors Y1, Y2, G1 and O1 and a partial overlap of the blue component for the phosphor Y3.

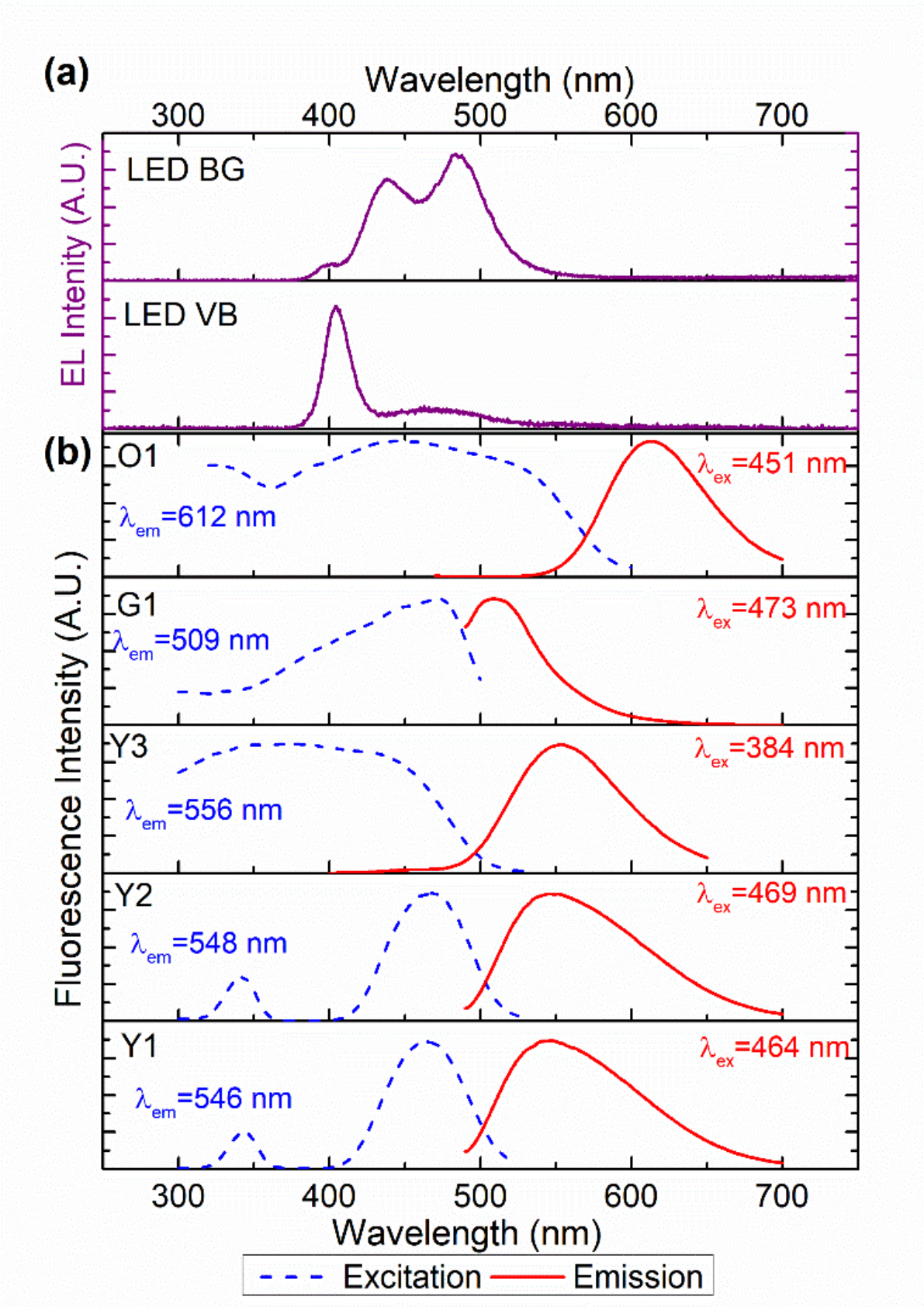

Figure 2-18. EL spectra of the pumping LEDs VB and BG at an injection current of 300 mA. (b) Excitation (blue dashed curves) and emission (red solid curves) spectra of the five analysed phosphors [193].

2.5.3 Second generation flexible white nanowire LEDs

Figure 2-19 displays the EL spectra of the second-generation flexible white LEDs measured with the two different LED pumps, at 300 mA, and the five different phosphors mixed in 300 µm thick PDMS membranes. Figure 2-19 (a) shows the EL spectra of the pump VB and of the flexible white LEDs for different PDMS phosphor doped capping layers mounted on top of the pump. Figure 2-19 (b) shows the respective EL spectra for the BG pump. As expected, all the white LEDs show the EL spectra with a long-wavelength component, which is in good agreement with the emission spectra of the phosphors traced in Figure 2-18.

Figure 2-19 (a) shows the EL spectra of the white LEDs pumped with the LED VB. The violet peak of the LED pump is partially absorbed by all the phosphors but remains present in the resulting EL spectra. The flexible white LEDs with Y1 and Y2 exhibit similar EL spectra. This is indeed expected since the Y1 and Y2 phosphors differ only by the grain size. The blue shoulder is almost entirely converted to the long wavelength emission thanks to the good spectral overlap with the excitation spectra of the phosphors.

This can be well observed in Figure 2-20 (a), which shows the details of the conversion process for one specific example. It compares the excitation and emission spectra of the phosphor Y3 with the EL spectrum of the pump LED VB, and the resulting EL spectrum of the white LED. No blue shoulder can be seen in the final spectrum of the white LED. The blue component is also strongly absorbed by G1. However, for the phosphors Y3 and O1, the blue shoulder markedly remains in the EL spectra of the white LEDs.

Figure 2-19 (b) shows the EL spectra of the white LEDs pumped with the LED BG. The phosphors Y2, Y3 and G1 exhibit a strong absorption of the blue component, while the phosphors Y3 and O1 only partially absorb the blue peak of the pumping LED. This result is consistent with the spectra obtained for the LED VB showing the nearly total absorption of the blue shoulder for Y2, Y3 and G1, but presenting a residue of this shoulder for the phosphors Y3 and O1. For the green peak at 485 nm of the LED BG pump, the white spectra for all the phosphors show an important unconverted residual peak. For G1, the green emission from the LED pump merges with the converted green emission of the phosphor, forming a broad green peak centred at 509 nm.

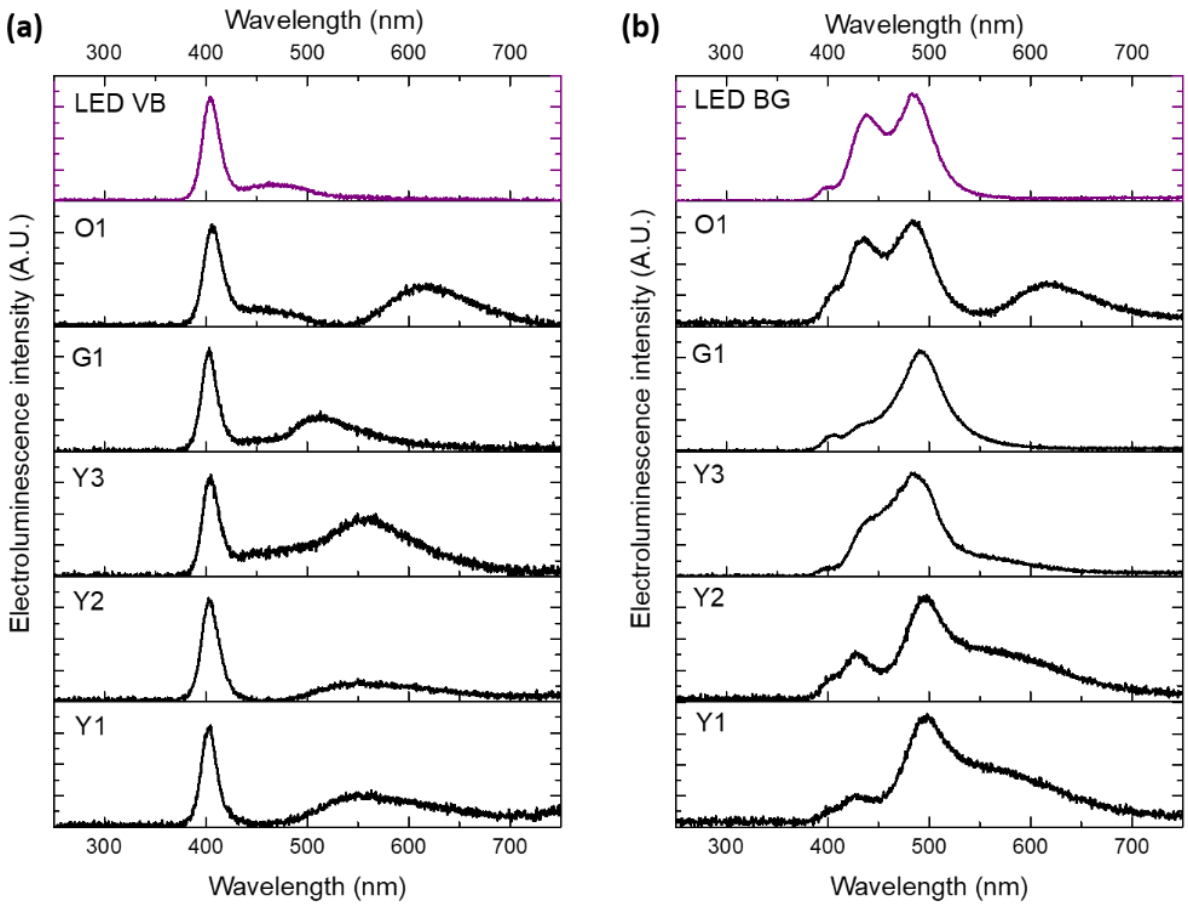

Figure 2-19. EL spectra of the pumping LEDs (purple curves) and of the white flexible LEDs with the different phosphors (black curves) pumped by (a) LED VB and (b) LED BG [193].

2.5.4 Demonstration of a high-colour quality white flexible LED

From the EL spectra of the white LEDs shown in the figures above, it is seen that the most wide-spread yellow phosphors, Y1, Y2, and Y3, lack the emission at wavelengths longer than 600 nm. This results in a rather poor colour quality of obtained white light. However, the O1 phosphor a shows strong emission in this wavelength range.

In order to demonstrate a white LED with a broad spectrum covering the whole visible spectral range, the third generation of flexible white LEDs was fabricated by stacking a PDMS membrane doped by the orange phosphor O1 onto a membrane doped with the yellow phosphor Y2. The stack of the two membranes is pumped by the LED VB. The EL spectrum of this third-generation LED is traced as the black solid curve in Figure 2-20 (b). This figure also displays the excitation and emission spectra of the phosphor O1 and the EL spectrum of the second-generation white LED consisting of an LED VB pumping the Y2 doped membrane alone. The violet residual emission from the pumping LED and the yellow component corresponding to the phosphor Y2 in the second-generation LED, are both partially converted to orange by the phosphor O1.

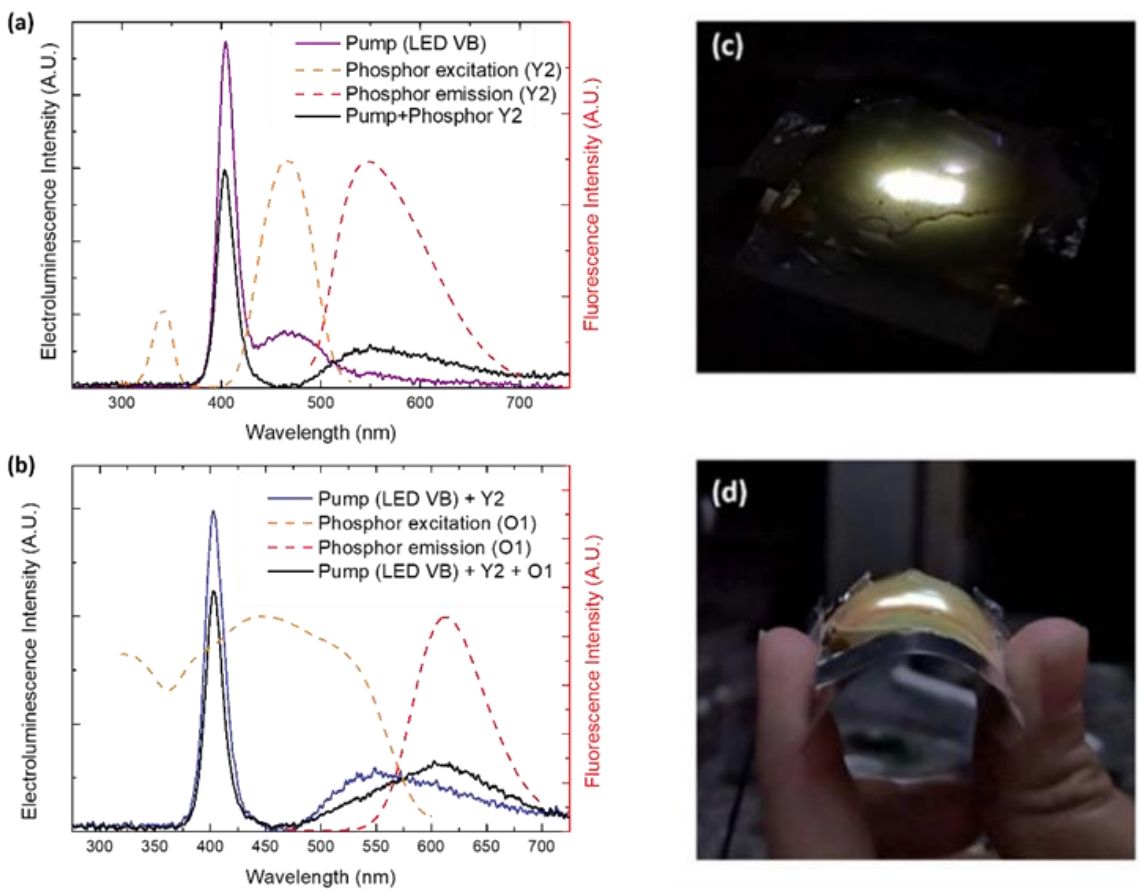

Figure 2-20. Spectra illustrating the colour conversion process of flexible white LEDs. (a) EL spectra of the pumping LED VB and the second-generation flexible white LED with the phosphor Y2 traced with the excitation and emission spectra of the phosphor Y2 in the same plot. (b) EL spectra of the second-generation flexible white LED with the phosphor Y2 as a pump, and the third-generation LED with the additional phosphor O1 on the top traced with the excitation and emission spectra of the phosphor O1 in the same plot; photos of the third-generation NW white LED under operation (c) in a flat condition and (d) with a bending radius of 1.5 cm [193].

To estimate the EQE and WPE, the emitting powers of the third-generation white LED and of the pump LED VB were measured using a power-meter with a large area sensor having a calibrated flat spectral response in the visible range.

The power meter with a diameter sensor of 16 mm was placed at 11 mm from the flexible LED.

The EQE is defines as follows:

$$EQE = \frac{n_{photons}}{n_{electrons}} \; ; \; n_{photons} = \int \frac{I(\lambda)}{hc/\lambda} d\lambda \qquad (2\text{-}1)$$

$$WPE = \frac{P_{optic}}{P_{electric}} \qquad (2\text{-}2)$$

where $n_{electrons}$ is the number of injected electrons, $n_{photons}$ is the number of photons, I(λ) is the optical intensity distribution, $^{hc}/_{\lambda}$ is the photon energy, $P_{electric}$ and P_{optic} are the injected electrical power and measured optical power of the flexible LED, respectively.

The EQE is the ratio between the photon number emitted by the LED and the number of injected electrons, as well the WPE is given by the ratio between the optical power of the LED and the injected electrical power.

It is important to highlight that, only the emission with a light cone angle of 72° is detected with this set-up geometry, which leads to an underestimation of the total emitted power [109]. For more accurate results an integrated sphere set up should be used, which unfortunately was not available.

At 300 mA, the values of the measured EQE and WPE of the third-generation white LED are 0.63% and 0.18%, respectively. These low values mainly originate from the low performance of the LED pump built from self-assembled NWs, which exhibit strong compositional and morphological inhomogeneities [107], [109], [190]. Indeed, at the same injected current, the pump LED VB has a measured EQE of 2.63% and WPE of 1.04%. The values for white LED are lower due to the conversion losses in phosphors, but also due to parasitic light absorption and scattering of the two phosphor-doped PDMS layers used in third generation white LED. Note that the EQE and WPE values are underestimated because of the detection system. By taking the ratio between the WPE values of the third-generation white LED and of the pump LED VB, the efficiency of the down conversion by the two layers of phosphors can be estimated at around 17%.

For comparison of the light quality of the second and third generation of NW based white flexible LEDs, and with the first white flexible LED generation, CIE coordinates, CCT and CRI were computed as found in Appendix A: Quality of the light.

Table 2-6 shows the CIE coordinates, CCT and CRI of the white flexible LEDs with different phosphors and different LED pumps. The locations on the CIE 1931 colour chart of each flexible LED are illustrated on Figure 2-21.

Table 2-6. Summary of CIE coordinates, CCT and CRI for the analyzed phosphors and LED pumps.

Phosphor	LED Pump	CIE coordinates	CCT (K)	CRI
Y1	LED VB	(0.3877, 0.4306)	4160	76
	LED BG	(0.3121, 0.3912)	6209	82
Y2	LED VB	(0.3852, 0.4180)	4147	70
	LED BG	(0.3038, 0.3657)	6665	86
Y3	LED VB	(0.3450, 0.4012)	5134	71
	LED BG	(0.2035, 0.2488)	>100000	NaN
G1	LED VB	(0.2751, 0.3924)	7641	71
	LED BG	(0.1932, 0.2965)	NaN	NaN
O1	LED VB	(0.4065, 0.2687)	2166	62
	LED BG	(0.2773, 0.2389)	18846	55
O1 on Y2	LED VB	(0.4268, 0.3824)	2993	85

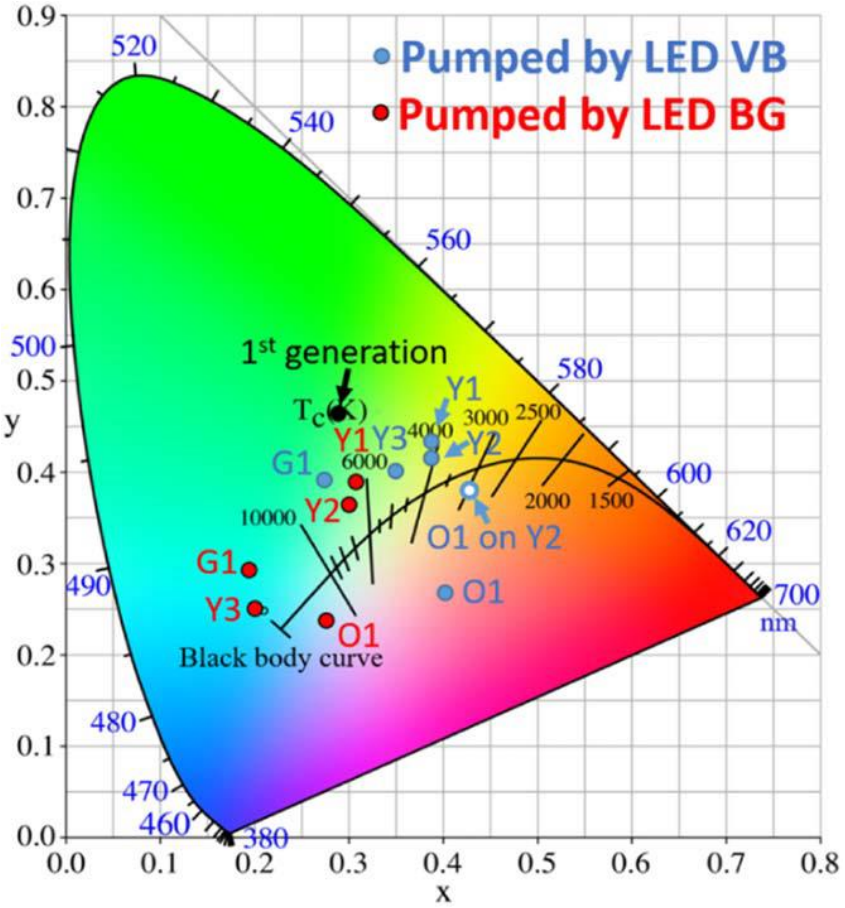

Figure 2-21. Location of the flexible white second generation LEDs with different phosphors pumped by LED VB (blue dots) and by LED BG (red dots) compared to the first generation (black dot) and the third generation LED (blue circle) in the CIE 1931 chromaticity diagram [193].

One of the objectives of this study is to optimize the quality of the white light produced by the flexible LEDs and to improve it from the first generation, getting closer to natural sunlight (CCT=4000-5000 K and CRI=100), which is also the target for the most lighting industrial applications.

Figure 2-21 shows that the second generation of white flexible LEDs are closer to the Planckian locus than the first generation LED, which means that they have a better CRI. Those LEDs pumped with the LED VB are located at the right region, warm whites, of the CIE 1931 chromaticity diagram, while those LEDs pumped with the LED GB are located on more cooler regions, at CCTs higher than 6000 K. All the devices are located on the upper region of the Planckian locus but the LEDs with O1 phosphor, which suggests that a mixture of phosphors, using O1, could produce a white light closer to the Planckian locus, with a better CRI.

The CCTs of the white LEDs with the pumping LED VB are 4150 K for Y1 and Y2, corresponding to a natural white colour. Note that, compared with the first generation flexible cool white LED, which was fabricated using Y1 phosphor,

described in section 2.2.4, the white colour became warmer by doubling the phosphor density (phosphor-to-PDMS mass ratio was increased from 1:20 to 1:10) in the membrane: the CCT shifted from 6306 K to 4160 K. This improvement is due to the stronger conversion of the phosphor, which leads to a lower residual bluish emission from the pump and a more important component in the long-wavelength range, which makes the final white LED spectrum "warmer". The CRI of the device is also improved, from an initial CRI of 54 to 76. This improvement from the first-generation white LED is not only due to the optimization of the mass ratio of phosphor, but also to a different LED pump. In addition, when pumping Y1 phosphor with BG pump, the CCT is similar to the first-generation device, 6209, however, with the improved mass ratio, and the BG pump, the CRI increases up to 82. Therefore, we can conclude regarding the phosphor grain size, that for the phosphor down conversion process, it is not necessary to fill the gaps between the nanowires with phosphor grains, an efficient conversion can be achieved by capping the top surface of the LED. The impact of the grain size on the mechanical properties is studied below.

The CCTs for Y1 and Y2 with the pumping LED BG, are 6209 and 6665 K, respectively, i.e. are more than 2000 K higher than those with the LED VB (4160 and 4147, respectively). This higher CCT corresponding to a cool white colour is due to the poorly converted green peak around 480 nm in the pump spectrum. This explanation is also applicable and extensible to the other phosphors, it clarifies why the emissions of white LEDs with the pump LED BG (red dots in Figure 2-21) are located toward a higher CCT in the colour chart than those with the pump LED VB (blue dots in Figure 2-21).

The CRIs with the LED BG are higher than those with the LED VB. The flexible white LED with only Y2 pumped by the LED BG has the best CRI value of all the tested devices (CRI=86), which is comparable with the commercial white rigid LEDs.

For the phosphors Y3, G1 and O1, with the pumping LED BG, the white LEDs have unbalanced strong components in the short-wavelength range so that their CCTs are shifted from the centre of the white colour zone in the CIE colour chart, therefore the CRI values are bad and the CCT are extremely high (see Figure 2-21). With the LED VB pump, the CCT decreases to 7641 K, 5134 K and to 2166 K for the phosphors G1, Y3, and O1, respectively. This is due to the increased emission wavelength of the phosphors, corresponding to the colours of green, yellow, and orange for G1, Y3, and O1, respectively. The CRI values improve to 71 for Y3 and G1 however for O1 the CRI reduces from 62 to 55.

For the third-generation flexible white LED, which combines Y2 and O1 (blue circle in Figure 2-21), compared to the second-generation white LEDs pumped with LED VB and having only one-layer of phosphor Y2, the colour shifts from natural white (CCT=4147 K) to warm white (CCT=2993 K). This decrease of the CCT is indeed expected, thanks to the richness of the long-wavelength component emitted by the additional O1. The broad spectrum of the white LED with this phosphor mixture also results in a high CRI of 85.

To summarize, these second- and third-generation white LEDs cover the warm white, natural white and cool white, corresponding to the CCTs varying from 2166–6665 K, and several of them have a high CRI.

2.6 MECHANCIAL FLEXIBILITY

The mechanical flexibility of the second- and third-generation white LEDs was tested by comparing the I–V curves and the EL spectra before and after 50 bending cycles for different curvature radii down to 1.5 cm. Bending tests were performed using a rather basic set-up consisting of two clips fixed on translation stages and a fibre fixed above the device to collect the emission as illustrated in Figure 2-22. The set-up was constructed by a M1 internship student Shirley Prado.

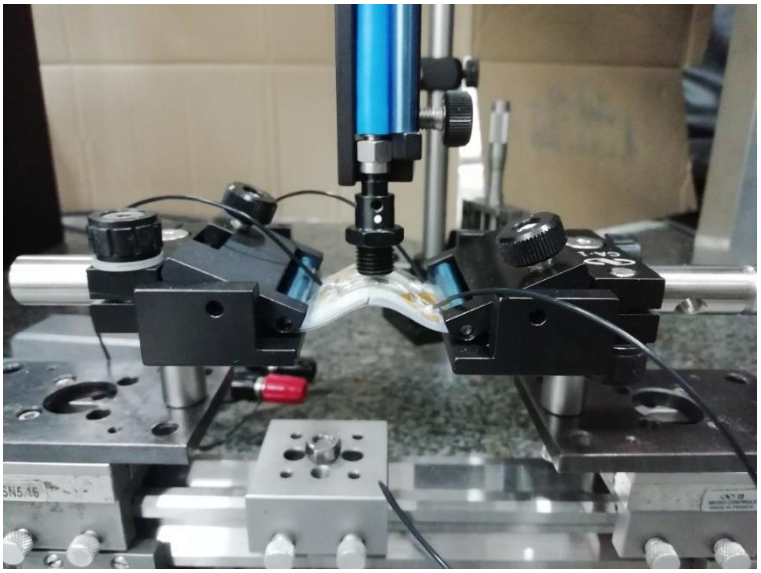

Figure 2-22. Picture of the set up used for bending tests.

In the tested range of the curvature radii, the behaviour of the second and third generation flexible white LEDs is comparable to the first-generation LEDs fabricated with the nanophosphors additionally filling the gaps between the nanowire arrays. This means that the nanometric size of the phosphor grains is not mandatory to fabricate the flexible LEDs for applications requiring bending curvature radii in a centimetre range and the standard micro-phosphors can ensure the mechanical flexibility in these conditions. Photos of the third-generation NW white LED under operation in a flat condition and with a bending radius of 1.5 cm are shown in Figure 2-20 (c), (d). All the flexible LEDs did not show significant intensity or spectral degradation after the bending tests. The devices had a good mechanical flexibility, even for the LEDs with the phosphors with a relatively large grain size, i.e., Y2, Y3, G1, and O1. However, it should be noted that later, Shirley Prado in her M1 internship found that after 1 year of storage in ambient atmosphere, bending tests on flexible LEDs started to induce electrical degradation especially for convex bending. This observation suggests that a protective encapsulation of the transparent flexible contact is desirable to increase the lifetime and stability of the flexible LEDs.

Nowadays the nanophosphors are mostly used for the biomedical applications where the shape and the nanometric size plays an important role [216]. However, it

is still challenging for nanophosphors to compete with the standard solutions in terms of the quantum efficiency. For commercial lighting applications, the luminescent quantum efficiency and the yield of synthesis are more important criteria than the grain size and shape. Here I show that the micro-phosphors, which are less challenging to synthesize than the nano-phosphors [217], are more suitable for the flexible lighting applications requiring a moderate bending.

To summarize, I demonstrated in this section that the colour performance of flexible white NW LEDs can be adjusted by changing the pumping LEDs and the phosphors. The use of phosphor with a submicrometric grain size is not mandatory to keep the mechanical flexibility of the white NW LED. It is possible to use a device configuration, where a phosphor doped PDMS membrane is mounted on top of the LED pump. Replacement of the nano phosphors infiltrated between the nanowires by micro-phosphors circumvents the challenging procedure of the synthesis of the phosphors with nanoscale grains, which show a high quantum yield. Compared to the first-generation flexible white NW LED, the second-generation LEDs using a single phosphor layer show an improvement of the CRI from 54 to 86 and tune the bluish cool white colour to natural white or warm white. The third-generation flexible white NW LED, obtained by stacking two layers of yellow and orange phosphors, emits a warm white light and has a high CRI of 85, which is higher than the white LED with the same pump but with only one layer of any phosphor. These high-CRI flexible LEDs with different CCTs can be used for lighting applications, e.g. for extended light sources integrated on non-rectilinear surfaces for ambient lighting. By using different NW LED pumps and changing phosphors, the colour quality can be adjusted to fit various applications, e.g., the high-CRI LED emitting a cosy warm white light (achieved with the third-generation LED) and the LED emitting natural white light with a good CRI (achieved for example with the second-generation LED with a phosphor Y1 pumped by an LED VB).

2.7 STRETCHABLE LIGHT EMITTING DIODES

Until now I have discussed flexible LEDs and their applications. It is noteworthy that today there are many works aiming to achieve not only flexibility but also stretchability of the light sources. Stretchable optoelectronics is a focus of research for companies specialized in numerical billboards and displays as a final phase of the evolution of flexible displays. The major advantage is their form factor adapting for various applications such as foldable screens [218], [219], bio-integrated devices [220]–[224] and wearable sensors [225]–[227]. In addition, stretchable devices are expected to have a better tolerance to shock hazards.

We attempted to push the technology to its extreme and to demonstrate a flexible and stretchable blue LED in collaboration with our colleagues from Alferov State University. For this demonstration, we used as an active material the same core-shell InGaN/GaN NWs grown by MOVPE as I described above.

To reach this goal, our collaborators developed a new design of the transparent electrode to make it strain-insensitive [228]. Instead of using a silver NWs network for the flexible and transparent contact as we did before, a mesh of pre-stretched single-walled carbon nanotube (SWCNT) was used on both sides of the LED membrane. To reduce the degradation of conductivity after stretching, the SWCNT film has been deposited on the membrane LED in a pre-stretched condition. As a result, the contact can stand up to 20% stretching while maintaining efficient current injection. However, it should be noted that the use of this stretchable contact reduces the transparency of the devices with respect to the silver NWs network contact (43% to be compared with 60% transparency for the fully processed transparent device). This light transmission reduction is spectrally flat on the visible range.

Optical and electrical properties of stretchable blue LEDs with strain insensitive SWCNT electrodes have been studied. Figure 2-23 (a) shows the current voltage I-V curves for as processed sample, during the stretching cycles (20% stretched) and in the relaxed state after stretching. The current for the initial state of the sample is 0.25 mA, while for the stretched and relaxed sample state it exhibits a reduction and becomes 0.2 mA, at the same bias of 8 V. This degradation of injection happens for the first stretching cycle, however no more current loses have been observed for further stretching cycles. For the stretched state, an increase of 15% of resistivity has been measured after 20 cycles of 20% stretching. Figure 2-23 (b) shows the bias required for a constant current of 0.4 mA increasing with the number of stretching cycles, however, for the relaxed state the bias remains constant. This degradation is attributed to micro damage of the SWCNT film in each cycle.

Regarding the electroluminescence, the spectra at different bias are shown in Figure 2-23 (c) for relaxed and 20% stretched state. Blue line at 450–460 nm, which originates from MQWs, dominated over the band centred at 560 nm. The origin of the latter emission is not fully clear since it may arise from the In-rich top QWs or from a defect band. Under stretching, the EL remained homogeneous and with a constant intensity, indicating stability of the device. Small blueshift is observed related to progressive redistribution of the current pumping towards more In-poor region increasing the bias. The stretching did not have any significant effect on the peak positions and spectrum shapes. However, the low energy emission became less intense under stretching, especially at lower voltages.

In summary, the method for application of SWCNT pads onto a pre-stretch PDMS/MW membrane is promising since it provides stable stretchable electrical contact. This technology opens new routes for efficient stretchable LED displays and other optoelectronic devices based on inorganic light-emitting materials. However, for our further studies I have kept the original flexible contact design based on silver nanowire network since it provides a better transmittance.

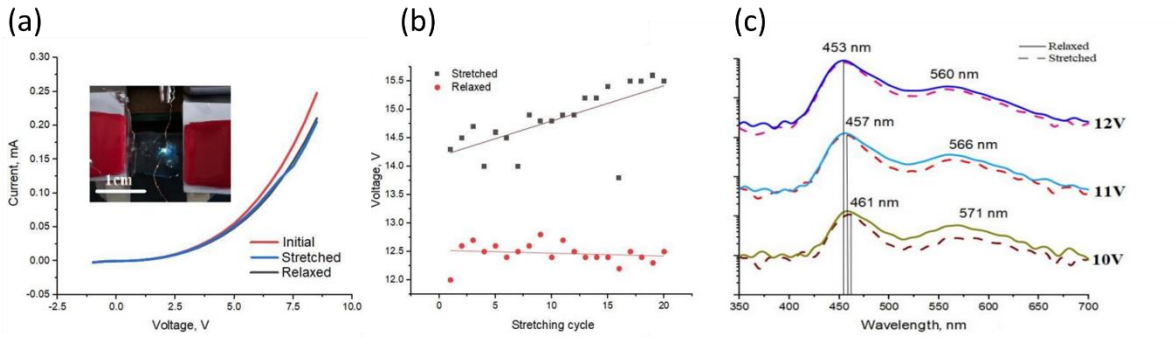

Figure 2-23.(a) I-V curves of the initial state of the LED (red line), stretched at 20% (blue line) and released state (black line). Inset shows the device under operation mounted on the stretchable set up. (b) shows the working bias for a constant current of 0.4 mA after consecutive stretching cycles, for stretched state (black squares) and for relaxed state (red dots). (c) shows the EL spectra at different biases for the relaxed state (solid line) and for stretched state (dashed line) [228].

2.8 THERMAL STUDY

Since our intension is to increase the lifetime and brightness of flexible LEDs in comparison to their organic counterparts, it is important to analyse possible origins of degradation in NW flexible LEDs. InGaN/GaN material composing the NWs has a long lifetime and can withstand high temperatures, however the embedding polymer is potentially prone to degradation. Indeed, the PDMS polymer, which encapsulates the NWs LEDs, is characterized by a poor thermal conductivity (~1.5 W $m^{-1}K^{-1}$ for PDMS [229] compared with ~200 W $m^{-1}K^{-1}$ for GaN [230]), so self-heating issues can be severe in NW/polymer composite membranes. The overheating would lead to a shorter lifetime and a lower efficiency of the LEDs. Therefore, it is important to study and test the ability of the flexible NW LEDs to operate at high current. In this section, I analyse the self-heating problem and related degradation of LEDs under thermal stress.

While the thermal properties of thin-film nitride LEDs were thoroughly studied in the literature [231]–[235], only a few studies address the thermal behaviour of NW LEDs, moreover, these reports only focus on axial-junction rigid devices [236], [237].

There are several methods for performing thermal studies, but they are difficult to be applied to NW devices. The methods for estimating the junction temperature most widely used in the LED industry are the forward-voltage method [5], [238], [239], which provides an accuracy of few degrees, and the thermal-resistance method [240], which provides ±0.1°C of accuracy. These methods require a precise assessment of the electrical properties of the devices, which is challenging and complex for flexible NWs LEDs.

Another widely applied method to probe LED temperature is based on the

measurement of the EL peak wavelength shift with temperature [239], [241]. It is commonly accepted that accuracy of the peak energy value is about 10% of the emission linewidth, yielding precision of ±24 °C for standard LEDs [5], [236], [239]. However, the EL peak-shift method is not very accurate for NWs due to the larger error of the energy peak and FWHM of the EL spectra. Indeed, it is challenging to determine the peak wavelength in NW-based nitride LEDs due to alloy-broadening effects that strongly degrades the accuracy of the method [5]. In addition, the emission colour of the NW LEDs may blueshift with injection due to progressive redistribution of the current pumping towards more In-poor regions. As a result, the peak wavelength shift method to assess the temperature is not well-suited for NW LEDs. Infrared (IR) thermal imaging [242]–[244], widely used in the semiconductor industry [245], appears to be the most appropriate method for assessing the flexible NW LED temperature variations and doesn't require any complex set up.

For thermal studies, I have fabricated a standard blue LED, making use of the NW LEDs grown by MOCVD with low In content, and applying the optimized fabrication process as described above.

For improving the current spreading on the sample, a silver paint frame was added at the LED edges, defining a square region of 1x1 cm^2. I-V curves and electroluminescence spectra were measured. The LED shows a rectifying behaviour, however with a significant leakage at reverse bias, which may be attributed to the large device area of 1 cm^2.

The electroluminescence appears from a bias of 3.5 V at an injected current of 100 mA. The EL spectra are dominated by a peak at 405 nm. The FWHM is quite large, about 150 meV due to the inhomogeneities of In composition from wire to wire. EL spectra also present a weak emission about 480 nm, probably arising from the c-plane QWs on the top of the NWs, with a higher In-content and therefore subjected to the internal electric field of the polar facets.

The inset of Figure 2-24 (b) shows that the EL emission is not homogenous on all the sample, it presents intensity fluctuations due to the inhomogeneities of the sample, which leads to current hot spots. The EL intensity emission is observed to reduce in the centre of the sample, probably due to a higher resistivity of the silver NWs network which favours a better injection close to the silver paint frame, while the injected current density is lower in the central part.

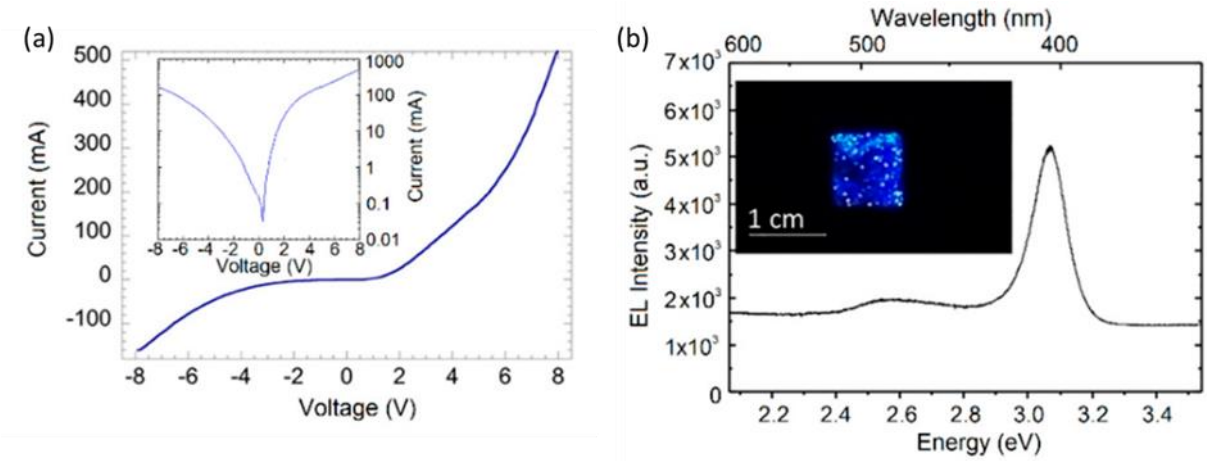

Figure 2-24.Current-voltage (IV) curve of the flexible LED with an inset showing the IV in logarithmic scale and (b) electroluminescence spectrum at 300 mA, emission is centred at 405 nm. Inset shows the photo of the LED under operation [194].

For the thermal studies the LED was mounted in a flat state on two different holders: 4 mm thick copper plate and 3 mm thick plastic holder. The copper plate was considered as a good heat sink while the plastic holder was considered a bad heat dissipating medium. The temperature distribution on the sample surface was recorded by using an infrared (IR) camera (with a spatial resolution about 150 µm per pixel) as described in ref. [236]. The IR imaging was performed for different injection currents increased by steps of 50 mA from 100 mA (light up current of the device) to 350 mA, after 3 min under operation at a given current for each holder.

Figure 2-25 (a) and (b) shows the thermal maps of the flexible NW LED mounted on the copper sink and on the plastic holder, respectively, at increasing currents. On the copper sink the temperature of the flexible NW LED increases from 33°C to 48°C while on the plastic holder it starts at 35°C under 100 mA and reaches 60°C at the maximum current tested, 350 mA. The thermal maps show a nonuniform heat distribution, where the edges reach the maximum temperatures. These inhomogeneities are similar to those observed on the EL picture (inset of Figure 2-24 (b)). The central region was less injected, therefore it has a lower temperature due to Joule heating. The inhomogeneities of the surface temperature were larger on the plastic holder than on the copper.

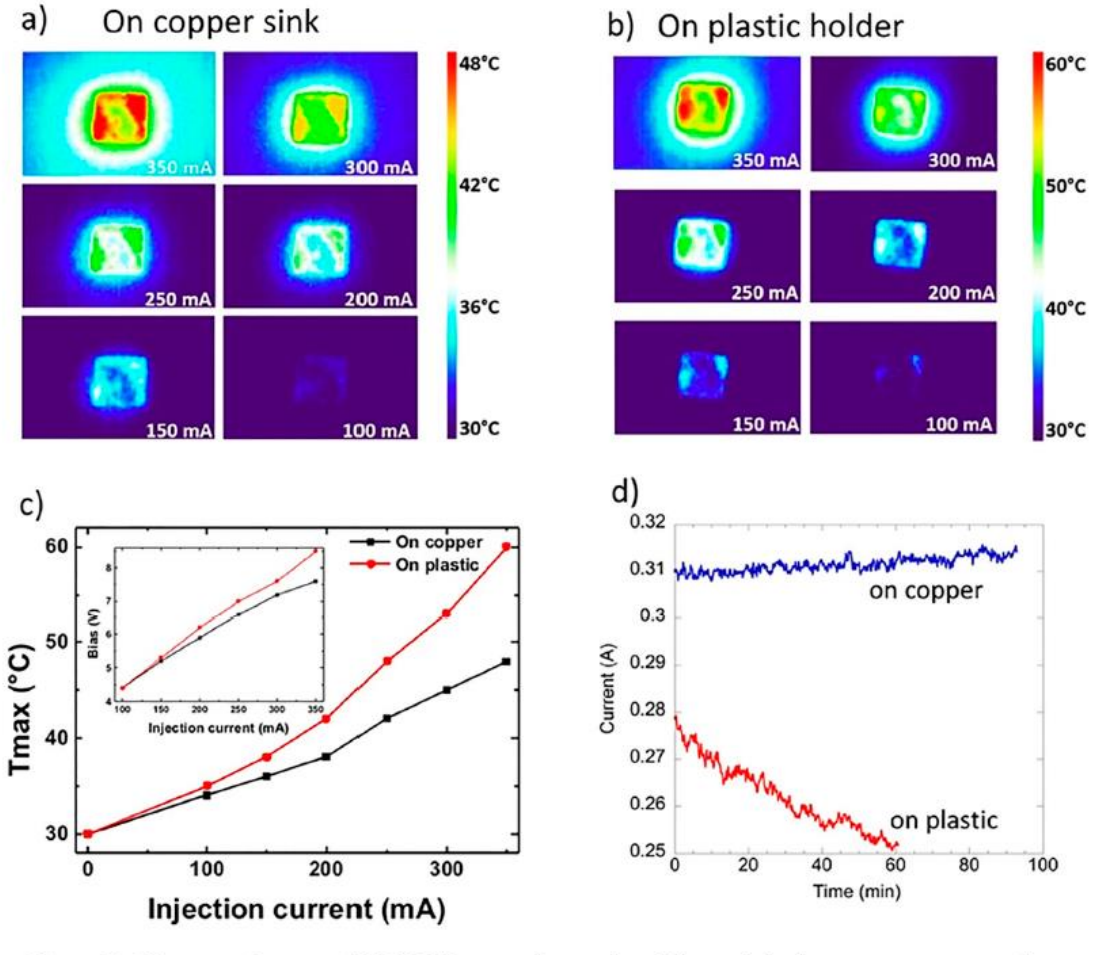

Figure 2-25. IR camera pictures of the flexible NW LED operating under different injection currents mounted on (a) copper sink and (b) plastic holder. (c) evolution of the maximum temperature with the injection current on the copper sink (black) and on the plastic holder (red). The inset shows the relation between the injected current and the bias applied depending on the holder. (d) variation of the current with time when forward bias was fixed at 7 V.

Figure 2-25 (c) shows the evolution of the maximum temperature and bias as a function of the injected current for both holders. As expected, the temperature was systematically higher on plastic than on copper, with the maximal difference of 12 °C for 350 mA. For a given injected current the bias applied to the NW flexible LED was larger on the plastic holder. The applied bias difference between the two holders increases with current, as shown in the inset.

After the thermal images were taken, the evolution of the current in time was measured. Figure 2-25 (d) shows the I(t) trace at a fixed bias of 7 V. The performance of the LED mounted on the copper sink was good, keeping a constant current of 300 mA for 90 min. On the plastic holder, the initial current started at 280 mA and it progressively decreased until the experiment was stopped after 60 min, with a current decrease of 13%. Then the experiment was interrupted to avoid critical damage to the device.

Despite the poor conductivity of the PDMS, a heat sink on the back side of the flexible NW LED is efficient for heat dissipation, allowing to have good performance during more than an hour without degradation. Thanks to the good thermal conductivity (200 W $m^{-1}K^{-1}$) of the GaN NWs, the heat is dissipated to the sink, and the device can keep working. The dissipation is efficient despite the low surface of the NWs in contact with the holder, which represents less than 5% of the total device area.

These experimental results were confirmed by modelling the temperature distribution in a NW/polymer composite performed by Nan Guan [158]. In this estimation, the complex real system was replaced by a simplified model, where the GaN NWs were represented by 30 µm tall cylinders, for which GaN bulk parameters were used. The cylinders were distributed in a square lattice with a density of 10^4 cm^{-2}, the top contact was represented as a thin Ag continuous layer, considered as the heat source of 4W/cm^2 (the experimental measured power density at 350 mA). In the real device the Joule's heat is generated in a distributed way along the NWs, however the contact resistance between the Ag NWs network and the p-GaN shell of the NWs is significant, therefore a heat generation at this position should be strong, which justifies this simplification. A heat sink at the bottom was used, with a temperature fixed at 20°C. As a reference sample, a PDMS layer with the same conditions was also simulated. The schematic of the simulated systems and the results of the calculated temperature distribution are shown in Figure 2-26. It is seen that in the reference system without GaN NWs, the temperature reaches 700 °C at the top surface (panel b). However, in the presence of NWs, the heat is conducted to the heat sink and the surface temperature does not exceed 40 °C (panel d). These simulations results confirm the ability of GAN NWs to efficiently conduct heat towards the heat sink despite the low thermal conductivity of the PSMD encapsulating layer.

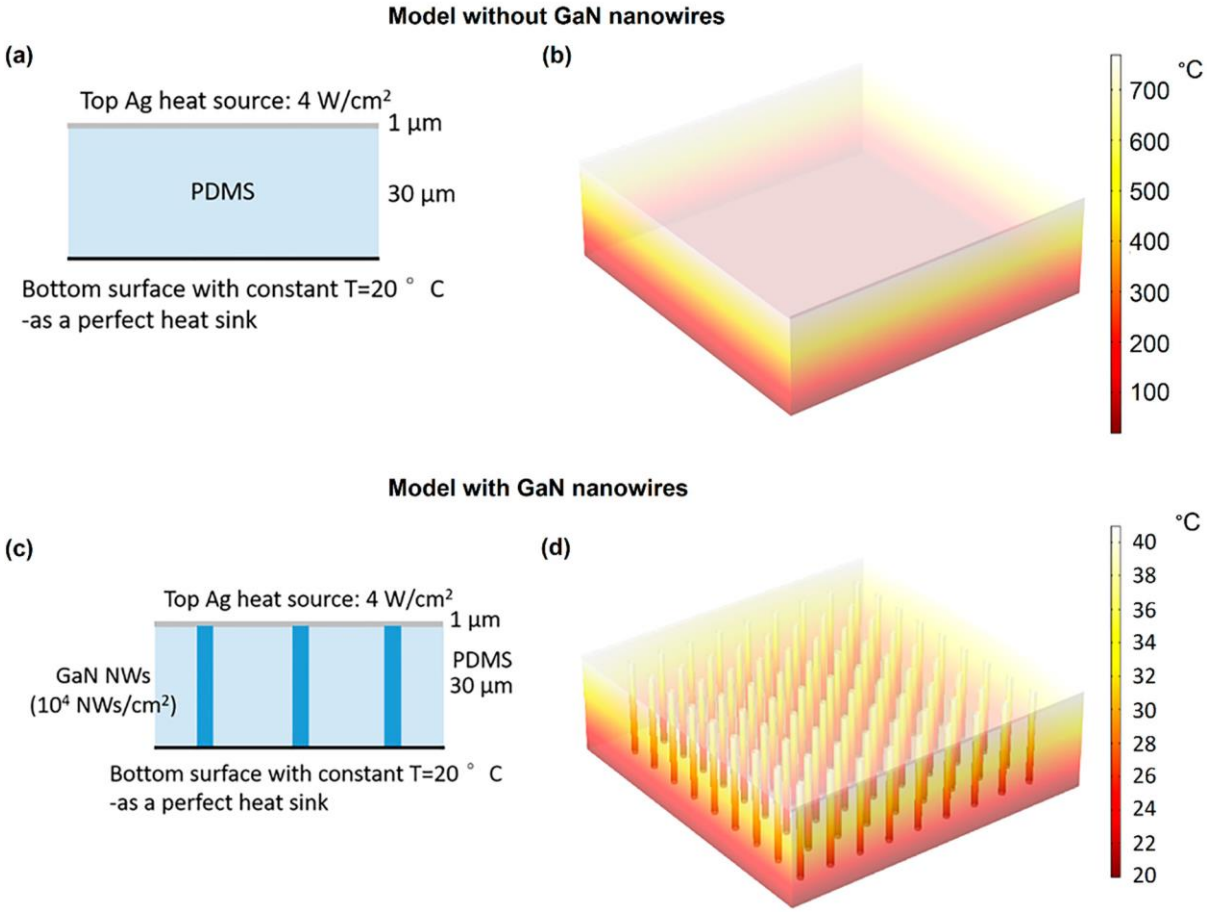

Figure 2-26. (a) Schematic of the reference system without GaN NWs and (b) the calculated temperature distribution in the reference system. (c) schematic of the flexible NW LED simplified system and (d) the temperature distribution calculated for the flexible NW LED system [194].

With this study, I demonstrated that the flexible NW LEDs fabricated following polymer embedding and peel-off lead to a robust device against self-heating.

2.9 CONCLUSION

In this chapter, flexible LEDs based on nitride core shell NW has been reviewed and reported. I first presented the state of art of flexible LEDs developed by our research group in the last years, consisting in the fabrication of flexible blue NW LED, green flexible NW LED, multicolor blue-green flexible LED and first generation of white flexible NW LED by phosphor down conversion. The LEDs are fabricated embedded nitride NWs on a membrane of PDMS. This fabrication technique combines the great optoelectronic properties of nitride LEDs, the improvement that core shell NWs bring to the nitride LEDs, and the flexibility of the polymer. One of the keys of this devices is the Ag NWs used for producing a network, which contact the NW LEDs with high flexibility and reasonable electrical conductivity.

I described the fabrication process of these devices focussing on the points that I have optimized, followed by the development of a second generation of flexible

white LEDs and the detailed description of the used phosphors. Warm, natural and cool white flexible LEDs have been demonstrated, with CCTs varying from 2166–6665 K, and high CRI [193].

Several studies have been performed regarding the mechanical properties of the flexible LEDs. I also presented the results of mechanical tests, proving a high robustness of these devices. In addition to the bending tests, stretchable flexible LEDs with a novel pre-stretched SWCNT pads was demonstrated [228], opening new routes for flexible and stretchable optoelectronic applications based on inorganic LEDs. To conclude the work related to flexible NW LEDs, a thermal analysis was performed on the devices, where no degradation was observed when a dedicated thermal sink was used.

The future work on this area is in relation to the development of pixel LEDs. Two kind of matrix have been considered, passive matrix and active matrix. After optimizing the fabrication of the pixel pads, apply them to green and blue LEDs. At the same time, we are working on the fabrication of a large area flexible NW LED.

3 TOWARDS RED FLEXIBLE LEDS

3.1 INTRODUCTION

Orange, red and infrared LEDs are dominated by the technology based on the AlGaInP material system $(Al_xGa_{1-x})InP$. In particular, the $(Al_xGa_{1-x})_{0.49}In_{0.51}P$ material system is lattice matched to GaAs substrates, the lattice constants of AlP and GaP are similar. Therefore, by keeping the Ga/Al ratio fixed at 49% in the AlGaInP alloy, a high-quality epitaxial growth on GaAs substrates can be achieved. Through a proper choice of the amount of Al and Ga, the bandgap energy can be tuned for engineering QWs or EBLs in order to achieve a good LED design. The $Ga_{0.5}In_{0.5}P$ energy bandgap is 1.91 eV, which corresponds to a red emission at 650 nm wavelength. By introducing Al into GaInP, the bandgap can be increased up to 2.52 eV [64], [67]. Figure 3-1 shows the bandgap, lattice constant and direct indirect regions for the AlGaInP alloys.

$GaAs_xP_{1-x}$ and $Al_yGa_{1-y}As$ are material systems which can be also used for the realization of red LEDs, GaAs at 300 K has a direct bandgap in the IR range, 1.422 eV [27], GaP and AlAs have indirect bandgap energy of 2.24 eV and 2.16 eV [27], respectively at 300 K. Therefore, the respective ternary alloys are not always suitable for light emission having a direct bandgap. (i) $GaAs_xP_{1-x}$ preserves a direct bandgap for an As concentration above x=0.55, with a bandgap of 1.96 eV. (ii) $Al_yGa_{1-y}As$ has a direct bandgap behaviour for Al concentrations lower than y=0.45 with a bandgap energy of 1.98 eV. The efficiency of the radiative recombination in the indirect bandgap region of $GaAs_xP_{1-x}$ can be increased by doping with nitrogen.

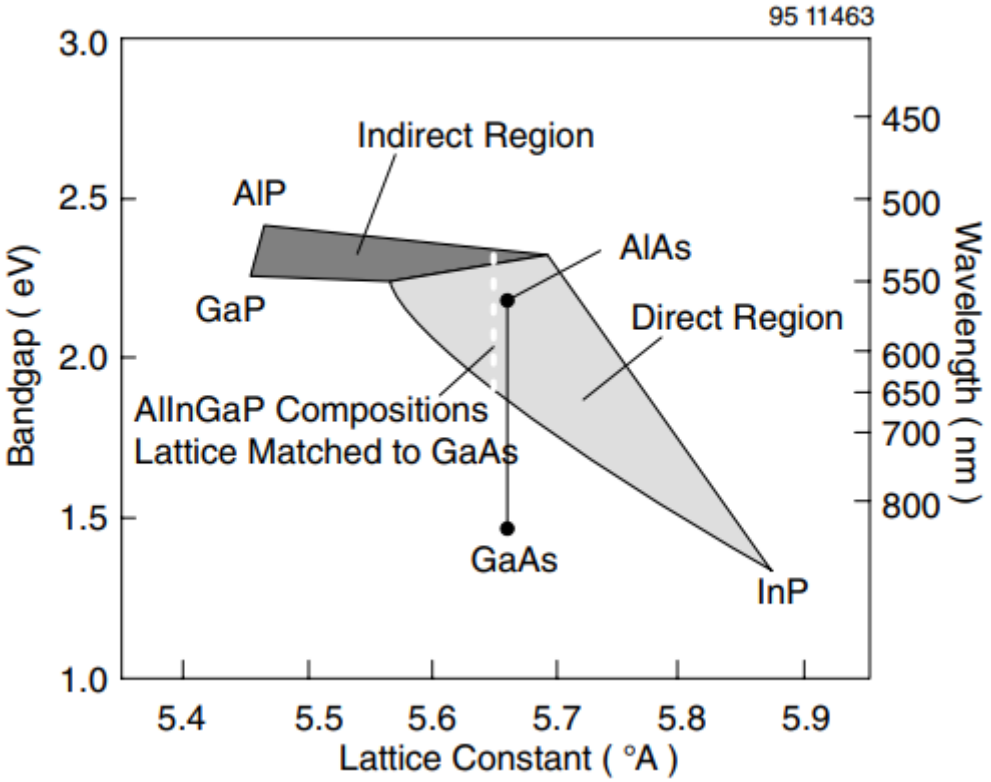

Figure 3-1. Bandgap and lattice constant of AlGaInP alloys [246].

As previously detailed, a nanowire architecture can be applied for developing optoelectronic devices with novel functionalities exploiting the properties arising from the large surface- to-volume ratio and the small footprint. Especially, radial core shell NW LEDs are particularly interesting since they offer a larger junction area compared to axial devices.

Radial core shell NWs with a large junction area as compared to axial have been reported in the IR (GaP/GaAs/GaInP [247], InP/InAsP/InP [248], [249], InP/InAs/InP [250], [251], GaAs/AlGaAs[252], [253]. In the red wavelength range, AlGaInP material system $(Al_xGa_{1-x})_{0.5}In_{0.5}P$ dominated the red emission applications [67].

InGaN alloys attracted much attention as key materials for LEDs. Blue and more recently green LEDs are a well established technology based on InGaN/GaN systems [254]–[256]. The possibility to tune the InGaN band gap energy to cover the full visible range makes this material system the best candidate for producing RGB primary colours LEDs. However, the homogeneous and defect-free incorporation of a high amount of In in InGaN is very challenging.

Because of the different size of Ga (covalent radius of 126 pm) and In (covalent radius of 144 pm) atoms and the small binding energy between In and N, the miscibility of In into GaN is very poor [257], [258]. The growth of InGaN requires lower growth temperatures than for GaN to avoid In desorption. By reducing the growth

temperature, it is possible to increase the In content in InGaN thin films up to approximately 20% while keeping a reasonably good crystalline quality. Above this concentration, the material degradation becomes critical. InGaN alloy becomes unstable for higher InN mole fraction. Phase separation may happen [259], [260].

Because of these issues, the InGaN alloy presents inhomogeneous distributions, evidenced with MBE and MOVPE [261], which induces a strong localization of carriers even in layers of a good material quality. In extreme cases, it may lead to the formation of In clusters: when there is a phase separation, some regions become poor in In content while others become very rich. From the LED perspective this results in current crowding and strong inhomogeneities in the light emission.

Finally, additional challenge for long wavelength emission from InGaN is the existence of a piezo-electric polarization fields within the quantum wells (QWs). For c-plane emitters, this causes band bending and a decrease in the overlap of the electron and hole wave functions due to the quantum-confined Stark effect (QCSE), resulting in low radiative recombination rates [262], [263].

Despite these difficulties, the nitride community did a strong effort to find solutions to these problems and to produce In rich LEDs emitting in the long wavelength spectral range. Red LEDs have been produced following different strategies, e.g. using strained structures to compensate the strain [264]–[266], developing InGaN native substrates [267], [268] or even by an alternative approach of doping the nitride layer with Eu for red emission [269], [270].

3.2 FLEXIBLE NW LEDS BASED ON INGAN/GAN

In my work, several ways to achieve red flexible NW LED have been explored. The first approach for the fabrication of flexible NW red LEDs was in line with previous studies. We attempted to use the same material as for blue, green, and white flexible NW LEDs, i.e. InGaN. However, as previously mentioned, the control of the high In composition in MOCVD is a big challenge. The growth of the NWs for the flexible LED presents high inhomogeneities and growth artifacts [191].

The growth of these NWs at temperatures below 650 °C leads to extremely inhomogeneous growth. The In incorporation became totally arbitrary and as a result the LEDs show a high colour dispersion and it is possible to find NWs emitting from violet to red within the same device. This is illustrated in Figure 3-2, which shows an attempt to fabricate an In-rich LED resulting in multi-colour emission.

As shown in Figure 3-2 (b) and (c), we have succeeded in finding in this inhomogeneous device individual NWs producing yellow (580 nm) and even red (650 nm) electroluminescence, respectively. However, these red emissions were only observed locally, and we could not achieve a large area red LED with this approach despite numerous attempts. It should be noted that we are not sure about the origin

of the observed long wavelength emission. Presumably, it arises from the top facet which may locally have a high In content and which also exhibits Stark shift increasing the emission wavelength.

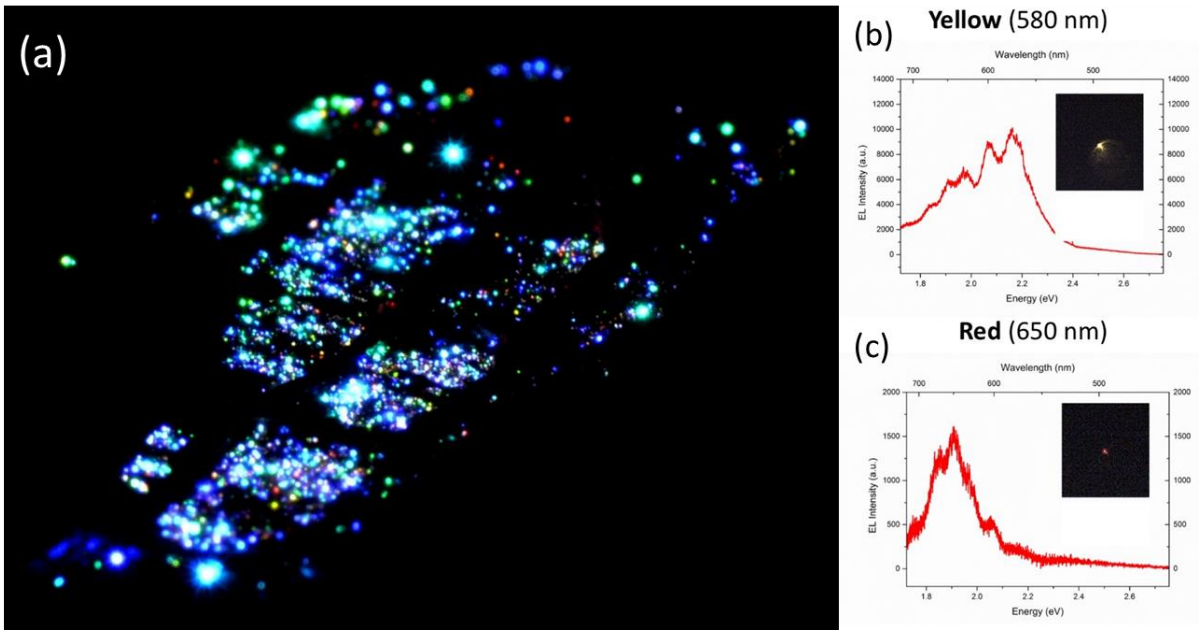

Figure 3-2. (a) Photography of a flexible LED with multiple colour arising from different NWs. (b) and (c) show the EL spectra of individual NWs emitting yellow and red light, the inset shows the corresponding optical microscope images.

Due to these inhomogeneities of the growth at low temperatures it was not possible to keep the same approach for red LEDs as for previous blue and green devices. Since the standard approach was ruled out, I analysed alternative solutions. Following the previously-described successful experience of using phosphors for down conversion, I decided to use red phosphor on blue LEDs to obtain red emission by down-conversion.

3.2.1 Red phosphors for down conversion

The commercially available oxides and sulphides red phosphors (Eu^{3+} doped Y_2O_3 or Y_2O_2S) have low absorption in the blue or near-UV region. Other sulphide phosphors like (Sr,Ca)S:Eu^{2+} are thermally unstable and degrade easily. Other commercial nitride red phosphors Eu^{2+} have a broad emission and require hard synthesis conditions, besides Eu^{2+} ions reabsorb light in the range 250-650 nm by the transition 4f-5d. The absence of a wide excitation band in the ultra-violet (UV) or blue region limits their applications in LEDs [271]. Therefore, the interest is growing in producing phosphors, which exhibit a broad absorption in the UV and blue regions and are able to emit sharp-band red or deep-red light [272]–[275].

Amongst all the transition metal ions, Mn^{4+} ions may be the better choice for red-emitting phosphors since the spectral position of the red emission (600–790 nm) can be tuned by appropriate modification in their crystal field environment as the

position of their emission peaks depends upon the host employed [271]–[273]. Mn^{4+} doped phosphors have a broad excitation in the UV and in the blue regions and provides a sharp emission in the red region. For this reason, we have selected this kind of phosphors in the present study.

3.2.2 Structure of the selected phosphors

Fluorides, oxides, and oxyfluorides are the three typical hosts where the Mn^{4+} ions can be doped efficiently. Mn^{4+} ions in fluoride hosts are associated with emissions ranging from 626 nm to 635 nm while in oxide hosts, its range becomes wider from 652 nm to 713 nm [275]. The Mn^{4+} activated red phosphors have been reported mainly with fluoride host materials, however the synthesis requires HF solution which is highly corrosive and the obtained fluorides are suffering from low stability and have a considerable moisture sensitivity [79].

The oxide hosts bear more advantages due to the excellent thermal and chemical stability and outstanding material properties including hardness, larger transparency, eco-friendly preparation, and emission in the deep-red region (above 650 nm) which suits Mn^{4+} activated oxide phosphors as good candidates for blue-red phosphor down conversion [275], [276].

Generally, Mn^{4+} ions prefer to occupy the octahedral site as they possess a strong crystal field stabilization energy in an octahedral environment. Therefore Mn^{4+} ions can be very well substituted for Ga^{3+} [277], Al^{+3} [278], Ge^{4+} [279] among others. In addition to the octahedral position, the ionic radii of Al^{3+} (0.535 Å) and Ge^{4+} (0.530 Å) are similar to Mn^{4+} (0.530 Å) which permits substitutional doping without perturbing the crystalline structure. Even though the octahedral sites of Mn^{4+} can be easily replaced by the Al^{3+} ions, these systems require the use of a charge compensator owing to the ionic mismatch between Al^{3+} and Mn^{4+} ions. Therefore germanate-based phosphors are a promising host as they provide the most optimal octahedral sites for Mn^{4+} ions due to the same ionic radii and charge of Ge^{4+} and Mn^{4+} [78].

For more detailed description, a review about Mn^{+4} doped germanates can be found in ref [275].

During my PhD, our team has established a collaboration with Subrata Das, from CSIR-NIIST, who is an expert in phosphor synthesis. He provided the nanophosphors used for the development and optimization of the white flexible NWs LEDs. He also provided five red nano phosphors (Mn^{4+} activated) that I have studied for red LED application. These five different phosphors have different host material and different cation sites. These are namely: three germanates, two germanate-oxide with different host material, R1 ($Li_3RbGe_{7.995}O_{18}$:0.005 Mn^{4+}) and R2 ($Mg_{14}Ge_{4.99}O_{24}$:0.01 Mn^{4+}), a germanate-oxyfluoride which is like R2 but substituting eight atoms of oxygen by fluor ($Mg_{14}Ge_{4.99}O_{16}F_8$:0.01 Mn^{4+}). Due to the similar ionic radii of the F^-

and O^{2-} ions, the formation of a stable anionic sublattice form oxyfluorides can take place, which shows excellent absorption and emission properties.

For exploring other candidates, another substitutional octahedral sites of elements with similar ionic radius are considered, where the Mn^{4+} activation dopant, instead of Ge^{4+}, substitutes Al^{3+} and Ga^{3+}, in R4 ($Mg_{2.73}Ba_{0.27}Al_{1.995}GeO_8$:0.005 Mn^{4+}) and R5 ($Mg_{2.87}Ba_{0.13}Ga_{1.995}GeO_8$:0.005 Mn^{4+}), respectively. A summary describing all the phosphors of this study is compiled in Table 3-1. The respective emission and excitation were measured by our collaborators and the results are shown in Figure 3-3.

Table 3-1. Properties of the five different phosphors studied for blue-red conversion.

Name	Compound	Substitutional site	Mn^{4+} doping
R1	$Li_3RbGe_{7.995}O_{18}$:0.005 Mn^{4+}	Ge^{4+}	0.5%
R2	$Mg_{14}Ge_{4.99}O_{24}$:0.01 Mn^{4+}	Ge^{4+}	1%
R3	$Mg_{14}Ge_{4.99}O_{16}F_8$:0.01 Mn^{4+}	Ge^{4+}	1%
R4	$Mg_{2.73}Ba_{0.27}Al_{1.995}GeO_8$:0.005 Mn^{4+}	Al^{3+}	0.5%
R5	$Mg_{2.87}Ba_{0.13}Ga_{1.995}GeO_8$:0.005 Mn^{4+}	Ga^{3+}	0.5%

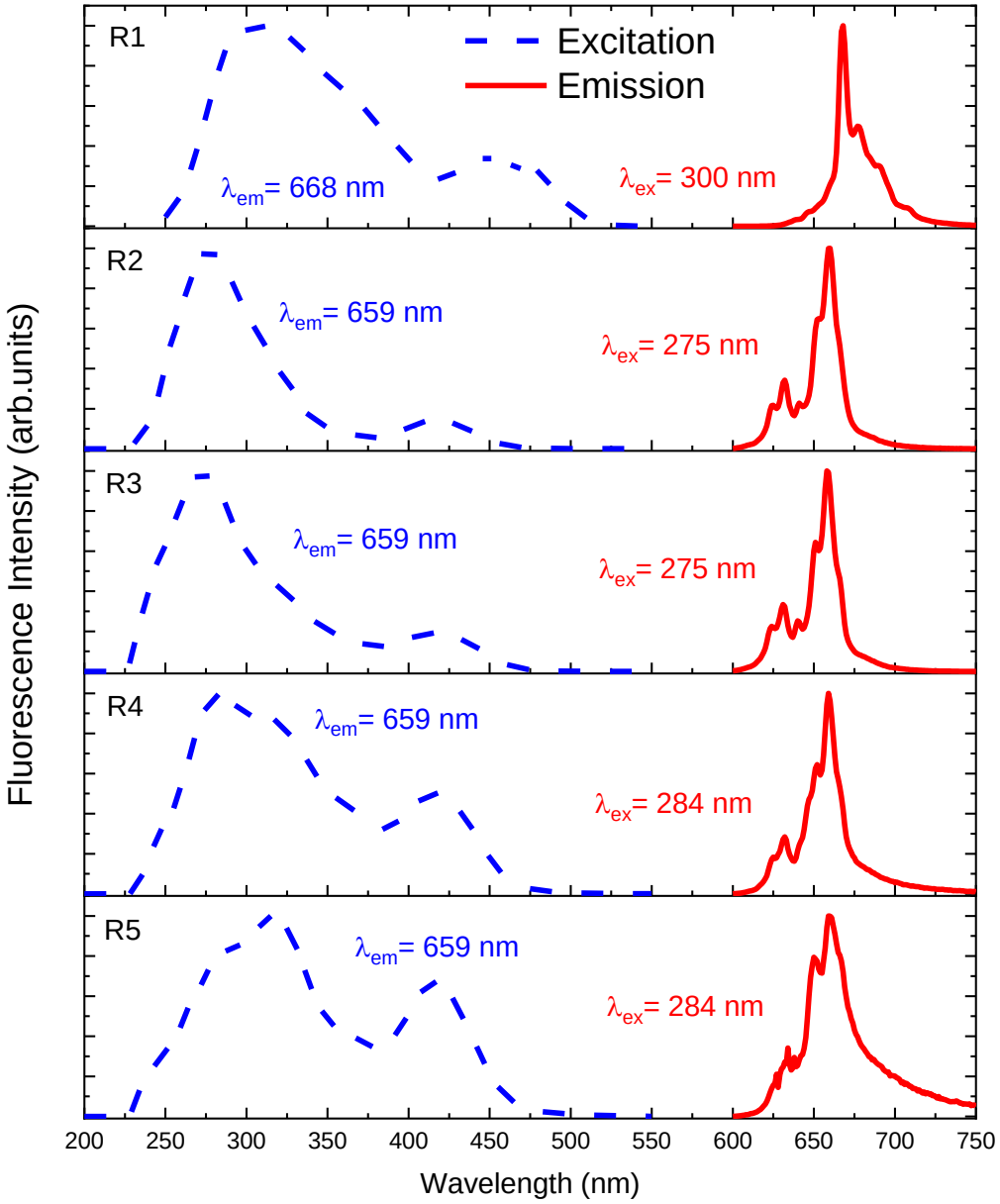

Figure 3-3. Normalized excitation (blue dashed curves) and emission (red solid curves) spectra of the five red phosphors. For each spectrum the excitation or emission wavelength used for the measurements is indicated.

R1 phosphor has markedly different emission and excitation spectra than the other phosphors. R2, R3, R4 and R5 shows an excitation range between 225nm to 475 nm, and similar emission spectra peaked at 660 nm with several emission lines at lower wavelength. However, R1 phosphor has excitation and emission bands redshifted with respect to the other phosphors. The excitation spectrum covers the range from 250 nm to 525 nm, and the emission spectrum is centred at 670 nm, with secondary emission lines at larger wavelengths.

All the phosphors show two main excitation bands, the one at lower wavelength with total maximum absorption, and a secondary band, at larger wavelength with

less absorption (425 nm for R2, R3, R4 and R5 and 450 nm for R1). The second band for the germanate phosphors, R2 and R3, is very low in terms of intensity, about a 20% regarding the maximum intensity, centred at 275 nm. R1 and R4 shows a middle term absorption intensity for the secondary band, of 40 and 50%, regarding the maximum intensity. R1 maximum absorption is centred at 310 nm. On the other hand, R5 secondary band intensity is about the 80% of the maximum intensity. Phosphor R4 and R5 shows two contributions in the excitation band at lower wavelengths, at 280 nm and 315 nm. R4 is dominated by the peak centred at 280 nm while R5 shows the maximum at 315 nm.

The main difference is due to the crystal field environment around the Mn^{4+} in R1, which has a different host lattice. A detailed discussion of R1 is founded in [276].

3.2.3 Cathodoluminescence analyses of the phosphor emission: evidence of the green band

Standard phosphors lose efficiency when decreasing their size. Due to the flexibility requirements for the desired LED and for future potential applications to screens with small pixels, the small size of the phosphors is an important requirement. To observe the optical response of the nanophosphors, cathodoluminescence measurements have been performed on different samples. For emission comparison, particles with a size of about 2 and 3 µm from the five different phosphors have been investigated. The spectra are normalized regarding the maximum emission of the red band and vertically shifted for better data visualization, in Figure 3-4.

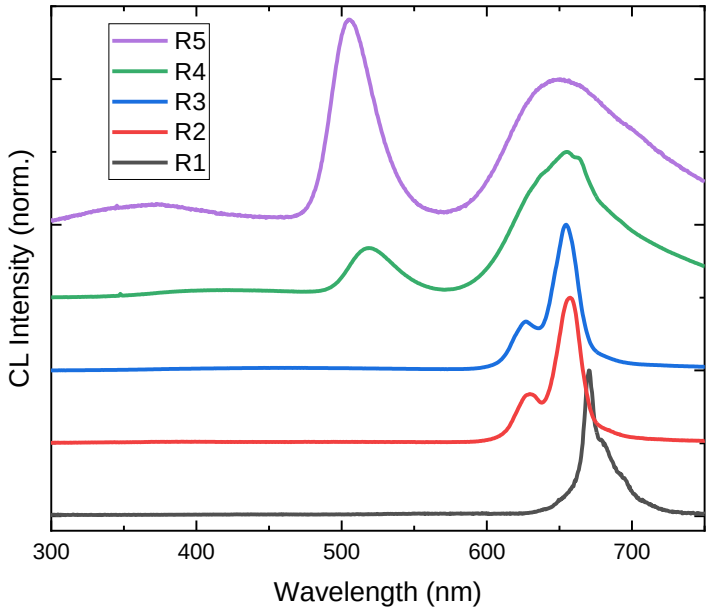

Figure 3-4. RT CL normalized spectra of the five different phosphors displayed with an offset for better visualization.

Phosphor R1 shows the emission at larger wavelength with the peak centred at 670 nm, and shoulders can be observed at even larger wavelengths. Phosphors R2 and R3 shows similar CL spectra with two emissions, the main emission is centred at 657 and 654 nm, and secondary emission at 630 and 627 nm, respectively. In these three phosphors, R1, R2 and R3, the Mn^{4+} is the active dopant of the host, substituting Ge^{4+} atoms, and all three-show red emission. However, unexpected results are observed in R4 and R5 which in addition to the red luminescence also show green emission in a narrower band, and in the case of R5, the intensity of this green emission is even higher than the one of the red band. R4 shows a broad peak centred at 654 nm with shoulders at larger and smaller wavelengths, and the secondary green emission centred at 518 nm, which has an intensity of 35% with respect to the main red peak. In the case of R5, the red band is centred at 650 nm, and the secondary peak is at 505 nm, with an intensity 40% larger than the emission of the red band.

Particles of different sizes (from 1 to 40 μm) selected from the dispersion of samples R1, R2 and R3 were measured by CL. For these samples, the spectra have exactly the same shape independently of the particles size, with the same ratio between the two emissions. On the other hand, samples R4 and R5 show size dependance. The trend is the same, but it is more pronounced for the R5. Figure 3-5 (a) illlustrates this behaviour by showing the spectra normalized to the maximum intensity peak (i.e. the green emission centred at 505 nm) of two phosphor particle of different size from R5. The red band emission is reduced by 40% in intensity for bigger particles, which is consistently observed for a large number of measurements of particles of different sizes. This decrease of the red emission is more pronounced in large particles. It should be noted that both particles shown in Figure 3-5 are relatively large (2 μm and above 40 μm, respectively), so neither quantum nor dielectric confinement effects can be expected. A similar behavior is observed for the sample R4.

Figure 3-5 (b) and (e) shows the panchromatic map corresponding to the SEM images of Figure 3-5 (c) and (f) of the small and big particles, respectively. The maximum intensity emission from the small particle is detected from almost everywhere while in the big particle, the maximum intensity comes from a small region at the edges. Figure 3-5 (d) ilustrates the filtred maps of the small particle for the green band emission (the map is filtered for emission from 450 to 570 nm), in green, and the red band emission (filtered from 570 to 800 nm), in red. Figure 3-5 (g) shows the same filtered maps with the same ranges but for the big particle. Green emission seems more homogeneous and coming from all the surfaces for both sizes while red emission shows stronger intensity fluctuations. For the small particle, the regions of intense red and green emission overlap in the map. For the big particle, the maps show conmplementarity with the red emission dominant from the region having a lower green emission. The origin of this observed dependence on the particle size is not clear. It may be related with the agglomeration of the formation

of Mn2+.

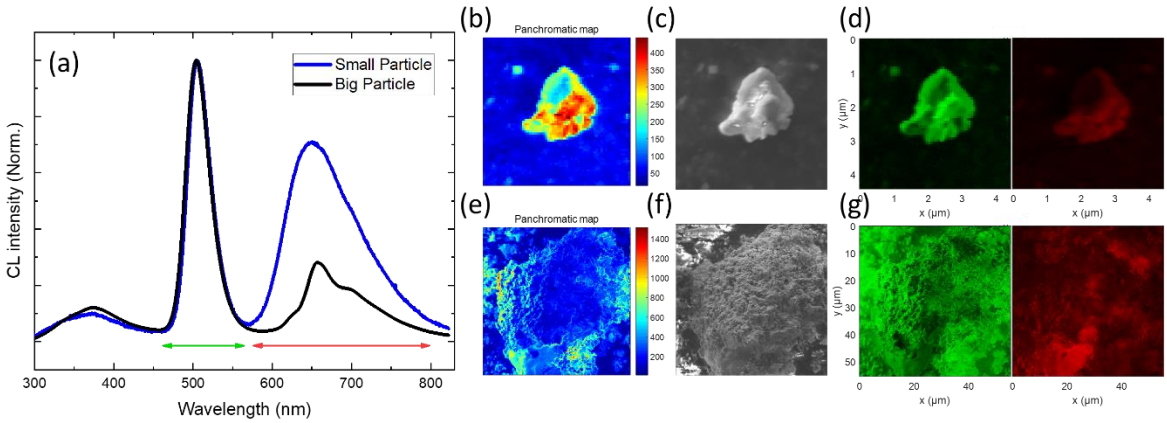

Figure 3-5. (a) Normalized spectra of two particles of different size of phosphor R5. Respectively for the small and big particle, (b) and (e) are the panchromatic maps, (c) and (f) are the SEM pictures, and (d) and (g) are the filtered maps for the green emission in the range from 450 to 570 nm and for the red emission filtered between 570 and 800 nm, both ranges are shown on the panel (a).

The results of CL displaying a strong green emission are surprising since the green emission is not observed in PL measurements. Therefore, the high-energy excitation source in CL should be responsible for the excitation of the green emission. Indeed, in PL experiments, the samples are excited with photons at 266 nm while in CL the sample is excited with an electron beam at 6 keV. In this second case, the electron beam creates high energy electrons in the specimen and excites all the available atomic states. It should be noted that we observed two kinds of phosphor behaviour: (i) R1, R2 and R3 don't show green emission in the CL measurements, and the emission spectra of different particle sizes have exactly the same shape; while (ii) R4 and R5 produce a strong green emission and show particle size dependence of the CL emission. The differences between the two kinds of phosphors are the host material and the cation substitutional. The samples which show the secondary green emission are those samples which have ionic mismatch between the active dopant Mn^{4+}, and Al^{3+} or Ga^{3+} for R4 and R5, respectively.

The basic host lattice of R4 (and R5) samples are $Mg_3Ga_2GeO_8$ ($Mg_3Al_2GeO_8$) which belongs to the space group of "*Imma*" with the orthorhombic crystal structure [280]. In this crystal structure, Mg^{2+} or Ga^{3+} (Al^{3+}) occupies the octahedral site and Ge^{4+} or Ga^{3+} (Al^{3+}) occupies the tetrahedral site. Therefore, Ga^{3+} (Al^{3+}) can be placed in both sites [281]. Mn^{4+} ions prefer to take the place in the octahedral coordination due to their ionic radii, but it generates a mismatch of the charge. To compensate this substitution, a vacancy of Ga^{3+} (Al^{3+}) should be formed every three atomic substitutions. However, there is another situation, reported in ref [282], which could happen for charge compensation, Mn^{4+} can substitute one atom of Ga^{3+} (Al^{3+}) at the octahedral site, and other Mn^{4+} can be reduced to Mn^{2+} and occupy a Ga^{3+} (Al^{3+}) tetrahedral site, which would result in a neutral charge [281], [282]. The cation Mn^{2+}

is expected to produce a green emission when it relaxes from atomic excited states, the expected wavelength corresponds well to the wavelength detected in CL spectra [282]. In the literature, this green band emission produced by the reduction of Mn^{4+} to Mn^{2+} to balance the material charge is indeed reported in ref. [282], but in this report it is weak. However, under the higher electron energy of the beam, Mn^{4+} can be reduced to Mn^{2+}, increasing the amount of Mn^{2+}, and thus, the intensity of the green emission.

Figure 3-6 presents the results of the emission and excitation luminescence spectra for R4 and R5 nanophosphors, focusing on the green band emission. Figure 3-6 (a) shows the excitation spectrum for a light detection at 520 nm, i.e. at the energy peak observed in CL for the green emission. A strong green emission is detected for several excitation bands, in particular, for excitation with λ= 423 nm. We have fixed this excitation wavelengths and analysed the photoluminescence spectrum. This spectrum shows indeed the green band in agreement with CL measurements. For comparison, Figure 3-6 (b) shows the respective results for R5, namely the excitation spectrum for the detection fixed at the green emission detected in CL, i.e. at 505 nm, and the photoluminescence spectrum of R5 excited at 421 nm. Again, the green emission is detected. These experiments confirm that the green emission in these phosphors can be produced under excitation with light for specific wavelengths.

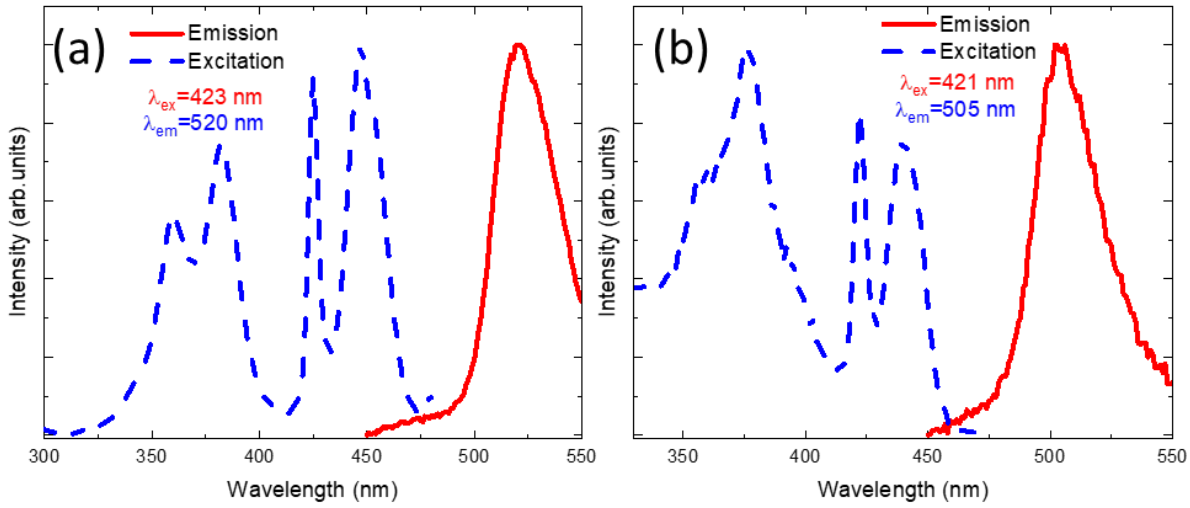

Figure 3-6. Emission and excitation spectra of the phosphor R4 (a) and R5 (b) focused on the emission of the green band produced by Mn^{2+}. Excitation spectra are shown with a dashed blue line, for the detection wavelength indicated, (520 nm for R4 phosphor (a) and 505 nm for R5 phosphor in (b)) and the emission spectra are shown with a red solid line, excited at the indicated wavelength (423 nm for R4 in (a) and 421 nm for R5 in (b)).

In initial PL experiments, the green emission was not observed because the chosen excitation wavelengths were not ideally matching the allowed transitions and therefore the atomic transition of Mn^{2+} was not efficiently excited.

3.3 INTEGRATION OF THE RED PHOSPHOR WITH INGAN NANOWIRES

For device testing, we have chosen $Li_3RbGe_{7.995}O_{18}$:0.005 Mn^{4+} named R1, which has no green band and has the red emission in the longest wavelength range. This phosphor has been studied in detail in Ref [276]. The excitation and the emission spectra from the phosphor R1 are shown in Figure 3-8 (a). The fluorescence intensity is recorded for a detection peaked at 668 nm (shown in dashed blue line), while the emission spectrum is recorded for an excitation wavelength of 300 nm (shown with a red solid line). The excitation spectrum shows an absorption band from 250 nm to 500 nm, with an absolute maximum at 300 nm and a secondary local maximum centred at 460 nm having an intensity lower by 60%.

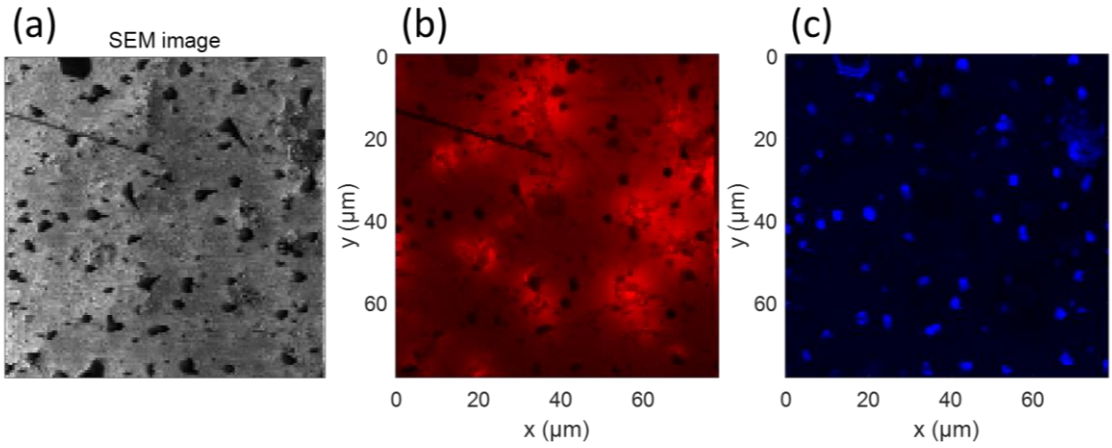

Figure 3-7. (a) SEM image of the NW LEDs / microphosphor system. (b) and (c) are the filtered maps for the phosphor emission in red (filtered from 640 to 1000 nm) and the emission from the InGaN MQW of the NW LEDs in blue (filtered from 400 to 470 nm), respectively.

Before device fabrication, the optical properties of the combined nanowire / microphosphor system were probed by CL. The phosphor particles were deposited on the as-grown nanowires to emulate the final device, however, without the insulating PDMS layer, which makes the analyses under electron beam excitation such as CL difficult. Figure 3-7 (a) shows the SEM picture of the region analysed, Figure 3-7 (b) and (c) illustrate the filtered maps for the phosphor emission (map filtered from 640 to 700 nm) in red, and the emission from the InGaN MQW of the NW LEDs (filtered from 400 to 470 nm), in blue. We note that in panel (a) the focus is taken on the NW tops so the phosphors particles lying on the substrate are blurred, however they can be well observed in panel (b). As expected, the InGaN emission is localized in correspondence with the standing NWs (dark contrast in panel (a)). Phosphor emission is spread around the phosphor micro-particles, which may be due to the excitation by the secondary electrons reemitted from the sapphire substrate.

3.4 INTEGRATION OF THE RED PHOSPHOR INTO THE BLUE FLEXIBLE LED

For the integration of the phosphor in the flexible LED, the same approach used for the optimization of the white flexible NW LED was applied. A PDMS cap layer of 300 µm was doped with R1, in a mass ratio of 10:1, and integrated on top of the blue LED pump.

The EL spectrum of the blue flexible NW LED pump with an emission wavelength centred at 425 nm is shown in Figure 3-8 (b) for an applied bias of 8 V. The EL spectrum of the combination of this pump with the R1 PDMS is shown in Figure 3-8 (c). This combination results in an LED with two emission peaks. One peak centred at 470 nm, arises from the blue pump. The other peak originates from the red phosphor emission at 668 nm, in agreement with the objective to convert blue light into red. Unfortunately, the down-conversion in this first device was insufficient and the residual blue emission remained more intense in comparison with the red emission. This insufficient conversion may be due to the bad spectral matching of the pump LED EL and the phosphor excitation band. This is illustrated in Figure 3-8 panel (a) showing the excitation spectrum of the phosphor. It is seen that the emission of the pump corresponds to a low absorption part of the phosphor excitation spectrum.

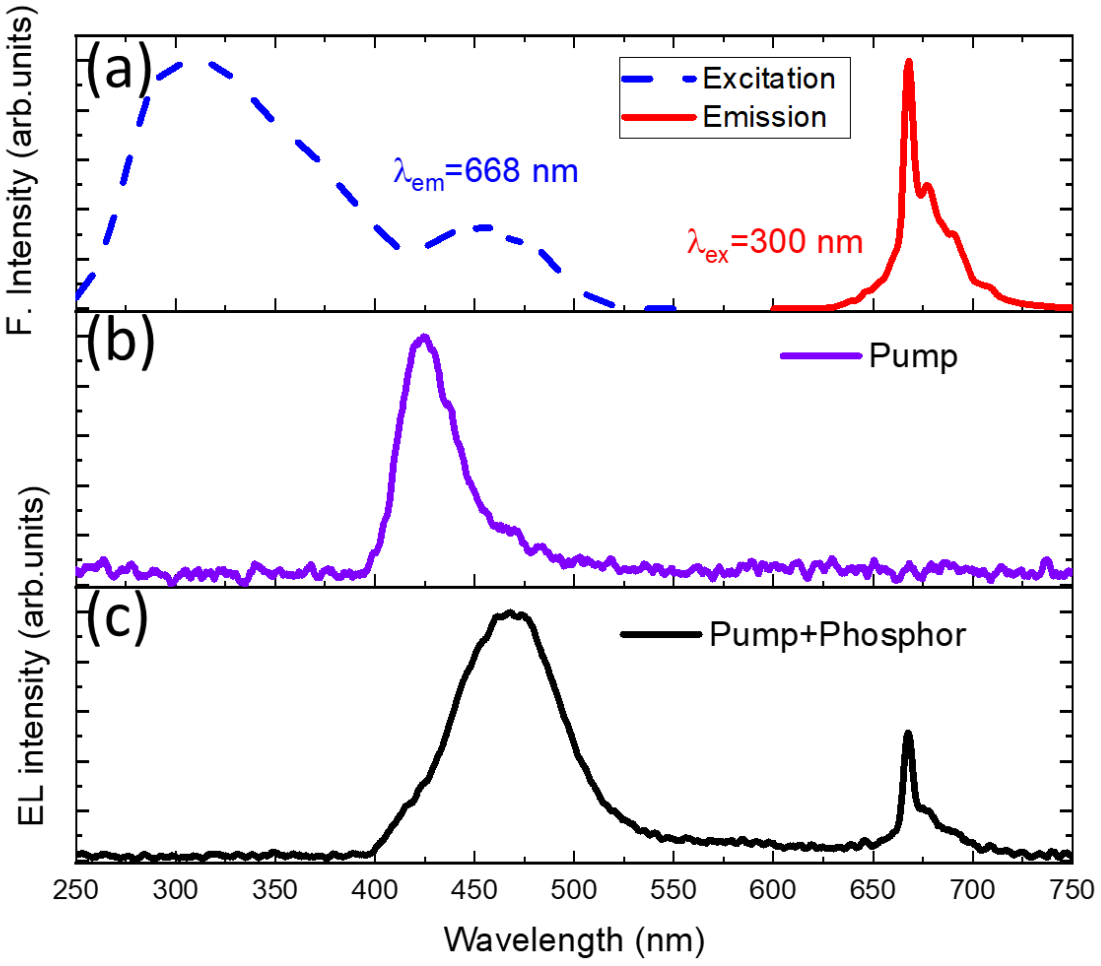

Figure 3-8. (a) Excitation (dashed blue) and emission (solid red) spectra for the phosphor R1. (b) EL spectrum of the blue flexible NW LED used for pumping the phosphor and (c) EL spectrum of the pump with the phosphor layer.

3.5 PERSPECTIVE: UV FLEXIBLE NW LED PUMP

To increase the red emission, the spectral match between the pump emission and the phosphor absorption should be improved. This can be done by using a UV LED pump, with a wavelength emission around 300 nm, where the maximum of the red phosphor absorption is located. To develop a UV flexible LED, the InGaN/GaN system is not well suited, the active material should be replaced by GaN/AlGaN system, where the QWs are made of GaN and the barriers are AlGaN.

Recently, our collaborators on the MOVPE NW LEDs growth, at CEA-Grenoble, have reported high quality non polar GaN/$Al_{0.6}Ga_{0.4}N$ multiple quantum wells grown in core shell geometry on the m-planes of hexagonal GaN NWs. They used the same approach as for the InGaN/GaN MQW NW LEDs to develop GaN/AlGaN MQWs NW LEDs. Reducing the m-plane GaN QW thickness from 4.3 to 0.7 nm leads to a shift of the emission from 347 up to 292 nm. An extensive report on the growth and optical properties can be found in ref. [283]. PL spectra of two different UV NW LEDs are showed inFigure 3-9. The future work will be focused on developing flexible UV NW LEDs making use of these structures. These LEDs will be further used as a pump for the fabrication of a red flexible LED. One technological issue to be solved is the choice of the appropriate encapsulating material to form the membrane. The standard PDMS may not be well suited for UV LEDs because of its absorption in this range.

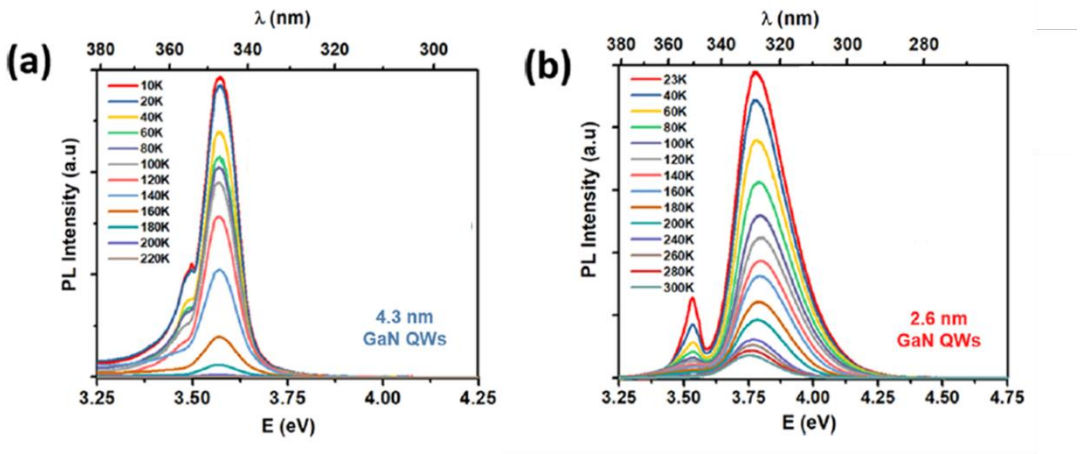

Figure 3-9. Temperature dependent PL spectra of GaN/AlGaN core shell NWs with (a) 4.3 nm and (b) 2.6 nm thick GaN QWs [283].

3.6 RED LEDS BASED ON ARSENIDE-PHOSPHIDE NANOWIRES

In addition to the down-conversion approach described in the previous section, I

also investigated GaAsP nanowires for their potential to produce red-emitting LEDs.

GaAsP is a standard material for the fabrication of LEDs. Indeed, historically, the first commercially available visible-red LEDs were fabricated using GaAsP thin films on a GaAs substrate. Later, other substrates and other materials like doped GaP or AlGaAsP were also explored, however thin film GaAsP still remains the game player for red emission. The As:P ratio of the GaAsP alloy can be adjusted to produce the colour of light from red to yellow.

In my PhD I have investigated the possibility to replace the well-known GaAsP thin film LEDs by nanowire LEDs in view of flexible devices. The material department of C2N masters the growth of GaAs and GaP nanowires using both self-assembled and patterned growth modes. For the LED application, the growth of ternary GaAsP NWs was optimized by a postdoc, Himwas Chalermachai.

3.6.1 Synthesis of GaAsP nanowires

GaAsP NWs were grown by MBE using self-catalysed growth mode. The designed structure consists of a p-i-n $GaAs_{0.6}P_{0.4}$ NW with a $GaAs_{0.7}P_{0.3}$ active insertion of 100 – 150 nm length.

The growth of GaAsP NWs was performed at 610 °C following the VLS mechanism catalysed by Ga droplets (i.e. in a self-catalysed growth mode) on a n+ Si substrate with a thin oxide layer. The growth was started by a short deposition of Ga at the growth temperature to form liquid Ga droplets [236], [284], [285]. Then the Arsenic (As) and Phosphorus (P) shutters were opened simultaneously to initiate the GaAsP NW growth. The Ga flux was set equivalent to a two-dimensional deposition rate on GaAs (001) of 0.2 nm·s-1, as calibrated from reflection high-energy electron diffraction oscillations [284], [286]. Group V materials were supplied by solid-source cells in the form of As_4 and P_2. Both cells were equipped with individual valves and shutters. The V-to-III beam equivalent pressure (BEP) ratio was set at 9 while the $P_2/(P_2+As_4)$ BEP ratio was adjusted to 0.2. The resulting P content in the GaAsP alloy in active insertion deduced from EDX analyses was close to 30%. The targeted alloy composition in the doped contact segments was 40% of P. The axial NW growth rate was in the 1.45 nm/s to 1.8 nm/s range.

Doping of GaAsP was studied in our team in the framework of the PhD of O. Saket [287] on photovoltaic applications. In particular, it has been demonstrated that contrary to GaAs nanowires, Si can be used for n-doping in self-catalyzed GaAsP nanowires [284], [287]. Here we applied this doping strategy optimized for solar cells to LEDs. Be and Si were used for p and n-doping, respectively. The temperature of the Si (Be) cell was set to 1150 °C (700 °C). As calibrated by EBIC measurements on axial GaAsP p-n structures, n-doped (p-doped) GaAs NWs with a doping concentration of 6×10^{18} cm^{-3} (2×10^{18}) could be achieved. The NW structure consists of a n-doped $GaAs_{0.6}P_{0.4}$ base, followed by the intrinsic $GaAs_{0.7}P_{0.3}$ active insertion

and a p-doped $GaAs_{0.6}P_{0.4}$ top part. To improve the ohmicity of the top contact, the Be doping concentration at the very top was increased. The average diameter of the NWs was 75 nm and the height was 1.1 um. A schema of the final structure and the SEM bird view of the NWs are illustrated in Figure 3-10.

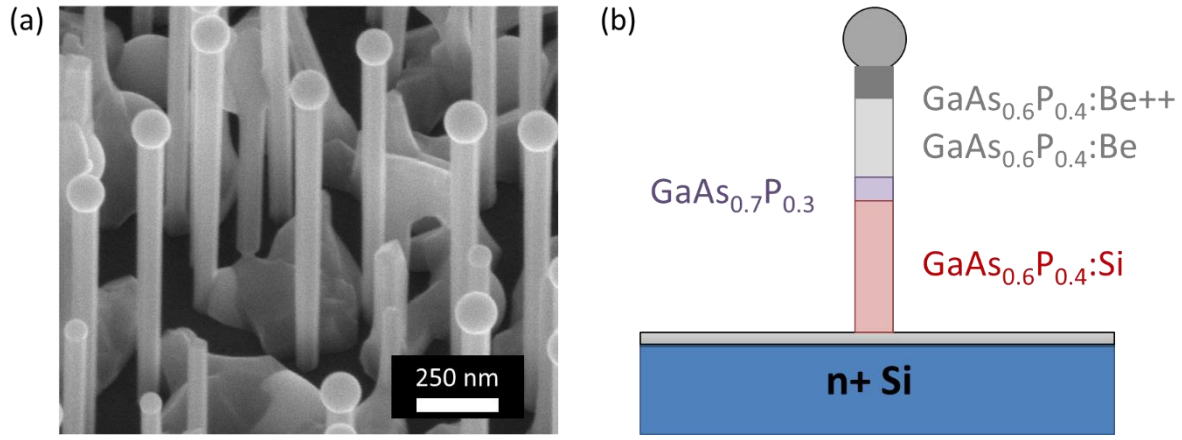

Figure 3-10. (a) SEM picture at 45° of the self-catalysed GaAsP NW LEDs, and (b) Schema of the NW LED structure.

3.6.2 Nanowire optical characterization

For optical characterizations, an additional sample with a passivated surface was synthesized. The surface passivation is achieved by an in-situ deposition of a GaP shell directly in the MBE chamber. This passivation procedure was optimized by Himwas Chalemchai for solar cells as detailed in ref [286] and it was applied to LED nanowires. The passivation consists in the Ga catalyst consumption under As+P flux without Ga supply, then few nanometers of GaP are deposited conformally on the nanowire sidewalls.

First, the passivated NWs were dispersed and studied by room temperature CL, as shown in Figure 3-11. The experiment was performed by a PhD student H.-L. Chen. The active insertion i- $GaAs_{0.7}P_{0.3}$ is detected at the middle of the structure with an emission peaked at 685 nm. It is important to notice that the NW in Figure 3-11 is flipped with respect to their natural growth direction, the n-base is on the top, and the p-doped top part is at the bottom.

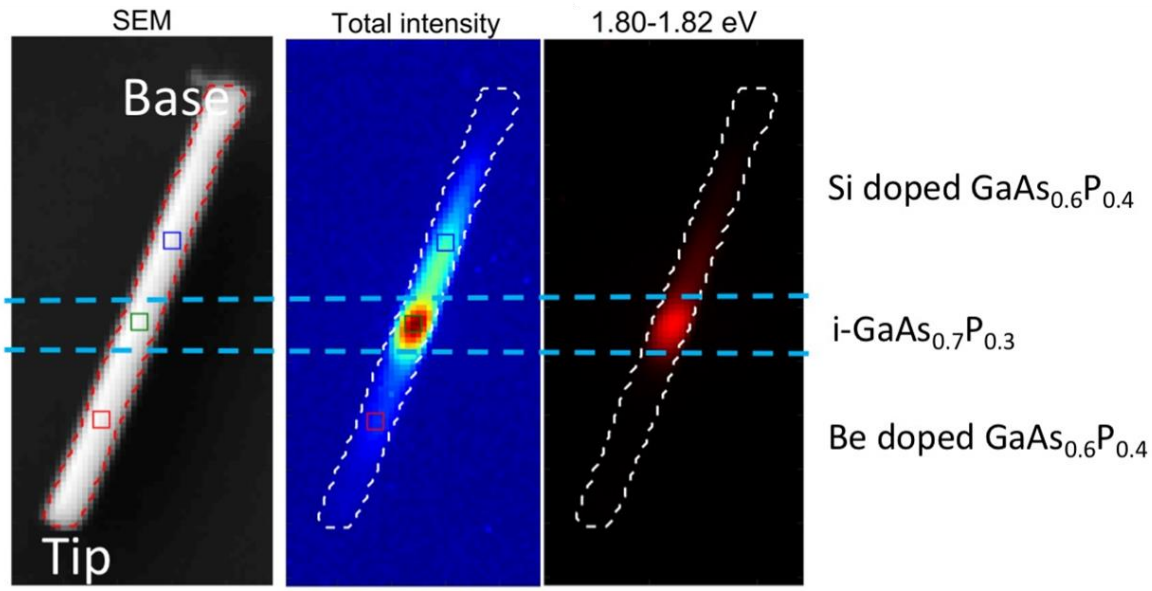

Figure 3-11. SEM, panchromatic map, and filtered for the insertion emission (1.8 – 1.81 eV) map at RT of a single dispersed NW studied by CL.

3.6.3 LED fabrication and testing

For device fabrication, I have chosen bare nanowires without the passivating GaP shell. In fact, we have attempted to contact passivated p-n NW test structures. However it was very challenging. Indeed, the catalyst consumption is accompanied with a growth of approx. 100 nm of twinned highly resistive segment, which should be removed for efficient contacting. The attempts to contact passivated NWs without etching of the GaP shell and this defective top segment resulted in a very high contact resistance. It is necessary to etch this top part of the NW, which requires a thorough optimization of the etching time. Therefore, to have a first feedback concerning the electrical properties of the GaAsP nanowires and their ability to produce electroluminescence, I decided to process unpassivated NW LEDs.

To avoid the technological challenges of the lift-off and flexible transparent contacting, I first processed GaAsP NW LEDs following a rigid architecture. The NWs were kept on their growth substrate, which was used for electron injection. NWs were encapsulated in a Benzocyclobutene (BCB) layer, then annealed for 120 min at 250 °C in a N_2 atmosphere for BCB reticulating and hardening, as described in Table 3-2.

Table 3-2. BCB spin coating, soft bake, annealing and RIE parameters used for the rigid device fabrication.

Spin coating			Soft bake	
Ramp (s)	Speed (rpm)	Time (s)	Temperature (°C)	Time (min)
5s	2000	60	125	1

Annealing			RIE Etching			
Ramp (min)	Temperature (°C)	Time (min)	RF Power (W)	Pressure (mTorr)	O_2 flow (sccm)	SF_6 flow (sccm)
30	250	120	50	100	50	10

To access the top of the NWs, BCB was etched by RIE for 120 s to expose the NW top. Then, ITO was deposited as a transparent electrode and structured by lift-off in a pattern previously defined by soft contact lithography. Finally, a metallic frame was deposited by lithography and lift-off around the mesa for better contacting on the top. As mentioned before, the Si substrate was used as a bottom contact. The morphology of the resulting device is illustrated in Figure 3-12 (a) showing an SEM image of the nanowire top part contacted with ITO.

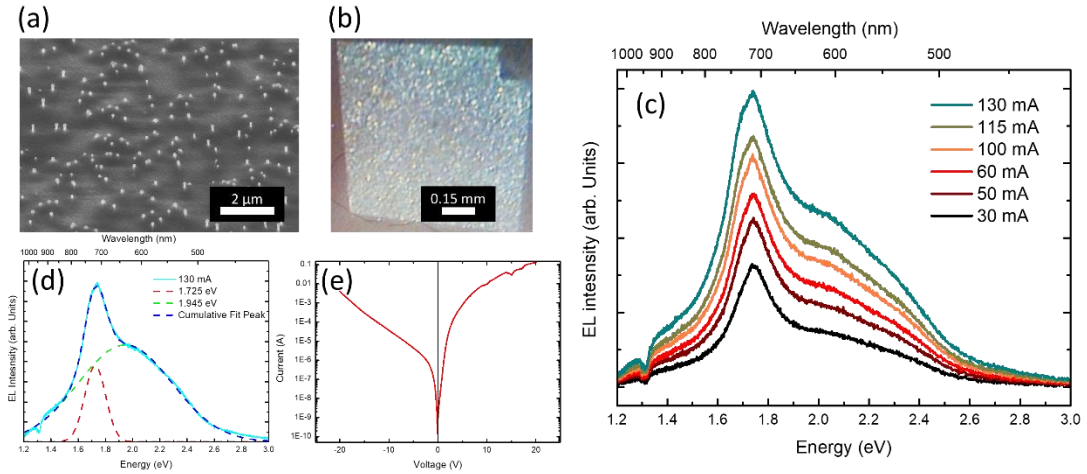

Figure 3-12. (a) Top surface of the GaAsP NW LED encapsulated into BCB with the top exposed after the RIE step, (b) photo of the device under operation (c) EL spectra of the device at different currents. (d) EL spectrum at 130 mA with a fitting consisting in two Gaussian curves and (e) IV curve of the LED in logarithmic scale.

Figure 3-12 (b) shows a photo of the LED under operation. The EL spectra at different

currents are displayed in Figure 3-12 (c). On the EL spectra one can see a narrow red emission peaked at 710 nm, which can be attributed to the emission from the GaAsP active insertion. The CL experiments have shown that the insertion emits around 695 nm which is in reasonable agreement with the observed EL peak wavelength accounting for the possible composition variations between the passivated and the unpassivated sample studied in EL. In addition to this resonant emission, a very broad background emission at shorter wavelengths was also observed (spreading from 750 nm to 550 nm with a maximum at about 600 nm) as illustrated in Figure 3-12 (d). This high broadening at short wavelengths indicates that this background may arise from the electron overshoot in the p doped $GaAs_{0.6}P_{0.4}$ segment. The higher P content of this segment would explain the observed shift to higher energies, while the alloy fluctuations in this long segment would be responsible for broadening. It should be noted that hole injection in the bottom n-doped segment is less likely due to the lower mobility of the holes, however it cannot be fully excluded. The presence of the broad background made the apparent LED colour yellowish instead of red as seen in the photo of Figure 3-12 (b).

Figure 3-12 (e) shows the I-V curve of the LED. One major issue of the fabricated devices is their low current and high opening voltage, above 10 V. These problems were reproducible for different fabrication runs performed on samples coming from two different growth runs, therefore we cannot attribute them to either fabrication or growth error. One possible reason for this high opening voltage could be a Schottky barrier between the p-GaAsP and the ITO contact. Moreover, the n-doped base part may be highly resistive due to possible compensation of the n-doping by Be diffusion during the growth of the top p-GaAsP segment.

3.6.4 Flexible red GaAsP LED

To develop the flexible devices, another problem has been encountered. The length of the GaAsP segment is very small, about 1 µm. For PDMS encapsulation, the PDMS was diluted in hexane (or Toluene) in a mas ratio 1:10, resulting in a less viscous PDMS, which after spin coating, can penetrate between the NWs and produces the encapsulation thickness well suited to cover the NWs. However, we have encountered a problem at the critical step of the peel off of this membrane. Indeed, the diluted PDMS layer is too thin and fragile, it breaks during the peeling off, so no membranes of macroscopic size could be produced.

To fabricate a second generation of GaAsP, we turned to our collaborators from Alferov State University in St Petersburg, who have developed reinforced PDMS. At the same time, several adjustments have been done: (i) the NW length was increased; (ii) the doping concentration was increased, and the doping order was reversed to avoid compensation by Be diffusion; (iii) ternary alloy doped segments were replaced by GaP segments to remove the broad background emission and (iv) the encapsulation matrix was changed from diluted PDMS to cross-linked graft-

copolymers of PDMS and polystyrene (referred to as "PDMS-St"). This last point allows to form thin membranes for the peel off thanks to the reinforced mechanical strength of the PDMS-St.

With these adjustments, the second generation flexible GaAsP LEDs developed in collaboration with Alferov State University are axial junctions in a GaP/GaAsP heterostructured NWs. The growth structure consists of n-GaP/i-GaPAs/p-GaP axial NW heterostructures, intentionally doped with Be and Si. Between the GaP doped segments, a 100-150 nm non-intentionally doped active insertion of $GaAs_{0.65}$ $P_{0.35}$ was grown. The resulting NW array has about 0.11 NW/μm^2 density, with 100 nm average wire diameter and 3-4 µm height. A more detailed description of the growth procedure can be found in ref [288]. Figure 3-13 (a) shows the cross section view of the GaAsP NWs as-grown and Figure 3-13 (b) presents bird's eye view SEM after the PDMS-St encapsulation.

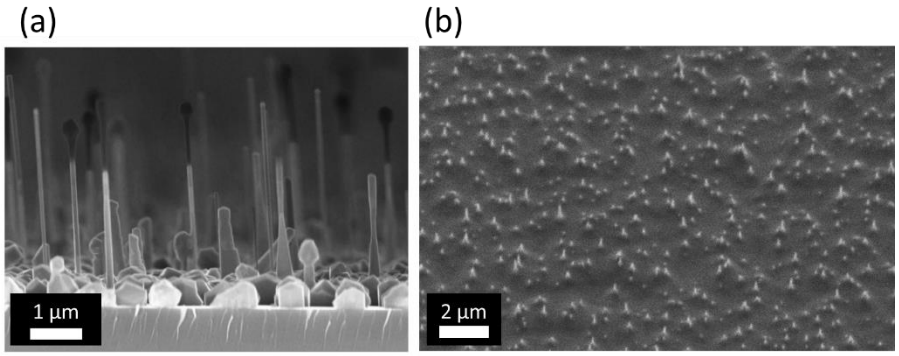

Figure 3-13. SEM pictures of the second generation of GaAsP NW LEDs in (a) as-grown cross section view and (b) bird's eye view after PDMS encapsulation.

The NW length was increased to 3-4 µm to facilitate the peel-off. The n-doped segment is now located in the top part, while the p-doped segment is at the bottom. The use of PDMS-St polymer allowed the peel-off of a 3 µm thick membrane. The LED was contacted using a carbon nanotube mesh (as described in section 2.7).

The contacted LED was measured in flat and bended conditions. The current-voltage characteristics of the device shown in Figure 3-14 (a) presented a high leakage. This is probably due to defective NWs or local holes in places where NW were not peel-off correctly in this very thin membrane. However, it should be noted that the open voltage was reduced compared to the rigid LED to 7 V for this flexible device.

Despite the high leakage, the LED produced red electroluminescence peaked around 675 nm, shown in Figure 3-14 (b). However, the EL signal was quite weak and broad.

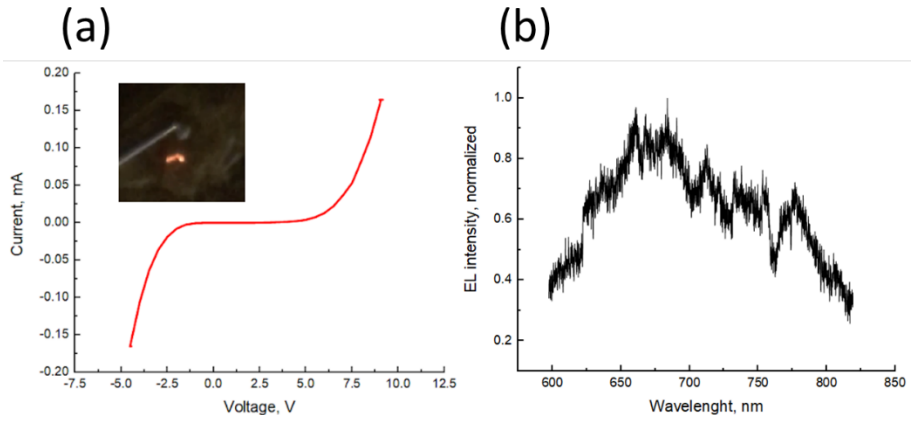

Figure 3-14. (a) Current voltage curve, with a device picture under operation in the inset, (b) the EL spectrum.

Further improvements are necessary to optimize the performance of the red GaAsP flexible LEDs both in terms of their structure and the fabrication technology.

3.7 CONCLUSIONS

Summarizing, we have concentrated in this chapter several approaches for achieving flexible RED LEDs in order to complete the RGB system. We have explored different ways to develop a flexible red LEDs. First, we use the same method used for achieving blue and green LEDs, make use of the InGaN/GaN materials system, however, the high In amount needed for tuning the bandgap till the red range is too much and the growth of the NWs presented high inhomogeneties. As secondary route for the fabrication of a flexible red LED, we use the same approach used for the fabrication of white flexible LEDs. Making use of red phosphor, pump them with a flexible LED, and integrate them in a capping layer which absorbed the light from the pump, an emits in the red range. For this purpose, several red phosphors based on Mn4+ were optically studied. Moreover, the fabrication of a prototype of the device was performed, nevertheless the wavelength pump, and the phosphor absorption range didn't match, so the pump emission keeps high while the phosphor emission was too small. We are working on flexible UV LEDs which match the absorption range of the phosphor in order to optimize this red LED fabrication.

Finally, the last route explored was use a material system with lower bandgap which allows to perform the growth without facing big challenges like In incorporation. The material system used was GaAsP NWs, which were grown by MBE, optically characterized, growth optimized, and the first generation of flexible red LED were fabricated. However, the efficiency is very low, it presents a huge leakage. In further studies we will work in optimize the device quality.

4 POROUS NITRIDE LEDS

4.1 INTRODUCTION: POROUS SEMICONDUCTORS AND THEIR PROPERTIES

The study of porous semiconductors is not a new topic. The most well-known porous semiconductor is Si, which has been widely studied since the first report in the 1950s [289]. It has known a renewed interest in 1990s when Canhman et al. demonstrated luminescence from porous Si [290], which opened a path for developing all Si photonics including light emitters. The fabrication of porous Si LEDs had become a field of high interest because of the easy integration with Si microelectronics, however the luminescence instability and the low efficiency reduced these possibilities (10^{-7}-10^{-6}) [291], [292]. In the last decades, porous Si LEDs have been improved and porous Si avalanche LEDs now offer a better stability of the luminescence however the efficiency remains low (<1%) [293]. The high resistivity, the instability of luminescence and the relatively low efficacy mitigate the expectations from this porous Si LED technology [291]–[296].

In the last decade, other porous materials have seen an increase of interest due to their unique and tuneable properties. Porous semiconductors can be designed to tune many parameters (e.g. the optical index, light scattering, electrical conductivity, specific surface area, etc) achieving a porous composite system, which combines some properties of the bulk material with properties of nanostructures.

The starting point for producing a porous morphology is the bulk material, where some regions are etched by different techniques. In the case of nitrides, these can be wet etching by HF or KOH [297], reactive ion etching (RIE) for top down etching [298] or electrochemical etching (ECE) and photoelectrochemical etching (PECE) [299], among others. Like in the first studies of porous silicon, and in the actual III-V porous studies, the main techniques for producing a porous morphology are ECE and PECE. These techniques consist in an electrolysis, where the material to porosify

is connected as the anode, an inert electrode as cathode, and a potential is applied between them while both electrodes are immersed in an electrolyte. In the PECE case, the sample is also illuminated, normally with a high energy UV lamp. By tuning the applied voltage, the electrolyte and the illumination it is possible to achieve a wide range of possible morphologies [297], [299], [300].

Porous nitrides present interest for a wide range of applications: in optical devices, but also for piezoelectric devices, chemical sensors or for improving material quality [299]. This last property is particularly attractive for nitrides. Indeed, III-nitrides, as explained in detail in chapter 2: Scientific background, don't have a lattice matched substrate for the growth. GaN based devices are mostly grown on foreign substrastes such as SiC, sapphire or Si because of the high cost of native GaN substrates. Because of the heteroepitaxy, GaN-based structures are affected by a large number of defects and high density of dislocations. For achieving high quality GaN-based layers, thick buffer layers are required. These buffer layers were implemented on sapphire wafers and it is in this way how the main industrial companies manufacture high efficiency blue LEDs for solid state lighting. Due to its low cost, availability in large size and the interest of the potential integration of GaN-based structures with CMOS technology, Si is the most atractive susbtrate for nitride elaboration. However, because of the lattice mismatch and the difference in the thermal expansion coefficient, the growth of III-nitride layers on Si results in highly deffective structures. In this case, the stress management layers become more complicated than for sapphire and also, the cost and complexitivity of the strucures increase.

In the last decades, there has been a strong focus on alternative approaches to replace the thin film technology for LED GaN-based structures grown on Silicon. One of the popular approaches is the growth of bottom-up nanowires, as previously discussed. The main idea is to replace thin films by nanostructures which release the strain and allow the defect free growth. In addition to the reduction of the defect's density, three dimensional LED nanostructures in the form of bottom-up nanowires offer nonpolar side walls for the elaboration of quantum wells. The growth of QWs on the m planes removes the internal electric field thus suppressing the quantum confined Stark effect and is expected to increase the LED efficiency. The 3D geometry also increases the aspect ratio, which leads to an increase of the active area [301]. Despite all the above-mentioned advantages, the nanowire approach also brings an additional complexity and makes the control of the structure homogeneity very challenging. From this perspective, porosification of thin films may bring a compromise by providing a good in-plane homogeneity while removing threading defects from the layer.

In particular, for growing thin film nitrides on Si, it is difficult to achieve a good crystal quality without the growth of thick stress management layers [302]. One potential solution for achieving a good quality epitaxial growth is the use of a porous

layer as a growth template. A porous layer relaxes the strain, and thus reduces the dislocation density in the epitaxial layers. There are several works which use a porous layer as a strain relaxed template for the growth of crack free III-nitride materials [297], [303]–[305]. Many studies demonstrated the strain relaxation of nitride films grown on a porous template compared to a bulk template [84], [297], [306], [307].

Regarding the control-by-design optical properties of porous semiconductors, a good example is a III-nitride porous Distributed Brag Reflector (DBR) reported in ref. [308] showed in Figure 4-1. DBRs are the key components for forming optical cavities, which can be used for fabricating vertical cavity surface emitting lasers. The refractive index of the material can be tuned by introducing pores [300]. Different III-nitride alloys have similar refractive indices. Therefore, in their bulk form a very thick DBR structure is required since the contrast between their refractive index is very small. Strain management in these thick DBRs is challenging and a long growth time is necessary. Porous DBRs could be a potential solution for developing this kind of devices in III-nitrides.

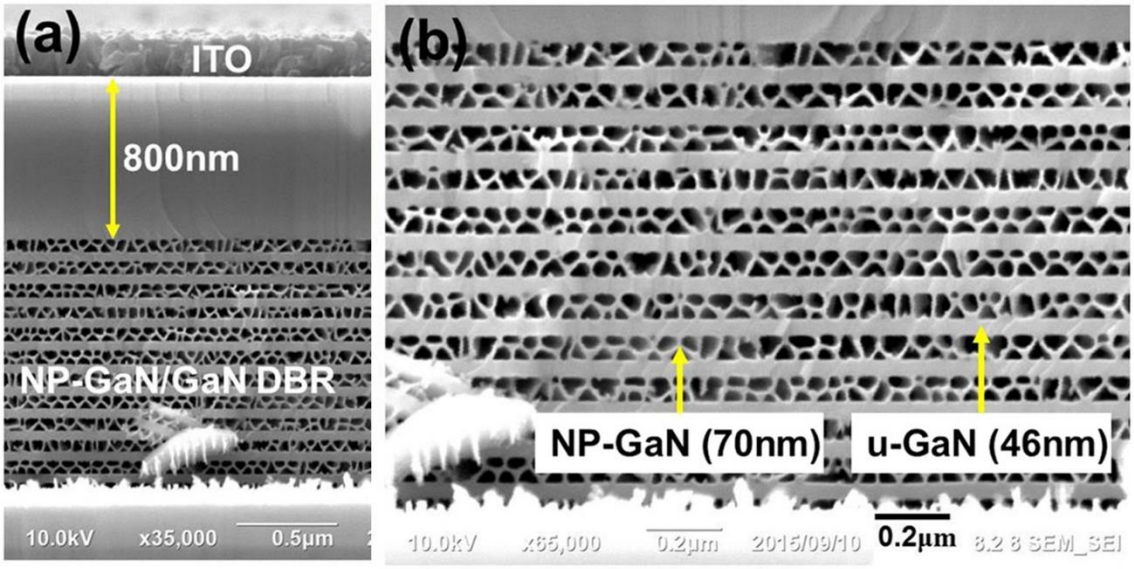

Figure 4-1. (a) The cross-sectional SEM micrograph of the DBR-LED structure. (b) Detail of the 70 nm-thick porous GaN layer and 46 nm-thick GaN layer in the stacked DBR structure [308].

In a LED, the light extraction efficiency is limited by the total internal reflection (TIR) at the semiconductor/ air interface [78]. The classical methods to improve light extraction from conventional thick film LEDs by enhancing the light scattering are surface texturing, the use of shaped substrates or micropatterning [78], [79]. A porous device intrinsically increases the light extraction by scattering.

The LED porosification process can be done in a top-down approach, widely used in the semiconductor technology. Starting from an epitaxial thin film, it is possible to define different kinds of nanostructures, such as NWs, walls or pores. Wet and dry etching requires the use of a mask, and it is limited by the lateral resolution of the lithographic process. Wet etching is difficult to control while dry etching (reactive

ion etching (RIE) or inductively coupled plasma (ICP)-RIE), are detrimental for optoelectronic properties.

4.2 POROUS NITRIDES BY SELECTIVE AREA SUBLIMATION

In my work, I studied porous structures produced by selective area sublimation (SAS) developed in CRHEA by the team of B. Damilano [86]. In addition to the epitaxial growth, this technique involves two steps which define the morphology of the porous structures. First, after the growth of the desired structure, a thin SiN_x layer is *in situ* grown on the surface (in the case of MBE growth). It partially covers the surface for protecting the material beneath. The SiN_x layer growth depends on two factors: the substrate temperature, the Si flux and the time. The aim of the layer is to locally protect the regions which should remain in the final structure after high temperature annealing.

The second and final step of the nanostructure fabrication is the sublimation of the unprotected parts of the structure. The sample is heated up under UHV conditions in the MBE chamber at high temperature (~900 °C). The SiN_x layer protects the covered surface while the uncovered regions will sublimate, producing pores in the epitaxial structure[79], [86], [309]. It is also possible to design nanostructures by patterning the protective SiN_x layer, which was applied for NWs fabrication [86]. It should be mentioned that SAS can also be used to produce nanowalls or even nanowires by removing the large part of the material leaving vertical regions interconnected [301]. When the amount of material left is larger than the amount of material sublimated, we will refer the resulting structures as a porous material.

From the thermodynamical considerations, sublimation should occur preferentially in the less stable regions, e.g. defects. As a result, SAS should lead to a lower defective material. The main advantage of SAS is an auto selectivity for remove defects such as dislocations. An indirect proof of this expected defect elimination in porous GaN layers on Si produced by SAS has been achieved by our collaborators Damilano et al. [309]. In this work they have grown, by MBE, two similar GaN films of 250 nm, one on Si <111> substrate and the other on a 2.5 µm thick GaN buffer layer grown by MOCVD on sapphire <0001> substrate, as shown in the schema of Figure 4-2 (a) and (b), respectively.

The sample grown on Si has a dislocation density of $3x10^{10}$ cm^{-2} while the one on sapphire has a dislocation density almost two orders of magnitude lower (of $5x10^{8}$ cm^{-2}). Both samples have been porosified by a similar SAS process. In this study, the authors compare the modification of the RT PL intensity before and after SAS. For the first sample grown on Si, with a high density of defects, the PL intensity has increased by more than 3 orders of magnitude while the PL intensity of the less defective sample on sapphire shows only an insignificant modification of intensity. Figure 4-2 (c) and (d) shows the RT PL spectra before and after porosification for the

sample grown on Si, and the sample grown on GaN- buffer on sapphire, respectively. Figure 4-2 (e) shows the RT PL of both porous samples in logarithmic scale, which shows similar intensities. Summarizing, SAS increases the PL intensity in samples with initially high density of dislocations and much less in samples with low density of defects.

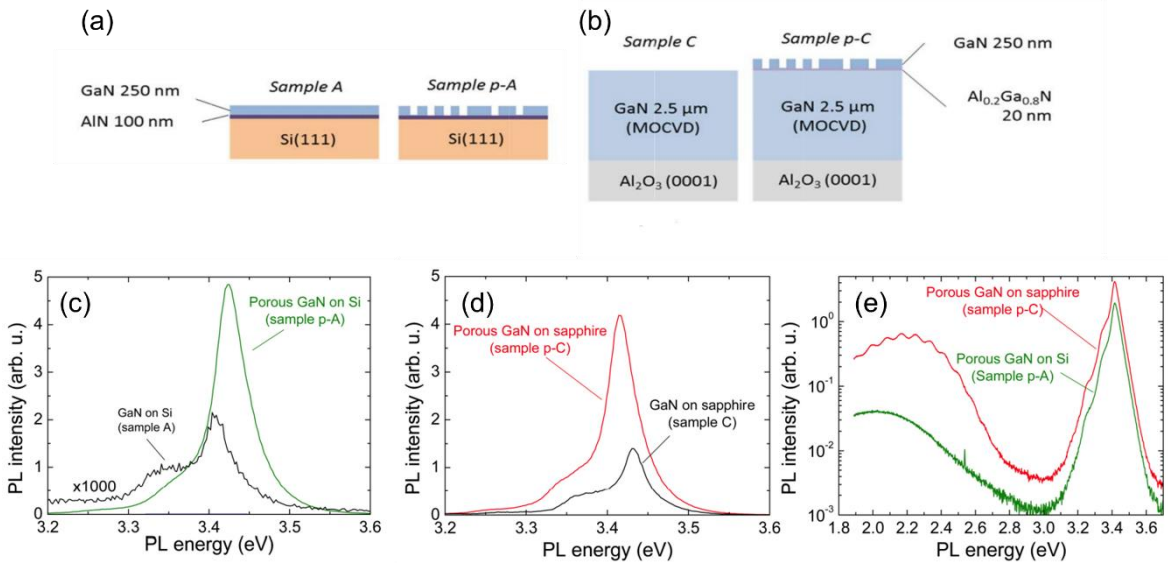

Figure 4-2. Schema of two similar GaN films of 250 nm grown by MBE, on (a) and (b) Si <111> substrate and (b) on a 2.5 µm thick GaN buffer layer grown by MOCVD on sapphire <0001> substrate. (c) and (d) RT PL spectra after and before porosification for samples on Si and on Sapphire, respectively. (e) RT PL spectra of the two samples after porosification on logarithmic scale [309].

The light extraction efficiency enhancement due to the porosification is estimated to be only a factor 2, according to this work. Therefore, the observed improvement of the luminescence intensity mainly originates from the improvement of the internal quantum efficiency (IQE). In summary, SAS on GaN thin layers grown on Si substrate improves their optical properties, making them comparable to thick GaN layers grown on sapphire [309].

It should be noted that porosification can be applied not only to binary GaN layers but also to InGaN/GaN heterostructures [309]. Similar experiments have been performed adding an InGaN QW. The PL improvement was also observed however not as high as in the binary GaN layer. This can be understood by the localization of excitons on potential minima in the QW, therefore the high density of dislocations has a less dramatic effect on the PL intensity of a QW that of a GaN bulk layer [309].

So far, several GaN-based porous LEDs have been reported in the literature [78], [297], [299]. However, these devices consist of a porous template, as previously mentioned, which is then regrown to form a continuous layer of high-quality, so that the epitaxial LED structure resembles the one of a conventional thin film LED [78], [297], [299], [304]–[306], [310]. No LEDs with a porous active region have been

reported so far. There is only one report of a porous p-n diode, however without the active QWs [311]. In my work, for the first time, all the LED structures have been grown, and then, by SAS we have produce a porous morphology through the active region to fully explore the advantages and drawbacks of these nanostructures.

The aim of this part of my PhD work is to develop and optimize the fabrication process of a fully porous LED, i.e. a device with III-N porous active region as well to characterize their optical and electrical properties. First, I consider a very simple structure containing a single InGaN/GaN QW and I analyse the impact of porosification on its optical properties. Next, I investigate the optical and electrical properties of full LED structures submitted to SAS using different surface masking.

4.3 GROWTH AND POROSIFICATION OF SINGLE QUANTUM WELL SAMPLES

The first part of this chapter will be focused on a heterostructure grown on Si (111). It is important to highlight that there is no intentional doping in the GaN layers (i.e. there is no p-i-n junction).

The samples were grown on Si (111) substrate by MBE in a Riber system. The epitaxial stack consists of a 95 nm AlN buffer layer, a 245 nm GaN layer, a 2 nm InGaN quantum well and a last 25 nm GaN layer. The procedure described in Refs. [312], [313] was applied to prepare the Si substrate and to initiate the AlN growth. Solid sources were used for Al, Ga and In. Nitrogen is provided by the thermal cracking of ammonia on the sample's surface. The temperatures were measured using an infra-red optical pyrometer and by calibrating the emissivity of the samples by considering the transition of the 7x7 to 1x1 surface reconstruction (as measured by reflection high energy electron diffraction) at 830°C. The growth temperature/ammonia flow were respectively 880°C/50sccm, 780°C/100sccm, and 540°C/500sccm for AlN, GaN, and InGaN layers. One sample is kept as a reference while the second sample is porosified using SAS. The first step is to expose the GaN surface to a Si flux to make a Si_xN_y nanomask with a thickness of less than 1 ML. Indeed, some unmasked areas of the GaN surface have to be free of Si_xN_y in order to be evaporated. After the last GaN layer, the growth temperature is decreased down to 670°C and the ammonia flow is switched off. The surface is then exposed to the flux of a Si cell heated at 1250°C for 13 minutes. The sample was annealed at 880°C with an ammonia flow of 10 sccm for 64 min and under vacuum for 36 min. This results in the formation of cylindrical nanopores. The schema of the sample structure and the SAS process is illustrated in Figure 4-3.

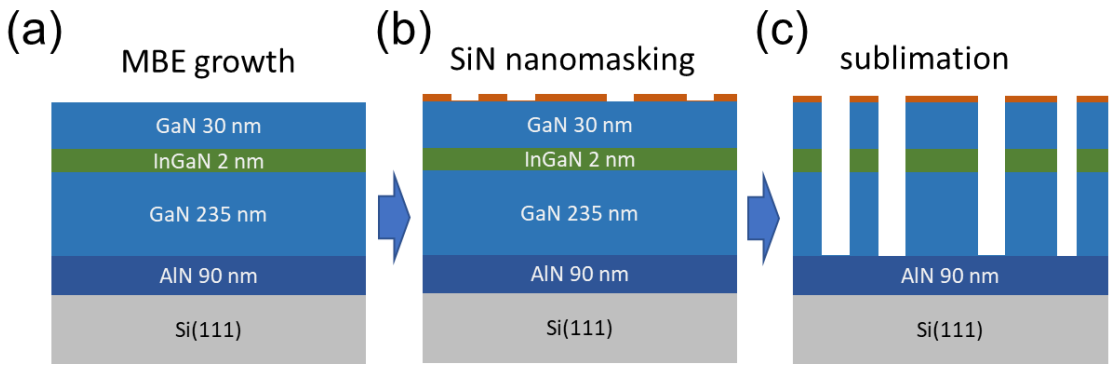

Figure 4-3. (a) Schema of the epitaxial structure grown by MBE, (b) followed by the SiN nanomasking and (c) sublimation process.

The filament used to heat up the substrate is not homogeneous, therefore the sample temperature differs from one region to another. This is very important because, the indium incorporation in the InGaN layer depends on the temperature, among others. In addition, the growth of the SiN_x layer and the temperature of the substrate during the sublimation, are other parameters affected by this temperature fluctuation. These inhomogeneities in the sample growth and sublimation will be reflected in different In incorporation, and different porosity level, from one region of the sample to another. This will be a factor to take into account always in our studies for this kind of nanostructured samples.

4.3.1 Morphology of the porosified single quantum well sample

Before focussing on the full LED structure, I first analysed the optical properties of a single InGaN/GaN QW grown on a thin GaN buffer on Si. The structure is described above (Figure 4-3 (a)) and the SEM images (top view and cross-section) are for the reference and the porous samples are showed in Figure 4-4. The pores are seen as a dark contrast.

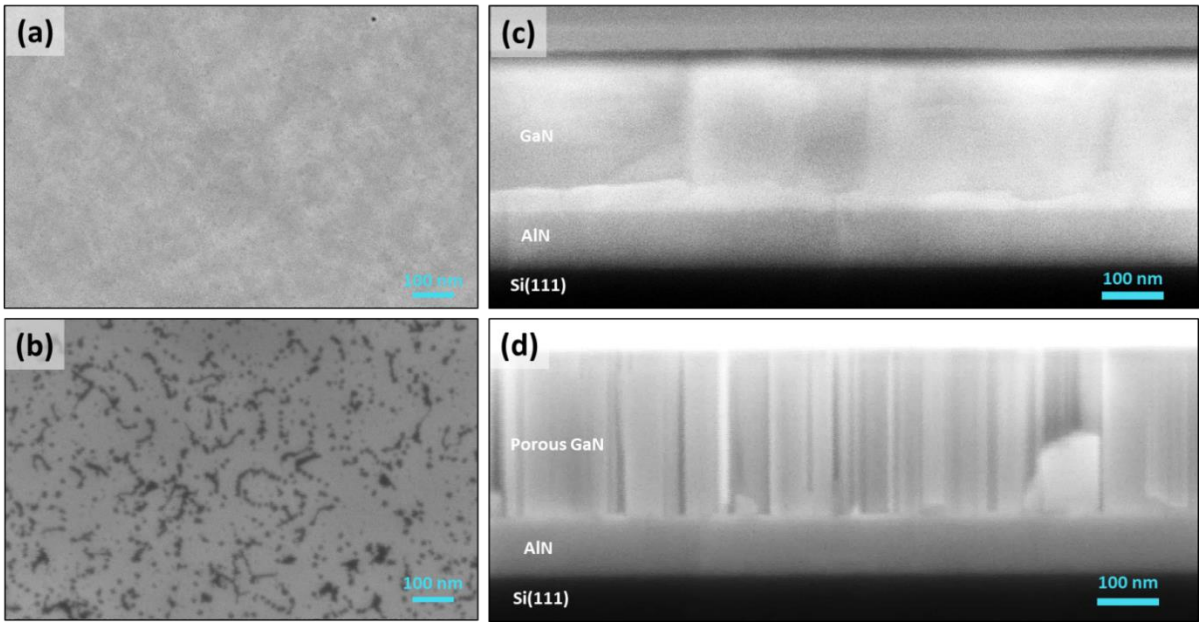

Figure 4-4. Scanning electron microscopy images of the surface and the cross section of the reference (a)(c) and the porous (b)(d) samples. The different layers visible (Si(111) substrate, AlN and GaN) are indicated on the cross section images. The very thin InGaN quantum well is difficult to see by scanning electron microscopy.

In this work, we will refer to porosity as a percentage of the surface sublimated material compared to the total initial surface. As I explained before, the SAS procedure leads to a variation of porosity throughout the wafer. In this specific case, at the centre of the sample the porosity is around 15%, and it increases up to 40% at the sample edges. As previously mentioned, one sample was kept as a reference while the second sample was porosified, both samples were cleaved in two halves. In the following, three regions respectively from the central, intermediate and edge areas were chosen for optical studies. Figure 4-5 (a) shows the top view of different regions along the porous sample and indicate the degree of porosity of each region. The positions are indicated on the wafer schema, been 0 mm the centre of the sample and +20 mm the edge. The porosity degrees from the center to the position -20 mm are similar to those indicated from 0 to +20. Figure 4-5 (b) and (d) shows the top view and the cross section of the sample in medium porosity region. It is important to notice on the cross-section image that the sublimation process stops at the AlN layer because of its higher sublimation temperature.

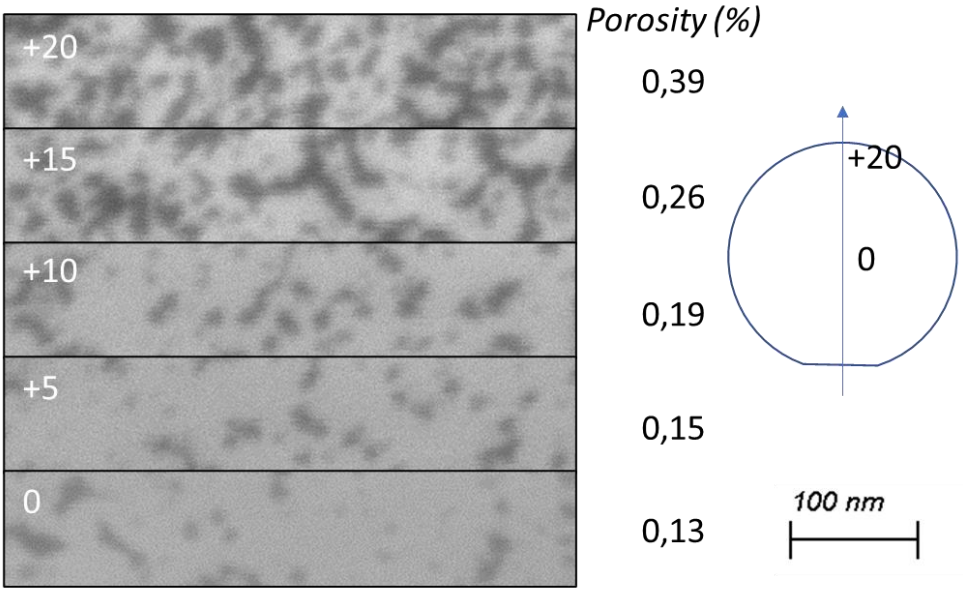

Figure 4-5. (a) Top view SEM of the porous sample at different positions, indicated on the wafer schema. The porosity degree is indicated at the right of the SEM picture. (b) Cross section SEM view of the porous sample.

4.3.2 Low-porosity central region

The optical properties of the porous and reference samples have been investigated by cathodoluminescence (CL). The CL measurements are performed at room temperature in an Attolight Chronos CL-scanning electron microscope (SEM) system. Light is collected by an achromatic reflective objective (numerical aperture 0.72) that provides constant a collection efficiency over a field of view of about 150~µm in diameter. The acceleration voltage of the electron beam is set to 6~kV, and the current of approximately 2~nA is kept constant. The diffraction grating used has 150 grooves/mm and it is blazed for 500 nm wavelength. The signal is recorded with an Andor Newton charge-coupled device (CCD) camera (1024x256 pixels, with a pixel width of 26µm). The corresponding spectral dispersion is 0.53~nm per pixel. The luminescence spectra were corrected for the diffraction efficiency of the grating and the sensitivity of the CCD camera. The luminescence intensity described in the text corresponds to a spectral density of photon flux per unit of energy (counts/(s.eV)).

First, I have analysed the central region of these two samples (porosified and non-porous reference). For both samples two luminescence peaks are observed in the CL spectra arising from the InGaN quantum well (QW) and from the bulk GaN. This last signal can originate both from the GaN capping layer and from the GaN buffer. The spectra are dominated by the QW emission, which presents a potential minimum and captures electrons and holes generated in GaN layers within the diffusion lengths.

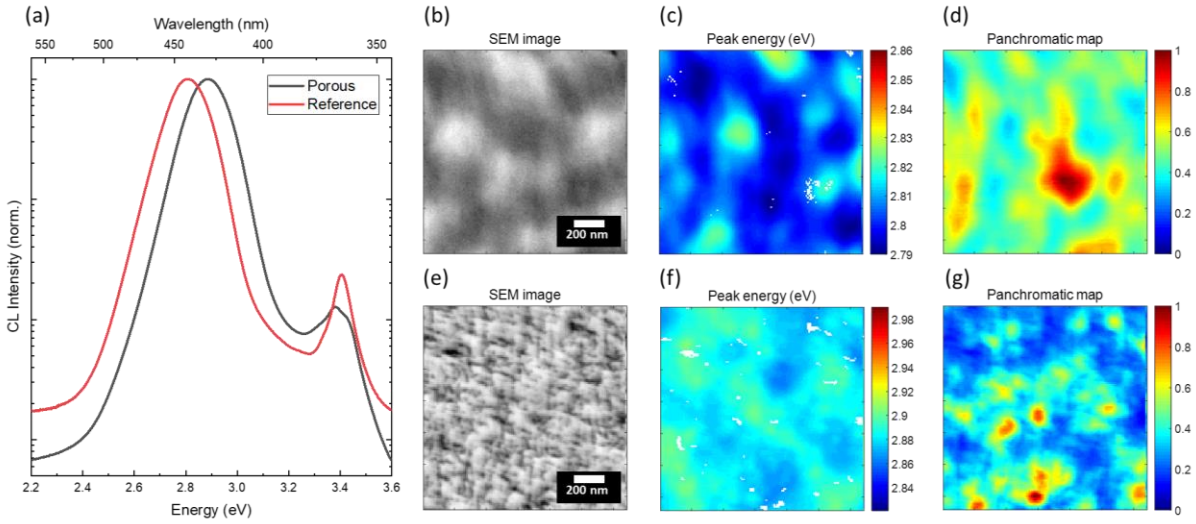

Figure 4-6. CL spectra of the samples, porous from low porosity region in black, and the non-porosified reference sample, in red, integrated over the regions shown in the SEM picture in (e) and (b) respectively. (c) and (f) are the peak energy position maps for reference and porous sample. (d) and (g) are the respective panchromatic maps.

Figure 4-6 panel (a) shows the normalized CL spectra of the porous sample, in black, and of the reference sample, in red, in logarithmic scale. We can see the two emission peaks from the InGaN QW, centred between 2.80 eV and 2.90 eV, and the GaN near band edge (NBE) emission around 3.4 and 3.45 eV. Panels (b), (c) and (d) display respectively the SEM picture, the peak energy position map, and the panchromatic CL map for the reference sample. Panels (e), (f) and (g) are the respective SEM picture and CL maps for the porous sample. The region analysed for both samples corresponds to the central area of the wafer where the degree of porosity is approximately 18%.

In the integrated CL spectrum of the reference sample the QW peak is centred at 2.81 eV, with a FWHM of 176 meV. The GaN NBE peak is centred at 3.40 eV with a FWHM of 73 meV. The spectrum of the porous sample has the InGaN peak at 2.89 eV, FWHM of 177 meV, and the GaN NBE is the result of the convolution of two emission peaks, the high energy sub-peak is centred at 3.435 eV and the low energy one is at 3.38 eV. If we consider the high energy sub-peak, the SAS induces a blueshift of both the QW emission and the NBE peak. The spectra of Figure 4-6 (a) are normalized, however from the raw CL spectra taken under the same excitation and detection conditions it was also observed that the CL intensity of the QW emission after SAS increases by a factor of 4. This increase can be explained by the improvement of the IQE, however a contribution from improved light extraction due the pores cannot be excluded. It should be noted that the QW emission intensity increase observed in CL is lower than the increase from PL experiments, which increases by a factor of 81 for the same sample. The reason for this difference is not totally clear, it may be related with the nature of the excitation source.

For the porous sample, the NBE GaN peak has a complex shape indicating that several contributions are present. Gaussian fitting of the curve shows that there are at least two contributions localized between 3.38 and 3.43 eV. Figure 4-7 shows the fitting for the NBE emission with two Gaussian functions, centred at 3.38 and 3.43 with a FWHM of 69 and 31 meV, respectively. These two contributions can be attributed to the emission of the GaN cap and of the GaN buffer, which can be easily excited through the pores contrary to the reference sample, where the excitation of the buffer is attenuated by the large material thickness that the e-beam should penetrate. The difference in the strain states of the buffer and the porosified GaN cap layer can produce this double-peak GaN NBE shape. Moreover, defects in the buffer layer may be responsible for the high broadening of the emission on the low energy side.

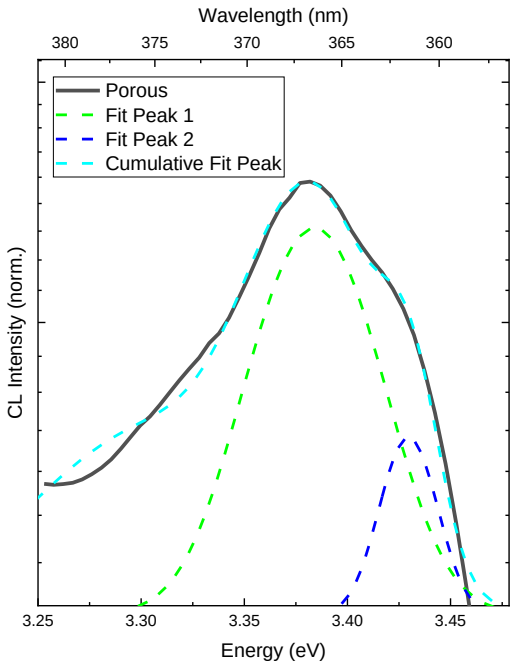

Figure 4-7. GaN NBE of the porous sample, and the fitting using two gaussian functions.

Regarding the InGaN QW emission, it is blueshifted by 80 meV, which can also be seen in Figure 4-6 (c) and (f), which shows the peak energy of each individual pixel. As mentioned before, it could have been attributed to the difference in In incorporation. However, the region analysed in both samples has the same central position, therefore we expect that the initial In content is the same or very close. Two other sources may modify the peak position: (i) Strain relaxation and (ii) Quantum Confined Stark Effect (QCSE).

The AlN and GaN buffer layers in the reference sample are grown on Si, they are under a biaxial tensile strain. On the other hand, the InGaN QW is under compressive strain imposed by the GaN layers. By SAS we introduce pores in the sample and the

material relaxes strain by the introduced free surface. GaN is under tensile strain on Si, so the relaxation of this strain produces a blueshift of the GaN NBE peak while InGaN is under a compressive strain by the GaN layers on the top and on the bottom, therefore strain relaxation for InGaN produces a redshift. It should be noted that the GaN buffer is not fully strained on Si, but partially relaxed by numerous structural defects. Therefore, the observed peak shift induced by the strain relaxation is not very pronounced for the GaN. For the InGaN QW, the strain relaxation affects both the bandgap and the internal piezoelectric field in the well.

Indeed, III-Nitrides are piezoelectric materials and the QWs are subject to a strong internal electric field. Valence and conduction bands are bended, the electron states shift to lower energies and those of the holes shift to higher energies. As a result, the energy difference between the electron and the hole is reduced compared to a hypothetical case of a square QW. In addition, the overlapping of the wavefunctions of the carriers is reduced, which decreases the recombination efficiency. QCSE is explained in detail in section 1.1.2. When the material releases strain, the band bending is reduced, decreasing the QCSE. As a consequence, the energy difference between the electron and the hole energies in the QW becomes larger and their recombination will produce a photon at a larger energy than in a strained QW. This is consistent with the blueshift observed between the reference and the porous samples.

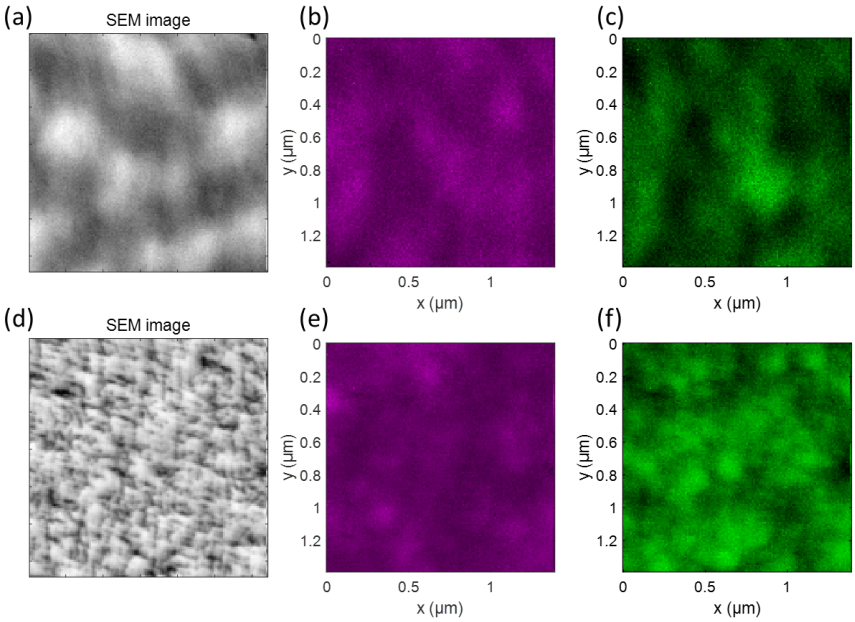

Figure 4-8. (a) and (d) are SEM pictures, (b) and (e) spectrally filtered maps for GaN NBE emission (350 nm to 380 nm), in purple, and (c), (f) spectrally filtered maps for SQW emission (390-500 nm) in green. Top row –non-porous reference, bottom row – porosified sample.

Figure 4-6 (d) shows the panchromatic map for the reference sample. Figure 4-8 (b) and (c) show the spectrally filtered maps of GaN NBE, in purple, and SQW emission, in green, of the reference sample. The panchromatic map represents the intensity

for each pixel of the analysed region, integrated over the full energy range, while on the spectrally filtered maps the intensity is integrated over a defined range of energies. On the panchromatic map, as well as on the two spectrally filtered maps, similar intensity fluctuations are observed, which occur on a large spatial scale, above 300 nm size. The size range of the intensity fluctuations is comparable to the small islands produced by the kinetic roughening [314] seen in the SEM image of panel (a). If we compare these maps with the respective maps after porosification, i.e. the panchromatic map shown in Figure 4-6 (g) and spectrally filtered maps for GaN NBE and SQW emission, shown in Figure 4-8 (e) and (f), respectively, we see that there are also fluctuations after SAS, however the fluctuations are at a smaller spatial scale, typically under 100 nm size.

Probably the change of the in-plane intensity fluctuations pattern is related to a different in plane carrier diffusion length. In the reference sample, the carriers generated by the electron beam directly diffuse to the energy minima over a big region, about 300 nm. The creation of pores after SAS reduces the in-plane diffusion length and the carriers recombine in local minima because the pores act as a potential barrier for diffusion and may also lead to surface recombination shortening the diffusion length.

4.3.3 Medium-porosity intermediate region

Moving along the axis, from the centre to a region in the middle, the porosity increases (Figure 4-5 (a)). Thus, a higher impact of the porosification process on the optical properties is expected.

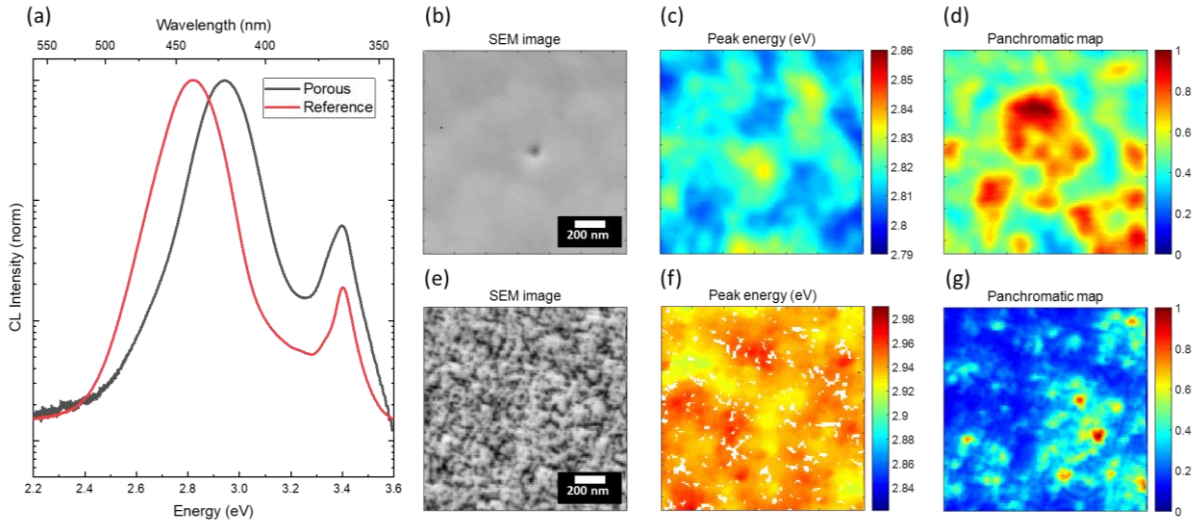

Figure 4-9. (a) Normalized integrated CL spectra in logarithmic scale of the middle region for the porous sample, in black, and reference sample, in red. SEM picture of the analysed region in (e) and (b) respectively. (c) and (f) are the peak energy position maps for the reference and porous sample, respectively. Panels (d) and (g) are the respective panchromatic maps.

The porosity of this middle region of the sample goes up to 24%. Reference sample

InGaN peak is centred at 2.82 eV with a FWHM of 174 meV while porous sample's peak is centred at 2.94 eV with a FWHM of 168 meV. For both samples, the GaN NBE is centred at 3.40 eV, with a FWHM of 43 meV, and 73 meV for the reference and porous sample, respectively. As previously discussed, the GaN NBE in porous sample may have other contributions at lower energy.

In this middle region of the reference sample, the energy of the InGaN peak is only 10 meV shifted with respect to the central region discussed in the previous section. Although thickness fluctuations may also lead to the peak shift, we attribute this shift mainly to the In composition variation between these two regions, which remains not very strong (approx. 0.3% according to the quadratic approximation for the composition of ternary compound using the values from ref. [27]). This composition variation may arise from the inhomogeneous heating of the sample during the growth. On the contrary, the blueshift of the InGaN peak after porosification is very significant, namely 120 meV (to be compared with 80 meV in the central region). The larger percentage of the pores with respect to the total area leads to a more efficient strain relaxation in the InGaN layer. Therefore, the decrease of the internal field is stronger than in the central region, making the peak shift larger. These results show how the degree of porosity affects the emission of a potential porous LED device that we plan to develop. To summarise, starting from a region with a similar In composition, we observe a larger blueshift with the increase of porosity because of a larger strain release.

It is important to notice that the effect on the reduction of the QCSE is related with the In composition, since for higher In contents the internal field is stronger, so the shift induced by relaxation is also expected to be stronger.

Regarding the intensity fluctuations, we observed the same effect discussed for the central region, and it may be larger due to the higher porosity degree of this region, observed in the panchromatic maps of Figure 4-9 (d) and (g).

4.3.4 High-porosity edge region

On the edge of the sample, the InGaN emission for the reference sample is peaked at 2.86 eV (to be compared to 2.81 eV for the central region). It means, that in this region the In composition is smaller with respect to the other regions and eventually the QW is also thinner. This is probably due to the inhomogeneities of the holder heating which result in a higher temperature at the sample edge. In incorporation is highly sensitive to the temperature, so that a lower In content is expected at the edge. We note that the internal electric field in the QW is lower in this In-poor region, therefore a smaller peak shift with the porosification is expected.

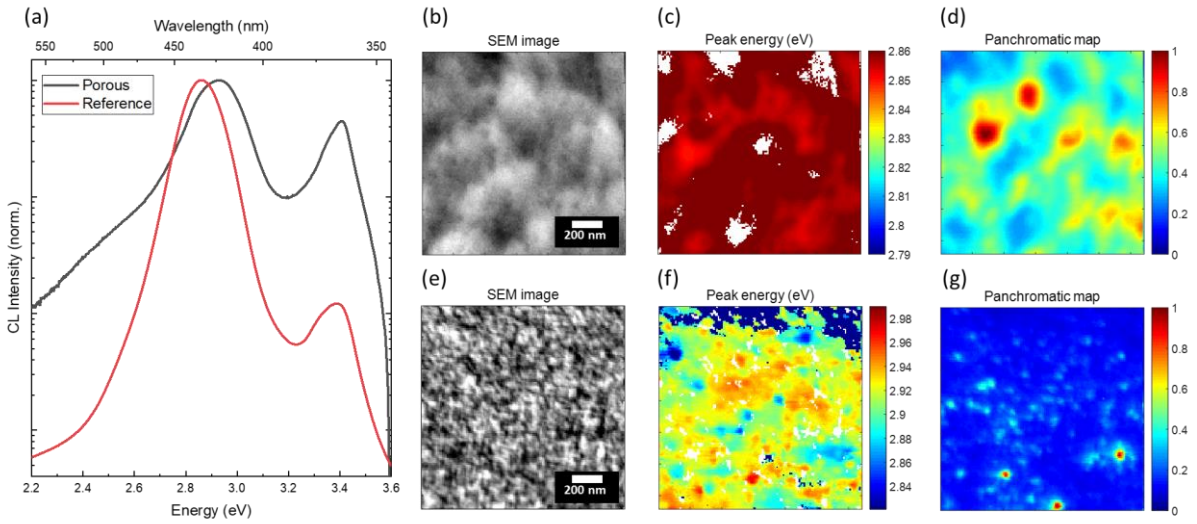

Figure 4-10. (a) Normalized integrated CL spectra in logarithmic scale of the edge region for the porous sample, in black, and reference sample, in red. SEM picture of the analysed region in (e) and (b), respectively. (c) and (f) are the peak energy position map for the non-porous reference and for the porous sample. Panels (d) and (g) display the respective panchromatic maps.

Figure 4-10 shows the average CL spectra of both samples in the edge region. This is the region with the largest density of pores, the degree of porosity is about 40%. In the reference sample, the InGaN emission is peaked at 2.86 eV with a FWHM of 159 meV while for the porous sample it is centred at 2.92 eV with a very broad FWHM equal to 228 meV. The GaN NBE is centred at 3.39 eV in the reference sample and at 3.40 eV in the porous sample. The GaN NBE is broad in both samples with a FWHM of 120 and 94 meV, respectively. Once again, a 60 meV blueshift of the InGaN SQW is observed.

As mentioned, the growth temperature in the edge region is higher, which leads to a lower In content. It affects in two different ways the QCSE. First, the piezoelectric coefficient of InGaN depends on the In content, reducing the impact of the internal field. Second, the change of In content also impacts the strain state of the SQW which has a strong influence on the internal field. Both reasons reduce the effective QCSE, which may explain the lower blueshift observed in this region than in the others. However, this region doesn't seem to be of very good quality since the broadenings are huge. SQW thickness fluctuations lead to significant variation of the emission which may explain the observed high broadening.

The FWHM of the GaN NBE of the porous edge sample is the highest among the other regions. A large porosified area leaves more GaN underlayer uncovered, which allows the electron beam to excite it directly, producing a larger intensity emission from the defective GaN buffer. This explains the complex shape of the NBE GaN emission as discussed above for the central region.

Figure 4-11. Average and normalized CL spectra of the (a) reference and (b)

porosified sample at the centre (black), middle (red) and edge (blue) regions.

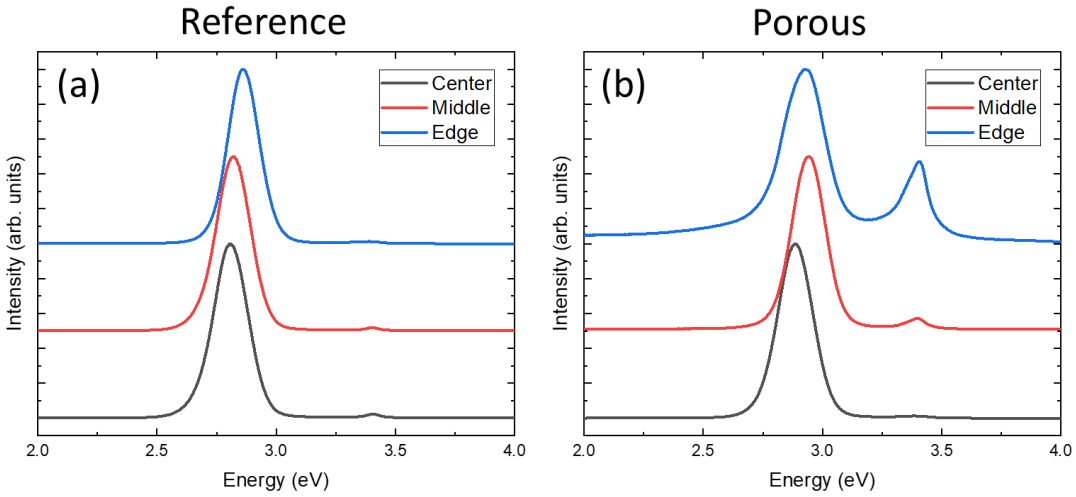

Figure 4-11. Average and normalized CL spectra of the (a) reference and (b) porosified sample at the centre (black), middle (red) and edge (blue) regions.

On the reference sample, a progressive shift to larger energies is observed when going from the centre to the edge, which is attributed to the reduction of the In content. It is accompanied with progressive increasing of the porosity degree. Both effects are related with the inhomogeneities of the heating filament of the MBE, resulting in a larger substrate temperature on the edges, which produces lower In content during the growth, and higher porosity degree during SAS.

All the samples show a blueshift of the InGaN SQW emission after porosification. The porosity increment from the centre to the middle region produces an increase of the blueshift from 80 meV to 120 meV, due to the higher strain relaxation, reducing more the QCSE.

In this section, we have studied the effect of the porosification on a simple heterostructure containing a single 2 nm thick InGaN/GaN QW on a thin GaN buffer grown on a Si substrate. The sample was porosified by SAS, introducing free surfaces in the pores which allow to relax the strain. The relaxation of the compressive strain in the QW has a major effect on the emission energy since it reduces the internal field and the quantum confined Stark effect. This results in a strong blueshift and also in an improvement of the recombination efficiency. This effect increases with the pores density, because the strain relaxation becomes more efficient. Some impact of the strain relaxation on the GaN emission was also observed, however the resulting shift of the NBE emission is weaker compared to the QW peak. Regarding the GaN NBE emission intensity, it increases with the pores density because of the direct excitation of the buffer layer through the pores.

4.4 ANALYSES OF THE ANNEALING TEMPERATURE ON THE FULL LED STRUCTURE

The main step of the SAS is heating up the sample at high temperature for a long time. In the previous section, we have analyzed the effect of porosification on the optical properties of a simple structure consisting of a single InGaN QW. However, it is also important to analyze how the porosification affects the LED electrical properties, which should be investigated on a full LED structure. It is instructive to disentangle the effect of the high temperature annealing and of the creation of pores in the material. This is indeed possible by using a surface protecting layer, which prevents sublimation.

4.4.1 LED structure growth

For electrical studies, we have used a more complex structure than in the previous section, which contains both the active region and the contact layers. Our collaborators from CRHEA have grown several full LED wafers in the same growth run in a 7x2 in. Aixtron AIX6 showerhead metal organic chemical vapor deposition (MOCVD) reactor. Trimethylgallium (TMGa), triethylgallium (TEGa), trimethylindium (TMIn), trimethylaluminium (TMAl), bis(cyclopentadienyl)magnesium (Cp_2Mg), silane (SiH_4) and ammonia (NH_3) were used as the precursors for Ga, In, Al, Mg, Si, and N, respectively. The growth temperatures were measured by pyrometry using a reflectivity corrected system from Laytec. The epitaxial stack is composed (starting from the substrate) of a 250 nm AlN buffer layer, 200 nm of undoped GaN, 400 nm of n-GaN, 20 nm of n-$Al_{0.05}Ga_{0.95}N$, 10 nm of n-GaN, a superlattice (SL) composed of 10 periods of 2.3 nm $In_{0.05}Ga_{0.95}N$ and 2.3 nm of GaN, 13 nm of an undoped GaN layer, a 4 periods multiple quantum well composed of 3.3 nm $In_{0.13}Ga_{0.87}N$ quantum wells and 13 nm quantum barriers, 100 nm of p-GaN and a last 15 nm p++ GaN contact layer. The schema of the epitaxial growth is illustrated in Figure 4-12 (a). The p-doping activation is performed *in situ* immediately after the growth under a pure N_2 atmosphere at 750°C. The thicknesses were extracted from cross-section transmission electron microscopy images and the compositions of the different layers were measured by energy dispersive X-ray spectroscopy. The total epitaxial thickness is 1.1 µm, which is much thinner than the 3.5-5 µm typically requested for high efficiency blue LEDs on Si substrates.[315], [316] As explained above, decreasing the total thickness of the structure can be an asset in order to decrease the total growth time. The purpose of the n-AlGaN is to act as a sublimation stop layer, however we will see in the following that locally the selective area sublimation process used to porosify the sample can go through this layer, probably because of a too low Al composition. The SL is expected to trap GaN surface defects to enhance the efficiency of the InGaN/GaN MQW as explained in Ref.[317]. Compared to regular InGaN-based LED structures, no AlGaN electron blocking layer is inserted between the MQW and the p-GaN. The Al composition of this layer has to be typically in the 0.15-0.2 range and with such a composition the sublimation would be stopped at this layer.

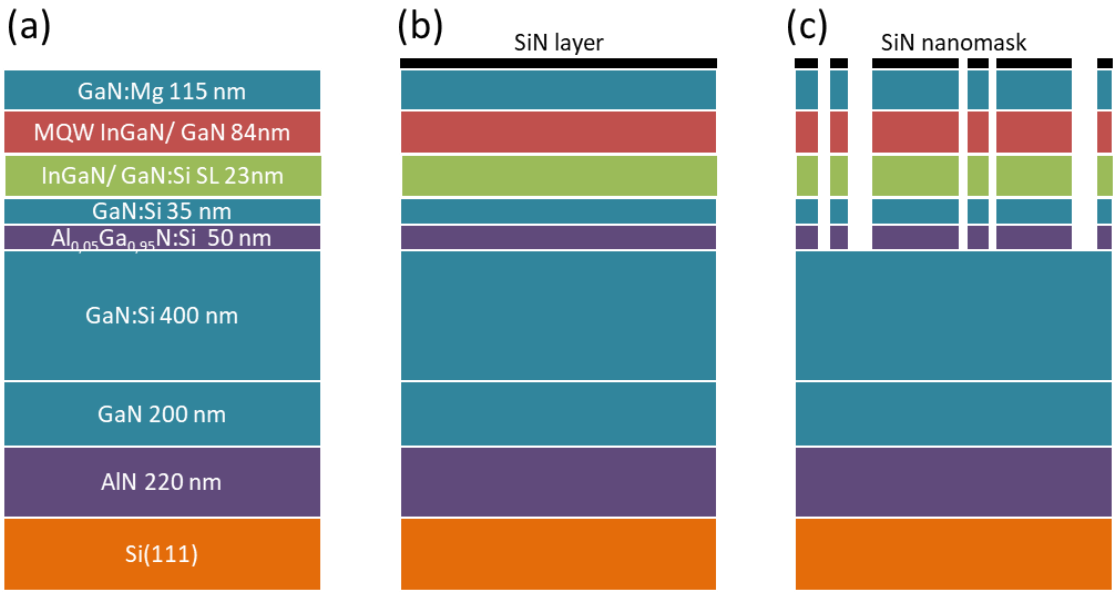

Figure 4-12. Schema of the epitaxial structure of the LED sample for (a) reference (as grown) for (b) annealed sample, protected by thermal process by a full SiN layer, and (c) porous LED sample, covered by a SiN nanomask, and porosified by sublimation in those unprotected areas.

After the growth of the LED structure, we made use of SAS. One LED wafer was kept as a reference, the second wafer was fully protected with a SiN layer, for assessing the impact of the thermal process, and the third one, a partial SiN layer, was grown on top as a nanomask for the porosification process. A schema of the three samples is sketched in Figure 4-12.

The first step is to form a Si_xN_y layer or nanomask at the surface of the LED structure. The samples are annealed under 100 sccm of ammonia at 800°C during 10 minutes in order to remove the surface contaminants due to the exposition at the air. It was verified that after this annealing, a clear 2x2 reflection high energy electron diffraction pattern (RHEED) was observed below 550°C, attesting of a well deoxidized GaN surface. Then the samples are heated at 670°C under vacuum and exposed to the flux of a Si cell heated at 1250°C for 70 minutes to grow a fully complete SiN layer and 35 minutes for a SiN nanomask. At this stage a faint $\sqrt{3}\times\sqrt{3}R30°$ surface reconstruction was observed on the RHEED pattern and was related to the formation of Ga/Si-N bonds.[318] Note that it was not necessary to provide an additional nitrogen source to form this layer, the nitrogen already presents at the surface or the background residual ammonia pressure in the reactor (10^{-9} to 10^{-8} Torr) was sufficient. The temperature of the samples are finally increased at 870°C, still under vacuum, for 240 minutes. During this last step the sublimation only occurs in areas not covered by the Si_xN_y nanomask, therefore, the sample fully covered by the SiN layer is only annealed, while the second sample, with partial SiN layer, is porosified by SAS. [86], [309], [319], [320]

After removing the SiN layer by wet etching (BOE) form the annealed sample, its surface remains with the same morphology as the reference sample, without pores.

Next, we present the results of the optical and electrical properties of the annealed fully protected sample and the impact of the thermal process. It is important to notice, that in these more complex structures, there is an InGaN SL deposited for strain management. As it will be shown, it is optically active and produces an emission in the CL spectra.

4.4.2 Effect of high temperature annealing while avoiding porosification

Figure 4-13 (a) shows the normalized CL spectra in linear scale integrated on the whole studied area of 2x2 um^2 of the annealed sample, in red, and of the reference sample, in black. These spectra show two main peaks: the emission originating from the active MQWs, which is dominant in intensity and is peaked at lower energy (about 2.7 eV) and the emission originating from the SL, having a lower intensity and peaked at higher energies (about 3.0 eV). The emission of the QWs of the reference sample and of the annealed sample is similar. The MQW peak energy in these two samples is centered at 2.738 eV (453 nm) and 2.766 eV (448 nm), respectively. The FWHM of the MQW peak is 140 meV for the reference and 182 meV for the annealed sample. The annealed sample peak energy is slightly blue-shifted (by 28 meV), however this blue-shift is smaller than the FWHM of the MQW emissions. Therefore, we can assume that the MQW emission is only weakly affected by the thermal process. However, the emission originating from the SL shows a strong modification after annealing. The emission for the annealed sample is blue-shifted by 140 nm with respect to the reference sample. The SL emission peak from the reference sample is peaked at 2.953 eV (420 nm) while the SL peak center for the annealed sample is at 3.093 eV (401 nm). The respective FWHMs are 156 meV and 173 meV. Figure 4-13 (a) show a large blueshift of the SL emission but also a reduction of the relative intensity of this emission after the thermal process, compared with the normalized MQW intensity energy peak.

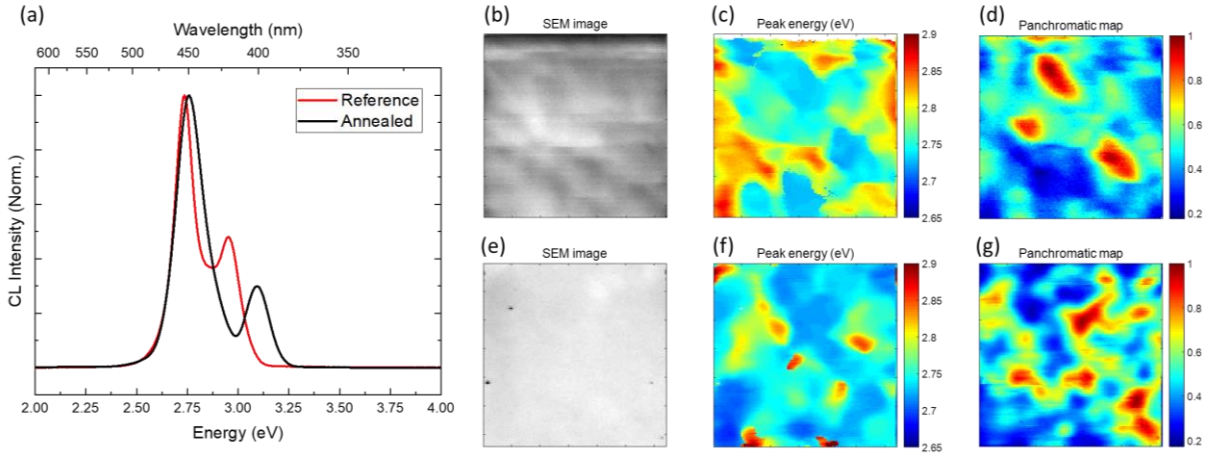

Figure 4-13. (a) Normalized integrated CL spectra in linear scale of the annealed sample, in black, and reference sample, in red. SEM picture of the analysed region in (e) and (b), respectively. (c) and (f) are the peak energy position maps for the reference and annealed sample. Panels (d) and (g) display the respective panchromatic maps.

The SEM images of the regions under study are shown in Figure 4-13 (b) and (e) for the reference and the annealed sample, respectively. Figure 4-13 (c) and (f) are the peak energy map of the respective areas shown on the SEM. It should be noted that the peak energy scale is the same in both panels, therefore they can be directly compared. It is seen in the reference sample peak energy map, the total area of high energy emissions (in red), related to the SL emission, is large, whereas in the annealed sample only few regions have the SL peak intensity higher than the MQW emission intensity.

Figure 4-13 (d) and (g) displays normalized panchromatic maps of the reference and of the annealed sample from the same region shown in panels (b) and (e). These maps show fluctuations of the integrated intensity, as previously observed in the simple SQW structures. The spatial size of these fluctuations in the reference sample is close to several hundreds of nanometers while in the annealed sample, this characteristic size is smaller, below a hundred of nanometers.

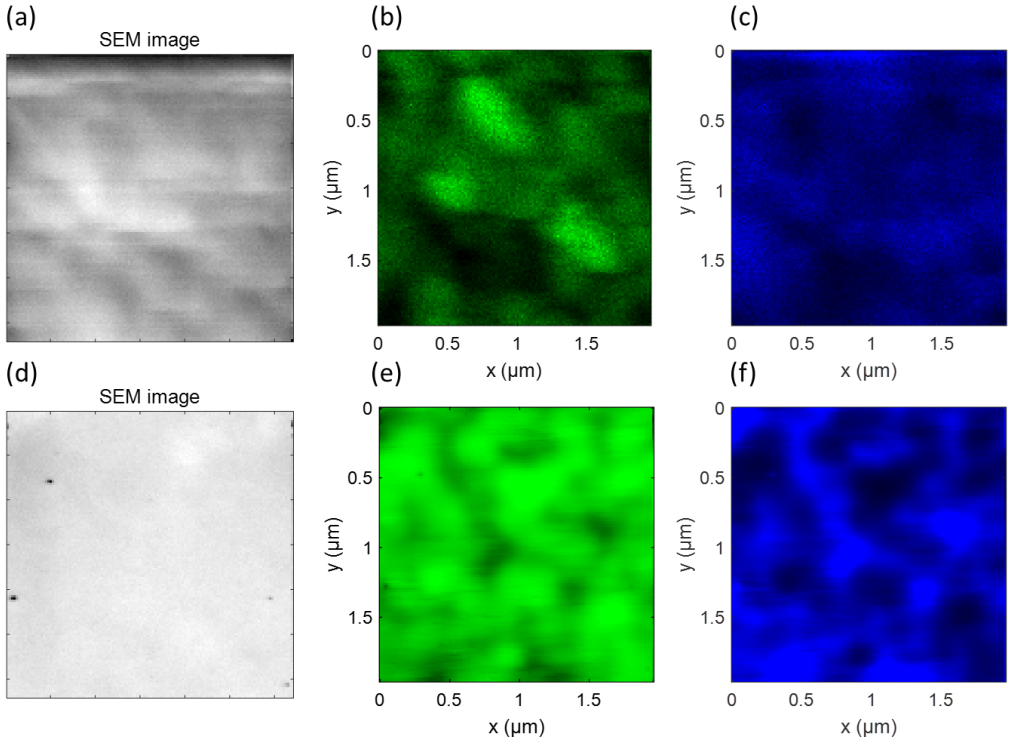

Figure 4-14. Filtered maps for the emission generated on the MQWs (b) (e), in green, for the emission coming from the SL (c) (f) from the areas shown in the SEM pictures (a) (d) from the reference and annealed sample, respectively.

Figure 4-14 shows the SEM images and the normalized maps filtered for the emission of the MQW, in green, and for the emission of the SL, in blue. Figure 4-14 (a), (b) and (c) correspond to the reference sample and Figure 4-14 (d), (e) and (f) are those of the annealed sample. The wavelength range for the MQW emission goes from 430 nm to 480 nm and for the SL covers 400 nm to 430 nm range. Similar to the panchromatic maps, in these filtered maps, the intensity fluctuations scale is

different between the two samples. The signal coming from the MQW is more homogeneous for the annealed sample.

The filtered maps of this sample, Figure 4-14 (e) and (f) are complementary: the SL emission has a higher intensity in regions where the MQW emission quenches. This may be related to the competition for the generated carriers which can either be trapped in the active QWs or can recombine in the local potential minimum of the SL QWs.

To summarize, the CL analyses demonstrate that a high temperature annealing under sublimation conditions doesn't degrade the MQW emission. The peak energy remains almost unchanged, while the spatial scale of the intensity fluctuations is only slightly modified. The emission coming from the SL is more strongly affected by the annealing, however this emission is not relevant for the LED characteristics.

4.5 LED POROSIFICATION, OPTICAL AND STRUCTURAL ANALYSES

Once it is proved that the thermal sublimation process doesn't have a huge impact on the LED structure, in this section, the optical properties of the porous LED and the impact of different degrees of porosification it is presented.

Due to the sublimation process using the MBE heater, which presents temperature inhomogeneities, the density of pores differs over the 2 inch wafer between the centre and the edges, as illustrated in Figure 4-14 (a): the porosity is about 10% in the sample centre, it increases to 25% and again decreases towards 4% at the wafer edges.

4.5.1 CL studies of Porous LED

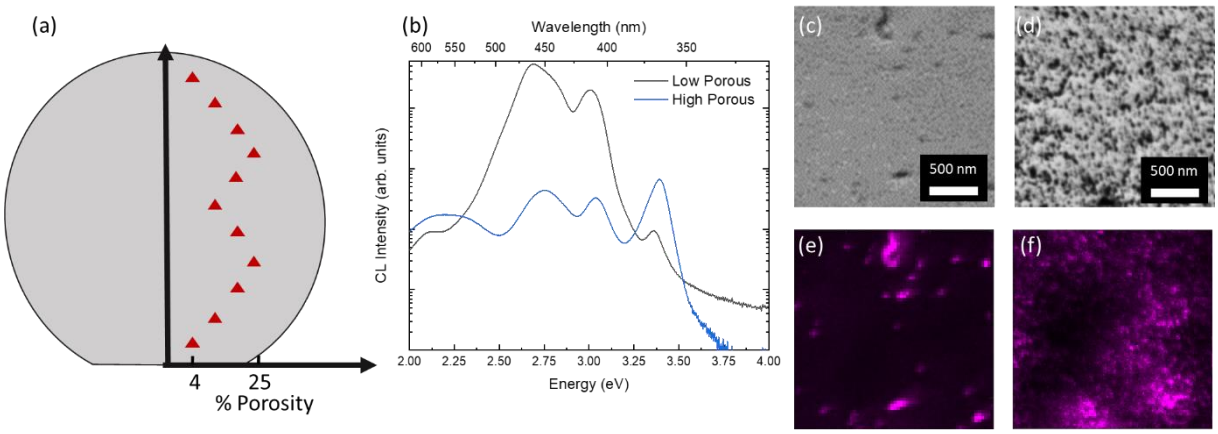

Figure 4-15. (a) Schematic showing the pores density variation along the wafer. (b) RT CL spectra in logaritmic scale collcted in low porosity and high porosity regions. (c) and (d) are the SEM images of the corresponding low porosity and high porosity regions, respectively. (e) and (f) are their GaN NBE filtered maps between 350 and 375 nm.

Figure 4-15 (b) shows room temperature CL spectra of low porosity and high porosity regions, which are characterized with a pore morphology shown in SEM images of panels (c) and (d), respectively. The CL maps were acquired under the same excitation and collection conditions, so their intensity can be compared.

In both regions the CL spectra display four spectral contributions. The high-energy peak at 3.4 eV is attributed to the near band edge emission of the GaN buffer. Some possible contribution from the p-GaN capping layer cannot be excluded, however the CL maps spectrally filtered around 3.4 eV (displayed in panels e and f) show that the intensity of this emission correlates with the pores visible on the surface: the intensity is maximal in the pores, where the electron beam efficiently excites the GaN buffer. Similarly, the broad low energy peak around 2.2 eV is attributed to the well-known yellow band originating from defects in the GaN buffer [321], [322]. The comparison between the CL spectra in high porosity and low porosity regions shows that these emission peaks have a higher relative intensity in high porosity regions which confirms that they both originate from the GaN buffer. Indeed, in the low porosity region the electron beam mainly excites the active region, while in the high porosity region the excitation of the GaN buffer through the pores is much more favorable, so that the GaN near band edge peak becomes the dominant emission.

The CL spectra also show peaks around 2.7 eV and 3.05 eV. These emissions arise from the active InGaN/GaN QWs and from the underlying InGaN/GaN super-lattice, respectively. These peaks are stronger by two orders of magnitude in the low porosity region compared to the high porosity region, which is related to the removal of the active region in the pores. We observe that the active QW peak position blueshifts from 461 nm to 450 nm when going from the low porosity region to the high porosity region. This can be attributed to strain relaxation in the QWs with the increase of porosity. As explained in Section 4.3, the strain relaxation leads to a reduction of the piezoelectric field, leading to a lower quantum confined Stark effect [37], [38] and thus to a transition blueshift.

For further experiments and the device fabrication, due to better optical efficiency, the low porosity region with the highest intensity of the active QW luminescence was selected.

4.5.2 Structural analyses of porous and reference LEDs

For assessing the morphology and the structure of the samples, electron microscopy analyses of the structure were performed. The investigations were carried out by scanning electron microscopy (SEM) in the dual beam FEI Helios NanoLab and next in the JEOL ARM 200 atomic resolution scanning transmission electron microscope (STEM) for EDS and imaging by Pierre Ruterana and his team in CIMAP Ensicaen. Using the focused ion beam technique (FIB), they prepared plane-view and cross section samples. This preparation uses focused Ga beams with energies that are varied from 30 down to 1 kV for final polishing and minimizing the beam generated

damage. The thinning process is closely monitored. During the process, primary structural and chemical information is systematically acquired using the electron beam first in the scanning mode and finally in the scanning transmission mode. The latter is only possible when the lamella is thin enough for transparency to low energy electrons (30 kV).

For the LED wafer, which was subjected to porosification, the structure can be seen in the low magnification STEM image of Figure 4-16 (b), where the active area of InGaN/GaN QWs is indicated by horizontal black arrows. Inside the GaN template and surface layers, the contrast changes are due to thickness changes and therefore to the porosity. As can be seen, the porosity is much more extended in the GaN template, and in this cross-section projection the pores appear much larger. There is an abrupt transition at the level of the AlGaN layer below the active region as indicated by the arrows in Figure 4-16 (b) to (a). This difference is better seen in plane-view SEM observations as shown in Figure 4-16 (c) and (d). In the surface region, Figure 4-16 (c), the pores are rather small (darkest contrast) and their morphology is highly complex. In contrast, the GaN template exhibits large pores with the geometry following the original distribution of dislocations as sub grain boundaries, Figure 4-16 (d). Detailed discussion about the dislocation is well discussed in ref. [332 (article under revisions)]. The higher magnification STEM image of Figure 4-16 (e) helps to explain what happens during the porosification. Inside the 20 nm thick $Al_{0.05}Ga_{0.95}N$ layer, the large pores from the GaN template as well as most of the smaller ones from the GaN surface layer are stopped. As can be clearly seen, the pores from the surface straightforwardly cross the QWs, the SL and the first GaN 20 nm layers to stop inside the AlGaN layer. However, some of the pores cross the whole stacking down to the AlN buffer layer on top of the Si substrate as shown with a white arrow in Figure 4-16 (b).

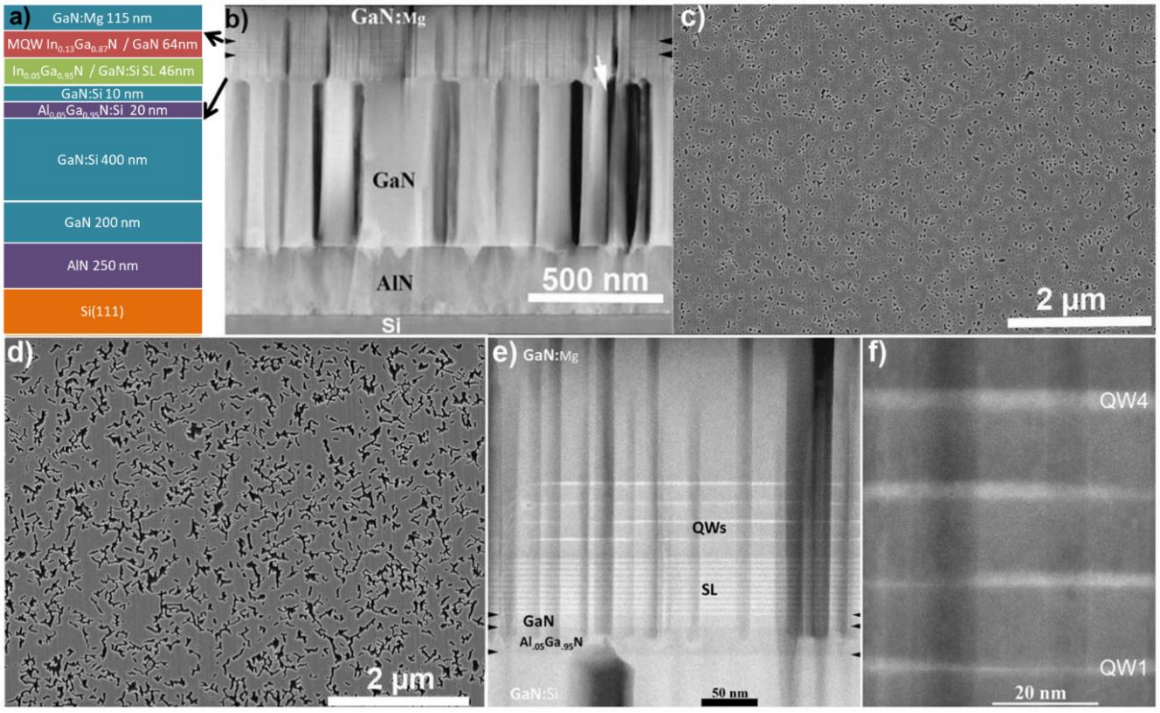

Figure 4-16. (a) Schematics of the LED structure, thicknesses of the various layers are displayed. (b) Low magnification STEM image of the whole heterostructure from the Si substrate to GaN:Mg surface layer after sublimation. (c) Plane-view SEM close to the surface region (d) SEM plane-view in the GaN buffer. (e) Cross-sectional view of the active QWs and the superlattice. (f) High magnification STEM image of the active InGaN/GaN QWs.

Figure 4-16 (f) shows a high magnification image of the QW region. The QWs are continuous, however they display a random fluctuation of their thickness. The EDS measurements give a maximum In composition in the QWs of 15%, obtained in thicker areas of the QWs. In the observed areas, there is no obvious formation of extended defects, so the QWs are locally elastically strained. However, as can be seen at large scale in the SEM image of Figure 4-16 (c), numerous pores are formed in this area and their distribution is completely different from that in the underlying GaN template, so the strain has many channels of relaxation.

As pointed out in the panels of Figure 4-16 (b) to (e), the behaviour during sublimation of the GaN template and of the upper active part is completely different. Large vertical pores of dendritic shape form inside the GaN template; they are fully stopped by the AlN buffer layer on top of the Si substrate and are mainly stopped by the AlGaN interlayer under the active heterostructures. A close examination of Figure 4-16 (c) and (d) shows that there are common features in the two figures which are recorded in the same sample area with FIB lamellas lifted-out respectively from the GaN template and from the surface region. In the surface region, we observe localised pores that have the form of round dots or small segments (the darkest contrast in Figure 4-16 (c)). For the GaN template, as can be seen in Figure 4-16 (d), the pores are large and they exhibit large dendritic shapes, in contrast to the surface area, where the pores are small. Therefore, there is a large change in the

porosification behaviour throughout the LED stack, which can be related with the dislocation pattern. TEM examinations of the reference sample performed by our collaborators in ENSI-Caen show that the heterostructure strongly modifies the edge dislocations distribution: the screw and mixed dislocations cross the heterostructures almost vertically, while edge dislocations are strongly in ref. [332 (article under revisions)]. This bending leads to a random homogeneous distribution of edge dislocations at the surface. One can suggest that during the sublimation process, the porosification starts from the surface and takes place along all the dislocation lines leading to a large number of small pores at the surface. At the AlGaN layer, the cross-sectional observations Figure 4-16 (b)) show that many small pores are stopped, they most certainly correspond to the porosification through the dislocation lines that were strongly bent. For the dislocations lines that cross the active heterostructure without deviation, the AlGaN layer appears less effective and the porosification process continues towards the GaN template where it is amplified by the subgrain boundary configuration as seen in Figure 4-16 (d).

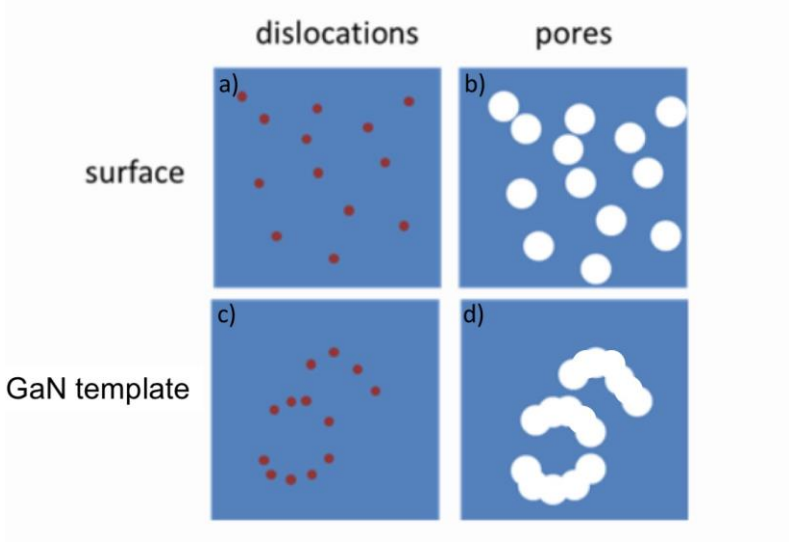

Figure 4-17. Schematic illustrating the formation of the double porosity (a) dislocation pattern at the surface; (b) formation of the small pores by submiation from the surface; (c) dislocation pattern in the GaN template (d) formation of big cavities in defective regions in the vicinity of the substrate.

The mechanism leading to the observed difference in porosity may be explained with the following schematic shown in Figure 4-17. First small pores are initiated from the sample surface by sublimation of regions close to dislocations (a) – (b). These pores propagate downward by sublimation. Some of them are stopped by the AlGaN layer, however the composition of the AlGaN is not sufficient to block all the pores, so the pores associated with vertical dislocations can cross the AlGaN and propagate further to the GaN template. Finally, these pores reach highly defective regions in the vicinity of the substrate, where they are amplified by the sub-grain boundary configuration and broadened into cavities (c) – (d).

Optical and electrical properties of the porous LED structure were characterized using CL mapping and EBIC microscopy and compared with the results for the reference structure, which was taken from the same wafer but has not undergone the sublimation process.

4.5.3 Room temperature cathodoluminescence analyses of the low porosity region

The CL experiments shown from now till the end of this chapter were performed in the laboratory of semiconductor materials (LMSC) at the "École Polytechnique Fédérale de Lausanne" (EPFL), led by Professor Anna Fontcuberta i Morral, and with the help of the CL expert and PhD candidate Nicolas Tappy. The equipment used is a CL-dedicated SEM, Attolight Allalin, with a beam energy from 3 to 5 keV and a beam current of approx. 4 nA. The spectra were acquired with a Horiba iHR 320 monochromator using 600 groves per mm grating blazed for a wavelength of 300 nm. The signal was recorded by a charge coupled device (CCD) Andor Newton 920. The spectrometer setup has a spectral resolution of 0.13 nm.

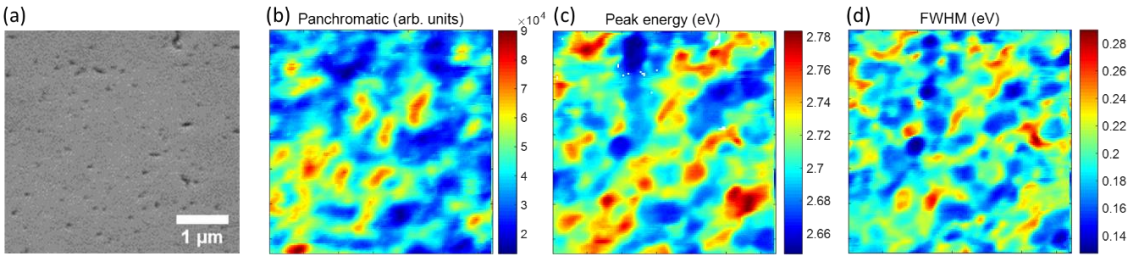

Figure 4-18. (a) SEM picture from the low porosity region. (b),(c) and (d) are the Panchromatic, QW peak energy and QW FWHM maps, respectively, from the region shown in the SEM image of panel (a).

Figure 4-18 (a) shows the SEM image and the corresponding RT CL maps: Panchromatic, MQW peak energy position and FWHM from the low porosity region, displayed in Figure 4-18 (b),(c) and (d), respectively. No correlation was found between the morphological features seen in the SEM and the spatial variations of the luminescence. Comparison with the reference shows that the fluctuations observed in all displayed maps are already present before the porosification and therefore we attribute them to the intrinsic fluctuations in the active QWs which are present independent from the porosification process. In low porosity regions, the pores density doesn't show impact on the carrier diffusion towards local or absolute potential energy minima.

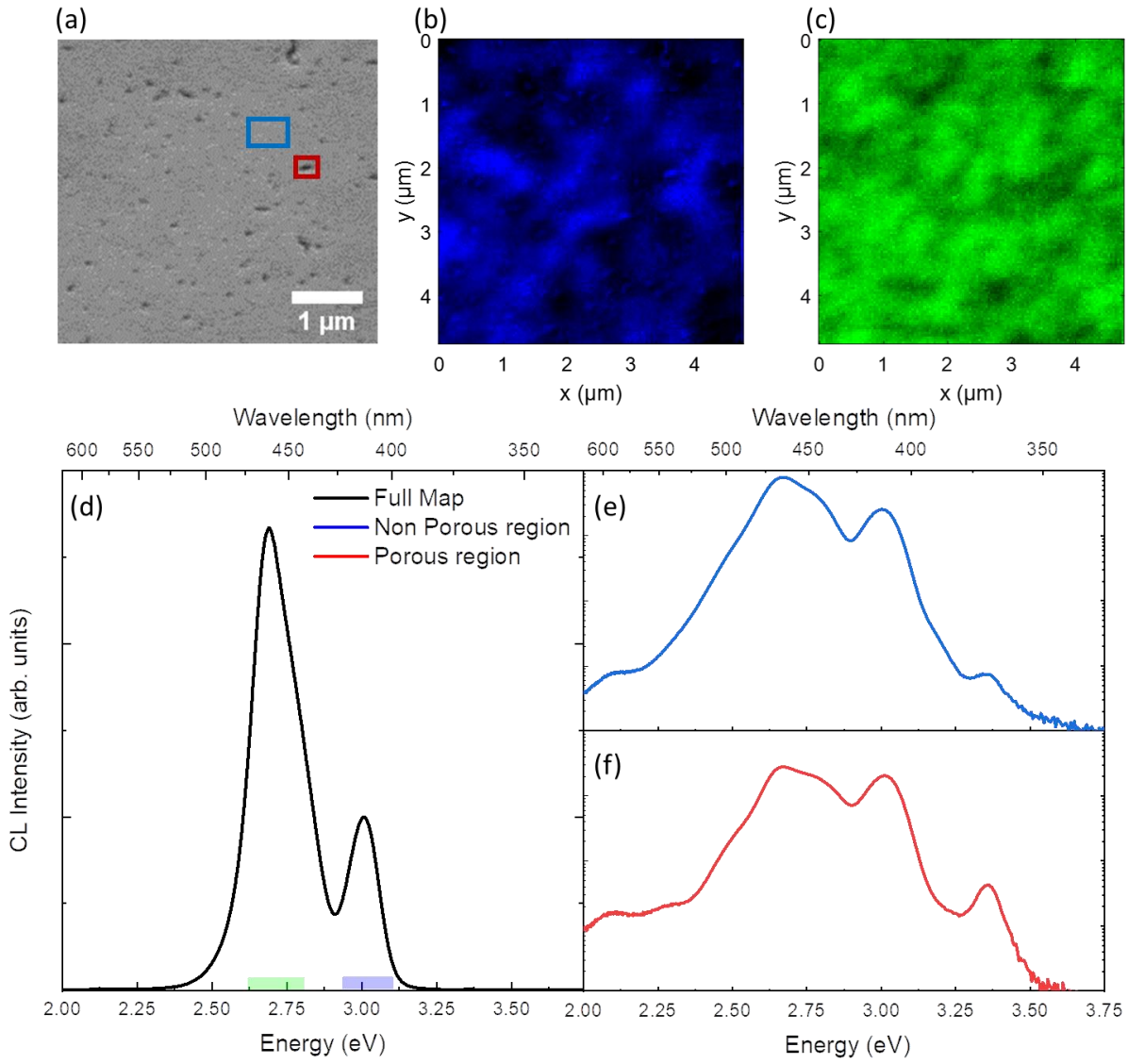

Figure 4-19. (a) SEM picture from the low porosity region. (b) and (c) are the filtered map for the emision coming from SL, in blue, filtered from 400 to 425 nm, and for the MQW, in green, filtered from 440 nm to 475 nm. The spectral regions are highlighted in the CL spectra (d) of the full region in linear scale (black solid line). The CL spectra in blue (e) and red (f), in logarithmic scale, correspond to the CL emission from the squares on the SEM image (a). The blue is selected as a region free of pores, and the red sqaure contains a pore.

Figure 4-19 (b) and (c) show the filtered CL maps or the SL and MQW emissions, respectively, in blue and green. The SL map, in blue is filtered from 400 to 425 nm and the MQW map, in green, is filtered from 440 to 475 nm. Both maps show spatial fluctuations like those shown previously without any correlation with the morphological features from the SEM. Figure 4-19 (d) shows the CL spectrum integrated over the region illustrated in the SEM picture, which exhibits the emission of the SL, having a low intensity and peaked at 413 nm and the MQW emission, peaked at 460 nm. The ranges used in the previously discussed filtered maps are highlighted in blue and green, respectively. The SEM picture of Figure 4-19 (a) have

a blue rectangle on a region free of pores. The respective CL integrated over this rectangle is shown in Figure 4-19 (e). The red rectangle shows a region with a pore, its integrated CL spectrum is shown in Figure 4-19 (f). Both spectra are in logarithmic scale and show two main differences. The region free of pores exhibit a larger emission coming from the MQWs, while in the pore region the relative intensity of the GaN NBE emission is increased, as can be expected from the filtered maps of Figure 4-15.

4.5.4 Low temperature Cathodoluminescence mapping of the porous LED

CL maps were acquired using the CL-dedicated SEM Attolight Allalin, in the same conditions described above. During the experiments, the sample was maintained at a temperature of 10 K using a liquid Helium flow-cryostat. These conditions allowed to use short integration times, between 1 and 10 ms per spectral acquisition.

First, top-view LT CL maps were recorded for the porous LED and for the non-porosified reference sample.

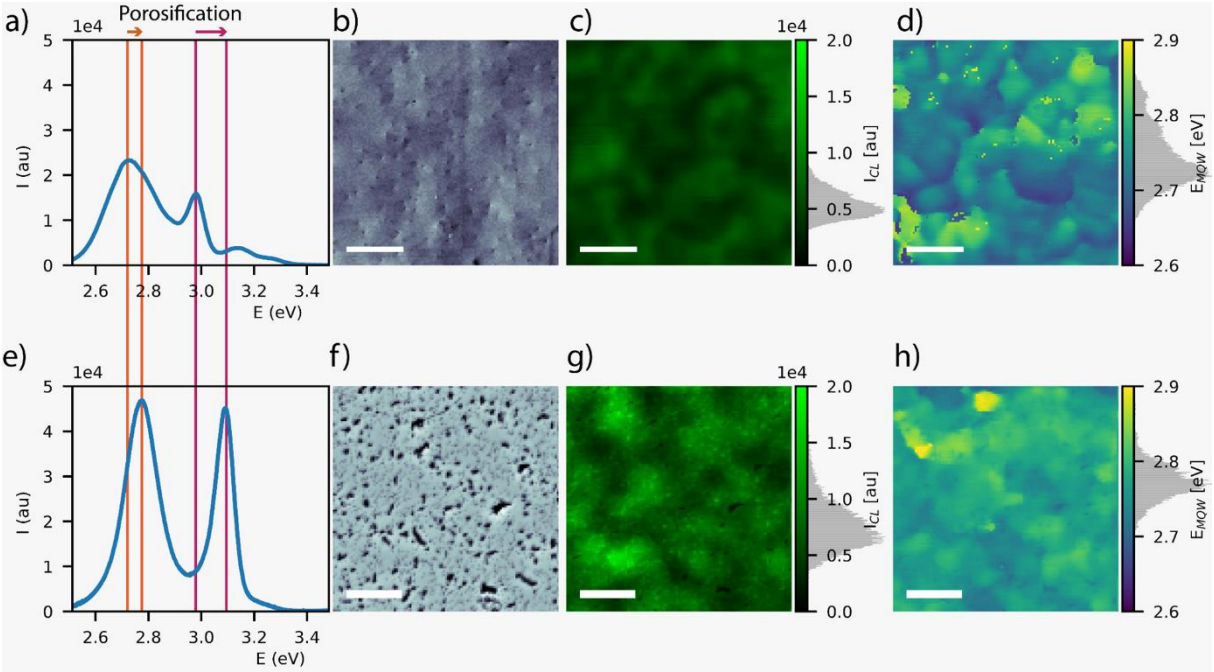

Figure 4-20. (a) and (e) integrated CL spectrum at 10 K; (b) and (f) SEM picture (c) and (g) CL map spectrally filtered for the QW emission peak. (d) and (h) Maps displaying the peak wavelength. The historiagrams on the color scale represents the distribution of pixel intensity in (c) and (f) and of the pixel energy in (d) and (h). Panels (a) – (c) refer to the reference sample, panels (d) – (f) refer to the porous LED. The scale bar is 500 nm.

Figure 4-20 (a) displays a low-temperature CL spectrum of the reference sample. The spectrum is integrated over a few square micron region shown in the SEM image of Figure 4-20 (b), which evidences the presence of pits at the surface. The spectrum shows two dominant emissions coming from the InGaN/GaN superlattice centred at 415 nm (2.99 eV) with a FWHM of 98 meV and from the multi-quantum wells centred

at 454 nm (2.74 eV) with a FWHM of 168 meV, respectively. Other contributions observed at higher energy are likely to be related with the DAP emission from GaN [323]. Figure 4-20 (c) presents a CL map spectrally filtered for the InGaN/GaN QW emission peak. Strong intensity fluctuations are observed at a sub-micrometer scale, which are partly correlated with the density of V-pit defects seen in the SEM image. These fluctuations are visualized in the histogram showing the distribution of pixel intensity of the map. The intensity fluctuations are also accompanied with a strong local shift of the QW peak in the 440-460 nm range (shown in panel (d)), which can be attributed to different effects like the In content variation, to the QW thickness fluctuation and to the inhomogeneous strain state in the vicinity of the defects. This is illustrated by a broad distribution of the peak energy for individual pixels shown on the histogram at the colour bar.

The same analyses were performed for the porous LED. Figure 4-20 (e) presents the integrated spectrum for the region shown in panel (f). The superlattice emission is peaked at 401 nm (3.09 eV) with a FWHM of 78 meV and the QW peak is located at 446 nm (2.78 eV) with a FWHM of 134 meV. The superlattice peak and the QW peak are blue-shifted with respect to the reference sample. This can be attributed to the strain relaxation leading to the reduction of the internal field and of the quantum confined Stark effect. Compared to the reference sample, a reduction of the peak broadening both for the SL and for the QW emission is observed for the porous LED. This favourable effect of porosification can also be seen in the peak wavelength map in panel (h) showing local peak shifts. This can be associated with the sublimation of defective areas in the vicinity of pit defects, which are associated with the variation of the InGaN content and strain state. This is reflected by a narrower distribution of the peak energy for individual pixels compared to the reference sample as shown on the histogram at the color bar of panel (h).

Figure 4-20 (g) presents the CL map of the porous LED spectrally filtered for the emission of the active QWs. Intensity fluctuations are observed with a characteristic spatial scale similar to the reference sample, however the intensity fluctuation remain strong as seen from the intensity histogram on the color scale bar of panel (g). The comparison of the SEM image and the CL map does not show a correlation between the intensity of the QW emission and the pores. The CL inhomogeneities are observed at a different scale than the pores, they arise from the initial growth and are not produced by the porosification process.

Fig. 4 presents the cross-sectional CL analyses of the reference sample and of the porous LED, which allow to localize the spatial origin of different spectral contributions.

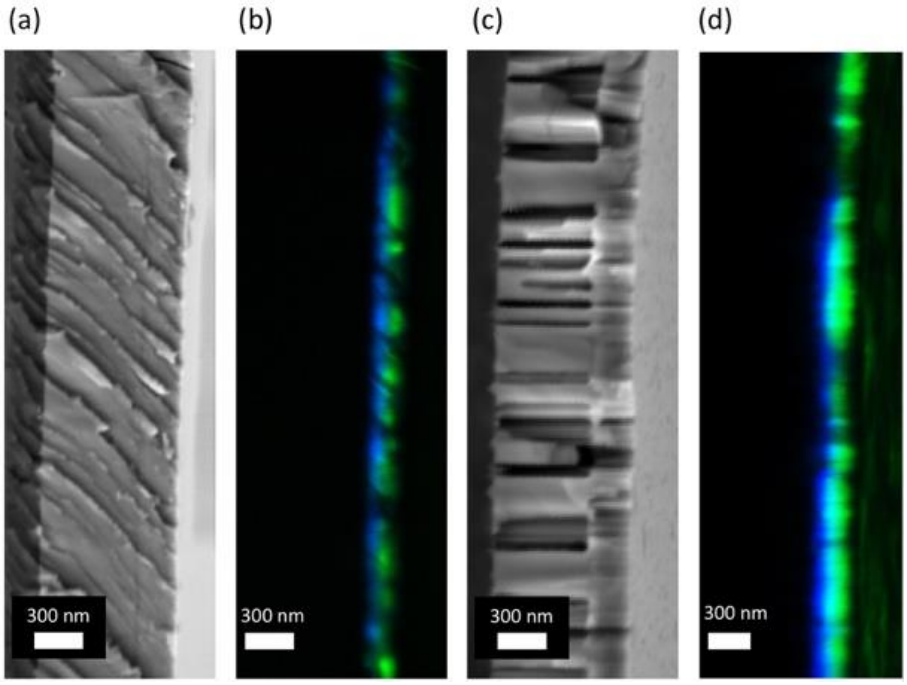

Figure 4-21. (a) Cross-sectional SEM image of the reference sample (surface is on the right) and (b) the corresponding spectrally filtered CL map at 10 K for the emission of the SL (blue) and of the QWs (green), respectively. (c) Cross-sectional SEM image of the porous LED (surface is on the right) and the corresponding (d) spectrally filtered CL map at 10 K for the emission of the SL (blue) and of the QWs (green), respectively

Figure 4-21 (a) and (b) show the cross-sectional SEM and the respective filtered map for the emissions of the super-lattice (between 400 and 430 nm, shown in blue) and of the active QWs (430 and 480 nm, shown in green) for the reference sample. Strong intensity fluctuations in the QW plane are observed, some of them may be related to the cleavage imperfections while others originate from non-radiative defects in the layers. The cross-sectional SEM of the porous LED shown in Figure 4-21 (c) evidences the above described double porosity. The super-lattice and the QW emissions can be easily localized in the CL map, they are located close to each other just above the porosity change in agreement with the structural analyses discussed in Figure 4-16 Intensity fluctuations in the QW plane are also observed, however, with respect to the reference sample, the emission of the porous LED is more homogeneous.

To summarize, the top-view and cross-sectional CL analyses show that the high temperature sublimation process does not degrade the QW emission on the full LED structure, in agreement with the results obtained for the optical studies in single quantum well structures. On the contrary, a narrowing of the QW peak and a better spatial homogeneity is observed after porosification.

4.5.5 EBIC on the cross-section

Electron-beam induced current (EBIC) microscopy was applied to the porous LED

and to the reference sample in order to probe the effect of porosification on the electrical properties of the p-n junction, by Tiphaine Mathieu-Pennober. The Hitachi SU8000 SEM microscope equipped with a Kleindiek micro probe-station was used for sample analyses (for details see setup description in [324]). The EBIC measurements were performed at room temperature using an acceleration voltage of 25 kV. This high acceleration voltage was chosen to probe the sample in-depth and to be less sensitive to the surface morphological imperfections. For cross-sectional measurements, the samples were cleaved, contacted on their bare top p-GaN surface with a nano-probe, while the bottom contact is provided by the substrate connected to the ground. A reverse bias of -1 V was applied to the sample to overcome the Schottky barrier between the probe and the p-doped GaN on the sample surface and thus to improve the signal-to-noise ratio. To measure the induced current, a low noise current preamplifier Keithley SR570 coupled with a Gatan Digiscan system was used. The EBIC maps were constructed point by point by scanning the sample surface.

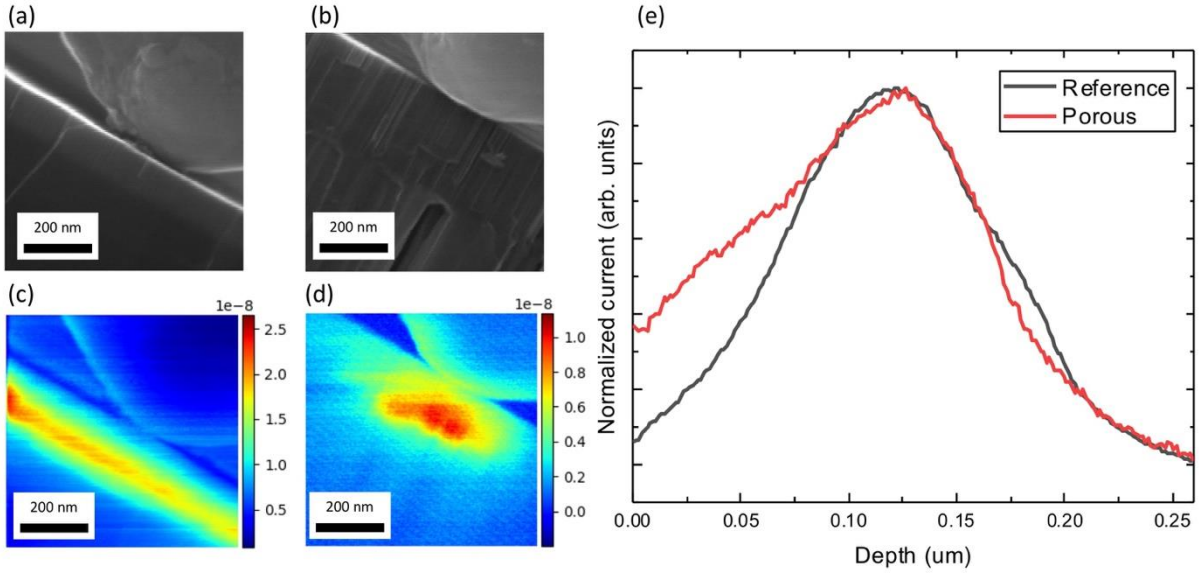

Figure 4-22. Cross section SEM (a) of the reference and (b) of the porous LED, corresponding EBIC maps under -1 V bias (c) of the reference and (d) of the porous LED (color scale shows the induced current in Amp). (e) EBIC profiles perpendicular to the layer plane of the reference and of the porous LED (sample surface corresponds to 0 µm).

Figure 4-22 (a) and (c) show the SEM image and the induced current map for the reference sample. The maximum of the signal corresponds to the nominal position of the active QWs located in the depleted region of the p-n junction and the signal quickly decreases in the p-GaN top layer and the n-doped bottom layer (cf. the EBIC profiles of Figure 4-22 (e)). In the junction plane the EBIC signal is rather homogeneous evidencing efficient in-plane current collection.

For the porous LED analyses shown in Figure 4-22 (b) and (d), the induced current can only be collected in the vicinity of the probe – the in-plane signal extension is smaller than 0.5 µm. This is indeed expected since the porosification reduces the in-

plane conductivity due to the creation of holes in the p-GaN layer. At the same time, the in-depth EBIC profile of the porous LED is similar to the one observed for the reference sample. The position of the signal maximum is the same, which shows that the doping profile of the p-n junction is not much affected by the high temperature sublimation process. This is important since one could have expected some interdiffusion or other electrical degradation due to the long annealing at high temperature. The decrease of the EBIC signal in the n-doped bottom layer has the same shape as for the reference sample. However, in the p-GaN part the profile shape is different, the decrease of the signal is non-exponential, which may be related to the modification of the electrical properties on the p-GaN layer. Indeed, an exponential profile is expected in situations when a unidimensional diffusion model is applicable, which is not the case of a porous material where the transport of minority carriers can be three-dimensional.

Overall, the comparative EBIC analyses demonstrate that the high temperature sublimation process preserves the electrical activity of the p-n junction, which is favorable for device fabrication.

4.5.6 LED fabrication and testing

To process the porous LED, the low porosity (8%) region was selected. A special care should be taken to electrically insulate the pores to avoid short-circuiting before depositing any kind of contact. After trying different materials for filling the pores, such as low viscosity SU-8 (2000.02), HSQ or BCB, finally for filling the pores, I deposited a 2 µm thick layer of parylene-C onto the top surface. Then, the excess of parylene was etched by an oxygen plasma to uncover the p-GaN top surface. Due to the inhomogeneities of the pore's density through the wafer, the resulting parylene coverage was not homogeneous, resulting in regions totally covered by the parylene and regions over etched. It is important to notice that the n-GaN is less than 200 nm deep, so the etching of the parylene is a critical step. In the central part of the sample, pores still filled, so we decide to select this optimal pore filling region for the characterization and continue with the LED fabrication.

Then, by optical lithography I defined square mesas of 300 µm side, for depositing the top transparent contact by ITO sputtering and lift-off. Finally, by a second lithography I deposited a thick Ti/Au (30nm/150nm) metal frame for device bonding purposes. The bottom contact was taken on the Si substrate. Figure 4-23 (a) shows the schematic of the porous LED.

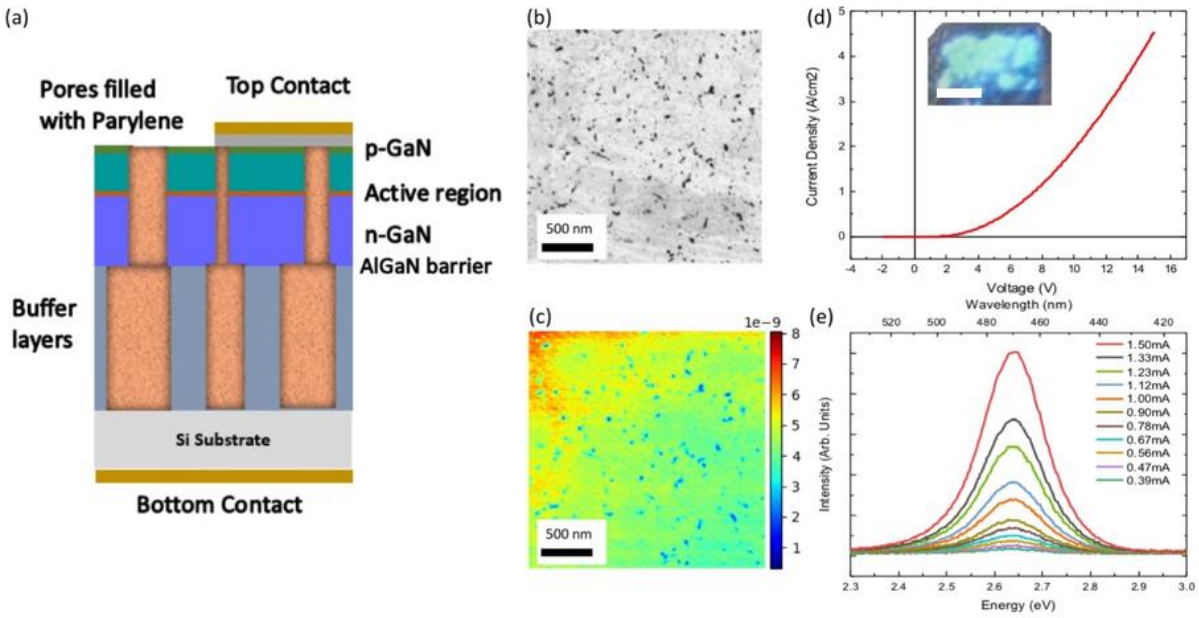

Figure 4-23. (a) Schema of the porous LED after fabrication; (b) top-view SEM image and (c) the corresponding EBIC map of the porous LED; (d) I-V curve of the porous LED with a photo of the device under operation, the scale bar is 150 µm and (e) electroluminescence spectra for different injection currents.

First, the fabrication process was validated by electrical measurements and EBIC microscopy. Figure 4-23 (b) and (c) show the SEM image and the corresponding EBIC map of a region on the top surface of the LED covered with ITO. The induced current shows dips in the pores since the p-n junction is removed by sublimation. However, these dips affect only the pores and not the neighbouring regions, where the induced current shows only slow variations. This shows the absence of local shunts through the pores and demonstrates that the pores do not affect the current generated in the neighbouring region of the p-n junction. Based on this observation we can assume that the eventual non-radiative recombination on the pore sidewalls is relatively low since it does not change the collection of the minority carriers in the pore vicinity. This agrees with the room-temperature CL mapping of the analysed LED, shown in Figure 4-19. The fluctuations of the CL intensity are not correlated with the pores, in particular no drop of the luminescence in the pore vicinity is observed.

The LED presents a rectifying diodic current-voltage (I-V) characteristic (cf. Figure 4-23 (d)), which again confirms that the parylene pore protection is efficient and the device is not short-circuited. The reverse leakage of the LED is relatively low (1 mA/cm^2 at -2 V).

The electroluminescence (EL) spectra of the LED were recorded for increasing injection current as shown in Figure 4-23 (e). The EL is peaked at 2.635 eV with a FWHM of 170 meV. The peak position shows only a negligible blueshift for increasing injection (going from 2.630 eV for 0.4 mA to 2.637 for 1.5 mA). This low

blueshift compared to standard non-porous LEDs [325] is consistent with the reduction of the internal electric field in the QWs thanks to porosification. The inset of Figure 4-23 (c) shows an optical microscopy image of the LED under operation, showing intensity fluctuations. These fluctuations of the electroluminescence are tentatively attributed to electrical inhomogeneities of the top contact, which may be caused by parylene residues on the surface due to insufficient etching. Further optimization of the parylene planarization step is expected to solve the issue.

4.6 CONCLUSIONS

The optical studies on SQW simple structures reveals a reduction of the QCSE on the porous samples due to strain relaxation. The In amount of the QW is a critical factor because it defines the internal electric field, responsible of the QCSE influence, and thus its reduction, as well it impacts on the strain state.

The impact of the high temperature process, in a full LED structure, shows a modification of the optical response of the emission originated from the SL, which is not relevant for the LED emission. However, the emission originating from the MQWs doesn't show a significant modification due to the exposure to high temperatures.

Fully porous LED obtained by high temperature sublimation was fabricated and analysed. Change of porosity between the active region and the GaN buffer is observed. This phenomenon is explained as due to the modification of the dislocation pattern in the heterostructure, which is evidenced by weak beam transmission electron microscopy on the non-porosified reference sample. The impact of high temperature sublimation on the optical and electrical properties of the LED structure is assessed using cathodoluminescence and electron beam induced current microscopy. It is observed that neither QW emission nor the p-n junction EBIC spatial profile were degraded after porosification with respect to the non-annealed reference sample. The LED is demonstrated using parylene insulation of the pores and its electroluminescence is analysed. To the best of our knowledge, it is the first InGaN-based LED with a fully porous active region.

4.6.1 Flip Chip

The main difficulty for the fabrication process of the porous LEDs is to achieve a low-resistance contact on the porous p-GaN layer without short-circuiting the device. Indeed, if the contact material penetrates into the pores, the p-GaN contact would become connected with the n-GaN. To avoid this problem in the porous LED parylene was deposited to insulate the pores. However, It appears that the contact procedure using parylene is not optimal for homogeneous current injection. To improve the emission homogeneity, I started to develop a flip chip fabrication process. For flip chip fabrication, a Ni/Au layer is deposited on the porous top, with a 60° tilt. In this way, for a pore size of 100 nm, the metal layer will cover the internal

surface pore up to 60 nm in depth, which is less than the p-GaN thickness and will not induce a short circuit of the LED. The LED is then flipped and bonded to the host substrate, covered with a Ti/Au layer. We have used Si substrate for this purpose. The wafer bonding of the sample to the host substrate is achieved by a thermal compression process. Once the wafer bonding is done, the next step consists in removing the initial Si growth substrate. Mechanical polishing process was tested for Si substrate removal. However, the sample being fragile, the mechanical substrate removal was too aggressive and induced cracking. To avoid this step, the Si substrate was removed by ICP, using Bosch process (Dry etch SF_6 + Passivation C_4F_8).

At this step of the fabrication process, the status of the sample is a Si host substrate, with the sample flipped and bonded, therefore the pore face is bonded to the new host Si substrate, and the AlN layer is on the top face. By optical lithography and contact fabrication, as explained in the previous section 4.5.6, a reference flip chip LED was fabricated. Figure 4-24 shows the (a) EL spectra at different bias (b) and (c) are optical microscope image and a picture of the reference LED, respectively and (d) the IV curve of the flip chip reference LED.

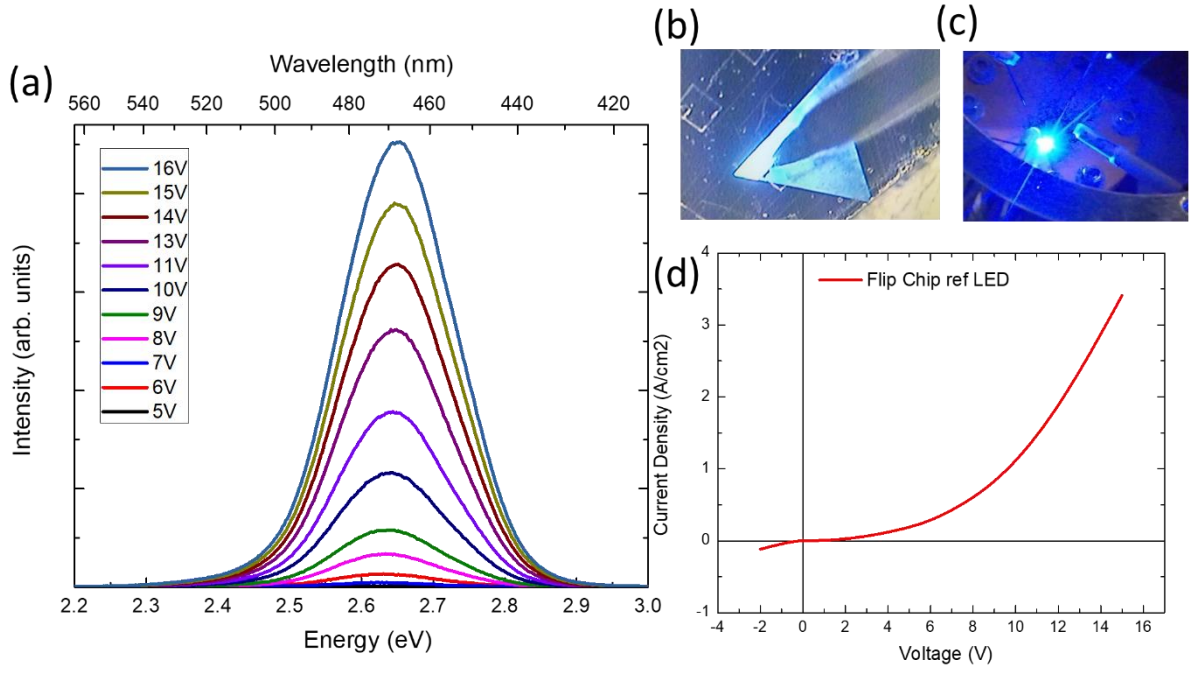

Figure 4-24.(a) Electroluminescence spectra of the reference flip chip LED at different bias (b) optical microscope image and (c) picture of the reference LED under working conditions. (d) Current voltage curve of the flip chip reference LED.

The EL spectra are centred at 470 nm, and there is no big shift of the peak position with increasing bias. Figure 4-24 (b) shows an optical microscope image of the sample where a triangular region is lighted up. The mesa previously defined by optical lithography has a smaller rectangular shape (seen in the same picture, on the top left corner), however the region which lighted up is defined by some cracks

which are present in the sample. To understand the results, transmission line model (TLM) contact resistivity measurements are the next step to be performed on the AlN layer.

To avoid the lateral current spreading, the approach is to cover the mesas with a thick photoresist and etch by ICP the AlN layer allowing direct access to n-GaN. Unfortunately, I could not finalize this technological optimization, which will be done by the team in the near future.

5 CONCLUSIONS

My PhD work concerns different aspects related to optimization and development of LEDs, as well as their characterizations before and after device fabrication.

First I described my work on flexible NW LEDs. This work was performed in collaboration with Christophe Durand's group from CEA-Grenoble, who performed the MOCVD growth of core shell NW LEDs, and in collaboration with Subrata DAS from CSIR-NIIST, who synthesized the nanophosphors used for the optimization of the white flexible NWs and development of the first prototypes of red flexible LEDs. By using the MOCVD NW LEDs I have fabricated blue and green flexible LEDs, optimizing the fabrication process. The fabrication steps consist in embedding the NWs in a PDMS membrane, peeling them off from the native sapphire substrate and doing contacts with a flexible and transparent Ag NWs network assembled by spin coating. By testing different combinations of nanophosphors and flexible LED pumps, I have fabricated the second generation of white flexible LEDs with a high CRI value and the ability of changing the CCT from a warm light of 2166 K to a cool white light of 6665 K. I have also tested the mechanical flexibility of the device using a bending set up, and contributed together with our collaborators from Alferov State University to the fabrication of a stretchable LED. I also performed thermal studies on a flexible blue LED and demonstrated that a good thermal heat evacuation towards the substrate through the GaN NWs is possible despite the low heat conductivity of the PDMS membrane. The future work related to this topic will be to develop a matrix of pixels (active or passive) which can serve as a prototype of a flexible screen. Another interesting perspective can be the fabrication of a large area NW LED, starting from a full 2-inch wafer, with the respective adaptation of the fabrication process.

The missing building block for the fabrication of a flexible RGB display or of a tuneable white light source is a red flexible LED. The MOCVD growth of InGaN/GaN

NWs is not well suited for incorporation of high In amount needed for red emission. I have evidenced strong array inhomogeneities in InGaN/GaN NWs grown by MOCVD at low temperatures in the attempt to achieve a red InGaN LED. Since the all-InGaN LEDs was not successful, I have explored two alternative routes for achieving a red flexible LED. The first is the use of a blue flexible NW LED for pumping of different red phosphors. This approach gave us good results for the white LED, however the spectral matching between the pump LED wavelength and the red phosphor absorption was not optimal, therefore the conversion of the blue emission into red was not sufficient. The peak of absorption of the investigated red phosphors is in the UV range. To improve the blue-to-red conversion, we are presently working on a UV flexible NW LED which would be better suited to pump the red phosphor and is expected to emit red at higher intensity. More details about this proposition are given below.

The second route for the red flexible NW LED fabrication that I have explored consists in changing the material system from InGaN to GaAsP. The self-catalysed growth of GaAsP NWs was optimized at C2N by MBE and the properties of these wires were intensively studied for photovoltaic applications. The main challenge for using these nanowires for flexible LED is their peeling and handling because of their small length in the 1-3 µm range. This technical problem was solved in collaboration with Alferov State University, where our colleagues developed a reinforced PDMS which allows the peeling off of dense short nanowire arrays without breaking the membrane. Using this approach, red flexible NW LEDs have been reported, however these devices need further improvements in order to increase their brightness.

Benjamin Damilano and his team at CRHEA developed a method for generating pores in a material by sublimation. The interest of this porosification procedure is that GaN emission properties have been improved by several orders of magnitude after the sublimation, which was attributed to elimination of dislocations as preferential sites for the pore formation. In my work, first, I have studied by cathodoluminescence the optical properties of a GaN sample containing a single QW of InGaN, relating the optical properties with the pores density, and taking into account the growth and the porosification process. I have observed that there is a blueshift of the InGaN emission due to the strain relaxation of the material which reduces the piezoelectric polarization, what reduces the QCSE. This results in a blueshift of the QW emission and in an increase of the recombination efficiency. Later, I studied the impact of the sublimation conditions on the optical properties of a full LED structure. For this purpose, we have analysed a sample having a full SiN protecting layer annealed under sublimation conditions. The CL analyses demonstrate that high temperature annealing doesn’t degrade the QW emission in comparison with the reference sample. Finally, I fabricated using parylene insulation of the pores a fully porous LED by high temperature sublimation. I applied cathodoluminescence and electron beam induced current microscopy to evaluate the impact of high temperature sublimation on the optical and electrical properties

of the LED structure. I observed that neither QW emission nor the p-n junction EBIC spatial profile were degraded after porosification with respect to the non-annealed reference sample. The electroluminescence of the device was analysed, which is the first report of the EL of a fully porous InGaN-based LED. The perspective for this work consists in optimizing the fabrication procedure by developing a flip chip porous LED to avoid issues with inhomogeneous p-contact.

APPENDIX A: QUALITY OF THE LIGHT

CHROMATICITY COORDINATES AND CHROMATICITY DIAGRAM

Commission Internationale de l'éclairage (CIE) is a 100-year-old organization that creates international standards related to light and colour. CIE 1931 is a Colour Matching System which allows to describe numerically a colour. CIE 1931 contains 3 functions called the RGB colour matching function: r(λ), g(λ), b(λ) illustrated in Figure 0-1. They are centred at 610 nm, 546.1 nm, and 435.8 nm, respectively. These curves express the amount of red at 610 nm, green at 546 nm, and blue at 436 nm needed to match light at any given wavelength [326].

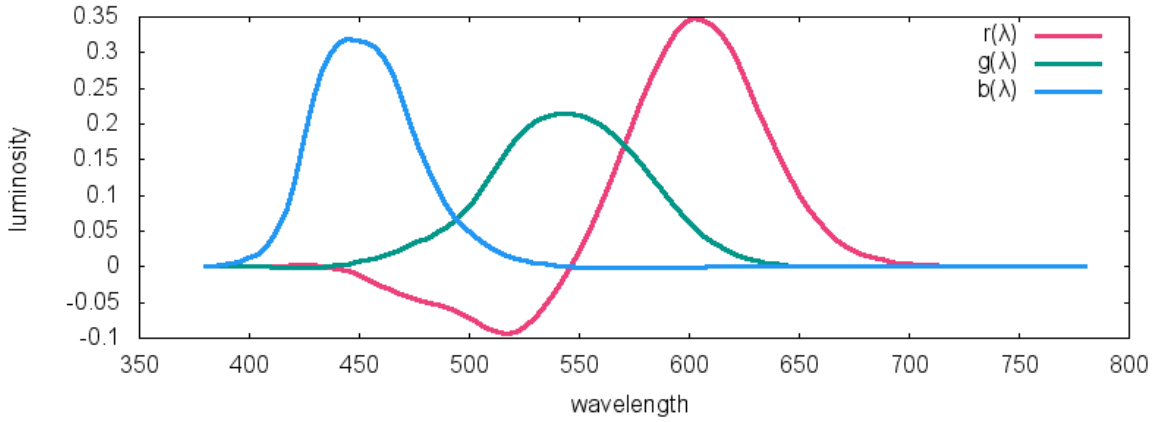

Figure 0-1. CIE 1931 RGB colour matching functions: r(λ), g(λ), b(λ) [327].

Notice that a portion of the red curve has negative values between 440 and 550 nm. This means that those wavelengths could not be matched by any mixture of the primaries. The negative values mean that they are mixed with the reference light to match the sum of the positive values [41]. Since it was not convenient to deal with negative values of the predefined colour matching functions, a linear transformation was used to convert them into x, y and z bar curves (shown in Figure 0-2), having no negative values:

$$x = 2.7688r + 1.7517g + 1.1301b \quad (0\text{-}1)$$

$$y = 1.0000r + 4.5906g + 0.0601b \quad (0\text{-}2)$$

$$z = 0.0000r + 0.0565g + 5.5942b \quad (0\text{-}3)$$

y is identical to the standard luminosity function, which is a dimension-less function describing the sensitivity to light of the human eye.

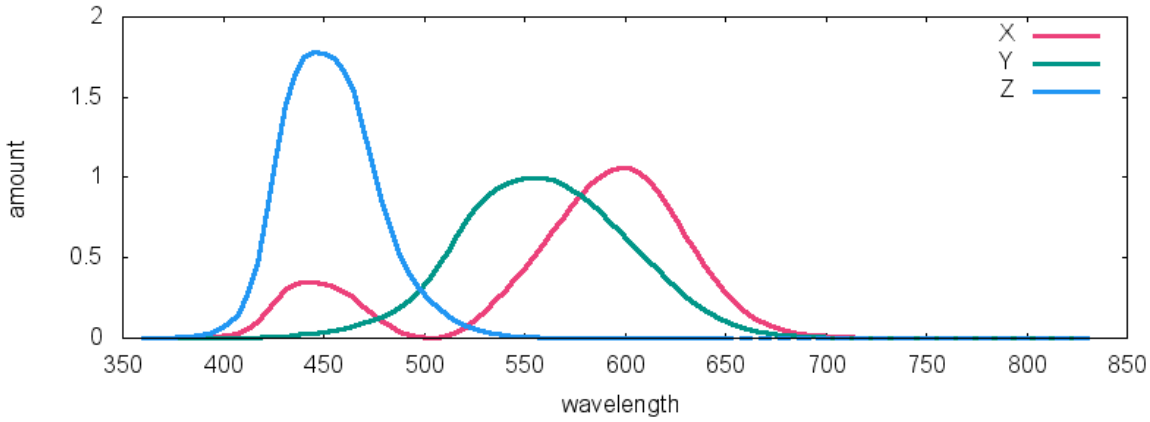

Figure 0-2. Linear transformation used to convert RGB colour matching functions into x, y and z bar curves for removing negative values [327].

Thus, y coefficients for r, g and b are the factors needed to scale the primaries lights to be equally bright. In this way, the tristimulus values R, G, and B are calculated:

$$R = \frac{r}{1.0000} \tag{0-4}$$

$$G = \frac{g}{4.5906} \tag{0-5}$$

$$B = \frac{b}{0.0601} \tag{0-6}$$

As mention before, avoiding negative values, it is possible to compute the tristimulus values from the CIE XYZ functions, for a light source with a spectral distribution E(λ):

$$X = \int_{380}^{740} x(\lambda)E(\lambda)d\lambda \tag{0-7}$$

$$Y = \int_{380}^{740} y(\lambda)E(\lambda)d\lambda \tag{0-8}$$

$$Z = \int_{380}^{740} z(\lambda)E(\lambda)d\lambda \tag{0-9}$$

Finally, with XYZ tristimulus values it is possible to assign the Chromaticity Coordinates, renamed as x and y, to a light source:

$$x = \frac{X}{X+Y+Z} \tag{0-10}$$

$$y = \frac{Y}{X+Y+Z} \tag{0-11}$$

With the chromaticity coordinates, it is possible to locate a light source on the CIE

1931 chromaticity diagram shown in Figure 0-3.

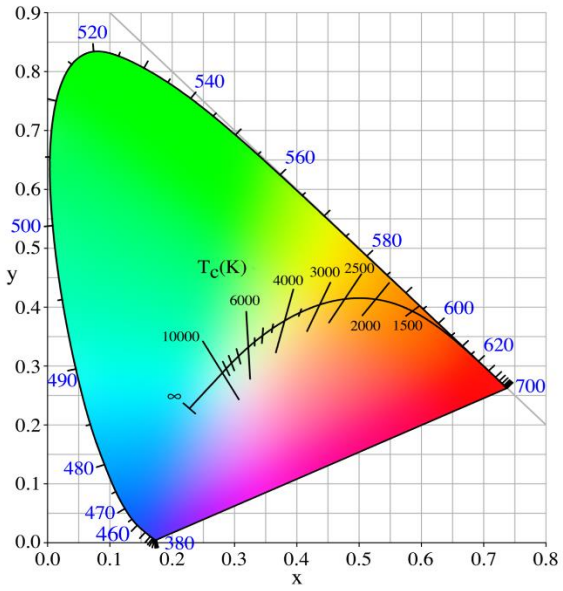

Figure 0-3. CIE 1931 chromaticity diagram [41].

The black line is called the Planckian locus, and it corresponds to the colour radiation of an incandescent perfect black body at different temperatures.

CCT

For white light characterization, two relevant quantities were introduced. The correlated colour temperature (CCT) of a light source is the temperature correlated to an ideal black-body radiator. Light sources can be cool (high temperature) or warm, which is illustrated in Figure 0-4

The CCT of a light source can be determined by extending an iso-temperature line from the blackbody locus out to the chromaticity coordinates of the source. It is also possible to calculate analytically by using McCamy's approximation algorithm the CCT from the xy chromaticity's:

$$CCT = -449n^3 + 3525n^2 - 6823n + 5520.33 \qquad (0\text{-}12)$$

Where

$$n = \frac{x - x_e}{y - y_e} \qquad (0\text{-}13)$$

being x_e and y_e the coordinates of the epicenter, x_e=0.332 and y_e=0.186.

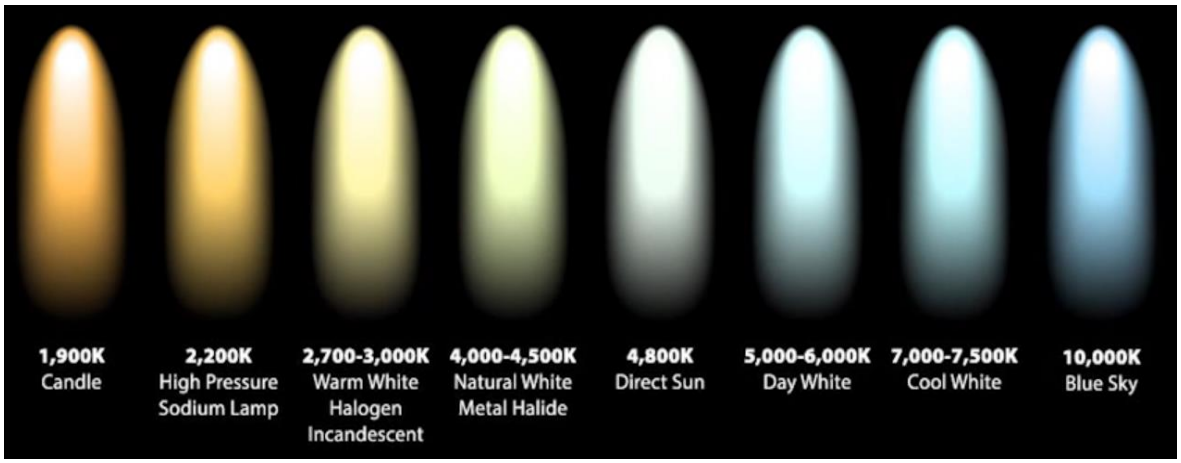

Figure 0-4. Example of light sources with different values of CCT [328].

CRI

Another relevant and quantitative value for characterization of a white light source is the colour rendering index (CRI) defined as the ability of a light source to reveal the colours of various objects faithfully. CRI values go from 1 to 100 (incandescent black body emission, Planckian locus).

The calculation of the CRI is based on comparison with CIE original test colour samples, it implies the computation of a specific CRI for each test colour sample, and then the average CRI is calculated based on the spectral power distribution (SPD) [327], [329]–[331].

As a quick estimation and comparison between different light sources, the maximum CRIs are on Planckian locus, and going further, the CRI becomes lower. The quality of light depending on its CRI is described in Figure 0-5. Schema of different values of CRI [332] .

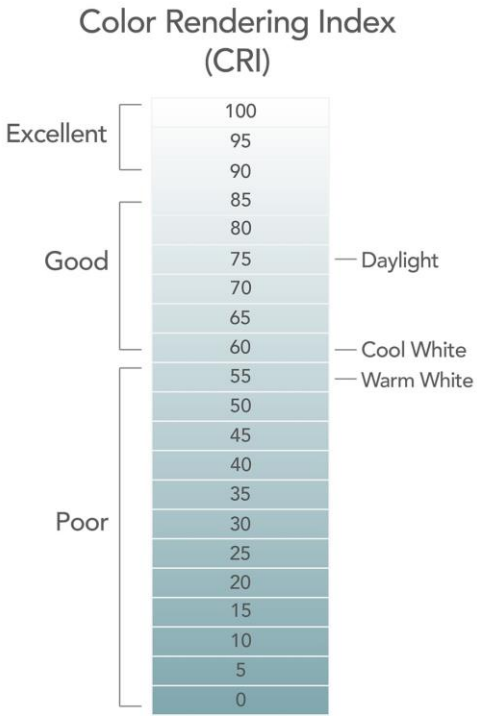

Figure 0-5. Schema of different values of CRI [332] .

REFERENCES

[1] H. J. Round, "A note on carborundum," *Electrical World*, vol. 49, p. 309, 1907.

[2] E. F. Schubert, *Light-Emitting Diodes*. Cambridge University Press, 2003.

[3] O. Vladimirovich Losev, "Luminous carborundum detector and detection with crystals," *Telegrafi ya i Telefoniya bez Provodov*, vol. 44, pp. 485–494, 1927.

[4] G. A. Wolff, R. A. Hebert, and J. D. Broder, "Electroluminescence of GaP," *Phys. Rev.*, vol. 100, no. 4, pp. 1144–1145, Nov. 1955, doi: 10.1103/PhysRev.100.1144.

[5] E. F. Schubert, *Light-Emitting Diodes*, 2nd ed. Cambridge: Cambridge University Press, 2006. doi: 10.1017/CBO9780511790546.

[6] O. G. Folberth, "Notizen: Mischkristallbildung bei AIII Bv-Verbindungen," *Zeitschrift für Naturforschung A*, vol. 10, no. 6, pp. 502–503, Jun. 1955, doi: 10.1515/zna-1955-0613.

[7] R. N. Hall, G. E. Fenner, J. D. Kingsley, T. J. Soltys, and R. O. Carlson, "Coherent Light Emission From GaAs Junctions," *Phys. Rev. Lett.*, vol. 9, no. 9, pp. 366–368, Nov. 1962, doi: 10.1103/PhysRevLett.9.366.

[8] N. Holonyak and S. F. Bevacqua, "COHERENT (VISIBLE) LIGHT EMISSION FROM Ga(As1−xPx) JUNCTIONS," *Appl. Phys. Lett.*, vol. 1, no. 4, pp. 82–83, Dec. 1962, doi: 10.1063/1.1753706.

[9] M. I. Nathan, W. P. Dumke, G. Burns, F. H. Dill, and G. Lasher, "STIMULATED EMISSION OF RADIATION FROM GaAs p-n JUNCTIONS," *Appl. Phys. Lett.*, vol. 1, no. 3, pp. 62–64, Nov. 1962, doi: 10.1063/1.1777371.

[10] T. M. Quist *et al.*, "SEMICONDUCTOR MASER OF GaAs," *Appl. Phys. Lett.*, vol. 1, no. 4, pp. 91–92, Dec. 1962, doi: 10.1063/1.1753710.

[11] F. A. Ponce and D. P. Bour, "Nitride-based semiconductors for blue and green light-emitting devices," *Nature*, vol. 386, no. 6623, Art. no. 6623, Mar. 1997, doi: 10.1038/386351a0.

[12] F. Fichter, "Über Aluminiumnitrid," *Zeitschrift für anorganische Chemie*, vol. 54, no. 1, pp. 322–327, 1907, doi: 10.1002/zaac.19070540128.

[13] W. C. Johnson, J. B. Parson, and M. C. Crew, "Nitrogen Compounds of Gallium. III," *The Journal of Physical Chemistry*, May 2002, doi: 10.1021/j150340a015.

[14] R. Juza and H. Hahn, "Über die Kristallstrukturen von Cu3N, GaN und InN Metallamide und Metallnitride," *Zeitschrift für anorganische und allgemeine Chemie*, vol. 239, no. 3, pp. 282–287, 1938, doi: 10.1002/zaac.19382390307.

[15] H. P. Maruska and J. J. Tietjen, "THE PREPARATION AND PROPERTIES OF VAPOR-DEPOSITED SINGLE-CRYSTAL-LINE GaN," *Appl. Phys. Lett.*, vol. 15, no. 10, pp. 327–329, Nov. 1969, doi: 10.1063/1.1652845.

[16] H. M. Manasevit, F. M. Erdmann, and W. I. Simpson, "The Use of Metalorganics in the Preparation of Semiconductor Materials: IV . The Nitrides of Aluminum and Gallium," *J. Electrochem. Soc.*, vol. 118, no. 11, p. 1864, Nov. 1971, doi: 10.1149/1.2407853.

[17] "Akasaki: Research on blue emitting devices - Google Académico." https://scholar.google.com/scholar_lookup?title=Research%20on%20blue%20emitting%20devices&journal=Ind.%20Sci.%20Technol.&volume=17&pages=48-52&publication_year=1976&author=Akasaki%2CI&author=Hayashi%2CI (accessed Jun. 21, 2021).

[18] R. Dingle, D. D. Sell, S. E. Stokowski, and M. Ilegems, "Absorption, Reflectance, and Luminescence of GaN Epitaxial Layers," *Phys. Rev. B*, vol. 4, no. 4, pp. 1211–1218, Aug. 1971, doi: 10.1103/PhysRevB.4.1211.

[19] S. Yoshida, S. Misawa, and S. Gonda, "Improvements on the electrical and luminescent properties of reactive molecular beam epitaxially grown GaN films by using AlN-coated sapphire substrates," *Appl. Phys. Lett.*, vol. 42, no. 5, pp. 427–429, Mar. 1983, doi: 10.1063/1.93952.

[20] H. Amano, N. Sawaki, I. Akasaki, and Y. Toyoda, "Metalorganic vapor phase epitaxial growth of a high quality GaN film using an AlN buffer layer," *Appl. Phys. Lett.*, vol. 48, no. 5, pp. 353–355, Feb. 1986, doi: 10.1063/1.96549.

[21] H. Amano, M. Kito, K. Hiramatsu, and I. Akasaki, "P-Type Conduction in Mg-Doped GaN Treated with Low-Energy Electron Beam Irradiation (LEEBI)," *Jpn. J. Appl. Phys.*, vol. 28, no. 12A, p. L2112, Dec. 1989, doi: 10.1143/JJAP.28.L2112.

[22] S. Nakamura, T. Mukai, and M. Senoh, "Candela-class high-brightness InGaN/AlGaN double-heterostructure blue-light-emitting diodes," *Appl. Phys. Lett.*, vol. 64, no. 13, pp. 1687–1689, Mar. 1994, doi: 10.1063/1.111832.

[23] "The Nobel Prize in Physics 2014," *NobelPrize.org*. https://www.nobelprize.org/prizes/physics/2014/press-release/ (accessed Dec. 04, 2021).

[24] S. Arafin, X. Liu, and Z. Mi, "Review of recent progress of III-nitride nanowire lasers," *J. Nanophoton*, vol. 7, no. 1, p. 074599, Sep. 2013, doi: 10.1117/1.JNP.7.074599.

[25] S. Albert, "Self assembled and ordered group III nitride nanocolumnar structures for light emitting applications," 2015.

[26] D. Zhu and C. J. Humphreys, "Solid-State Lighting Based on Light Emitting Diode Technology," in *Optics in Our Time*, M. D. Al-Amri, M. El-Gomati, and M. S. Zubairy, Eds. Cham: Springer International Publishing, 2016, pp. 87–118. doi: 10.1007/978-3-319-31903-2_5.

[27] I. Vurgaftman and J. R. Meyer, "Band parameters for nitrogen-containing semiconductors," *Journal of Applied Physics*, vol. 94, no. 6, pp. 3675–3696, Sep. 2003, doi: 10.1063/1.1600519.

[28] K. Harafuji, T. Tsuchiya, and K. Kawamura, "Molecular dynamics simulation for evaluating melting point of wurtzite-type GaN crystal," *Journal of Applied Physics*, vol. 96, no. 5, pp. 2501–2512, Sep. 2004, doi: 10.1063/1.1772878.

[29] C.-Y. Yeh, Z. W. Lu, S. Froyen, and A. Zunger, "Zinc-blende--wurtzite polytypism in semiconductors," *Phys. Rev. B*, vol. 46, no. 16, pp. 10086–10097, Oct. 1992, doi: 10.1103/PhysRevB.46.10086.

[30] S. Albert, "Self assembled and ordered group III nitride nanocolumnar structures for light emitting applications," http://purl.org/dc/dcmitype/Text, Universidad Politécnica de Madrid, 2015. Accessed: Jun. 23, 2021. [Online]. Available: https://dialnet.unirioja.es/servlet/tesis?codigo=118149

[31] A. Urban, "Position-controlled selective area growth of Ga-polar GaN nanocolumns by molecular beam epitaxy," *A versatile approach towards semipolar GaN and the characterization of single nanocolumns*, Dec. 2013, Accessed: Sep. 21, 2021. [Online]. Available: https://ediss.uni-goettingen.de/handle/11858/00-1735-0000-0022-609E-3

[32] B. Gil, *Low-dimensional Nitride Semiconductors*. Oxford University Press, 2002.

[33] L. Vegard, "Die Konstitution der Mischkristalle und die Raumfüllung der Atome," *Z. Physik*, vol. 5, no. 1, pp. 17–26, Jan. 1921, doi: 10.1007/BF01349680.

[34] A. E. Romanov *et al.*, "Basal plane misfit dislocations and stress relaxation in III-nitride semipolar heteroepitaxy," *Journal of Applied Physics*, vol. 109, no. 10, p. 103522, May 2011, doi: 10.1063/1.3590141.

[35] F. Bernardini, V. Fiorentini, and D. Vanderbilt, "Spontaneous polarization and piezoelectric constants of III-V nitrides," *Phys. Rev. B*, vol. 56, no. 16, pp. R10024–R10027, Oct. 1997, doi: 10.1103/PhysRevB.56.R10024.

[36] N. Guan, "Nitride nanowire light-emitting diode," phdthesis, Université Paris Saclay (COmUE), 2018. Accessed: Jul. 29, 2021. [Online]. Available: https://tel.archives-ouvertes.fr/tel-01915009

[37] M. Leroux *et al.*, "Quantum confined Stark effect due to built-in internal polarization fields in (Al,Ga)N/GaN quantum wells," *Phys. Rev. B*, vol. 58, no. 20, pp. R13371–R13374, Nov. 1998, doi: 10.1103/PhysRevB.58.R13371.

[38] J.-H. Ryou *et al.*, "Control of quantum-confined Stark effect in InGaN/GaN multiple quantum well active region by p-type layer for III-nitride-based visible light emitting diodes," *Appl. Phys. Lett.*, vol. 92, no. 10, p. 101113, Mar. 2008, doi: 10.1063/1.2894514.

[39] P. Iskander, "Chemical sensors based on GaN heterostructures," 2017.

[40] Y. P. Varshni, "Temperature dependence of the energy gap in semiconductors," *Physica*, vol. 34, no. 1, pp. 149–154, Jan. 1967, doi: 10.1016/0031-8914(67)90062-6.

[41] P. M. Corfdir, “Physics of the Ultrafast Dynamics of Excitons in GaN Nanostructures PAR,” 2011.
[42] R. Pässler, “Dispersion-related assessments of temperature dependences for the fundamental band gap of hexagonal GaN,” *Journal of Applied Physics*, vol. 90, no. 8, pp. 3956–3964, Oct. 2001, doi: 10.1063/1.1402147.
[43] Y.-H. Cho *et al.*, “‘S-shaped’ temperature-dependent emission shift and carrier dynamics in InGaN/GaN multiple quantum wells,” *Appl. Phys. Lett.*, vol. 73, no. 10, pp. 1370–1372, Sep. 1998, doi: 10.1063/1.122164.
[44] X. A. Cao, S. F. LeBoeuf, L. B. Rowland, C. H. Yan, and H. Liu, “Temperature-dependent emission intensity and energy shift in InGaN/GaN multiple-quantum-well light-emitting diodes,” *Appl. Phys. Lett.*, vol. 82, no. 21, pp. 3614–3616, May 2003, doi: 10.1063/1.1578539.
[45] Y. Li *et al.*, “Visualizing carrier transitions between localization states in a InGaN yellow–green light-emitting-diode structure,” *Journal of Applied Physics*, vol. 126, no. 9, p. 095705, Sep. 2019, doi: 10.1063/1.5100989.
[46] S. M. Reimann and M. Manninen, “Electronic structure of quantum dots,” *Rev. Mod. Phys.*, vol. 74, no. 4, pp. 1283–1342, Nov. 2002, doi: 10.1103/RevModPhys.74.1283.
[47] C. Pfüller, “Optical properties of single semiconductor nanowires and nanowire ensembles,” Jul. 2011, doi: 10.18452/16360.
[48] S. L. Chuang and C. S. Chang, “k–p method for strained wurtzite semiconductors”.
[49] S. L. Chuang and C. S. Chang, “k p method for strained wurtzite semiconductors,” *Phys. Rev. B*, vol. 54, no. 4, pp. 2491–2504, Jul. 1996, doi: 10.1103/PhysRevB.54.2491.
[50] M. Suzuki, T. Uenoyama, and A. Yanase, “First-principles calculations of effective-mass parameters of AlN and GaN,” *Phys. Rev. B*, vol. 52, no. 11, pp. 8132–8139, Sep. 1995, doi: 10.1103/PhysRevB.52.8132.
[51] K. Kornitzer *et al.*, “Photoluminescence and reflectance spectroscopy of excitonic transitions in high-quality homoepitaxial GaN films,” 1999.
[52] H. Selke, V. Kirchner, H. Heinke, S. Einfeldt, P. L. Ryder, and D. Hommel, “Polytypism in epitaxially grown gallium nitride,” *Journal of Crystal Growth*, vol. 208, no. 1, pp. 57–64, Jan. 2000, doi: 10.1016/S0022-0248(99)00462-5.
[53] N. Vainorius, S. Lehmann, D. Jacobsson, L. Samuelson, K. A. Dick, and M.-E. Pistol, “Confinement in Thickness-Controlled GaAs Polytype Nanodots,” *Nano Lett.*, vol. 15, no. 4, pp. 2652–2656, Apr. 2015, doi: 10.1021/acs.nanolett.5b00253.
[54] L. Liu and J. H. Edgar, “Substrates for gallium nitride epitaxy,” *Materials Science and Engineering: R: Reports*, vol. 37, no. 3, pp. 61–127, Apr. 2002, doi: 10.1016/S0927-796X(02)00008-6.
[55] C. Wetzel *et al.*, “GaN epitaxial layers grown on 6H-SiC by the sublimation sandwich technique,” *Appl. Phys. Lett.*, vol. 65, no. 8, pp. 1033–1035, Aug. 1994, doi: 10.1063/1.112143.
[56] J. A. Powell *et al.*, “Controlled growth of 3C-SiC and 6H-SiC films on low-tilt-angle vicinal (0001) 6H-SiC wafers,” *Appl. Phys. Lett.*, vol. 59, no. 3, pp. 333–335, Jul. 1991, doi: 10.1063/1.105587.
[57] R. C. Powell, N. -E. Lee, Y. -W. Kim, and J. E. Greene, “Heteroepitaxial wurtzite and zinc-blende structure GaN grown by reactive-ion molecular-beam epitaxy: Growth kinetics, microstructure, and properties,” *Journal of Applied Physics*, vol. 73, no. 1, pp. 189–204, Jan. 1993, doi: 10.1063/1.353882.
[58] X. Gu *et al.*, “GaN epitaxy on thermally treated c-plane bulk ZnO substrates with O and Zn faces,” *Appl. Phys. Lett.*, vol. 84, no. 13, pp. 2268–2270, Mar. 2004, doi: 10.1063/1.1690469.
[59] H. Okumura, S. Misawa, and S. Yoshida, “Epitaxial growth of cubic and hexagonal GaN on GaAs by gas-source molecular-beam epitaxy,” *Appl. Phys. Lett.*, vol. 59, no. 9, pp. 1058–1060, Aug. 1991, doi: 10.1063/1.106344.
[60] D. A. Neumayer and J. G. Ekerdt, “Growth of Group III Nitrides. A Review of Precursors and Techniques,” *Chem. Mater.*, vol. 8, no. 1, pp. 9–25, Jan. 1996, doi: 10.1021/cm950108r.

[61] R. R. Reeber and K. Wang, “Lattice Parameters and Thermal Expansion of Important Semiconductors and Their Substrates,” *MRS Online Proceedings Library (OPL)*, vol. 622, ed 2000, doi: 10.1557/PROC-622-T6.35.1.

[62] “Semiconductor Devices: Physics and Technology, 3rd Edition | Wiley,” *Wiley.com*. https://www.wiley.com/en-us/Semiconductor+Devices%3A+Physics+and+Technology%2C+3rd+Edition-p-9780470537947 (accessed Sep. 25, 2021).

[63] H. Sugawara, M. Ishikawa, and G. Hatakoshi, “High-efficiency InGaAlP/GaAs visible light-emitting diodes,” *Appl. Phys. Lett.*, vol. 58, no. 10, pp. 1010–1012, Mar. 1991, doi: 10.1063/1.104407.

[64] C. P. Kuo, R. M. Fletcher, T. D. Osentowski, M. C. Lardizabal, M. G. Craford, and V. M. Robbins, “High performance AlGaInP visible light-emitting diodes,” *Appl. Phys. Lett.*, vol. 57, no. 27, pp. 2937–2939, Dec. 1990, doi: 10.1063/1.103736.

[65] R. M. Fletcher, C. P. Kuo, T. D. Osentowski, K. H. Huang, M. G. Craford, and V. M. Robbins, “The growth and properties of high performance AlGaInP emitters using a lattice mismatched GaP window layer,” *Journal of Elec Materi*, vol. 20, no. 12, pp. 1125–1130, Dec. 1991, doi: 10.1007/BF03030219.

[66] R. D. Dupuis and M. R. Krames, “History, Development, and Applications of High-Brightness Visible Light-Emitting Diodes,” *J. Lightwave Technol., JLT*, vol. 26, no. 9, pp. 1154–1171, May 2008.

[67] A. Berg *et al.*, “Radial Nanowire Light-Emitting Diodes in the (AlxGa1–x)yIn1–yP Material System,” *Nano Lett.*, vol. 16, no. 1, pp. 656–662, Jan. 2016, doi: 10.1021/acs.nanolett.5b04401.

[68] I. E. Titkov, S. Y. Karpov, A. Yadav, D. Mamedov, V. L. Zerova, and E. Rafailov, “Efficiency of True-Green Light Emitting Diodes: Non-Uniformity and Temperature Effects,” *Materials*, vol. 10, no. 11, Art. no. 11, Nov. 2017, doi: 10.3390/ma10111323.

[69] S. Dutta Gupta and B. Jatothu, “Fundamentals and applications of light-emitting diodes (LEDs) in in vitro plant growth and morphogenesis,” *Plant Biotechnology Reports*, vol. 7, Jul. 2013, doi: 10.1007/s11816-013-0277-0.

[70] C. R. Ronda, *Luminescence: From Theory to Applications*. John Wiley & Sons, 2007.

[71] H. Hirayama, Y. Tsukada, T. Maeda, and N. Kamata, “Marked Enhancement in the Efficiency of Deep-Ultraviolet AlGaN Light-Emitting Diodes by Using a Multiquantum-Barrier Electron Blocking Layer,” *Appl. Phys. Express*, vol. 3, no. 3, p. 031002, Feb. 2010, doi: 10.1143/APEX.3.031002.

[72] X. Zhao *et al.*, “Influence of an InGaN superlattice pre-layer on the performance of semipolar (11–22) green LEDs grown on silicon,” *Sci Rep*, vol. 10, no. 1, p. 12650, Jul. 2020, doi: 10.1038/s41598-020-69609-4.

[73] D. Schiavon, M. Binder, M. Peter, B. Galler, P. Drechsel, and F. Scholz, “Wavelength-dependent determination of the recombination rate coefficients in single-quantum-well GaInN/GaN light emitting diodes,” *physica status solidi (b)*, vol. 250, no. 2, pp. 283–290, 2013, doi: 10.1002/pssb.201248286.

[74] S. Karpov, “ABC-model for interpretation of internal quantum efficiency and its droop in III-nitride LEDs,” in *Numerical Simulation of Optoelectronic Devices, 2014*, Sep. 2014, pp. 17–18. doi: 10.1109/NUSOD.2014.6935334.

[75] J. Peretti, C. Weisbuch, J. Iveland, M. Piccardo, L. Martinelli, and J. S. Speck, “Identification of Auger effect as the dominant mechanism for efficiency droop of LEDs,” in *Light-Emitting Diodes: Materials, Devices, and Applications for Solid State Lighting XVIII*, Feb. 2014, vol. 9003, pp. 82–95. doi: 10.1117/12.2038698.

[76] “Auger effect identified as main cause of efficiency droop in LEDs.” https://spie.org/news/5109-auger-effect-identified-as-main-cause-of-efficiency-droop-in-leds (accessed Sep. 27, 2021).

[77] M. Auf der Maur, A. Pecchia, G. Penazzi, W. Rodrigues, and A. Di Carlo, “Efficiency Drop in Green $\mathrm{InGaN}/\mathrm{GaN}$ Light Emitting Diodes: The Role of Random Alloy

Fluctuations," *Phys. Rev. Lett.*, vol. 116, no. 2, p. 027401, Jan. 2016, doi: 10.1103/PhysRevLett.116.027401.

[78] T. Dai *et al.*, "Light Extraction Improvement From GaN-Based Light-Emitting Diodes With Nano-Patterned Surface Using Anodic Aluminum Oxide Template," *IEEE Photonics Technology Letters*, vol. 20, no. 23, pp. 1974–1976, Dec. 2008, doi: 10.1109/LPT.2008.2005645.

[79] T. H. Ngo *et al.*, "Enhanced excitonic emission efficiency in porous GaN," *Sci Rep*, vol. 8, no. 1, p. 15767, Dec. 2018, doi: 10.1038/s41598-018-34185-1.

[80] T. Fujii, Y. Gao, R. Sharma, E. L. Hu, S. P. DenBaars, and S. Nakamura, "Increase in the extraction efficiency of GaN-based light-emitting diodes via surface roughening," *Appl. Phys. Lett.*, vol. 84, no. 6, pp. 855–857, Feb. 2004, doi: 10.1063/1.1645992.

[81] J. H. Son, J. U. Kim, Y. H. Song, B. J. Kim, C. J. Ryu, and J.-L. Lee, "Design Rule of Nanostructures in Light-Emitting Diodes for Complete Elimination of Total Internal Reflection," *Advanced Materials*, vol. 24, no. 17, pp. 2259–2262, 2012, doi: 10.1002/adma.201104648.

[82] K. Kim, J. Choi, T. S. Bae, M. Jung, and D. H. Woo, "Enhanced Light Extraction from Nanoporous Surfaces of InGaN/GaN-Based Light Emitting Diodes," *Jpn. J. Appl. Phys.*, vol. 46, no. 10R, p. 6682, Oct. 2007, doi: 10.1143/JJAP.46.6682.

[83] S. J. An, J. H. Chae, G.-C. Yi, and G. H. Park, "Enhanced light output of GaN-based light-emitting diodes with ZnO nanorod arrays," *Appl. Phys. Lett.*, vol. 92, no. 12, p. 121108, Mar. 2008, doi: 10.1063/1.2903153.

[84] K. J. Lee *et al.*, "Enhanced optical output power of InGaN/GaN light-emitting diodes grown on a silicon (111) substrate with a nanoporous GaN layer," *Opt. Express, OE*, vol. 24, no. 5, pp. 4391–4398, Mar. 2016, doi: 10.1364/OE.24.004391.

[85] A. David, "Surface-roughened light-emitting diodes: an accurate model," *JOURNAL OF DISPLAY TECHNOLOGY*, p. 17.

[86] B. Damilano, S. Vézian, J. Brault, B. Alloing, and J. Massies, "Selective Area Sublimation: A Simple Top-down Route for GaN-Based Nanowire Fabrication," *Nano Lett.*, vol. 16, no. 3, pp. 1863–1868, Mar. 2016, doi: 10.1021/acs.nanolett.5b04949.

[87] R. S. Wagner and W. C. Ellis, "Vapor-liquid-solid mechanism of single crystal growth," *Appl. Phys. Lett.*, vol. 4, no. 5, pp. 89–90, Mar. 1964, doi: 10.1063/1.1753975.

[88] L. Güniat, P. Caroff, and A. Fontcuberta i Morral, "Vapor Phase Growth of Semiconductor Nanowires: Key Developments and Open Questions," *Chem. Rev.*, vol. 119, no. 15, pp. 8958–8971, Aug. 2019, doi: 10.1021/acs.chemrev.8b00649.

[89] A. Trampert, J. Ristic, U. Jahn, E. Calleja, and K. H. Ploog, "TEM study of (Ga,Al)N nanocolumns and embedded GaN nanodiscs," in *Microscopy of Semiconducting Materials 2003*, CRC Press, 2003.

[90] L.-W. Jang *et al.*, "Enhanced light output of InGaN/GaN blue light emitting diodes with Ag nano-particles embedded in nano-needle layer," *Opt. Express, OE*, vol. 20, no. 6, pp. 6036–6041, Mar. 2012, doi: 10.1364/OE.20.006036.

[91] Q. Li *et al.*, "Optical performance of top-down fabricated InGaN/GaN nanorod light emitting diode arrays," *Opt. Express, OE*, vol. 19, no. 25, pp. 25528–25534, Dec. 2011, doi: 10.1364/OE.19.025528.

[92] M. A. Sanchez-Garcia *et al.*, "The effect of the III/V ratio and substrate temperature on the morphology and properties of GaN- and AlN-layers grown by molecular beam epitaxy on Si(1 1 1)," *Journal of Crystal Growth*, vol. 183, no. 1, pp. 23–30, Jan. 1998, doi: 10.1016/S0022-0248(97)00386-2.

[93] M. Yoshizawa, A. Kikuchi, M. Mori, N. F. N. Fujita, and K. K. K. Kishino, "Growth of Self-Organized GaN Nanostructures on Al2O3(0001) by RF-Radical Source Molecular Beam Epitaxy," *Jpn. J. Appl. Phys.*, vol. 36, no. 4B, p. L459, Apr. 1997, doi: 10.1143/JJAP.36.L459.

[94] S. Li and A. Waag, "GaN based nanorods for solid state lighting," *Journal of Applied Physics*, vol. 111, no. 7, p. 071101, Apr. 2012, doi: 10.1063/1.3694674.

[95] A. Waag *et al.*, "The nanorod approach: GaN NanoLEDs for solid state lighting," *physica status solidi c*, vol. 8, no. 7–8, pp. 2296–2301, 2011, doi: 10.1002/pssc.201000989.

[96] Y.-H. Hsiao, M.-L. Tsai, and J.-H. He, “GaN-Based Multiple-Quantum-Well Light-Emitting Diodes Employing Nanotechnology for Photon Management,” *IEEE Transactions on Industry Applications*, vol. 51, no. 2, pp. 1277–1283, Mar. 2015, doi: 10.1109/TIA.2014.2360984.

[97] M. Djavid and Z. Mi, “Enhancing the light extraction efficiency of AlGaN deep ultraviolet light emitting diodes by using nanowire structures,” *Appl. Phys. Lett.*, vol. 108, no. 5, p. 051102, Feb. 2016, doi: 10.1063/1.4941239.

[98] T. Schimpke *et al.*, “Phosphor-converted white light from blue-emitting InGaN microrod LEDs,” *physica status solidi (a)*, vol. 213, no. 6, pp. 1577–1584, 2016, doi: 10.1002/pssa.201532904.

[99] H.-W. (林弘偉) Lin, Y.-J. (呂宥蓉) Lu, H.-Y. (陳虹穎) Chen, H.-M. (李弘貿) Lee, and S. (果尚志) Gwo, “InGaN/GaN nanorod array white light-emitting diode,” *Appl. Phys. Lett.*, vol. 97, no. 7, p. 073101, Aug. 2010, doi: 10.1063/1.3478515.

[100] B. Monemar, B. J. Ohlsson, N. F. Gardner, and L. Samuelson, “Chapter Seven - Nanowire-Based Visible Light Emitters, Present Status and Outlook,” vol. 94, Elsevier, 2016, pp. 227–271. Accessed: Oct. 04, 2021. [Online]. Available: http://urn.kb.se/resolve?urn=urn:nbn:se:liu:diva-123959

[101] H. Sekiguchi, K. Kishino, and A. Kikuchi, “Emission color control from blue to red with nanocolumn diameter of InGaN/GaN nanocolumn arrays grown on same substrate,” *Appl. Phys. Lett.*, vol. 96, no. 23, p. 231104, Jun. 2010, doi: 10.1063/1.3443734.

[102] K. Kishino, A. Yanagihara, K. Ikeda, and K. Yamano, “Monolithic integration of four-colour InGaN-based nanocolumn LEDs,” *Electronics Letters*, vol. 51, no. 11, pp. 852–854, 2015, doi: 10.1049/el.2015.0770.

[103] M. D. Brubaker *et al.*, “On-Chip Optical Interconnects Made with Gallium Nitride Nanowires,” *Nano Lett.*, vol. 13, no. 2, pp. 374–377, Feb. 2013, doi: 10.1021/nl303510h.

[104] M. Tchernycheva *et al.*, “Integrated Photonic Platform Based on InGaN/GaN Nanowire Emitters and Detectors,” *Nano Lett.*, vol. 14, no. 6, pp. 3515–3520, Jun. 2014, doi: 10.1021/nl501124s.

[105] D. Massoubre *et al.*, “Micro-structured light emission from planar InGaN light-emitting diodes,” *Semicond. Sci. Technol.*, vol. 29, no. 1, p. 015005, Dec. 2013, doi: 10.1088/0268-1242/29/1/015005.

[106] J. Herrnsdorf *et al.*, “Active-Matrix GaN Micro Light-Emitting Diode Display With Unprecedented Brightness,” *IEEE Transactions on Electron Devices*, vol. 62, no. 6, pp. 1918–1925, Jun. 2015, doi: 10.1109/TED.2015.2416915.

[107] X. Dai *et al.*, “Flexible Light-Emitting Diodes Based on Vertical Nitride Nanowires,” *Nano Lett.*, vol. 15, no. 10, pp. 6958–6964, Oct. 2015, doi: 10.1021/acs.nanolett.5b02900.

[108] N. Guan, X. Dai, A. V. Babichev, F. H. Julien, and M. Tchernycheva, “Flexible inorganic light emitting diodes based on semiconductor nanowires,” *Chem. Sci.*, vol. 8, no. 12, pp. 7904–7911, Nov. 2017, doi: 10.1039/C7SC02573D.

[109] N. Guan *et al.*, “Flexible White Light Emitting Diodes Based on Nitride Nanowires and Nanophosphors,” *ACS Photonics*, vol. 3, no. 4, pp. 597–603, Apr. 2016, doi: 10.1021/acsphotonics.5b00696.

[110] G. Jacopin *et al.*, “Single-Wire Light-Emitting Diodes Based on GaN Wires Containing Both Polar and Nonpolar InGaN/GaN Quantum Wells,” *Appl. Phys. Express*, vol. 5, no. 1, p. 014101, Dec. 2011, doi: 10.1143/APEX.5.014101.

[111] J.-R. Chang *et al.*, “Fabrication and luminescent properties of core-shell InGaN/GaN multiple quantum wells on GaN nanopillars,” *Appl. Phys. Lett.*, vol. 100, no. 26, p. 261103, Jun. 2012, doi: 10.1063/1.4731629.

[112] Y. J. Hong *et al.*, “Inorganic Optoelectronics: Visible-Color-Tunable Light-Emitting Diodes (Adv. Mater. 29/2011),” *Advanced Materials*, vol. 23, no. 29, pp. 3224–3224, 2011, doi: 10.1002/adma.201190109.

[113] M. Tchernycheva *et al.*, "InGaN/GaN Core–Shell Single Nanowire Light Emitting Diodes with Graphene-Based P-Contact," *Nano Lett.*, vol. 14, no. 5, pp. 2456–2465, May 2014, doi: 10.1021/nl5001295.

[114] Y.-H. Ra, R. Navamathavan, J.-H. Park, and C.-R. Lee, "High-Quality Uniaxial InxGa1–xN/GaN Multiple Quantum Well (MQW) Nanowires (NWs) on Si(111) Grown by Metal-Organic Chemical Vapor Deposition (MOCVD) and Light-Emitting Diode (LED) Fabrication," *ACS Appl. Mater. Interfaces*, vol. 5, no. 6, pp. 2111–2117, Mar. 2013, doi: 10.1021/am303056v.

[115] R. Koester *et al.*, "M-Plane Core–Shell InGaN/GaN Multiple-Quantum-Wells on GaN Wires for Electroluminescent Devices," *Nano Lett.*, vol. 11, no. 11, pp. 4839–4845, Nov. 2011, doi: 10.1021/nl202686n.

[116] X. J. Chen, G. Perillat-Merceroz, D. Sam-Giao, C. Durand, and J. Eymery, "Homoepitaxial growth of catalyst-free GaN wires on N-polar substrates," *Appl. Phys. Lett.*, vol. 97, no. 15, p. 151909, Oct. 2010, doi: 10.1063/1.3497078.

[117] C.-F. Lu *et al.*, "Phosphor-Free Monolithic White-Light LED," *IEEE Journal of Selected Topics in Quantum Electronics*, vol. 15, no. 4, pp. 1210–1217, Jul. 2009, doi: 10.1109/JSTQE.2009.2013184.

[118] T. Schimpke *et al.*, "The influence of MOVPE growth conditions on the shell of core-shell GaN microrod structures," *Journal of Crystal Growth*, vol. 465, pp. 34–42, May 2017, doi: 10.1016/j.jcrysgro.2017.02.035.

[119] H. Zhang *et al.*, "Color control of nanowire InGaN/GaN light emitting diodes by post-growth treatment," *Nanotechnology*, vol. 26, no. 46, p. 465203, Oct. 2015, doi: 10.1088/0957-4484/26/46/465203.

[120] M. Tchernycheva *et al.*, "Core–shell InGaN/GaN nanowire light emitting diodes analyzed by electron beam induced current microscopy and cathodoluminescence mapping," *Nanoscale*, vol. 7, no. 27, pp. 11692–11701, Jul. 2015, doi: 10.1039/C5NR00623F.

[121] N. Anttu, "Modifying the emission of light from a semiconductor nanowire array," *Journal of Applied Physics*, vol. 120, no. 4, p. 043108, Jul. 2016, doi: 10.1063/1.4960017.

[122] A. Kikuchi, M. Kawai, M. Tada, and K. Kishino, "InGaN/GaN Multiple Quantum Disk Nanocolumn Light-Emitting Diodes Grown on (111) Si Substrate," *Jpn. J. Appl. Phys.*, vol. 43, no. 12A, p. L1524, Nov. 2004, doi: 10.1143/JJAP.43.L1524.

[123] R. Vadivelu, Y. Igawa, and K. Kishino, "633 nm Red Emissions from InGaN Nanocolumn Light-Emitting Diode by Radio Frequency Plasma Assisted Molecular Beam Epitaxy," *Jpn. J. Appl. Phys.*, vol. 52, no. 8S, p. 08JE18, May 2013, doi: 10.7567/JJAP.52.08JE18.

[124] K. Kishino, J. Kamimura, and K. Kamiyama, "Near-Infrared InGaN Nanocolumn Light-Emitting Diodes Operated at 1.46 µm," *Appl. Phys. Express*, vol. 5, no. 3, p. 031001, Feb. 2012, doi: 10.1143/APEX.5.031001.

[125] K. Kishino, K. Nagashima, and K. Yamano, "Monolithic Integration of InGaN-Based Nanocolumn Light-Emitting Diodes with Different Emission Colors," *Appl. Phys. Express*, vol. 6, no. 1, p. 012101, Dec. 2012, doi: 10.7567/APEX.6.012101.

[126] M. Nami *et al.*, "Tailoring the morphology and luminescence of GaN/InGaN core-shell nanowires using bottom-up selective-area epitaxy," *Nanotechnology*, vol. 28, no. 2, p. 025202, Jan. 2017, doi: 10.1088/0957-4484/28/2/025202.

[127] N. Sakakibara, K. Narita, T. Oto, and K. Kishino, "Independent drive of integrated multicolor (RGBY) micro-LED array using regularly arrayed InGaN based nanocolumns," in *2017 22nd Microoptics Conference (MOC)*, Tokyo, Nov. 2017, pp. 108–109. doi: 10.23919/MOC.2017.8244514.

[128] K. Kishino, N. Sakakibara, K. Narita, and T. Oto, "Two-dimensional multicolor (RGBY) integrated nanocolumn micro-LEDs as a fundamental technology of micro-LED display," *Appl. Phys. Express*, vol. 13, no. 1, p. 014003, Dec. 2019, doi: 10.7567/1882-0786/ab5ad3.

[129] R. Wang, H. P. T. Nguyen, A. T. Connie, J. Lee, I. Shih, and Z. Mi, "Color-tunable, phosphor-free InGaN nanowire light-emitting diode arrays monolithically integrated on silicon," *Opt. Express, OE*, vol. 22, no. 107, pp. A1768–A1775, Dec. 2014, doi: 10.1364/OE.22.0A1768.

[130] H. P. T. Nguyen, S. Zhang, K. Cui, A. Korinek, G. A. Botton, and Z. Mi, "High-Efficiency InGaN/GaN Dot-in-a-Wire Red Light-Emitting Diodes," *IEEE Photonics Technology Letters*, vol. 24, no. 4, pp. 321–323, Feb. 2012, doi: 10.1109/LPT.2011.2178091.

[131] H. P. T. Nguyen *et al.*, "Engineering the Carrier Dynamics of InGaN Nanowire White Light-Emitting Diodes by Distributed p-AlGaN Electron Blocking Layers," *Sci Rep*, vol. 5, no. 1, p. 7744, Jan. 2015, doi: 10.1038/srep07744.

[132] C. Zhao *et al.*, "An enhanced surface passivation effect in InGaN/GaN disk-in-nanowire light emitting diodes for mitigating Shockley–Read–Hall recombination," *Nanoscale*, vol. 7, no. 40, pp. 16658–16665, Oct. 2015, doi: 10.1039/C5NR03448E.

[133] S. M. Sadaf, Y.-H. Ra, H. P. T. Nguyen, M. Djavid, and Z. Mi, "Alternating-Current InGaN/GaN Tunnel Junction Nanowire White-Light Emitting Diodes," *Nano Lett.*, vol. 15, no. 10, pp. 6696–6701, Oct. 2015, doi: 10.1021/acs.nanolett.5b02515.

[134] J. Simon *et al.*, "Polarization-Induced Zener Tunnel Junctions in Wide-Band-Gap Heterostructures," *Phys. Rev. Lett.*, vol. 103, no. 2, p. 026801, Jul. 2009, doi: 10.1103/PhysRevLett.103.026801.

[135] S. Krishnamoorthy, D. N. Nath, F. Akyol, P. S. Park, M. Esposto, and S. Rajan, "Polarization-engineered GaN/InGaN/GaN tunnel diodes," *Appl. Phys. Lett.*, vol. 97, no. 20, p. 203502, Nov. 2010, doi: 10.1063/1.3517481.

[136] C. Kuhn *et al.*, "MOVPE-grown AlGaN-based tunnel heterojunctions enabling fully transparent UVC LEDs," *Photon. Res., PRJ*, vol. 7, no. 5, pp. B7–B11, May 2019, doi: 10.1364/PRJ.7.0000B7.

[137] A. Yanagihara, S. Ishizawa, and K. Kishino, "Directional radiation beam from yellow-emitting InGaN-based nanocolumn LEDs with ordered bottom-up nanocolumn array," *Appl. Phys. Express*, vol. 7, no. 11, p. 112102, Nov. 2014, doi: 10.7567/APEX.7.112102.

[138] H. Hayashi *et al.*, "Thermally Engineered Flip-Chip InGaN/GaN Well-Ordered Nanocolumn Array LEDs," *IEEE Photonics Technology Letters*, vol. 27, no. 22, pp. 2343–2346, Nov. 2015, doi: 10.1109/LPT.2015.2463756.

[139] F. Limbach *et al.*, "Current path in light emitting diodes based on nanowire ensembles," *Nanotechnology*, vol. 23, no. 46, p. 465301, Nov. 2012, doi: 10.1088/0957-4484/23/46/465301.

[140] A.-L. Bavencove *et al.*, "Submicrometre resolved optical characterization of green nanowire-based light emitting diodes," *Nanotechnology*, vol. 22, no. 34, p. 345705, Jul. 2011, doi: 10.1088/0957-4484/22/34/345705.

[141] S. Jahangir, M. Mandl, M. Strassburg, and P. Bhattacharya, "Molecular beam epitaxial growth and optical properties of red-emitting (λ = 650 nm) InGaN/GaN disks-in-nanowires on silicon," *Appl. Phys. Lett.*, vol. 102, no. 7, p. 071101, Feb. 2013, doi: 10.1063/1.4793300.

[142] T. Andreev *et al.*, "Eu locations in Eu-doped InGaN⁄GaN quantum dots," *Appl. Phys. Lett.*, vol. 87, no. 2, p. 021906, Jul. 2005, doi: 10.1063/1.1992667.

[143] H. Sekiguchi *et al.*, "Stable-wavelength operation of europium-doped GaN nanocolumn light-emitting diodes grown by rf-plasma-assisted molecular beam epitaxy," *Electronics Letters*, vol. 53, no. 10, pp. 666–668, 2017, doi: 10.1049/el.2017.0447.

[144] G. Calabrese *et al.*, "Molecular beam epitaxy of single crystalline GaN nanowires on a flexible Ti foil," *Appl. Phys. Lett.*, vol. 108, no. 20, p. 202101, May 2016, doi: 10.1063/1.4950707.

[145] C. Zhao *et al.*, "Droop-Free, Reliable, and High-Power InGaN/GaN Nanowire Light-Emitting Diodes for Monolithic Metal-Optoelectronics," *Nano Lett.*, vol. 16, no. 7, pp. 4616–4623, Jul. 2016, doi: 10.1021/acs.nanolett.6b01945.

[146] C. Zhao *et al.*, "Facile Formation of High-Quality InGaN/GaN Quantum-Disks-in-Nanowires on Bulk-Metal Substrates for High-Power Light-Emitters," *Nano Lett.*, vol. 16, no. 2, pp. 1056–1063, Feb. 2016, doi: 10.1021/acs.nanolett.5b04190.

[147] K. Bando, K. Sakano, Y. Noguchi, and Y. Shimizu, "Development of High-bright and Pure-white LED Lamps," *Journal of Light & Visual Environment*, vol. 22, no. 1, p. 1_2-1_5, 1998, doi: 10.2150/jlve.22.1_2.

[148] Y. Hu, W. Zhuang, H. Ye, D. Wang, S. Zhang, and X. Huang, "A novel red phosphor for white light emitting diodes," *Journal of Alloys and Compounds*, vol. 390, no. 1, pp. 226–229, Mar. 2005, doi: 10.1016/j.jallcom.2004.07.063.

[149] D. Yang, L. Wang, W.-B. Lv, Z.-B. Hao, and Y. Luo, "Growth and characterization of phosphor-free white light-emitting diodes based on InGaN blue quantum wells and green–yellow quantum dots," *Superlattices and Microstructures*, vol. 82, pp. 26–32, Jun. 2015, doi: 10.1016/j.spmi.2015.02.005.

[150] B. Damilano, N. Grandjean, C. Pernot, and J. Massies, "Monolithic White Light Emitting Diodes Based on InGaN/GaN Multiple-Quantum Wells," *Jpn. J. Appl. Phys.*, vol. 40, no. 9A, p. L918, Sep. 2001, doi: 10.1143/JJAP.40.L918.

[151] M. Yamada, Y. Narukawa, and T. Mukai, "Phosphor Free High-Luminous-Efficiency White Light-Emitting Diodes Composed of InGaN Multi-Quantum Well," *Jpn. J. Appl. Phys.*, vol. 41, no. 3A, p. L246, Mar. 2002, doi: 10.1143/JJAP.41.L246.

[152] D. Schiavon, M. Binder, A. Loeffler, and M. Peter, "Optically pumped GaInN/GaN multiple quantum wells for the realization of efficient green light-emitting devices," *Appl. Phys. Lett.*, vol. 102, no. 11, p. 113509, Mar. 2013, doi: 10.1063/1.4796117.

[153] W. Guo, A. Banerjee, P. Bhattacharya, and B. S. Ooi, "InGaN/GaN disk-in-nanowire white light emitting diodes on (001) silicon," *Appl. Phys. Lett.*, vol. 98, no. 19, p. 193102, May 2011, doi: 10.1063/1.3588201.

[154] R. Armitage and K. Tsubaki, "Multicolour luminescence from InGaN quantum wells grown over GaN nanowire arrays by molecular-beam epitaxy," *Nanotechnology*, vol. 21, no. 19, p. 195202, May 2010, doi: 10.1088/0957-4484/21/19/195202.

[155] H. P. T. Nguyen *et al.*, "Breaking the carrier injection bottleneck of phosphor-free nanowire white light-emitting diodes," *Nano Lett*, vol. 13, no. 11, pp. 5437–5442, 2013, doi: 10.1021/nl4030165.

[156] H. P. T. Nguyen *et al.*, "p-Type modulation doped InGaN/GaN dot-in-a-wire white-light-emitting diodes monolithically grown on Si(111)," *Nano Lett*, vol. 11, no. 5, pp. 1919–1924, May 2011, doi: 10.1021/nl104536x.

[157] M. R. Philip *et al.*, "Controlling color emission of InGaN/AlGaN nanowire light-emitting diodes grown by molecular beam epitaxy," *Journal of Vacuum Science & Technology B*, vol. 35, no. 2, p. 02B108, Mar. 2017, doi: 10.1116/1.4977174.

[158] N. Guan, "Nitride nanowire light-emitting diode," These de doctorat, Université Paris-Saclay (ComUE), 2018. Accessed: Jul. 29, 2021. [Online]. Available: http://www.theses.fr/2018SACLS372

[159] T. Kim *et al.*, "Injectable, Cellular-Scale Optoelectronics with Applications for Wireless Optogenetics," *Science*, vol. 340, no. 6129, pp. 211–216, Apr. 2013, doi: 10.1126/science.1232437.

[160] A. Sugimoto, H. Ochi, S. Fujimura, A. Yoshida, T. Miyadera, and M. Tsuchida, "Flexible OLED displays using plastic substrates," *IEEE Journal of Selected Topics in Quantum Electronics*, vol. 10, no. 1, pp. 107–114, Jan. 2004, doi: 10.1109/JSTQE.2004.824112.

[161] D. Y. Kondakov, W. C. Lenhart, and W. F. Nichols, "Operational degradation of organic light-emitting diodes: Mechanism and identification of chemical products," *Journal of Applied Physics*, vol. 101, no. 2, p. 024512, Jan. 2007, doi: 10.1063/1.2430922.

[162] N. Thejokalyani and S. J. Dhoble, "Novel approaches for energy efficient solid state lighting by RGB organic light emitting diodes – A review," *Renewable and Sustainable Energy Reviews*, vol. 32, no. C, pp. 448–467, 2014.

[163] "Organic Light-Emitting Materials and Devices," *Routledge & CRC Press*. https://www.routledge.com/Organic-Light-Emitting-Materials-and-Devices/Li/p/book/9781138749696 (accessed Jul. 29, 2021).

[164] Y. Zhang, J. Lee, and S. R. Forrest, "Tenfold increase in the lifetime of blue phosphorescent organic light-emitting diodes," *Nat Commun*, vol. 5, no. 1, p. 5008, Sep. 2014, doi: 10.1038/ncomms6008.

[165] A. Fallahi, F. A. Taromi, A. Mohebbi, J. D. Yuen, and M. Shahinpoor, “A novel ambipolar polymer: from organic thin-film transistors to enhanced air-stable blue light emitting diodes,” *J. Mater. Chem. C*, vol. 2, no. 32, pp. 6491–6501, Jul. 2014, doi: 10.1039/C4TC00684D.

[166] H. X. Jiang and J. Y. Lin, “Nitride micro-LEDs and beyond - a decade progress review,” *Opt. Express, OE*, vol. 21, no. 103, pp. A475–A484, May 2013, doi: 10.1364/OE.21.00A475.

[167] Y. Narukawa, M. Ichikawa, D. Sanga, M. Sano, and T. Mukai, “White light emitting diodes with super-high luminous efficacy,” *J. Phys. D: Appl. Phys.*, vol. 43, no. 35, p. 354002, Aug. 2010, doi: 10.1088/0022-3727/43/35/354002.

[168] J. Yoon, S.-M. Lee, D. Kang, M. A. Meitl, C. A. Bower, and J. A. Rogers, “Heterogeneously Integrated Optoelectronic Devices Enabled by Micro-Transfer Printing,” *Advanced Optical Materials*, vol. 3, no. 10, pp. 1313–1335, 2015, doi: 10.1002/adom.201500365.

[169] C. Goßler *et al.*, “GaN-based micro-LED arrays on flexible substrates for optical cochlear implants,” *J. Phys. D: Appl. Phys.*, vol. 47, no. 20, p. 205401, Apr. 2014, doi: 10.1088/0022-3727/47/20/205401.

[170] J.-H. Seo *et al.*, “A Simplified Method of Making Flexible Blue LEDs on a Plastic Substrate,” *IEEE Photonics Journal*, vol. 7, no. 2, pp. 1–7, Apr. 2015, doi: 10.1109/JPHOT.2015.2412459.

[171] L. Wang, J. Ma, Z. Liu, X. Yi, H. Zhu, and G. Wang, “In Situ Fabrication of Bendable Microscale Hexagonal Pyramids Array Vertical Light Emitting Diodes with Graphene as Stretchable Electrical Interconnects,” *ACS Photonics*, vol. 1, no. 5, pp. 421–429, May 2014, doi: 10.1021/ph500133w.

[172] S. H. Lee, S. Y. Park, and K. J. Lee, “Laser lift-off of GaN thin film and its application to the flexible light emitting diodes,” in *Biosensing and Nanomedicine V*, Oct. 2012, vol. 8460, pp. 150–155. doi: 10.1117/12.964095.

[173] N. Yulianto *et al.*, “Ultrashort Pulse Laser Lift-Off Processing of InGaN/GaN Light-Emitting Diode Chips,” *ACS Appl. Electron. Mater.*, vol. 3, no. 2, pp. 778–788, Feb. 2021, doi: 10.1021/acsaelm.0c00913.

[174] P. Tian *et al.*, “Fabrication, characterization and applications of flexible vertical InGaN micro-light emitting diode arrays,” *Opt. Express, OE*, vol. 24, no. 1, pp. 699–707, Jan. 2016, doi: 10.1364/OE.24.000699.

[175] C.-W. Cheng, K.-T. Shiu, N. Li, S.-J. Han, L. Shi, and D. K. Sadana, “Epitaxial lift-off process for gallium arsenide substrate reuse and flexible electronics,” *Nat Commun*, vol. 4, no. 1, p. 1577, Mar. 2013, doi: 10.1038/ncomms2583.

[176] C. K. Jeong *et al.*, “Self-powered fully-flexible light-emitting system enabled by flexible energy harvester,” *Energy Environ. Sci.*, vol. 7, no. 12, pp. 4035–4043, Nov. 2014, doi: 10.1039/C4EE02435D.

[177] K. Chung, C.-H. Lee, and G.-C. Yi, “Transferable GaN Layers Grown on ZnO-Coated Graphene Layers for Optoelectronic Devices,” *Science*, vol. 330, no. 6004, pp. 655–657, Oct. 2010, doi: 10.1126/science.1195403.

[178] Y. Kobayashi, K. Kumakura, T. Akasaka, and T. Makimoto, “Layered boron nitride as a release layer for mechanical transfer of GaN-based devices,” *Nature*, vol. 484, no. 7393, pp. 223–227, Apr. 2012, doi: 10.1038/nature10970.

[179] S.-I. Park *et al.*, “Printed Assemblies of Inorganic Light-Emitting Diodes for Deformable and Semitransparent Displays,” *Science*, vol. 325, no. 5943, pp. 977–981, Aug. 2009, doi: 10.1126/science.1175690.

[180] H. D. Espinosa, R. A. Bernal, and M. Minary-Jolandan, “A Review of Mechanical and Electromechanical Properties of Piezoelectric Nanowires,” *Advanced Materials*, vol. 24, no. 34, pp. 4656–4675, 2012, doi: 10.1002/adma.201104810.

[181] M. Willander *et al.*, “Zinc oxide nanorod based photonic devices: recent progress in growth, light emitting diodes and lasers,” *Nanotechnology*, vol. 20, no. 33, p. 332001, Aug. 2009, doi: 10.1088/0957-4484/20/33/332001.

[182] N. Bano *et al.*, "ZnO-organic hybrid white light emitting diodes grown on flexible plastic using low temperature aqueous chemical method," *Journal of Applied Physics*, vol. 108, no. 4, p. 043103, Aug. 2010, doi: 10.1063/1.3475473.
[183] A. Nadarajah, R. C. Word, J. Meiss, and R. Könenkamp, "Flexible Inorganic Nanowire Light-Emitting Diode," *Nano Lett.*, vol. 8, no. 2, pp. 534–537, Feb. 2008, doi: 10.1021/nl072784l.
[184] H. Guo, J. Zhou, and Z. Lin, "ZnO nanorod light-emitting diodes fabricated by electrochemical approaches," *Electrochemistry Communications*, vol. 10, no. 1, pp. 146–150, Jan. 2008, doi: 10.1016/j.elecom.2007.11.010.
[185] M. Guo, P. Diao, and S. Cai, "Hydrothermal growth of well-aligned ZnO nanorod arrays: Dependence of morphology and alignment ordering upon preparing conditions," *Journal of Solid State Chemistry*, vol. 178, no. 6, pp. 1864–1873, Jun. 2005, doi: 10.1016/j.jssc.2005.03.031.
[186] B. J. May, A. T. M. G. Sarwar, and R. C. Myers, "Nanowire LEDs grown directly on flexible metal foil," *Appl. Phys. Lett.*, vol. 108, no. 14, p. 141103, Apr. 2016, doi: 10.1063/1.4945419.
[187] J. Liu, Y. H. Ahn, J.-Y. Park, K. H. Koh, and S. Lee, "Hybrid light-emitting diodes based on flexible sheets of mass-produced ZnO nanowires," *Nanotechnology*, vol. 20, no. 44, p. 445203, Oct. 2009, doi: 10.1088/0957-4484/20/44/445203.
[188] C.-H. Lee *et al.*, "Flexible Inorganic Nanostructure Light-Emitting Diodes Fabricated on Graphene Films," *Advanced Materials*, vol. 23, no. 40, pp. 4614–4619, 2011, doi: 10.1002/adma.201102407.
[189] K. Chung *et al.*, "Growth and characterizations of GaN micro-rods on graphene films for flexible light emitting diodes," *APL Materials*, vol. 2, no. 9, p. 092512, Sep. 2014, doi: 10.1063/1.4894780.
[190] A. Kapoor, "Core-shell InGaN/GaN wires for flexible LEDs," These de doctorat, Université Grenoble Alpes, 2020. Accessed: Aug. 12, 2021. [Online]. Available: http://www.theses.fr/2020GRALY013
[191] A. Kapoor *et al.*, "Green Electroluminescence from Radial m-Plane InGaN Quantum Wells Grown on GaN Wire Sidewalls by Metal–Organic Vapor Phase Epitaxy," *ACS Photonics*, vol. 5, no. 11, pp. 4330–4337, Nov. 2018, doi: 10.1021/acsphotonics.8b00520.
[192] M. L. Saladino, A. Zanotto, D. Chillura Martino, A. Spinella, G. Nasillo, and E. Caponetti, "Ce:YAG Nanoparticles Embedded in a PMMA Matrix: Preparation and Characterization," *Langmuir*, vol. 26, no. 16, pp. 13442–13449, Aug. 2010, doi: 10.1021/la9042809.
[193] N. Guan *et al.*, "Colour optimization of phosphor-converted flexible nitride nanowire white light emitting diodes," *J. Phys. Photonics*, vol. 1, no. 3, p. 035003, Jul. 2019, doi: 10.1088/2515-7647/ab2c84.
[194] N. Guan *et al.*, "Heat Dissipation in Flexible Nitride Nanowire Light-Emitting Diodes," *Nanomaterials*, vol. 10, no. 11, Art. no. 11, Nov. 2020, doi: 10.3390/nano10112271.
[195] R. Koester, J. S. Hwang, C. Durand, D. L. S. Dang, and J. Eymery, "Self-assembled growth of catalyst-free GaN wires by metal–organic vapour phase epitaxy," *Nanotechnology*, vol. 21, no. 1, p. 015602, Nov. 2009, doi: 10.1088/0957-4484/21/1/015602.
[196] P. Tchoulfian, F. Donatini, F. Levy, B. Amstatt, P. Ferret, and J. Pernot, "High conductivity in Si-doped GaN wires," *Appl. Phys. Lett.*, vol. 102, no. 12, p. 122116, Mar. 2013, doi: 10.1063/1.4799167.
[197] J. Eymery, D. Salomon, X. Chen, and C. Durand, "Process for Catalyst-Free Selective Growth on a Semiconductor Structure," Oct. 11, 2012 Accessed: Aug. 12, 2021. [Online]. Available: https://patentscope.wipo.int/search/en/detail.jsf?docId=WO2012136665
[198] C. Tessarek *et al.*, "The Role of Si during the Growth of GaN Micro- and Nanorods," *Crystal Growth & Design*, vol. 14, no. 3, pp. 1486–1492, Mar. 2014, doi: 10.1021/cg500054w.
[199] A. P. Tsapenko *et al.*, "Highly conductive and transparent films of HAuCl4-doped single-walled carbon nanotubes for flexible applications," *Carbon*, vol. 130, pp. 448–457, Apr. 2018, doi: 10.1016/j.carbon.2018.01.016.

[200] J. K. Sheu *et al.*, “High-transparency Ni/Au ohmic contact to p-type GaN,” *Appl. Phys. Lett.*, vol. 74, no. 16, pp. 2340–2342, Apr. 1999, doi: 10.1063/1.123844.
[201] X. A. Cao *et al.*, “Electrical effects of plasma damage in p-GaN,” *Appl. Phys. Lett.*, vol. 75, no. 17, pp. 2569–2571, Oct. 1999, doi: 10.1063/1.125080.
[202] R. Chu *et al.*, “Impact of CF4 Plasma Treatment on GaN,” *IEEE Electron Device Letters*, vol. 28, no. 9, pp. 781–783, Sep. 2007, doi: 10.1109/LED.2007.902849.
[203] W.-H. Chung, Y.-R. Jang, Y.-T. Hwang, S.-H. Kim, and H.-S. Kim, “The surface plasmonic welding of silver nanowires via intense pulsed light irradiation combined with NIR for flexible transparent conductive films,” *Nanoscale*, vol. 12, no. 34, pp. 17725–17737, Sep. 2020, doi: 10.1039/C9NR10819J.
[204] T. Mathieu-Pennober, M. Foldyna, S.-T. Zhang, F. H. Julien, N. Schneider, and M. Tchernycheva, “Improvement of carrier collection in Si/a-Si:H nanowire solar cells by using hybrid ITO/silver nanowires contacts,” *Nanotechnology*, vol. 31, no. 43, p. 435408, Aug. 2020, doi: 10.1088/1361-6528/aba4ce.
[205] M. Que, W. Que, T. Zhou, J. Shao, and L. Kong, “Photoluminescence and energy transfer of YAG: Ce3+, Gd3+, Bi3+,” *J. Adv. Dielect.*, vol. 06, no. 04, p. 1650029, Dec. 2016, doi: 10.1142/S2010135X16500296.
[206] Z. Song, X. Liu, L. He, and Q. L. Liu, “Correlation between the energy level structure of cerium-doped yttrium aluminum garnet and luminescent behavior at varying temperatures,” *Mater. Res. Express*, vol. 3, no. 5, p. 055501, May 2016, doi: 10.1088/2053-1591/3/5/055501.
[207] D. J. Robbins, “The Effects of Crystal Field and Temperature on the Photoluminescence Excitation Efficiency of Ce3+ in YAG,” *J. Electrochem. Soc.*, vol. 126, no. 9, p. 1550, Sep. 1979, doi: 10.1149/1.2129328.
[208] Q. Yao *et al.*, “YAG:Ce3+ Transparent Ceramic Phosphors Brighten the Next-Generation Laser-Driven Lighting,” *Advanced Materials*, vol. 32, no. 19, p. 1907888, 2020, doi: 10.1002/adma.201907888.
[209] Z. Hassan, H. R. Abd, F. H. Alsultany, A. F. Omar, and N. M. Ahmed, “Investigation of sintering temperature and Ce3+ concentration in YAG:Ce phosphor powder prepared by microwave combustion for white-light-emitting diode luminance applications,” *Materials Chemistry and Physics*, vol. 229, pp. 22–31, May 2019, doi: 10.1016/j.matchemphys.2019.02.090.
[210] D. Michalik, M. Sopicka-Lizer, J. Plewa, and T. Pawlik, “Application of mechanochemical processing to synthesis of YAG: Ce Garnet Powder,” *Archives of Metallurgy and Materials*, vol. 56, no. 4, pp. 1257–1264, 2011, doi: 10.2478/v10172-011-0144-3.
[211] “OSA | Luminescence properties of YAG:Ce, Gd phosphors synthesized under vacuum condition and their white LED performances.” https://www.osapublishing.org/ome/fulltext.cfm?uri=ome-4-4-649&id=281687 (accessed Aug. 30, 2021).
[212] K. A. Denault *et al.*, “Consequences of Optimal Bond Valence on Structural Rigidity and Improved Luminescence Properties in SrxBa2–xSiO4:Eu2+ Orthosilicate Phosphors,” *Chem. Mater.*, vol. 26, no. 7, pp. 2275–2282, Apr. 2014, doi: 10.1021/cm500116u.
[213] Y. Sato, H. Kuwahara, H. Kato, M. Kobayashi, T. Masaki, and M. Kakihana, “Large Redshifts in Emission and Excitation from Eu2+-Activated Sr2SiO4 and Ba2SiO4 Phosphors Induced by Controlling Eu2+ Occupancy on the Basis on Crystal-Site Engineering,” *Optics and Photonics Journal*, vol. 5, no. 11, Art. no. 11, Nov. 2015, doi: 10.4236/opj.2015.511031.
[214] K. Van den Eeckhout, P. F. Smet, and D. Poelman, “Luminescent Afterglow Behavior in the M2Si5N8: Eu Family (M = Ca, Sr, Ba),” *Materials*, vol. 4, no. 6, Art. no. 6, Jun. 2011, doi: 10.3390/ma4060980.
[215] A. Setlur, “Phosphors for LED-based Solid-State Lighting,” 2009, doi: 10.1149/2.f04094if.
[216] “Size and Shape Effect on Biomedical Applications of Nanomaterials | IntechOpen.” https://www.intechopen.com/chapters/38778 (accessed Aug. 31, 2021).

[217] A. Jain, P. Sengar, and G. A. Hirata, “Rare-earth-doped Y3Al5O12 (YAG) nanophosphors: synthesis, surface functionalization, and applications in thermoluminescence dosimetry and nanomedicine,” *J. Phys. D: Appl. Phys.*, vol. 51, no. 30, p. 303002, Jun. 2018, doi: 10.1088/1361-6463/aaca49.

[218] C. H. Yang, B. Chen, J. Zhou, Y. M. Chen, and Z. Suo, “Electroluminescence of Giant Stretchability,” *Advanced Materials*, vol. 28, no. 22, pp. 4480–4484, 2016, doi: 10.1002/adma.201504031.

[219] J. Wang, C. Yan, G. Cai, M. Cui, A. Lee-Sie Eh, and P. See Lee, “Extremely Stretchable Electroluminescent Devices with Ionic Conductors,” *Advanced Materials*, vol. 28, no. 22, pp. 4490–4496, 2016, doi: 10.1002/adma.201504187.

[220] T. Someya, Z. Bao, and G. G. Malliaras, “The rise of plastic bioelectronics,” *Nature*, vol. 540, no. 7633, pp. 379–385, Dec. 2016, doi: 10.1038/nature21004.

[221] T. Yokota *et al.*, “Ultraflexible organic photonic skin,” *Science Advances*, vol. 2, no. 4, p. e1501856, Apr. 2016, doi: 10.1126/sciadv.1501856.

[222] A. Chortos, J. Liu, and Z. Bao, “Pursuing prosthetic electronic skin,” *Nature Mater*, vol. 15, no. 9, pp. 937–950, Sep. 2016, doi: 10.1038/nmat4671.

[223] X. Chen *et al.*, “A Stretchable and Transparent Nanocomposite Nanogenerator for Self-Powered Physiological Monitoring,” *ACS Appl. Mater. Interfaces*, vol. 9, no. 48, pp. 42200–42209, Dec. 2017, doi: 10.1021/acsami.7b13767.

[224] C. M. Zgierski-Johnston *et al.*, “Cardiac pacing using transmural multi-LED probes in channelrhodopsin-expressing mouse hearts,” *Progress in Biophysics and Molecular Biology*, vol. 154, pp. 51–61, Aug. 2020, doi: 10.1016/j.pbiomolbio.2019.11.004.

[225] Z. Zhou *et al.*, “Sign-to-speech translation using machine-learning-assisted stretchable sensor arrays,” *Nat Electron*, vol. 3, no. 9, pp. 571–578, Sep. 2020, doi: 10.1038/s41928-020-0428-6.

[226] H. Huang *et al.*, “Super-stretchable, elastic and recoverable ionic conductive hydrogel for wireless wearable, stretchable sensor,” *J. Mater. Chem. A*, vol. 8, no. 20, pp. 10291–10300, May 2020, doi: 10.1039/D0TA02902E.

[227] B.-U. Hwang *et al.*, “A transparent stretchable sensor for distinguishable detection of touch and pressure by capacitive and piezoresistive signal transduction,” *NPG Asia Mater*, vol. 11, no. 1, pp. 1–12, May 2019, doi: 10.1038/s41427-019-0126-x.

[228] F. M. Kochetkov *et al.*, “Stretchable Transparent Light-Emitting Diodes Based on InGaN/GaN Quantum Well Microwires and Carbon Nanotube Films,” *Nanomaterials*, vol. 11, no. 6, Art. no. 6, Jun. 2021, doi: 10.3390/nano11061503.

[229] M. Asad, Q. Li, M. Sachdev, and W. S. Wong, “Thermal and optical properties of high-density GaN micro-LED arrays on flexible substrates,” *Nano Energy*, vol. 73, p. 104724, Jul. 2020, doi: 10.1016/j.nanoen.2020.104724.

[230] Q. Zheng, C. Li, A. Rai, J. H. Leach, D. A. Broido, and D. G. Cahill, “Thermal conductivity of GaN, $^{71}\mathrm{GaN}$, and SiC from 150 K to 850 K,” *Phys. Rev. Materials*, vol. 3, no. 1, p. 014601, Jan. 2019, doi: 10.1103/PhysRevMaterials.3.014601.

[231] H. Nishizawa, M. Nishiguchi, A. Miki, and M. Fujihira, “Method of measuring junction temperature,” US5401099A, Mar. 28, 1995 Accessed: Sep. 01, 2021. [Online]. Available: https://patents.google.com/patent/US5401099/en

[232] J. Park, M. Shin, and C. C. Lee, “Measurement of temperature profiles on visible light-emitting diodes by use of a nematic liquid crystal and an infrared laser,” *Opt. Lett., OL*, vol. 29, no. 22, pp. 2656–2658, Nov. 2004, doi: 10.1364/OL.29.002656.

[233] C.-N. Hsu, C.-C. Huang, and Y.-H. Wu, “Effect of heat convection on the thermal and structure stress of high-power InGaN light-emitting diode,” *J Therm Anal Calorim*, vol. 119, no. 2, pp. 1245–1257, Feb. 2015, doi: 10.1007/s10973-014-4221-5.

[234] Z. Su *et al.*, “Layer-by-layer thermal conductivities of the Group III nitride films in blue/green light emitting diodes,” *Appl. Phys. Lett.*, vol. 100, no. 20, p. 201106, May 2012, doi: 10.1063/1.4718354.

[235] V. Schwegler *et al.*, "Ohmic Heating of InGaN LEDs during Operation: Determination of the Junction Temperature and Its Influence on Device Performance," *physica status solidi (a)*, vol. 176, no. 1, pp. 783–786, 1999, doi: 10.1002/(SICI)1521-396X(199911)176:1<783::AID-PSSA783>3.0.CO;2-Z.

[236] D. Priante *et al.*, "Diode junction temperature in ultraviolet AlGaN quantum-disks-in-nanowires," *Journal of Applied Physics*, vol. 124, no. 1, p. 015702, Jul. 2018, doi: 10.1063/1.5026650.

[237] S. Zhang *et al.*, "On the Carrier Injection Efficiency and Thermal Property of InGaN/GaN Axial Nanowire Light Emitting Diodes," *IEEE Journal of Quantum Electronics*, vol. 50, no. 6, pp. 483–490, Jun. 2014, doi: 10.1109/JQE.2014.2317732.

[238] "INTEGRATED CIRCUIT THERMAL MEASUREMENT METHOD - ELECTRICAL TEST METHOD (SINGLE SEMICONDUCTOR DEVICE): | JEDEC." https://www.jedec.org/standards-documents/docs/jesd-51-1 (accessed Sep. 01, 2021).

[239] Y. Xi *et al.*, "Junction and carrier temperature measurements in deep-ultraviolet light-emitting diodes using three different methods," *Appl. Phys. Lett.*, vol. 86, no. 3, p. 031907, Jan. 2005, doi: 10.1063/1.1849838.

[240] Q. Chen, X. Luo, S. Zhou, and S. Liu, "Dynamic junction temperature measurement for high power light emitting diodes," *Review of Scientific Instruments*, vol. 82, no. 8, p. 084904, Aug. 2011, doi: 10.1063/1.3624699.

[241] R. R. Zhuang, P. Cai, and J. L. Huang, "Study the Effect of Junction Temperature on the Peak Wavelength in GaN-Based High-Power Green Light Emitting Diodes," *Advanced Materials Research*, vol. 399–401, pp. 1034–1038, 2012, doi: 10.4028/www.scientific.net/AMR.399-401.1034.

[242] K. S. Chang *et al.*, "Precise Temperature Mapping of GaN-Based LEDs by Quantitative Infrared Micro-Thermography," *Sensors*, vol. 12, no. 4, Art. no. 4, Apr. 2012, doi: 10.3390/s120404648.

[243] N. Narendran, Y. Gu, and R. Hosseinzadeh, "Estimating junction temperature of high-flux white LEDs," in *Light-Emitting Diodes: Research, Manufacturing, and Applications VIII*, Jun. 2004, vol. 5366, pp. 158–160. doi: 10.1117/12.537628.

[244] T. Sannicolo *et al.*, "Direct Imaging of the Onset of Electrical Conduction in Silver Nanowire Networks by Infrared Thermography: Evidence of Geometrical Quantized Percolation," *Nano Lett.*, vol. 16, no. 11, pp. 7046–7053, Nov. 2016, doi: 10.1021/acs.nanolett.6b03270.

[245] D. U. Kim, K. S. Park, C. B. Jeong, G. H. Kim, and K. S. Chang, "Quantitative temperature measurement of multi-layered semiconductor devices using spectroscopic thermoreflectance microscopy," *Opt. Express, OE*, vol. 24, no. 13, pp. 13906–13916, Jun. 2016, doi: 10.1364/OE.24.013906.

[246] "Vishay Intertechnology." https://www.vishay.com/ (accessed Dec. 02, 2021).

[247] C. P. T. Svensson *et al.*, "Monolithic GaAs/InGaP nanowire light emitting diodes on silicon," *Nanotechnology*, vol. 19, no. 30, p. 305201, Jun. 2008, doi: 10.1088/0957-4484/19/30/305201.

[248] K. Kawaguchi, H. Sudo, M. Matsuda, K. Takemoto, T. Yamamoto, and Y. Arakawa, "Radial InP/InAsP/InP heterostructure nanowires on patterned Si substrates using self-catalyzed growth for vertical-type optical devices," *Appl. Phys. Lett.*, vol. 106, no. 1, p. 012107, Jan. 2015, doi: 10.1063/1.4905555.

[249] K. Kawaguchi, H. Sudo, M. Matsuda, M. Ekawa, T. Yamamoto, and Y. Arakawa, "Room-temperature electroluminescence from radial p–i–n InP/InAsP/InP nanowire heterostructures in the 1.5-μm-wavelength region," *Jpn. J. Appl. Phys.*, vol. 54, no. 4S, p. 04DN02, Feb. 2015, doi: 10.7567/JJAP.54.04DN02.

[250] K. Hiruma *et al.*, "Fabrication of Axial and Radial Heterostructures for Semiconductor Nanowires by Using Selective-Area Metal-Organic Vapor-Phase Epitaxy," *Journal of Nanotechnology*, vol. 2012, p. e169284, Oct. 2011, doi: 10.1155/2012/169284.

[251] P. Mohan, J. Motohisa, and T. Fukui, “Fabrication of InP/InAs/InP core-multishell heterostructure nanowires by selective area metalorganic vapor phase epitaxy,” *Appl. Phys. Lett.*, vol. 88, no. 13, p. 133105, Mar. 2006, doi: 10.1063/1.2189203.

[252] L. Mancini *et al.*, “Three-dimensional nanoscale study of Al segregation and quantum dot formation in GaAs/AlGaAs core-shell nanowires,” *Appl. Phys. Lett.*, vol. 105, no. 24, p. 243106, Dec. 2014, doi: 10.1063/1.4904952.

[253] M. Heiss *et al.*, “Self-assembled quantum dots in a nanowire system for quantum photonics,” *Nat Mater*, vol. 12, no. 5, pp. 439–444, May 2013, doi: 10.1038/nmat3557.

[254] S. Nakamura, M. Senoh, N. Iwasa, and S. N. S. Nagahama, “High-Brightness InGaN Blue, Green and Yellow Light-Emitting Diodes with Quantum Well Structures,” *Jpn. J. Appl. Phys.*, vol. 34, no. 7A, p. L797, Jul. 1995, doi: 10.1143/JJAP.34.L797.

[255] A. I. Alhassan *et al.*, “High luminous efficacy green light-emitting diodes with AlGaN cap layer,” *Opt. Express, OE*, vol. 24, no. 16, pp. 17868–17873, Aug. 2016, doi: 10.1364/OE.24.017868.

[256] S. Nakamura, M. Senoh, N. Iwasa, S. Nagahama, T. Yamada, and T. Mukai, “Superbright Green InGaN Single-Quantum-Well-Structure Light-Emitting Diodes,” *Jpn. J. Appl. Phys.*, vol. 34, no. 10B, p. L1332, Oct. 1995, doi: 10.1143/JJAP.34.L1332.

[257] A. Even, “Amélioration de l’incorporation d’indium dans zone active à base d’InGaN grâce à la croissance sur pseudo-substrat InGaN pour l’application à la DEL blanche monolithique,” These de doctorat, Université Grenoble Alpes (ComUE), 2018. Accessed: Sep. 03, 2021. [Online]. Available: http://www.theses.fr/2018GREAY008

[258] J. Adhikari and D. A. Kofke, “Molecular simulation study of miscibility of ternary and quaternary InGaAlN alloys,” *Journal of Applied Physics*, vol. 95, no. 11, pp. 6129–6137, Jun. 2004, doi: 10.1063/1.1728317.

[259] A. Koukitu and H. Seki, “Thermodynamic study on phase separation during MOVPE growth of InxGa1−xN,” *Journal of Crystal Growth*, vol. 189–190, pp. 13–18, Jun. 1998, doi: 10.1016/S0022-0248(98)00147-X.

[260] D. Doppalapudi, S. N. Basu, K. F. Ludwig, and T. D. Moustakas, “Phase separation and ordering in InGaN alloys grown by molecular beam epitaxy,” *Journal of Applied Physics*, vol. 84, no. 3, pp. 1389–1395, Aug. 1998, doi: 10.1063/1.368251.

[261] V. Potin *et al.*, “Comparison of the In distribution in InGaN/GaN quantum well structures grown by molecular beam epitaxy and metalorganic vapor phase epitaxy,” *Journal of Crystal Growth*, vol. 262, no. 1, pp. 145–150, Feb. 2004, doi: 10.1016/j.jcrysgro.2003.10.082.

[262] J.-I. Hwang, R. Hashimoto, S. Saito, and S. Nunoue, “Development of InGaN-based red LED grown on (0001) polar surface,” *Appl. Phys. Express*, vol. 7, no. 7, p. 071003, Jun. 2014, doi: 10.7567/APEX.7.071003.

[263] S. Chichibu, T. Azuhata, T. Sota, and S. Nakamura, “Spontaneous emission of localized excitons in InGaN single and multiquantum well structures,” *Appl. Phys. Lett.*, vol. 69, no. 27, pp. 4188–4190, Dec. 1996, doi: 10.1063/1.116981.

[264] D. Iida, Z. Zhuang, P. Kirilenko, M. Velazquez-Rizo, M. A. Najmi, and K. Ohkawa, “633-nm InGaN-based red LEDs grown on thick underlying GaN layers with reduced in-plane residual stress,” *Appl. Phys. Lett.*, vol. 116, no. 16, p. 162101, Apr. 2020, doi: 10.1063/1.5142538.

[265] W. Yao *et al.*, “Stress engineering for reducing the injection current induced blue shift in InGaN-based red light-emitting diodes,” *CrystEngComm*, vol. 23, no. 12, pp. 2360–2366, 2021, doi: 10.1039/D0CE01769H.

[266] Z. Zhuang, D. Iida, P. Kirilenko, and K. Ohkawa, “Improved performance of InGaN-based red light-emitting diodes by micro-hole arrays,” *Opt. Express, OE*, vol. 29, no. 19, pp. 29780–29788, Sep. 2021, doi: 10.1364/OE.435556.

[267] A. Dussaigne *et al.*, “Full InGaN red (625 nm) micro-LED (10 $\upmu$m) demonstration on a relaxed pseudo-substrate,” *Appl. Phys. Express*, vol. 14, no. 9, p. 092011, Sep. 2021, doi: 10.35848/1882-0786/ac1b3e.

[268] A. Dussaigne *et al.*, “Full InGaN red light emitting diodes,” *Journal of Applied Physics*, vol. 128, no. 13, p. 135704, Oct. 2020, doi: 10.1063/5.0016217.
[269] B. Mitchell, V. Dierolf, T. Gregorkiewicz, and Y. Fujiwara, “Perspective: Toward efficient GaN-based red light emitting diodes using europium doping,” *Journal of Applied Physics*, vol. 123, no. 16, p. 160901, Apr. 2018, doi: 10.1063/1.5010762.
[270] Y. Fujiwara, S. Ichikawa, D. Timmerman, and J. Tatebayashi, “Eu-doped GaN-based red LED for ultrahigh-resolution micro-LED displays,” in *Gallium Nitride Materials and Devices XVI*, Mar. 2021, vol. 11686, p. 1168615. doi: 10.1117/12.2577199.
[271] Y. Li, S. Qi, P. Li, and Z. Wang, “Research progress of Mn doped phosphors,” *RSC Adv.*, vol. 7, no. 61, pp. 38318–38334, Aug. 2017, doi: 10.1039/C7RA06026B.
[272] D. Chen, Y. Zhou, and J. Zhong, “A review on Mn4+ activators in solids for warm white light-emitting diodes,” *RSC Adv.*, vol. 6, no. 89, pp. 86285–86296, Sep. 2016, doi: 10.1039/C6RA19584A.
[273] R. Cao *et al.*, “Rare-earth-free Li5La3Ta2O12:Mn4+ deep-red-emitting phosphor: Synthesis and photoluminescence properties,” *Journal of the American Ceramic Society*, vol. 102, no. 10, pp. 5910–5918, 2019, doi: 10.1111/jace.16447.
[274] E. Song *et al.*, “Highly Efficient and Thermally Stable K3AlF6:Mn4+ as a Red Phosphor for Ultra-High-Performance Warm White Light-Emitting Diodes,” *ACS Appl. Mater. Interfaces*, vol. 9, no. 10, pp. 8805–8812, Mar. 2017, doi: 10.1021/acsami.7b00749.
[275] K. K. Thejas, M. Abraham, A. K. Kunti, M. Tchernycheva, S. Ahmad, and S. Das, “Review on deep red-emitting rare-earth free germanates and their efficiency as well as adaptability for various applications,” *Applied Materials Today*, vol. 24, p. 101094, Sep. 2021, doi: 10.1016/j.apmt.2021.101094.
[276] M. Abraham *et al.*, “The elevated colour rendering of white-LEDs by microwave-synthesized red-emitting (Li, Mg)3RbGe8O18:Mn4+ nanophosphors,” *Dalton Trans.*, vol. 50, no. 8, pp. 3044–3059, Mar. 2021, doi: 10.1039/D0DT04309E.
[277] Y. Zhong *et al.*, “Enhancing quantum efficiency and tuning photoluminescence properties in far-red-emitting phosphor Ca14Ga10Zn6O35:Mn4+ based on chemical unit engineering,” *Chemical Engineering Journal*, vol. 374, pp. 381–391, Oct. 2019, doi: 10.1016/j.cej.2019.05.201.
[278] J. Hu *et al.*, “Enhanced deep-red emission from Mn4+/Mg2+ co-doped CaGdAlO4 phosphors for plant cultivation,” *Dalton Trans.*, vol. 48, no. 7, pp. 2455–2466, Feb. 2019, doi: 10.1039/C8DT04955F.
[279] S. P. Singh, M. Kim, W. B. Park, J.-W. Lee, and K.-S. Sohn, “Discovery of a Red-Emitting Li3RbGe8O18:Mn4+ Phosphor in the Alkali-Germanate System: Structural Determination and Electronic Calculations,” *Inorg. Chem.*, vol. 55, no. 20, pp. 10310–10319, Oct. 2016, doi: 10.1021/acs.inorgchem.6b01576.
[280] H. Wondratschek, “The mathematical theory of symmetry in solids. Representation theory for point groups and space groups by C. J. Bradley and A. P. Cracknell,” *Acta Cryst A*, vol. 29, no. 5, Art. no. 5, Sep. 1973, doi: 10.1107/S0567739473001476.
[281] X. Ding, G. Zhu, W. Geng, Q. Wang, and Y. Wang, “Rare-Earth-Free High-Efficiency Narrow-Band Red-Emitting Mg3Ga2GeO8:Mn4+ Phosphor Excited by Near-UV Light for White-Light-Emitting Diodes,” *Inorg. Chem.*, vol. 55, no. 1, pp. 154–162, Jan. 2016, doi: 10.1021/acs.inorgchem.5b02048.
[282] J. Lu, Y. Pan, J. Wang, X. Chen, S. Huang, and G. Liu, “Reduction of Mn4+ to Mn2+ in CaAl12O19 by co-doping charge compensators to obtain tunable photoluminescence,” *RSC Adv.*, vol. 3, no. 14, pp. 4510–4513, Mar. 2013, doi: 10.1039/C3RA22938F.
[283] V. Grenier *et al.*, “UV Emission from GaN Wires with m-Plane Core–Shell GaN/AlGaN Multiple Quantum Wells,” *ACS Appl. Mater. Interfaces*, vol. 12, no. 39, pp. 44007–44016, Sep. 2020, doi: 10.1021/acsami.0c08765.

[284] O. Saket *et al.*, "Nanoscale electrical analyses of axial-junction GaAsP nanowires for solar cell applications," *Nanotechnology*, vol. 31, no. 14, p. 145708, Jan. 2020, doi: 10.1088/1361-6528/ab62c9.
[285] F. Oehler, A. Cattoni, A. Scaccabarozzi, G. Patriarche, F. Glas, and J.-C. Harmand, "Measuring and Modeling the Growth Dynamics of Self-Catalyzed GaP Nanowire Arrays," *Nano Lett.*, vol. 18, no. 2, pp. 701–708, Feb. 2018, doi: 10.1021/acs.nanolett.7b03695.
[286] O. Saket *et al.*, "Influence of surface passivation on the electrical properties of p–i–n GaAsP nanowires," *Appl. Phys. Lett.*, vol. 117, no. 12, p. 123104, Sep. 2020, doi: 10.1063/5.0022157.
[287] O. Saket, "Caractérisation électrique de nanofils de semi-conducteurs III-V pour des applications photovoltaïques," These de doctorat, université Paris-Saclay, 2020. Accessed: Nov. 29, 2021. [Online]. Available: http://www.theses.fr/2020UPASS123
[288] A. D. Bolshakov *et al.*, "Growth and Characterization of GaP/GaPAs Nanowire Heterostructures with Controllable Composition," *physica status solidi (RRL) – Rapid Research Letters*, vol. 13, no. 11, p. 1900350, 2019, doi: 10.1002/pssr.201900350.
[289] A. Uhlir, "Electrolytic shaping of germanium and silicon," *The Bell System Technical Journal*, vol. 35, no. 2, pp. 333–347, Mar. 1956, doi: 10.1002/j.1538-7305.1956.tb02385.x.
[290] L. T. Canham, "Silicon quantum wire array fabrication by electrochemical and chemical dissolution of wafers," *Appl. Phys. Lett.*, vol. 57, no. 10, pp. 1046–1048, Sep. 1990, doi: 10.1063/1.103561.
[291] P. M. Fauchet *et al.*, "Light-emitting porous silicon: materials science, properties, and device applications," *IEEE Journal of Selected Topics in Quantum Electronics*, vol. 1, no. 4, pp. 1126–1139, Dec. 1995, doi: 10.1109/2944.488691.
[292] P. Steiner, F. Kozlowski, and W. Lang, "Light-emitting porous silicon diode with an increased electroluminescence quantum efficiency," *Appl. Phys. Lett.*, vol. 62, no. 21, pp. 2700–2702, May 1993, doi: 10.1063/1.109236.
[293] P. Jaguiro, P. Katsuba, L. Serguei, and A. Smirnov, "Porous Silicon Avalanche LEDs and their Applications in Optoelectronics and Information Displays," *Acta Physica Polonica A - ACTA PHYS POL A*, vol. 112, Nov. 2007, doi: 10.12693/APhysPolA.112.1031.
[294] O. Bisi, S. Ossicini, and L. Pavesi, "Porous silicon: a quantum sponge structure for silicon based optoelectronics," *Surface Science Reports*, vol. 38, no. 1, pp. 1–126, Apr. 2000, doi: 10.1016/S0167-5729(99)00012-6.
[295] G. Barillaro, F. Pieri, and U. Mastromatteo, "A porous silicon LED based on a standard BCD technology," *Optical Materials*, vol. 17, no. 1, pp. 91–94, Jun. 2001, doi: 10.1016/S0925-3467(01)00026-X.
[296] P. M. Fauchet, L. Tsybeskov, S. P. Duttagupta, and K. D. Hirschman, "Stable photoluminescence and electroluminescence from porous silicon," *Thin Solid Films*, vol. 297, no. 1, pp. 254–260, Apr. 1997, doi: 10.1016/S0040-6090(96)09438-2.
[297] C. B. Soh *et al.*, "Nanopore morphology in porous GaN template and its effect on the LEDs emission," *J. Phys. D: Appl. Phys.*, vol. 46, no. 36, p. 365102, Sep. 2013, doi: 10.1088/0022-3727/46/36/365102.
[298] C.-C. Kao *et al.*, "Study of dry etching for GaN and InGaN-based laser structure using inductively coupled plasma reactive ion etching," *Materials Science and Engineering: B*, vol. 107, no. 3, pp. 283–288, Mar. 2004, doi: 10.1016/j.mseb.2003.11.023.
[299] P. H. Griffin and R. A. Oliver, "Porous nitride semiconductors reviewed," *J. Phys. D: Appl. Phys.*, vol. 53, no. 38, p. 383002, Sep. 2020, doi: 10.1088/1361-6463/ab9570.
[300] C. Zhang *et al.*, "Mesoporous GaN for Photonic Engineering—Highly Reflective GaN Mirrors as an Example," *ACS Photonics*, vol. 2, no. 7, pp. 980–986, Jul. 2015, doi: 10.1021/acsphotonics.5b00216.
[301] J. Hartmann *et al.*, "High Aspect Ratio GaN Fin Microstructures with Nonpolar Sidewalls by Continuous Mode Metalorganic Vapor Phase Epitaxy," *Crystal Growth & Design*, vol. 16, no. 3, pp. 1458–1462, Mar. 2016, doi: 10.1021/acs.cgd.5b01598.

[302] D. Zolotukhin *et al.*, "Control of stress and threading dislocation density in the thick GaN/AlN buffer layers grown on Si (111) substrates by low- temperature MBE," *J. Phys.: Conf. Ser.*, vol. 741, p. 012025, Aug. 2016, doi: 10.1088/1742-6596/741/1/012025.

[303] R. S. Q. Fareed *et al.*, "Air-bridged lateral growth of crack-free Al0.24Ga0.76N on highly relaxed porous GaN," *Appl. Phys. Lett.*, vol. 84, no. 5, pp. 696–698, Jan. 2004, doi: 10.1063/1.1644621.

[304] C. B. Soh, H. Hartono, S. Y. Chow, S. J. Chua, and E. A. Fitzgerald, "Dislocation annihilation in regrown GaN on nanoporous GaN template with optimization of buffer layer growth," *Appl. Phys. Lett.*, vol. 90, no. 5, p. 053112, Jan. 2007, doi: 10.1063/1.2437056.

[305] M. Mynbaeva *et al.*, "Strain relaxation in GaN layers grown on porous GaN sublayers," *Materials Research Society Internet Journal of Nitride Semiconductor Research*, vol. 4, no. 1, ed 1999, doi: 10.1557/S1092578300000703.

[306] H. Hartono, C. B. Soh, S. J. Chua, and E. A. Fitzgerald, "High Quality GaN Grown from a Nanoporous GaN Template," *J. Electrochem. Soc.*, vol. 154, no. 12, p. H1004, Oct. 2007, doi: 10.1149/1.2792344.

[307] L.-W. Jang *et al.*, "Electrical and structural properties of GaN films and GaN/InGaN light-emitting diodes grown on porous GaN templates fabricated by combined electrochemical and photoelectrochemical etching," *Journal of Alloys and Compounds*, vol. 589, pp. 507–512, Mar. 2014, doi: 10.1016/j.jallcom.2013.12.034.

[308] G.-Y. Shiu *et al.*, "InGaN Light-Emitting Diodes with an Embedded Nanoporous GaN Distributed Bragg Reflectors," *Sci Rep*, vol. 6, no. 1, p. 29138, Jul. 2016, doi: 10.1038/srep29138.

[309] B. Damilano, S. Vézian, and J. Massies, "Photoluminescence properties of porous GaN and (Ga,In)N/GaN single quantum well made by selective area sublimation," *Opt. Express*, vol. 25, no. 26, p. 33243, Dec. 2017, doi: 10.1364/OE.25.033243.

[310] S. S. Pasayat *et al.*, "Color-tunable <10 µm square InGaN micro-LEDs on compliant GaN-on-porous-GaN pseudo-substrates," *Applied Physics Letters*, vol. 117, no. 6, p. 061105, Aug. 2020, doi: 10.1063/5.0011203.

[311] O. V. Bilousov *et al.*, "Fully Porous GaN p–n Junction Diodes Fabricated by Chemical Vapor Deposition," *ACS Appl. Mater. Interfaces*, vol. 6, no. 20, pp. 17954–17964, Oct. 2014, doi: 10.1021/am504786b.

[312] A. Le Louarn, S. Vézian, F. Semond, and J. Massies, "AlN buffer layer growth for GaN epitaxy on (111) Si: Al or N first?," *Journal of Crystal Growth*, vol. 311, no. 12, pp. 3278–3284, Jun. 2009, doi: 10.1016/j.jcrysgro.2009.04.001.

[313] F. Semond *et al.*, "Molecular Beam Epitaxy of Group-III Nitrides on Silicon Substrates: Growth, Properties and Device Applications," *physica status solidi (a)*, vol. 188, Dec. 2001, doi: 10.1002/1521-396X(200112)188:23.0.CO;2-6.

[314] N. A. Smith, H. H. Lamb, A. J. McGinnis, and R. F. Davis, "Surface-roughness correlations in homoepitaxial growth of GaN(0001) films by NH3 supersonic jet epitaxy," *Journal of Applied Physics*, vol. 96, no. 8, pp. 4556–4562, Oct. 2004, doi: 10.1063/1.1785869.

[315] L. Zhang *et al.*, "High Brightness GaN-on-Si Based Blue LEDs Grown on 150 mm Si Substrates Using Thin Buffer Layer Technology," *IEEE Journal of the Electron Devices Society*, vol. 3, no. 6, pp. 457–462, Nov. 2015, doi: 10.1109/JEDS.2015.2463738.

[316] S. Nunoue *et al.*, "LED manufacturing issues concerning gallium nitride-on-silicon (GaN-on-Si) technology and wafer scale up challenges," in *2013 IEEE International Electron Devices Meeting*, Dec. 2013, p. 13.2.1-13.2.4. doi: 10.1109/IEDM.2013.6724622.

[317] C. Haller *et al.*, "GaN surface as the source of non-radiative defects in InGaN/GaN quantum wells," *Appl. Phys. Lett.*, vol. 113, no. 11, p. 111106, Sep. 2018, doi: 10.1063/1.5048010.

[318] T. Markurt *et al.*, "Blocking Growth by an Electrically Active Subsurface Layer: The Effect of Si as an Antisurfactant in the Growth of GaN," *Phys. Rev. Lett.*, vol. 110, no. 3, p. 036103, Jan. 2013, doi: 10.1103/PhysRevLett.110.036103.

[319] B. Damilano, S. Vézian, and J. Massies, “Mesoporous GaN Made by Selective Area Sublimation for Efficient Light Emission on Si Substrate,” *physica status solidi (b)*, vol. 255, no. 5, p. 1700392, 2018, doi: 10.1002/pssb.201700392.

[320] B. Damilano *et al.*, “Optical properties of InxGa1−xN/GaN quantum-disks obtained by selective area sublimation,” *Journal of Crystal Growth*, vol. 477, pp. 262–266, Nov. 2017, doi: 10.1016/j.jcrysgro.2017.01.010.

[321] M. A. Reshchikov, J. D. McNamara, H. Helava, A. Usikov, and Y. Makarov, “Two yellow luminescence bands in undoped GaN,” *Sci Rep*, vol. 8, no. 1, p. 8091, May 2018, doi: 10.1038/s41598-018-26354-z.

[322] X. Li, P. W. Bohn, and J. J. Coleman, “Impurity states are the origin of yellow-band emission in GaN structures produced by epitaxial lateral overgrowth,” *Appl. Phys. Lett.*, vol. 75, no. 26, pp. 4049–4051, Dec. 1999, doi: 10.1063/1.125532.

[323] C. Díaz-Guerra, J. Piqueras, A. Castaldini, A. Cavallini, and L. Polenta, “Defect assessment of Mg-doped GaN by beam injection techniques,” *Journal of Applied Physics*, vol. 94, no. 12, pp. 7470–7475, Dec. 2003, doi: 10.1063/1.1628832.

[324] P. Lavenus *et al.*, “Experimental and theoretical analysis of transport properties of core–shell wire light emitting diodes probed by electron beam induced current microscopy,” *Nanotechnology*, vol. 25, no. 25, p. 255201, Jun. 2014, doi: 10.1088/0957-4484/25/25/255201.

[325] S. F. Chichibu *et al.*, “Optical properties of InGaN quantum wells,” in *Materials Science and Engineering B: Solid-State Materials for Advanced Technology*, May 1999, vol. 59, no. 1–3, pp. 298–306. doi: 10.1016/S0921-5107(98)00359-6.

[326] M. Bertalmío, Ed., “Advance Praise for ‘Vision Models for High Dynamic Range and Wide Colour Gamut Imaging: Techniques and Applications,’” in *Vision Models for High Dynamic Range and Wide Colour Gamut Imaging*, Academic Press, 2020, pp. vii–viii. doi: 10.1016/B978-0-12-813894-6.00019-3.

[327] C. Abraham, “A Beginner’s Guide to (CIE) Colorimetry,” *Color and Imaging*, Feb. 15, 2019. https://medium.com/hipster-color-science/a-beginners-guide-to-colorimetry-401f1830b65a (accessed Aug. 24, 2021).

[328] “How to choose suitable LED color temperature,” *LED Light Manufacturer*. https://www.klmlighting.com/how-to-choose-suitable-led-color-temperature/ (accessed Sep. 02, 2021).

[329] “Appendix 7: Calculation of the CIE Colour Rendering Indices,” in *Measuring Colour*, John Wiley & Sons, Ltd, 2011, pp. 383–392. doi: 10.1002/9781119975595.app7.

[330] “Appendix B: Calculating color rendering metrics | Light Sources and Color | Lighting Answers | NLPIP.” https://www.lrc.rpi.edu/programs/nlpip/lightinganswers/lightsources/appendixB.asp (accessed Aug. 25, 2021).

[331] “Color Rendering Index Calculator | Waveform Lighting.” https://www.waveformlighting.com/tech/color-rendering-index-calculator (accessed Aug. 25, 2021).

[332] “Light Bulb Facts: What Is the Color Rendering Index?,” *Lumens.com*. https://www.lumens.com/on/demandware.store/Sites-Lumens-Site/default/Page-Show?cid=color-rendering-index (accessed Sep. 02, 2021).

LIST OF PUBLICATIONS

ARTICLES

- *Nan Guan, Nuño Amador-Mendez, Junkang Wang, Subrata Das, Akanksha Kapoor, François H Julien, Noëlle Gogneau, Martin Foldyna, Sudipta Som, Joël Eymery, Christophe Durand and Maria Tchernycheva.* "Colour optimization of phosphor-converted flexible nitride nanowire white light emitting diodes", 2019 J. Phys. Photonics 1 035003.
https://doi.org/10.1088/2515-7647/ab2c84

- *Junseok Jeong, Dae Kwon Jin, Janghwan Cha, Bong Kyun Kang, Qingxiao Wang,Joonghoon Choi, Sang Wook Lee, Vladimir Yu. Mikhailovskii, Vladimir Neplokh, Nuño Amador-Mendez, Maria Tchernycheva, Woo Seok Yang, Jinkyoung Yoo, Moon J. Kim, Suklyun Hong and Young Joon Hong*"Selective-Area Remote Epitaxy of ZnO Microrods Using Multilayer–Monolayer-Patterned Graphene for Transferable and Flexible Device Fabrications" ACS Appl. Nano Mater. 2020, 3, 9, 8920–8930.
https://doi.org/10.1021/acsanm.0c01656

- *Nan Guan, Nuño Amador-Mendez, Arup Kunti, Andrey Babichev, Subrata Das, Akanksha Kapoor, Noëlle Gogneau, Joël Eymery, François Henri Julien, Christophe Durand, Maria Tchernycheva.* "Heat Dissipation in Flexible Nitride Nanowire Light-Emitting Diodes" Nanomaterials 2020, 10(11), 2271; https://doi.org/10.3390/nano10112271

- *Omar Saket, Junkang Wang, Nuño Amador-Mendez, Martina Morassi, Arup Kunti, Fabien Bayle, Stéphane Collin, Arnaud Jollivet, Andrey Babichev, Tanbir Sodhi, Jean-Christophe Harmand, François H Julien, Noelle Gogneau, Maria Tchernycheva.* "Investigation of the effect of the doping order in GaN nanowire p–n junctions grown by molecular-beam epitaxy" Nanotechnology, Volume 32, Number 8.
https://doi.org/10.1088/1361-6528/abc91a

- *Malini Abraham, Arup K Kunti, KK Thejas, Nuño Amador-Mendez, Noëlle Gogneau, KG Nishanth, Maria Tchernycheva, Subrata Das* "The elevated colour rendering of white-LEDs by microwave-synthesized red-emitting $(Li, Mg)_3 RbGe_8O_{18}:Mn^{4+}$ nanophosphors" Dalton Trans., 2021, 50, 3044-3059.
https://doi.org/10.1039/D0DT04309E

- *Fedor M Kochetkov, Vladimir Neplokh, Viktoria A Mastalieva, Sungat Mukhangali, Aleksandr A Vorob'ev, Aleksandr V Uvarov, Filipp E Komissarenko,*

Dmitry M Mitin, Akanksha Kapoor, Joel Eymery, Nuño Amador-Mendez, Christophe Durand, Dmitry Krasnikov, Albert G Nasibulin, Maria Tchernycheva, Ivan S Mukhin. "Stretchable Transparent Light-Emitting Diodes Based on InGaN/GaN Quantum Well Microwires and Carbon Nanotube Films" Nanomaterials 2021, 11(6), 1503; https://doi.org/10.3390/nano11061503

- *Vladimir Neplokh, Vladimir Fedorov, Alexey Mozharov, Fedor Kochetkov, Konstantin Shugurov, Eduard Moiseev, Nuño Amador-Mendez, Tatiana Statsenko, Sofia Morozova, Dmitry Krasnikov, Albert G Nasibulin, Regina Islamova, George Cirlin, Maria Tchernycheva, Ivan Mukhin*. "Red GaPAs/GaP Nanowire-Based Flexible Light-Emitting Diodes" Nanomaterials 2021, 11(10), 2549;
  https://doi.org/10.3390/nano11102549

- *Nuño Amador-Mendez, Tiphaine Mathieu-Pennober, Stéphane Vézian, Marie-Pierre Chauvat, Pierre Ruterana, Andrey V. Babichev, Fabien Bayle, François H. Julien, Stephane Collin, Bernard Gil, Nicolas Tappy, Anna Fontcuberta i Morral, Benjamin Damilano, Maria Tchernycheva* "Porous nitride light emitting diodes" ACS Photonics , 2022, XXXX,XXX-XXX
  https://doi.org/10.1021/acsphotonics.1c01729

- *B. Damilano, S. Vézian, J. Massies M.P. Chauvat, P. Ruterana, Nuño Amador-Mendez, M. Tchenycheva, P. Valvin, B. Gi* "Selective area sublimation as a top down approach to make porous and dislocation-free" [under revisions]

- *Thejas K.K., Malini Abraham, Arup K. Kunti, Nuño Amador-Mendez, Maria Tchernycheva, Subrata Das* **"**Structurally modified strong deep red $Mg_{3-x}Ba_xM_2GeO_8$: Mn^{4+} (M=Al, Ga) for light emitting diodes" [under revisions]

- *Malini Abraham, Thejas K.K., Arup K. Kunti, Nuño Amador-Mendez, Nishanth K.G., Sushanta Kumar Sahoo, Maria Tchernycheva, Subrata Das,* "Tunable Photoluminescence properties of Mn4+-activated Mg14Ge5O24-xFx phosphors for WLED application" [under revisions]

CONFERENCES

- *Nuño Amador-Mendez*, N. Guan, X. Dai, H. Zhang, V. Piazza, A. Kapoor, C. Bougerol, L. Mancini, F. H. Julien, H. Chalermchai, A. Cattoni, S. Collin, F. Oehler, J.-C. Harmand, J. Eymery, C. Durand and M. Tchernycheva 2018. Flexible Nanowire Light Emitting Diodes. (Poster), Nanostructures for photonics 2018.

- *Nuño Amador-Mendez*, N. Guan, X. Dai, H. Zhang, A. Kapoor, C. Bougerol, L. Mancini, M. Foldyna, S. Das, S. Som, F. H. Julien, J. Eymery, C. Durand and M.

Tchernycheva 2018. Thermal studies and color optimization of white flexible nanowire Light Emitting Diodes. (Oral presentation), International workshop of nitrides 2018.

- *Nuño Amador-Mendez*, N. Guan, X. Dai, H. Zhang, A. Kapoor, C. Bougerol, L. Mancini, M. Foldyna, S. Das, S. Som, F. H. Julien, J. Eymery, C. Durand and M. Tchernycheva 2018. Flexible Nanowire Light Emitting Diodes: White Color optimization. (Oral presentation), Materials Research Society Fall 2018.

- *Nuño Amador-Mendez*, Nan Guan, Junkang Wang, Subrata Das, Akanksha Kapoor, François H Julien, Noëlle Gogneau, Martin Foldyna, Sudipta Som, Joël Eymery, Christophe Durand and Maria Tchernycheva 2019. Colour optimization of phosphor-converted flexible nitride nanowire white light emitting diodes. (Poster), 1D 2D NanoMat .

- *Nuño Amador-Mendez*, Nan Guan, Junkang Wang, Subrata Das, Akanksha Kapoor, François H Julien, Noëlle Gogneau, Martin Foldyna, Sudipta Som, Joël Eymery, Christophe Durand and Maria Tchernycheva 2019. Colour optimization of phosphor-converted flexible nitride nanowire white light emitting diodes. (Poster), Nanowire Week 2019.

DIODES ELECTROLUMINESCENTES NANOSTRUCTUREES A BASE DE NITRURES D'ELEMENTS III

De nos jours, le marché des LEDs est dominé par la technologie des couches minces. Les prototypes existants de LEDs à nanofils (NFs) montrent une efficacité inférieure par rapport à la technologie mature basée sur des films minces. Pour les applications d'éclairage, une forte augmentation de l'efficacité est nécessaire pour être compétitif avec la technologie actuelle. Cependant, pour les applications demandant des nouvelles fonctionnalités, les NFs à base de nitrures ou d'autres types des LED nanostructurées peuvent devenir compétitifs. Pour les gammes spectrales difficiles, telles que les LEDs vert-rouges ou les LEDs UV profonds, les LEDs nanostructurées ou à base de NFs peuvent exploiter leurs propriétés uniques pour répondre aux défis existants. De plus, les LEDs nanostructurées peuvent apporter de nouvelles fonctionnalités qui ne sont pas accessibles en utilisant la technologie des couches minces. Une fonctionnalité intéressante offerte par les LED nanostructurées est la réalisation des LEDs à NFs flexibles à base de matériaux inorganiques, avec une luminescence élevée et une grande durée de vie. La fabrication de dispositifs flexibles à partir de structures en couches minces est assez difficile et nécessite une microstructuration et un décollement de la couche active. Dans cette thèse, deux types de nanostructures de nitrures d'éléments III sont étudiées : (i) une stratégie ascendante utilisant des nanofils cœur/coquille, et (ii) une stratégie descendante utilisant une structure poreuse.

Les nitrures d'éléments III sont la troisième génération de matériaux semi-conducteurs composés d'azote et d'atomes métalliques de la troisième colonne, GaN, InN, AlN, leurs alliages ternaires ou encore un alliage quaternaire. L'importance de ces matériaux pour les applications optoélectroniques provient de leur bande interdite directe et de la possibilité de l'accorder sur une large gamme de longueurs d'onde, du proche infrarouge pour l'InN (environ 1900 nm), l'UV (360 nm) pour le GaN, jusqu'à la gamme UV-C, à savoir 210 nm pour l'AlN [23], [24]. En raison de l'absence de symétrie d'inversion, du caractère ionique partiel de la liaison et de l'arrangement tétraédrique dans la structure wurtzite, les nitrures d'éléments III sont soumis à de forts effets de polarisation conduisant à une polarisation spontanée. La présence d'un champ électrique interne dans les puits quantiques (PQs) conduit à une séparation spatiale des électrons et des trous à l'intérieur du potentiel de confinement, connue sous le nom d'effet Stark confiné quantique (QCSE) [29], [35]–[37]. Le champ électrique interne produit une flexion de bande d'énergie, qui induit deux effets importants sur les PQs : i) un décalage vers le rouge de l'énergie de transition de bande en raison de la modification du niveau d'énergie du porteur confiné, entraînant une réduction de l'énergie de transition et ii) la séparation spatiale des porteurs, réduisant le chevauchement des fonctions d'onde, donc la probabilité de recombinaison ($|\psi|2$), conduisant à une grande durée de vie radiative

et à une efficacité moindre.

Les nanofils sont des structures avec un grand rapport d'aspect qui leur permet de s'adapter au désaccord du paramètre de maille avec le substrat soit par la déformation de la paroi latérale libre, soit, pour les diamètres plus importants, à travers un réseau de dislocations de confinés à l'interface [88]. Ainsi, les NFs sont des monocristaux totalement relaxés et exempts de dislocations qui peuvent croître sur une grande variété de substrats, sans la condition nécessaire d'accord de maille avec le substrat.

Aujourd'hui, toute la technologie flexible est dominée par les semi-conducteurs organiques. Concernant l'optoélectronique, la technologie la plus utilisée pour les LEDs flexibles est celle des LEDs organiques (OLEDs). En effet, les écrans OLED ont déjà été commercialisés grâce à leur faible coût de matière et de traitement et leur bonne flexibilité. De plus, ils sont compatibles avec les substrats en plastique, ce qui simplifie la fabrication et les rend plus adaptés à la production à grande échelle [159].

Cependant, les dispositifs organiques sont confrontés à la dégradation causée par l'oxydation, la recristallisation ou les variations de température, qui dégradent la conductivité électrique des couches organiques, des interfaces et de la région active. De plus, les LEDs organiques dans le domaine visible (en particulier dans la région spectrale bleue) sont limitées en termes de qualité et souffrent d'un vieillissement différentiel, en particulier pour des couleurs différentes.

LEDs FLEXIBLES A BASE DE NANOFILS

Il est avantageux d'utiliser des nanostructures naturellement micro ou nanostructurées, telles que des nanofils. Les nanofils présentent des propriétés mécaniques et optoélectroniques remarquables. Ils peuvent supporter des déformations élevées sans relaxation plastique [179] et ont une empreinte petite par rapport au rayon de courbure de flexion typique. Le rapport d'aspect élevé facilite le décollement du matériau actif par rapport aux films minces ou à d'autres structures fortement attachées à leur substrat comme les nanopyramides. Ces propriétés font des NFs d'excellents candidats pour la fabrication des LEDs inorganiques flexibles.

Les nanofils enrobés dans des polymères combinent le rendement élevé et la longue durée de vie des matériaux semi-conducteurs inorganiques avec la flexibilité et la transparence élevées des polymères. Dans mon travail, des NFs de cœur/coquille MOCVD ont été utilisés pour la fabrication des LEDs bleues et vertes flexibles. Leur combinaison avec des nanophosphors ayant les couleurs d'émission différentes a été utilisée pour la fabrication d'une deuxième génération des LEDs blanches et des LEDs flexibles rouges.

Le processus de fabrication des LEDs flexibles à base de NFs comprend les étapes suivantes : (i) dépôt d'une fine couche métallique semi-transparente sur les coquilles p-GaN pour améliorer l'ohmicité du contact p, (ii) encapsulation en PDMS, (iii) décollement mécanique de la couche composite, (iv) dépôt du contact n métallique, (v) gravure sèche de l'excès de PDMS sur les sommets de NFs, (vi) dépôt par centrifugation de nanofils d'Ag pour former le contact supérieur transparent.

La LED blanche peut être obtenue en mélangeant les trois couleurs primaires de la lumière, rouge, vert et bleu. Une autre façon d'obtenir de la lumière blanche est la conversion conventionnelle de la couleur utilisant de la lumière bleue et un phosphore jaune. Le mélange de la lumière bleue d'une LED et de l'émission jaune d'un phosphore excité par la même lumière bleue donne une émission blanche, bien adaptée aux applications d'éclairage. Sur la base de la LED à NFs flexible bleue, une LED flexible blanche a été produite en ajoutant des nano-phosphores au mélange PDMS où les NFs ont été encapsulés.

Le phosphore est un matériau constitué d'une matrice hôte diélectrique dopée avec un activateur (généralement constitué d'ions de métaux des terres rares) et responsable des gammes de longueurs d'onde d'excitation et d'émission. La LED blanche de première génération a intégré les nanophosphores dans la couche d'encapsulation de PDMS entre les NFs et également dans une couche de surface sur le dessus. Pour l'optimisation des couleurs, cinq luminophores différents ont été testés. Les luminophores ont été fournis par Subrata Das, du CSIR-NIIST dans le cadre d'un projet collaboratif franco-indien CEFIPRA. Deux luminophores sont caractérisés avec une émission jaune (marquée Y2 et Y3), une a une émission orange (O1) et une est verte (G1).

Deux LEDs de pompage différentes avec une teneur en In différente dans les PQs ont été utilisées pour exciter les membranes PDMS dopées au phosphore. Les émissions sont décalées spectralement et ont donc une correspondance différente avec l'absorption des luminophores analysés.

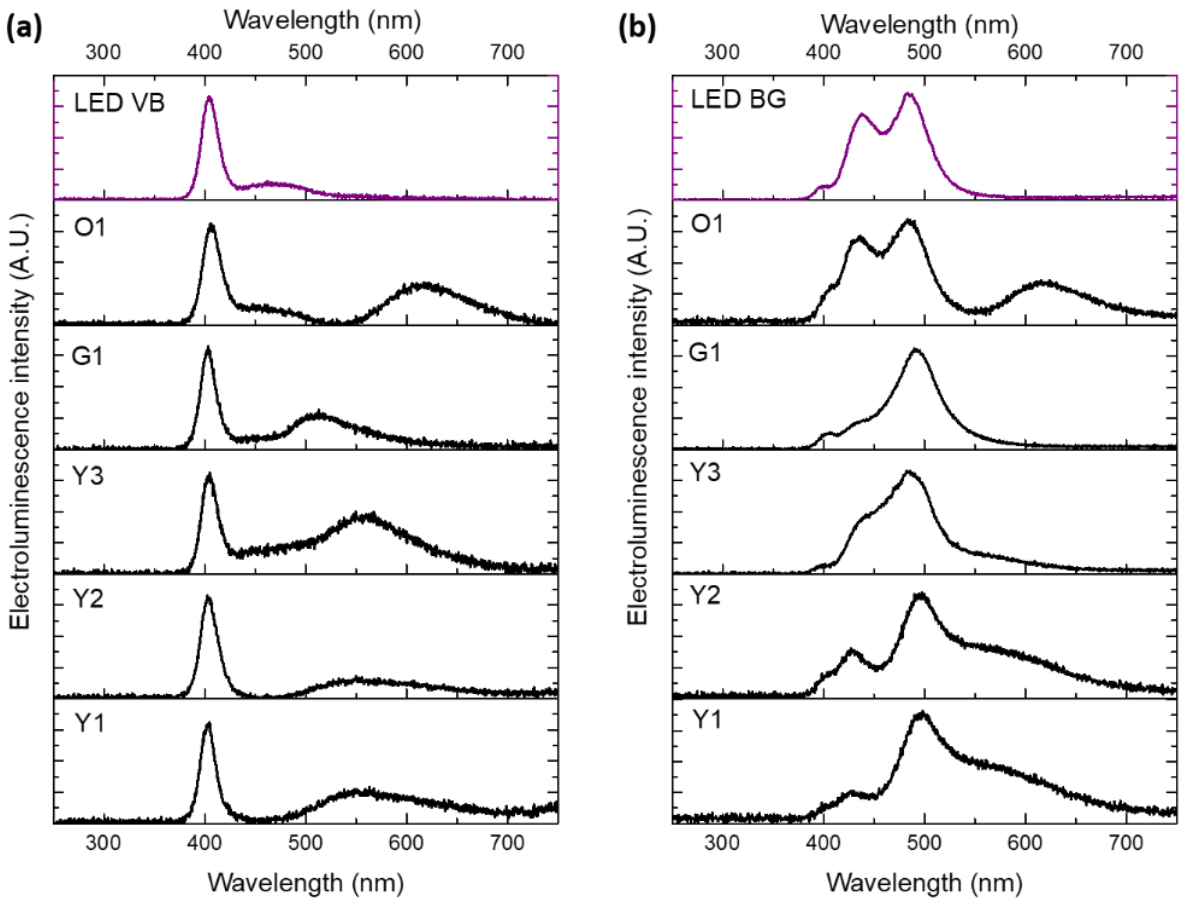

Figure 6. Spectres d'électroluminescence des LEDs de pompage (courbes violettes) et des LEDs flexibles blanches avec les différents luminophores (courbes noires) pompés par (a) LED VB et (b) LED BG [192].

La Figure 6 (b) montre les spectres d'électroluminescence des LEDs blanches pompées avec la LED bleue-verte (BG). Les luminophores Y2, Y3 et G1 présentent une forte absorption de la composante bleue, tandis que les luminophores Y3 et O1 n'absorbent que partiellement le pic bleu de la LED de pompage. Ce résultat est cohérent avec les spectres obtenus pour la LED violet-bleue (VB) montrant l'absorption quasi totale de l'épaulement bleu pour Y2, Y3 et G1, mais présentant un résidu de cet épaulement pour les luminophores Y3 et O1. Pour le pic vert à 485 nm de la pompe LED BG, les spectres blancs pour tous les luminophores montrent un important pic résiduel non converti. Pour G1, l'émission verte de la LED de pompage se confond avec l'émission verte convertie du phosphore, formant un large pic vert centré à 509 nm.

L'un des objectifs de cette étude est d'optimiser la qualité de la lumière blanche produite par les LEDs flexibles et de l'améliorer par rapport à la première génération, en se rapprochant de la lumière naturelle du soleil (CCT=4000-5000 K et CRI=100), qui est également la cible des applications industrielles les plus éclaircissantes.

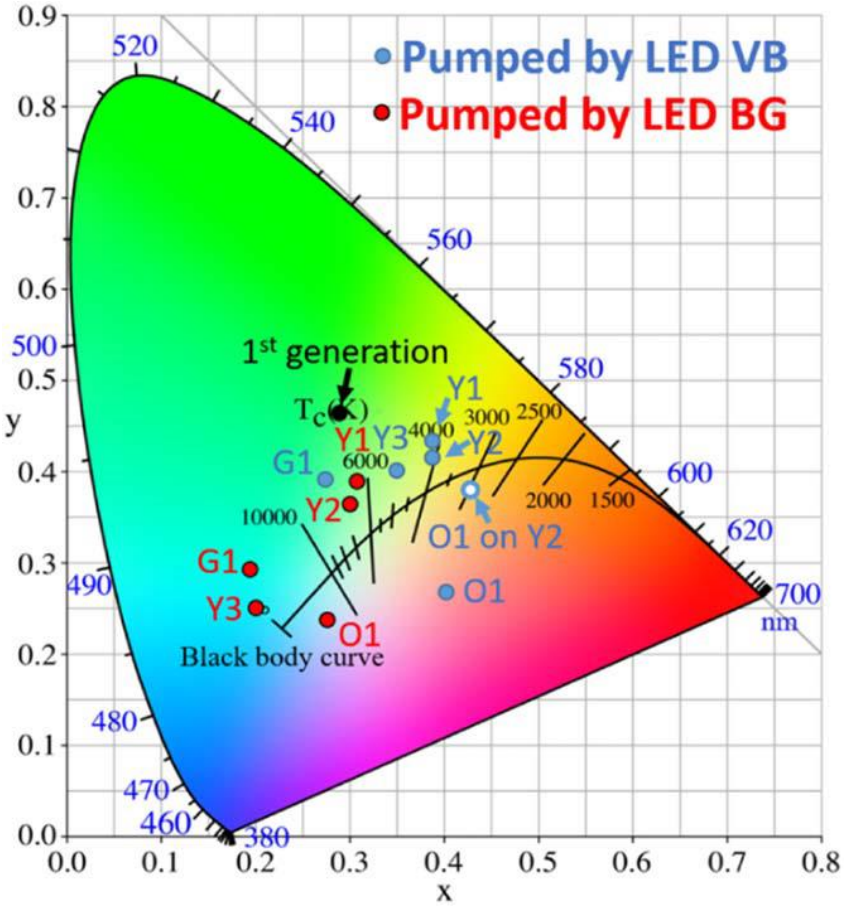

Figure 7. Emplacement des LED blanches flexibles de deuxième génération avec différents luminophores pompés par LED VB (points bleus) et par LED BG (points rouges) par rapport à la première génération (point noir) et à la LED de troisième génération (cercle bleu) dans le diagramme de chromaticité CIE 1931 [192].

La Figure 7 montre que la deuxième génération de LED flexibles blanches est plus proche du locus planckien que la première génération de LED, ce qui signifie qu'elles ont un meilleur CRI. Ces LEDs pompées avec la LED VB sont situées dans la bonne région, blancs chauds, du diagramme de chromaticité CIE 1931, tandis que ces LEDs pompées avec la LED GB sont situées sur des régions plus froides, à des CCT supérieurs à 6000 K. Tous les composants sont situés sur la région supérieure du locus planckien sauf les LEDs avec du phosphore O1, ce qui suggère qu'un mélange de phosphores, utilisant O1, pourrait produire une lumière blanche plus proche du locus planckien, avec un meilleur CRI.

De plus, plusieurs études ont été réalisées concernant les propriétés mécaniques des LEDs flexibles. J'ai également fait des tests mécaniques, prouvant une grande robustesse de ces composants. En plus des tests de flexion, des LEDs flexibles extensibles avec un nouveau contact transparent à base de nanotubes de carbone pré-étiré ont été démontrées [227], ouvrant de nouvelles voies pour des applications optoélectroniques flexibles et extensibles basées sur des LEDs inorganiques. Pour conclure les travaux liés aux LEDs flexibles à base de NFs, une analyse thermique a été réalisée sur les dispositifs, où aucune dégradation n'a été observée lorsqu'un

dissipateur thermique dédié a été utilisé.

Pour la fabrication de LEDs flexibles rouges, différentes stratégies ont été testées, à savoir les NFs à PQs InGaN/GaN riches en In, la conversion par des phosphore rouges et les NFs GaAsP.

La première approche pour la fabrication de LEDs rouges à base de NFs flexibles était conforme aux études précédentes. Nous avons essayé d'utiliser le même matériau que pour les LEDs à NFs flexibles bleues, vertes et blanches, c'est-à-dire l'InGaN. Cependant, comme mentionné précédemment, le contrôle de la composition élevée en In dans le MOCVD est un défi majeure. La croissance de ces PQs dans des NFs à des températures inférieures à 650 °C conduisent à une croissance extrêmement inhomogène. Par conséquent, les LEDs présentent une dispersion de couleur élevée, et il est possible de trouver des NFs émettant du violet au rouge dans le même dispositifs.

Suite à l'expérience réussie décrite précédemment d'utilisation de phosphores pour la down-conversion, j'ai décidé d'utiliser du phosphore rouge sur des LEDs bleues pour obtenir une émission rouge par down-conversion. Parmi tous les ions de métaux de transition, les ions Mn4+ peuvent être le meilleur choix pour les luminophores émetteurs rouges puisque la position spectrale de l'émission rouge (600-790 nm) peut être ajustée par une modification appropriée dans leur environnement de champ cristallin puisque la position de leur émission les pics dépendent de l'hôte utilisé [270]–[272]. Les luminophores dopés Mn4+ ont une large bande d'excitation dans l'UV et dans les régions bleues et fournissent une émission nette dans la région rouge. Pour cette raison, nous avons sélectionné ce type de luminophores dans la présente étude.

Les cinq luminophores différents testés ont un matériau hôte différent et des sites cationiques différents. Ce sont à savoir : trois germanates, deux germanate-oxyde avec un matériau hôte différent, R1 (Li3RbGe7.995O18:0.005 Mn4+) et R2 (Mg14Ge4.99O24:0.01 Mn4+), un germanate-oxyfluorure qui est comme R2 mais substituant huit atomes d'oxygène par le fluor (Mg14Ge4.99O16F8 : 0,01 Mn4+). En raison des rayons ioniques similaires des ions F− et O2-, la formation d'un sous-réseau anionique stable sous forme d'oxyfluorures peut avoir lieu, qui présente d'excellentes propriétés d'absorption et d'émission. Pour explorer d'autres candidats, d'autres sites octaédriques substitutionnels d'éléments de rayon ionique similaire sont considérés, où le dopant d'activation Mn4+, au lieu de Ge4+, substitue Al3+ et Ga3+, dans R4 (Mg2.73Ba0.27Al1.995GeO8:0.005 Mn4+) et R5 (Mg2.87Ba0.13Ga1.995GeO8:0.005 Mn4+), respectivement.

Pour l'intégration du phosphore dans la LED flexible, la même approche utilisée pour l'optimisation de la LED à NFs flexible blanche a été appliquée. Une couche de protection en PDMS de 300 µm a été dopée avec R1, dans un rapport massique de 10:1, et intégrée au-dessus de la pompe à LED bleue. Le spectre

d'électroluminescence de la pompe LED bleue flexible avec une longueur d'onde d'émission centrée à 425 nm est illustré dans la Figure 8 (b) pour un biais appliqué de 8 V. Le spectre d'EL de la combinaison de cette pompe avec le R1 dans PDMS est illustré dans la Figure 8(c). Cette combinaison donne une LED avec deux pics d'émission. Un pic centré à 470 nm, provient de la pompe bleue. L'autre pic provient de l'émission de phosphore rouge à 668 nm, en accord avec l'objectif de convertir la lumière bleue en rouge. Malheureusement, la down-conversion dans ce premier composant était insuffisante et l'émission bleue résiduelle restait plus intense que l'émission rouge. Cette conversion insuffisante peut être due à la mauvaise adaptation spectrale de la LED de pompe et de la bande d'excitation du phosphore. Ceci est illustré sur la Figure 8 (a) montrant le spectre d'excitation du luminophore. On voit que l'émission de la pompe correspond à une partie à faible absorption du spectre d'excitation du phosphore.

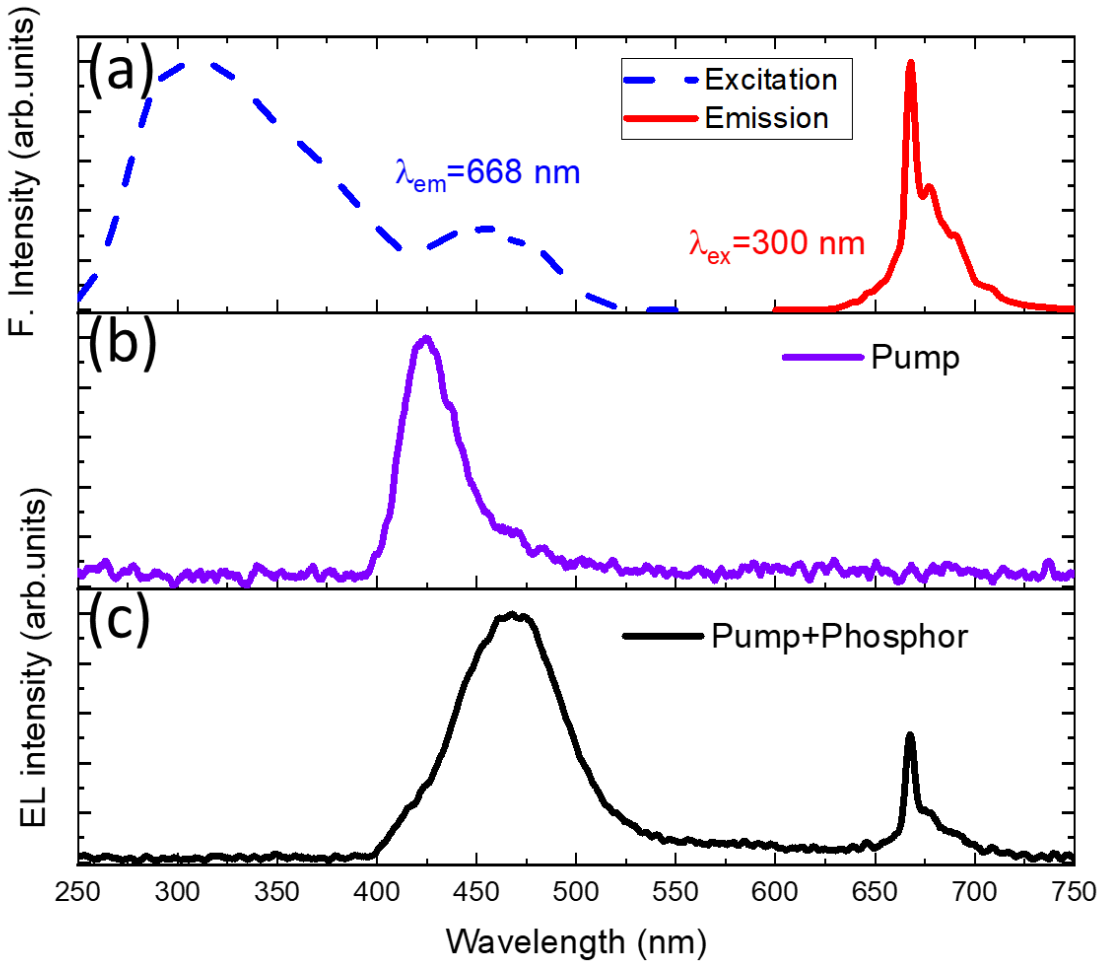

Figure 8. (a) Spectres d'excitation (bleu pointillé) et d'émission (rouge continu) pour le phosphore R1. (b) Spectre EL de la LED à NFs flexible bleue utilisée pour pomper le phosphore et (c) spectre EL de la pompe avec la couche de phosphore.

La troisième voie explorée consiste en la possibilité de remplacer les fameuses LED à couches minces GaAsP par des LEDs à nanofils en vue de dispositifs flexibles. Le département matériaux du C2N maîtrise la croissance des nanofils GaAs et GaP en

utilisant à la fois des modes de croissance auto-assemblés et organisés. Pour l'application LED, la croissance des NFs GaAsP ternaires a été optimisée par un post-doctorant, Himwas Chalermachai.

Pour éviter les défis technologiques du lift-off et du contact transparent flexible, j'ai d'abord réalisé des LEDs à NFs GaAsP suivant une architecture rigide. Les NFs ont été conservés sur leur substrat de croissance, qui a été utilisé pour l'injection d'électrons. Les NFs ont été encapsulés dans une couche de benzocyclobutène (BCB), puis recuits pendant 120 min à 250 °C dans une atmosphère N2 pour la réticulation et le durcissement du BCB. Pour accéder au sommet des NFs, le BCB a été gravé par RIE pendant 120 s pour exposer le haut des NFs. Ensuite, l'ITO a été déposé pour former l'électrode transparente et structuré par lift-off selon un motif préalablement défini par lithographie optique. Enfin, un cadre métallique a été déposée par lithographie et lift-off autour de la mesa pour un meilleur contact. Comme mentionné précédemment, le substrat de Si a été utilisé comme contact inférieur. La morphologie du dispositif résultant est illustrée sur la Figure 9 (a) montrant une image MEB de la partie supérieure du nanofil en contact avec l'ITO.

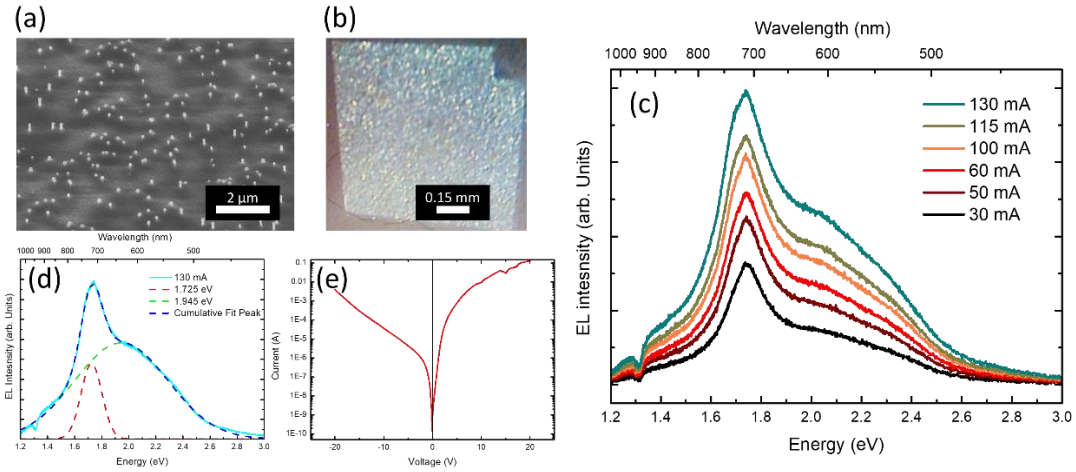

Figure 9. (a) Surface supérieure de la LED à NFs GaAsP encapsulés dans le BCB avec le haut exposé après l'étape de gravure RIE, (b) photo du dispositif en fonctionnement (c) spectres EL du composant à différents courants. (d) Spectre EL à 130 mA avec un montage constitué de deux courbes gaussiennes et (e) courbe IV de la LED en échelle logarithmique.

Cependant, nous avons rencontré un problème à l'étape critique du décollement de cette membrane. En effet, la couche de PDMS dilué est trop fine et fragile, elle se casse lors du décollement, donc aucune membrane de taille macroscopique n'a pu être produite.

Pour fabriquer une deuxième génération de GaAsP, nous nous sommes tournés vers nos collaborateurs de l'Université d'État d'Alferov à Saint-Pétersbourg, qui ont développé un PDMS renforcé. Parallèlement, plusieurs ajustements ont été effectués : (i) la longueur de NFs a été augmentée ; (ii) la concentration de dopage

a été augmentée et l'ordre de dopage a été inversé pour éviter une compensation par diffusion de Be ; (iii) les segments dopés d'alliage ternaire ont été remplacés par des segments de GaP pour éliminer la large émission de fond et (iv) la matrice d'encapsulation a été changée de PDMS dilué en copolymères greffés réticulés de PDMS et de polystyrène (appelés « PDMS-St »). Ce dernier point permet de former des membranes fines pour le pelage grâce à la résistance mécanique renforcée du PDMS-St. Ainsi, la LED flexible rouge a pu être démontré.

LEDs POREUSES

Dans mon travail, j'ai étudié des structures poreuses produites par sublimation sélective (SAS) développées au CRHEA par l'équipe de B. Damilano [85]. En plus de la croissance épitaxiale, cette technique comporte deux étapes qui définissent la morphologie des structures poreuses. Tout d'abord, après la croissance de la structure souhaitée, une fine couche de SiNx est déposée in situ sur la surface (dans le cas de la croissance MBE). Il recouvre partiellement la surface dans le but de protéger localement les régions qui devraient rester dans la structure finale après un recuit à haute température.

La deuxième et dernière étape de la fabrication de la nanostructure est la sublimation des parties non protégées de la structure. L'échantillon est chauffé dans des conditions UHV dans la chambre MBE à haute température (>1000 °C). La couche de SiNx protège la surface couverte tandis que les régions découvertes vont être sublimés, produisant des pores dans la structure épitaxiale [78], [85], [308]. Lorsque la quantité de matériau restant est supérieure à la quantité de matériau sublimé, nous désignerons les structures résultantes comme un matériau poreux.

La première partie de mon étude est centrée sur une hétérostructure simple du type puit quantique InGaN. Nous avons étudié l'effet de la porosification sur un seul PQ InGaN/GaN de 2 nm d'épaisseur sur un tampon GaN mince développé sur un substrat Si. Il est important de souligner qu'il n'y a pas de dopage intentionnel dans les couches de GaN (c'est-à-dire qu'il n'y a pas de jonction p-i-n). L'échantillon a été porosifié par SAS, introduisant des surfaces libres dans les pores qui permettent de détendre la contrainte. La relaxation de la contrainte de compression dans le PQ a un effet majeur sur l'énergie d'émission car elle réduit le champ interne et l'effet Stark confiné quantique. Il en résulte un fort décalage vers le bleu et également une amélioration de l'efficacité de la recombinaison. Cet effet augmente avec la densité des pores, car la relaxation de contrainte devient plus efficace. Un certain impact de la relaxation de contrainte sur l'émission de GaN a également été observé, cependant le décalage résultant de l'émission du bord de bande de GaN est plus faible par rapport au pic du PQ d'InGaN. Concernant l'intensité d'émission du GaN, elle augmente avec la densité des pores en raison de l'excitation directe de la couche tampon à travers les pores. Les études optiques sur les structures simples contenant un PQ unique révèlent une réduction du QCSE sur les échantillons poreux en raison

de la relaxation des contraintes. La quantité d'In du PQ est un facteur critique car elle définit le champ électrique interne, responsable de l'influence du QCSE, et donc de sa réduction, ainsi qu'il a un impact sur l'état de contrainte.

Les analyses de cathodoluminescence (CL) démontrent qu'un recuit à haute température dans des conditions de sublimation ne dégrade pas l'émission du PQ. L'énergie du pic reste quasiment inchangée, tandis que l'échelle spatiale des fluctuations d'intensité n'est que légèrement modifiée.

Pour évaluer la morphologie et la structure des échantillons, des analyses en microscopie électronique de la structure ont été effectuées. Les analyses CL en vue de dessus et en coupe transversale montrent que le processus de sublimation à haute température ne dégrade pas l'émission du PQ sur la structure LED complète, en accord avec les résultats obtenus pour les études optiques dans des structures à puits quantiques uniques. Au contraire, un rétrécissement du pic du PQ et une meilleure homogénéité spatiale sont observés après porosification.

Pour traiter la LED poreuse, la région à faible porosité (8 %) a été sélectionnée. Un soin particulier doit être apporté à l'isolation électrique des pores pour éviter les courts-circuits avant de déposer tout type de contact. Après avoir essayé différents matériaux pour remplir les pores, tels que le SU-8 à faible viscosité (2000.02), HSQ ou BCB, j'ai sélectionné le dépôt d' une couche de 2 µm d'épaisseur de parylène-C sur la surface supérieure qui isole bien les pores. Ensuite, l'excès de parylène a été gravé par un plasma d'oxygène pour découvrir la surface supérieure de p-GaN. En raison des inhomogénéités de la densité des pores à travers la plaque, la couverture de parylène résultante n'était pas homogène, résultant en des régions totalement couvertes par le parylène et des régions surgravées. Il est important de noter que le p-GaN a une profondeur inférieure à 200 nm, la gravure du parylène est donc une étape critique. Dans la partie centrale de l'échantillon, les pores sont encore remplis, nous décidons donc de sélectionner cette région de remplissage de pores optimale pour la caractérisation et de poursuivre la fabrication des LEDs à partir de cette région.

Ensuite, par lithographie optique j'ai défini des mesas carrés de 300 µm de côté, pour déposer le contact transparent supérieur par pulvérisation cathodique ITO et lift-off. Enfin, par une seconde lithographie, j'ai déposé un cadre métallique épaisse Ti/Au (30nm/150nm) à des fins de microsoudure du dispositif. Le contact du bas a été pris sur le substrat de Si. La Figure 4-23 (a) montre le schéma de la LED poreuse.

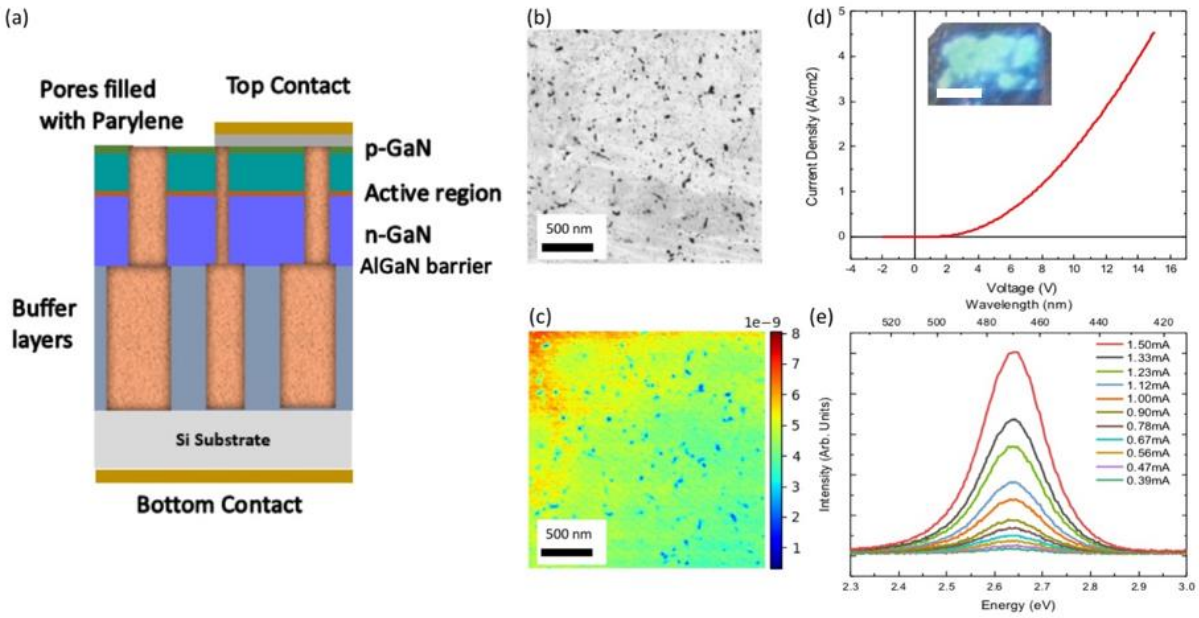

Figure 10. (a) (a) Schéma de la LED poreuse après fabrication ; (b) une image SEM vue de dessus et (c) la carte EBIC correspondante de la LED poreuse ; (d) Courbe I-V de la LED poreuse avec une photo de l'appareil en fonctionnement, la barre d'échelle est de 150 µm et (e) spectres d'électroluminescence pour différents courants d'injection.

L'impact du procédé à haute température, dans une structure LED complète, montre une modification de la réponse optique de l'émission issue du super-réseau déposé sous la région active pour la gestion des contraintes, qui n'est pas pertinente pour l'émission de la LED. Toutefois, l'émission provenant des PQs ne montre pas de modification significative due à l'exposition à des températures élevées.

Une LED entièrement poreuse obtenue par sublimation à haute température a été fabriquée en utilisant une isolation parylène des pores et son électroluminescence est analysée. À notre connaissance, il s'agit de la première LED à base d'InGaN avec une région active entièrement poreuse.